THEORETICAL AND EXPERIMENTAL INVESTIGATION OF AXIALLY GRADED SMART STRUCTURES

A Thesis Submitted in

Partial Fulfillment of the Requirements

for the Degree of

DOCTOR OF PHILOSOPHY

By

VIWEK KUMAR

(Roll No.176103111)

DEPARTMENT OF MECHANICAL ENGINEERING

INDIAN INSTITUTE OF TECHNOLOGY GUWAHATI

GUWAHATI-781039, ASSAM, INDIA

September, 2023

TH-3234_176103111

DEDICATION

I dedicate this thesis to my parents for their endless love, support, and encouragement throughout my academic endeavors. I hope this achievement will fruition their dream.

TH-3234_176103111

Certificate

This is to certify that the thesis entitled "**Theoretical and Experimental Investigation of Axially Graded Smart Structures**" being submitted by **Viwek Kumar** to the Indian Institute of Technology, Guwahati, for the award of the degree of Doctor of Philosophy in Mechanical Engineering is a record of original bonafide research work carried out by him under my supervision and guidance. The thesis work, in my opinion, has reached the requisite standard fulfilling the requirements for the degree of Doctor of Philosophy.

The results contained in this thesis have not been submitted in part or full to any other University or Institute for the award of any degree or diploma.

Dr. Poonam Kumari

Associate Professor

Department of Mechanical Engineering

Indian Institute of Technology Guwahati,

Guwahati - 781039, Assam, India

TH-3234_176103111

Declaration

I, Viwek Kumar (Roll no: 176103111) declare that the present written submission is my thoughts in my own words. I have adequately cited and referenced the original sources, where other's ideas have been involved. I also declare that I have adhered to all principles of academic honesty and integrity and have neither fabricated nor falsified any idea/data/fact/source in my submission. I understand that any violation of the above will be cause for disciplinary action by the Institute and can also evoke penal action from the sources which have thus not been properly cited or from whom proper permission has not been taken when needed.

Viwek Kumar

Date: **Roll No. 176103111**

TH-3234_176103111

Acknowledgements

"Patience is bitter, but its fruit is sweet"– Aristotle

"It does not matter how slowly you go as long as you do not stop"- Confucius

Since I was a young child, these two quotes were taught in school days which have always inspired me to move forward steadily and never to give up in difficult times.

First and foremost, I want to thank the almighty God, my teachers, my parents, and my elders for their blessing, which gave me the strength, wisdom, knowledge, and health that made it possible to pursue my studies so far.

I want to convey my deep gratitude to my Ph.D. supervisor, Dr. Poonam Kumari, for believing in me and allowing me to pursue my research under her supervision. I will always be grateful for her consistent guidance, motivation, patience, kindness, and support over these years. Her passion, exceptional work ethic, analytical skills, and never-give-up outlook on study and life have all fostered my scientific abilities and motivated me to put in a lot of effort. I am proud to have her as my thesis supervisor. Thanks a lot, Ma'am, for all your assistance, advice, and support.

Besides my supervisor, I sincerely acknowledge my doctoral committee members, Prof. K. S. R. Krishna Murthy, Prof. Arbind Kumar Singh, and Dr. Arup Nandy, for their precious time, encouragement, insightful comments, and suggestions that refined and widened my research from various perspectives. My sincere gratitude also goes to the present Head of the Department of Mechanical Engineering, Prof. K. S. R. Krishna Murthy (present), Prof. S. K Dwivedy, and Prof. S. Senthilvelan (former) for providing all the resources needed for my research. I am also thankful to the faculties and staff members of the Mechanical Engineering department who help me whenever needed. Without their help, it would not have been possible to conduct my research. It is an honor to thank the Indian Institute of Technology Guwahati for giving me an excellent opportunity to

TH-3234_176103111

undergo my examination.

I especially acknowledge the Science and Engineering Research Board (India) for financially supporting this research work through the Women's Excellence Award (SB/WEA04/2019). I am also grateful to the Ministry of Education (MOE), Government of India, for providing financial support during my Ph.D. at IIT Guwahati. I would also like to acknowledge the Central Instrument Facility (CIF), Central Workshop, and Material Science Laboratory of IIT Guwahati for providing instruments to perform experimental tests.

Furthermore, I want to thank my seniors and labmates of Smart Materials and Structure Laboratory, Dr. Susanta Behera, Dr. Agyapal Singh, Dr. Sharnish Kar, Dhirendra, Mridusmita, Vaibhav, Abhimanyu, Vaishnavi, Animesh, Tejdeep and Nitin for their timely help. I express a special thanks to my labmates Mukesh Kumar, Abir Saha, and Nikhil Kulkarni for being available in my time of need for suggestions and help. I am indebted to my friends, Vivekananda, Sukanta, Sunil, Pardeep, Sanjay, Priyabrata, Dr. Sujit, Dr. Pranay, Bhavik, Rahul and Antash, with whom I spent joyful time during my hostel days. I am also thankful to my departmental badminton teammates Akshay, Dhiraj, Suraj, Bastav, and Dr. Uttam; with them, I enjoyed precious moments of winning many championships for the department. I am also thankful to my M.Tech friends Vinit, Shashi, Pradyumna, Anurag, and Ankur, who helped me emotionally during the tough time of my life. It is difficult for me to accommodate a long list of my friends who were part of this academic journey, I want to thank everyone for being with me.

My special gratitude goes to my family for their role in my life. I offer my regards to my loving parents, Mr. Kameshwar Prasad Singh and Mrs. Karuna Devi, whose love, teachings, sacrifices, and blessings have brought me this far. I am also grateful to my brothers Rupesh, Diwesh, Amitesh, and Ayush; and sisters Rupa, Komal, Puja, Punam, and Muskan; for their eternal love, support, and respect. Last but not least, I am immensely grateful to Dr. Arpita, who has always motivated and pushed me to stay ambitious. My family, teachers, and friends are the backbone of my happiness, and I dedicate my thesis to them.

Viwek Kumar

TH-3234_176103111

Abstract

The multi-segmented smart structures are a promising and versatile approach to designing complex systems that can be adapted to various applications. They offer greater flexibility, durability, and efficiency than monolithic structures and have the potential to transform the way of building structures. By breaking down a design into smaller segments, it is possible to make repairs or modifications to individual components without affecting the entire system. Additionally, segmented structures can be optimized for specific applications by adjusting the number, size, and shape of the segments. A variety of materials can be used to construct multi-segmented structures, including metals, composites, and polymers. This concept is extensively used in automobiles, aerospace, robotics, locomotive etc., to reduce the structure weight, material and cost. In this, the segments of different high-strength materials like steel are joined with lighter materials like composites. These segments may be joined along the longitudinal or transverse direction within the system. But, it cause formation of interfaces at the segment joints and the generation of stress concentration due to sudden changes in the material. It may result in the failure of structures under different loading conditions. So, to tackle the issue of a sudden change in material properties, an idea was proposed to vary the material properties in a gradual manner along the span or thickness. Such advanced materials are known as functionally graded materials (FGMs). Hence, an appropriate method is required to investigate the behaviour of such structures, which can also serve as the benchmark for their optimal design and fabrication. Although numerical methods and commercial finite element packages are available for a variety of structural problems, there is always a need for analytical solutions. The analytical elasticity models can predict the behaviour of segmented structures more accurately as compared to the one or two-dimensional theories or numerical solutions. The extended Kantorovich method is undoubtedly one of the best techniques that offer an analytical solution for

TH-3234_176103111

complicated problems.

An analytical 2D elasticity solution using the multi-term extended Kantorovich method (EKM) has been presented for the static analysis of multi-segmented dissimilar beams subjected to arbitrary boundary conditions. The beam segments are considered as perfectly joined along the span or axial (x) direction. The segment with different material and length combinations are considered. Reissner's type mixed variation principle is applied to derive the weak form of coupled governing equations in which all the stresses and displacements act as primary variables. Further, the EKM is applied to reduce the governing equations into sets of ordinary differential equations (ODEs) along the axial (x) and thickness (z) directions. The system of ODEs along the z and x-direction have constant coefficients, which are solved analytically. Interface continuity and boundary conditions are satisfied in an exact point-wise manner, which ensures the same order of accuracy for all field variables (stresses and displacements). The efficacy and accuracy of the present methodology are verified thoroughly with a 2D finite element solution. Benchmark numerical results are presented for various cases of material combinations under a different types of boundary conditions. A significant effect of segment length and thickness on the static behaviour of the beam is observed. This development mimics the axially graded behaviour of the beam and is able to predict results accurately.

The developed extended Kantorovich approach is further extended to more complex problems such as in-plane multi-segmented angle-ply flat panels. Benchmark numerical results are presented for single-layered in-plane angle-ply flat panels. The influence of segment material, length and ply-angle variation on the deflections and stresses are studied and discussed comprehensively for arbitrary boundary conditions and configurations. Apart from the above analysis of segmented elastic structures, a piezoelectricity-based analytical solution is also developed for piezoelectric flat laminated panels under arbitrary boundary conditions. The effect of the hard and soft piezoelectric segments on the static behaviour of the panels is investigated. Moreover, a case of linearly graded piezoelectric material is also assumed, which can mimic the axially functionally graded (AFG) behaviour. The presented 2D analytical solution will be helpful in the assessment of various 1D theories and numerical methods. The above analysis is more severe than a homogenous beam and

TH-3234_176103111

panel. The current research will also be beneficial to model real-life panel structures in which their material properties are piece-wise homogenous.

Apart from the analytical and numerical analysis, a fabrication method may be adopted for the experimentation of such structures. In this point of view, a multi-segmented metal-ceramic-based axially graded FGM systems of copper/silicon carbide (Cu/SiC) specimens are fabricated, synthesized and characterized considering various volume percentage of ceramic concentrations through the powder metallurgy route. Apart from the characterization of the powders, ceramic particle distribution, microhardness and effect of ball-milling on the powder is also carried out. Further, the effective elastic properties and modal frequency of the fabricated specimens are obtained using the resonant frequency dynamic analyser (RFDA) technique. A 3D finite element model of the specimen has been modeled in ABAQUS to validate the experimental natural frequencies under different modes. A percentage difference in the experimental and numerical frequencies are presented and discussed for different specimens.

TH-3234_176103111

Contents

Certificate i

Declaration ii

Acknowledgements iii

Abstract v

List of Symbols xvii

1 Introduction 1

1.1 PREFACE 1

1.2 HYBRID AND MULTI-MATERIAL STRUCTURES 3

1.3 AN OVERVIEW ON FGMs 5

1.3.1 A Brief History of FGMs 5

1.3.2 Classification of FGMs 7

1.3.3 Fabrication Methods of FGMs 8

1.3.4 Applications of FGMs 12

1.4 SMART STRUCTURES 14

1.5 MOTIVATION 15

2 Literature Review 16

2.1 REVIEW FOR ANALYSIS OF MULTI-MATERIAL, FGM AND SMART STRUCTURES 16

2.1.1 Static and Dynamic Solutions for Multi-material and FGM Structures 16

TH-3234_176103111

2.1.2 Based on Elasticity Solution 17
2.1.3 Based on Analytical Solution 20
2.1.4 Based on Numerical Solution 23
2.1.5 2-D Solutions for Smart Structures 26
2.2 REVIEW ON FABRICATION METHODS OF FGMs 27
2.2.1 Powder Metallurgy 27
2.2.2 Spark Plasma Sintering (SPS) 29
2.2.3 Laser Metal Deposition (LMD) 30
2.3 EVALUATION OF EFFECTIVE MATERIAL PROPERTIES 31
2.4 OBJECTIVES OF THE PRESENT WORK 33
2.5 ORGANISATION OF THE THESIS 34

3 Two-Dimensional Bending Solutions for the Multi-Segmented Dissimilar Beams 37

3.1 INTRODUCTION 37
3.2 THEORETICAL FORMULATION 39
3.3 THE GENERALIZED MULTI-TERM EKM 42
3.3.1 First Iteration Step 42
3.3.2 Second Iteration Step 44
3.4 NUMERICAL RESULTS AND DISCUSSIONS 45
3.5 SUMMARY 54

4 2-D Analytical Solutions for the Bending of Multi-Segmented Panels 55

4.1 INTRODUCTION 55
4.2 THEORETICAL FORMULATION 57
4.3 THE GENERALIZED MULTI-TERM EKM 60
4.3.1 First Iteration Step 60
4.3.2 Second Iteration Step 62
4.4 NUMERICAL RESULTS AND DISCUSSIONS 64
4.5 SUMMARY 77

TH-3234_176103111

5 Two-Dimensional Bending Solutions for the Multi-Segmented Dissimilar Piezoelectric Panels **78**

5.1 INTRODUCTION . . . 78

5.2 THEORETICAL FORMULATION . . . 80

5.3 INTERFACE AND BOUNDARY CONDITIONS . . . 83

5.4 THE GENERALISED EKM . . . 84

5.4.1 First Iteration Step . . . 85

5.4.2 Second Iteration Step . . . 87

5.5 NUMERICAL RESULTS AND DISCUSSIONS . . . 88

5.6 SUMMARY . . . 97

6 Fabrication and Characterization of Cu/SiC Based Axially Functionally Graded Beam **98**

6.1 INTRODUCTION . . . 98

6.2 EXPERIMENTATION . . . 99

6.2.1 Material System . . . 99

6.2.2 Preprocessing of Raw Materials . . . 99

6.2.3 Powder Blending or Mixing . . . 100

6.2.4 Powder Compaction . . . 100

6.2.5 Sintering . . . 103

6.3 RESULTS AND DISCUSSION . . . 103

6.3.1 Powder Characterization . . . 103

6.3.2 Characterization of Cu/SiC Specimens . . . 111

6.3.3 Hardness Test . . . 115

6.4 SUMMARY . . . 115

7 Evaluation of Elastic Property for Axially Graded Powder Metallurgy Specimen by RFDA **117**

7.1 INTRODUCTION . . . 117

TH-3234_176103111

7.2 SYNTHESIS OF SPECIMENS 118
7.3 WORKING OF RFDA AND EXPERIMENTATION 118
7.4 NUMERICAL RESULTS AND DISCUSSION 121
7.5 SUMMARY 126

8 Conclusions **127**

8.1 CONCLUSIONS FROM THE PRESENT WORK 128
8.2 FUTURE SCOPE OF WORK 133

TH-3234_176103111

List of Figures

1.1 Modern automobile body consisting multi-material (Naito and Suzuki [1]) 3

1.2 Historical development in the field of FGMs (Saleh et al. [9]) 5

1.3 Particle distribution in ordinary composite and FGM (Somiya [11]) 6

1.4 Variation of material in FGMs 8

1.5 Showing different gradient of FGMs based on: (a) fraction (b) shape (c) orientation and (d) size (El-Wazery and El-Desouky [18]) 9

1.6 Powder metallurgy processing steps 11

1.7 Applications of FGM in various sectors (Saleh et al. [9]) 13

2.1 FG beam under bending for different approximation numbers (Giunta et al. [41]) . . 18

2.2 Showing variation of transverse displacement for FG beam using different theories (Filippi et al. [42]) 18

2.3 Showing static FE analysis of bi-directional functionally graded sandwich plates under thermal loading (Nguyen et al. [121]) 24

2.4 Showing variation of Young's modulus through FE analysis of FG plate (Amirpour et al. [128]) 25

3.1 A flowchart of EKM approach for edge bonded beam 38

3.2 Geometry of the axially segmented beam 40

3.3 Configuration lay up for beams (S= 5) 46

3.4 Showing meshed beam 47

3.5 Variation of deflections and stresses for Al/Gr-Ep beam (a) with S=5 48

3.6 Variation of deflections and stresses for Al/Gr-Ep beam (b) with S=5 50

TH-3234_176103111

3.7 Variation of deflections and stresses for Steel/Gr-Ep beam (c) with S=5 51
3.8 Variation of shear stresses for Steel/Gr-Ep beam (c) with S=5 51
3.9 Variation of deflections and stresses for four segmented Al/Sic beam (d) with S=5, 10 and 20 52
3.10 Variation of shear stresses for four segmented Al/Sic beam (d) with S=5, 10 and 20 53
3.11 Variation of stresses for Steel/Gr-Ep beam (c) with S=5 53
3.12 Variation of shear stresses for Steel/Gr-Ep beam (c) with S=5 54
3.13 Variation of shear stresses for Steel/Gr-Ep beam in ABAQUS under CC case 54

4.1 A flow chart of EKM approach for multi-segmented panel 56
4.2 The multi-segmented panel geometry. 57
4.3 Panel configurations 65
4.4 Meshed panel geometry 66
4.5 Variation of deflections and stresses along the length for panel (a) with S=5 68
4.6 Variation of stresses along the length and thickness for panel (a) with S=5 69
4.7 Variation of deflections and stresses for panel (b) with S=5 70
4.8 Variation of deflections and stresses along the length for panel (c) with S=5 71
4.9 Variation of shear stresses along the length for panel (c) with S=5 72
4.10 Variation of deflections and stresses along the length for panel (d) 72
4.11 Variation of shear stresses along the length for panel (d) 73
4.12 Variation of deflections and stresses along the length for 30 degree angle-ply panel (a) with S=5 74
4.13 Variation of deflections and stresses along the length for 45 degree angle-ply panel (a) with S=5 75
4.14 Effect of ply-angles on the stresses for panel (a) with S=5 76

5.1 A flowchart of EKM approach for segmented piezoelectric panel 79
5.2 Geometry of the piezoelectric panel 80
5.3 Configuration lay-up of piezoelectric panel under S-S case 89

TH-3234_176103111

5.4 Showing meshed panel 91

5.5 Longitudinal variation of deflections, stresses, electric potential and $\bar{D}_z$ for single layer piezoelectric panel (a) under S-S condition 91

5.6 Longitudinal variation of deflections, stresses, electric potential and $\bar{D}_z$ for two segmented piezoelectric panel (b) 92

5.7 Longitudinal variation of deflections, stresses, electric potential and $\bar{D}_z$ for two segmented piezoelectric panel (b) 94

5.8 Longitudinal variation of deflections, stresses, electric potential and $\bar{D}_z$ for four segmented piezoelectric panel (c) 95

5.9 Longitudinal variation of deflections, stresses, electric potential and $\bar{D}_z$ for four segmented piezoelectric panel (c) 96

6.1 (a) Test sieves (b) Sieve shaker (c) Mono-ball milling machine (d) Zirconia balls (e) Grinding jar and (f) Intial Cu powder and ball-milled mixed Cu/SiC 101

6.2 (a) Uni-axial compaction at UTM (zoomed view) (b) Rubber molds (c) Sealed rubber mold for compaction (d) CIP unit (e) Cu/SiC green specimen (f) Sintered and polished specimen 102

6.3 Powder XRD plots 105

6.4 Scherrer plots for: (a) Initial Cu powder (b) Ball-milled Cu powder and (c) Ball-milled Cu/SiC (90/10) 107

6.5 Williamson-Hall UDM plots for: (a) Initial Cu powder (b) Ball-milled Cu powder and (c) Ball-milled Cu/SiC (90/10) 108

6.6 TEM images showing: (a) Inter-planar spacing for (111) plane (b) SAED pattern and (c) Ball-milled Cu grain morphology 109

6.7 FESEM images: (a) Initial Cu powder (b) Ball milled Cu powder and (c) Initial SiC powder 110

6.8 Showing optical microscope images of the specimen (a) 100/0 layer (b) 90/10 layer (c) 80/20 layer 112

TH-3234_176103111

6.9 Showing FESEM results of 3-layered sintered Cu/SiC specimen (a) 100/0 layer (b) 90/10 layer (c) 80/20 layer 113
6.10 Showing EDS results of 80/20 layer for different spectrums 113
6.11 Showing mapped EDS results for spectrum 3 114
6.12 SiC content Vs Hardness value plot of the sintered sample 115

7.1 (a) Cylindrical rubber mold and (b) Sintered Specimens 118
7.2 Showing weight of (a) Specimen S1 (b) Specimen S2 (c) Specimen S3 (d) Specimen S1 length and (e) Specimen S2 diameter 119
7.3 Showing schematic diagram of RFDA working set-up 120
7.4 RFDA in working 121
7.5 Recorded signal for specimen S1 121
7.6 Showing FE flexural mode shape of S1 for Mode 1 122
7.7 Showing FE flexural mode shape of S1 for Mode 2 123
7.8 Showing FE flexural mode shape of S2 for Mode 1 123
7.9 Showing FE flexural mode shape of S2 for Mode 2 124
7.10 Showing FE flexural mode shape of S3 for Mode 1 124
7.11 Showing FE flexural mode shape of S3 for Mode 2 125

TH-3234_176103111

List of Tables

1.1 Comparison Between FGMs and Other Materials 7

3.1 Material Properties 46

4.1 Material Properties 64

5.1 Material Properties 89

6.1 Properties of FGM constituents (Metal-ceramic and binders) 99

7.1 Specimen dimensions 119

7.2 Experimental results for specimens S1, S2 and S3 122

7.3 % difference in natural frequencies 125

TH-3234_176103111

List of Abbreviations

EKM = Extended Kantorovich Method

FGM = Functionally Graded Material

PZT = Lead Zirconate Titanate

PFRC = Piezoelectric Fiber Reinforced Composite

ODEs = Ordinary Differential Equations

MEKM = Multi-term EKM

Gr-Ep = Graphite-Epoxy

FE = Finite element

FEA = Finite Element Analysis

FEM = Finite Element Method

Al = Aluminium

Cu = Copper

SiC = Silicon Carbide

PVA = Poly-Vinyl Alcohol

CIP = Cold Iso-static Pressing

UTM = Universal Testing Machine

XRD = X-ray Diffraction

FESEM = Field Emisson Scanning Electron Microscopy

EDS = Energy Dispersive Spectroscopy

TEM = Transmission Electron Microscope

FFT = Fast Fourier Transform

RFDA = Resonant Frequency Dynamic Analyzer

TH-3234_176103111

Chapter 1

Introduction

1.1 PREFACE

Scientists and researchers have recently focused on developing eco-friendly and fuel-efficient vehicles to reduce carbon footprints. In this aspect, electric and hybrid electric vehicles play a very significant role. But, these electric vehicles have heavy batteries and engines, making them bulky and less efficient. Therefore, the vehicle weight is reduced up to a certain extent by implementing multi-material concepts. The traditional monolithic materials, like steel, aluminum, etc., are joined with lighter composite laminated materials. This strategy has prompted the engineers to decrease weight while enhancing environmental friendliness, fuel efficiency, and safety performance. Moreover, dissimilar materials joining, like composite laminated materials combined with lightweight metals, has been extensively used in the aerospace, aviation, defense, and automotive industries. The automotive components often need the materials segment to be aligned and joined along the span. The prosthetic limbs, impellers, turbine blades, etc., are also designed to have material variation along the length for better performance and suitability. In practicality, producing or manufacturing components with very smooth variations along the length is not always possible. During operation, these structural members are subjected to different loading and support conditions. Therefore, at the joining or interface point, local in-plane and transverse stresses rise sharply and may cause debonding and failure of structures. So, the designers must study and analyze the behavior in such conditions for better reliability of the systems. Researchers have developed various theories for axially graded structures where material properties vary linearly, exponentially, or by power law along the longitudinal direction. But in reality, the material property does not follow

TH-3234_176103111

any particular variation for the above cases. Therefore, such problems cannot be analyzed using functionally graded theories/concepts. Hence, an appropriate method is needed to investigate the static and dynamic behavior for optimal design and performance. One-dimensional analysis based on classical assumption or higher order can not accurately predict the stress behavior at these places. The analytical elasticity models can predict stress behavior more accurately. Therefore, this research proposed an accurate analytical elasticity solution for static analysis of dissimilarly joined multi-segmented structures. A 2-D closed-form solution has been developed to analyze the mechanical behavior of dissimilarly joined structures under transverse loading. Moreover, this technique is also capable of analyzing the structuresthat mimic an axially graded behavior. However, numerous fabrication methods are developed for the functionally graded systems, which have gradation along the thickness direction. In such scenarios, the thickness is minimal compared to length and width, making fabrication easy. For real-time application, a processing technique should also be adopted to fabricate an axially graded structure. But, in this case, processing parameters, fabrication procedures, die design, etc., will be different, which makes it challenging. The experimental investigation on this issue is still unavailable. Hence, in this research work, an attempt is made to develop a processing technique and evaluate the elastic properties of an axially graded beam.

This thesis presents **a**) development of a 2-D closed-form solution to analyze the bending behavior of multi-segmented beams made with different materials and segment lengths under different support conditions, **b**) analytical solution for different configurations of multi-segmented panels and an effect of ply-angles on the bending behavior of panel under various support conditions, **c**) development of 3-D piezoelectricity to analyze the static bending behavior of different piezoelectric panel configurations, **d**) synthesis of metal-ceramic based axially graded FGM beams using powder metallurgy route, material characterization and mechanical testing of the specimens and **e**) evaluation of elastic property and natural frequencies of the fabricated specimens using the non-destructive RFDA technique.

In this chapter, a brief discussion on the multi-material structure is presented in Sec. 1.2, fabrication methods and applications of functionally graded materials (FGMs) in Sec. 1.3 and smart structures in Sec. 1.4.

TH-3234_176103111

1.2 HYBRID AND MULTI-MATERIAL STRUCTURES

Hybrid structures combine two or more different materials or components to create a structure with unique properties and performance characteristics. The materials can be combined in various ways to create structures with unique characteristics and functions that cannot be achieved with a single material. This design creates a structure that is both strong and lightweight, making it ideal for applications such as marine vessels, aerospace, automobiles, construction, biomedical, etc. An automobile body consisting of different materials is shown below in Fig. 1.3, which is to save material, reduce weight, and improve strength.

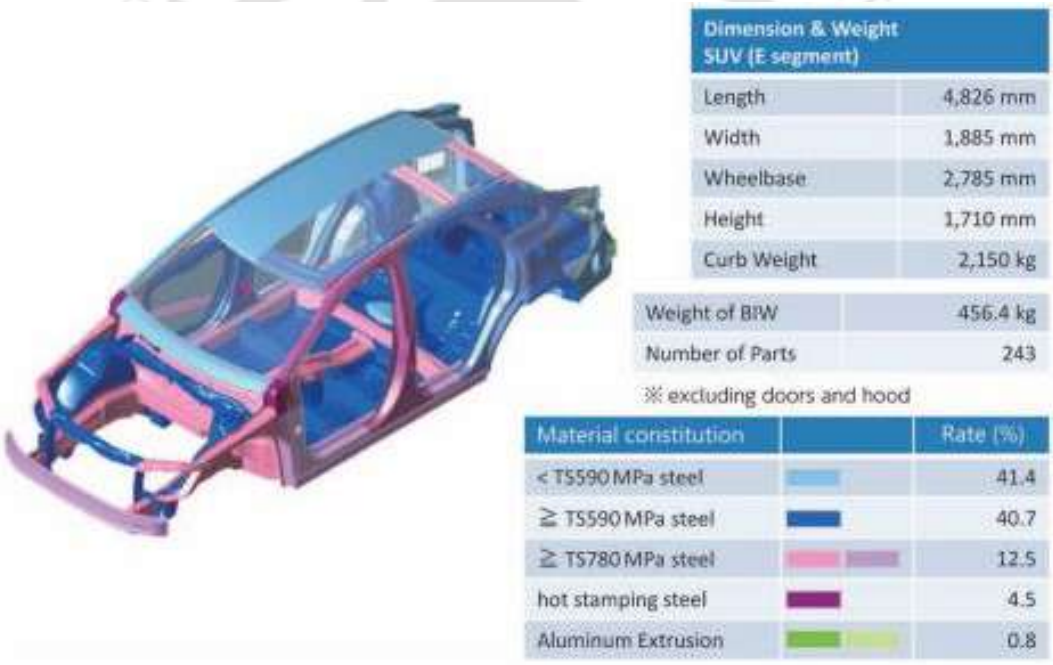

Fig. 1.1: Modern automobile body consisting multi-material (Naito and Suzuki [1])

Hybrid structures have been used for centuries in various forms and have become popular in engineering and materials science advancement. It makes it possible to create more robust and durable hybrid constructions. One notable example of a hybrid structure is the Eiffel Tower, which was built in 1889 using a combination of wrought iron and steel [2]. In the mid-20th century, advances in computer-aided design and manufacturing allowed for the creation of even more complex hybrid structures, such as bridges and tunnels, that combine multiple materials and building techniques to create strong and lightweight structures. Today, hybrid structures continue to be

TH-3234_176103111

used in a wide range of applications, where they may combine metal and composite materials. This type of combination provides high strength and stiffness of composite materials with the toughness and ductility of metals. Hence, the resulting structure can have a high strength-to-weight ratio, making it ideal for aerospace applications where weight is critical. Furthermore, hybrid structures may also be used to create structures that are resistant to extreme conditions, such as high temperatures, radiation, or corrosive environments. A hybrid ceramic-metal structure can be used in high-temperature applications where ceramics provide the necessary heat resistance while the metal provides the necessary ductility and toughness [3]. Multi-material structures can be designed for specific functions, which can change their functionality in response to load or temperature change. Moreover, it can also be used to develop smart structures that behave distinctively in response to external stimuli such as light, load, heat, or electric fields.

Some of the advantages of multi-material structures over traditional structures are listed as:

1. Improved structural performance: The combination of different materials in multi-material structures results in improved structural performance. For example, a metal-polymer structure has the high strength and stiffness of metal and the damping and noise reduction of polymer.

2. Light weight: Multi-material structures can be designed to be lighter than traditional structures, which can lead to reduced fuel consumption in transportation applications.

3. Increased durability: Multi-material structures can be designed to be more durable than traditional structures, which can lead to longer service life and reduced maintenance costs.

4. Design flexibility: These structures also offer greater design flexibility than traditional structures, as different materials can be combined in various ways to achieve the desired performance and aesthetics.

Apart from the advantages, these structures also possess a few disadvantages like complexity in design, compatibility of materials, cost of the materials used, requirement of skilled workers for the design, etc.

TH-3234_176103111

1.3 AN OVERVIEW ON FGMs

1.3.1 A Brief History of FGMs

FGMs are not new to nature; human beings have been using them since their evolution for different purposes, such as hunting, decoration, construction, etc. Some natural FGMs, like bamboo, bones, teeth, human skin, sea shells, etc., existed for decades, but researchers learned about these in the 19th century. Some theoretical work based on designing and implications of graded composite structures had reported in the 1970s, but due to limited fabrication methods, the development in this field was delayed [4]. According to many authors [5–7], the first idea of FGMs was proposed in the mid of 1980s by Japanese researchers during a space-plane project at National Aerospace Laboratory (NAL) in Japan. Here, the composite materials were tested for thermal barrier application to work under a very high-temperature gradient, i.e., the inner and outer surface temperature was at 1000K and 2000K, respectively, and had a thickness of 10mm. But, it was found that the composite materials were unable to withstand such conditions because of inadequate adhesion and the abrupt change in thermal stress at the sharp interface of materials (due to mismatch of mechanical properties) [8]. So, a concept was proposed to eliminate this sharp interface with the gradually changing interface. This progressive change in the properties of one material to another material is named as FGMs. The year-wise historical development in the field of FGMs is shown below in Fig 1.2.

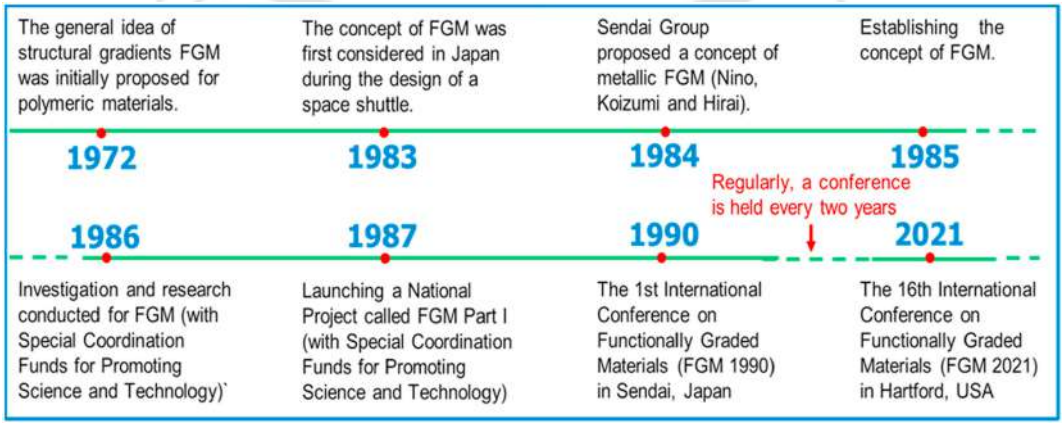

Fig. 1.2: Historical development in the field of FGMs (Saleh et al. [9])

Metal-ceramic-based FGMs are very popular for thermal barrier applications because ceramics

TH-3234_176103111

can withstand high temperatures, and a high thermally conductive metal is used as a matrix (to support the ceramics and dissipate heat). Such FGMs possess an alternating layer of ceramic and metal with a gradually increasing ceramic content from the surface to the core. This arrangement of material distribution improves fracture toughness and thermal shock resistance compared to homogeneous ceramics [10]. A difference between the compositions and properties of ordinary composite material and FGM is shown in Fig. 1.3. A distinct interface between metals and ceramics in an ordinary composite material can be seen, but not in an FGM. This difference greatly affects to the distribution of properties such as thermal expansion coefficient, thermal conductivity, and thermal resistance. It has been reported that an FGM may reduce thermal stress by almost 30% and can prevent the destruction of the interface [11]. In recent years, rapid growth in using FGMs

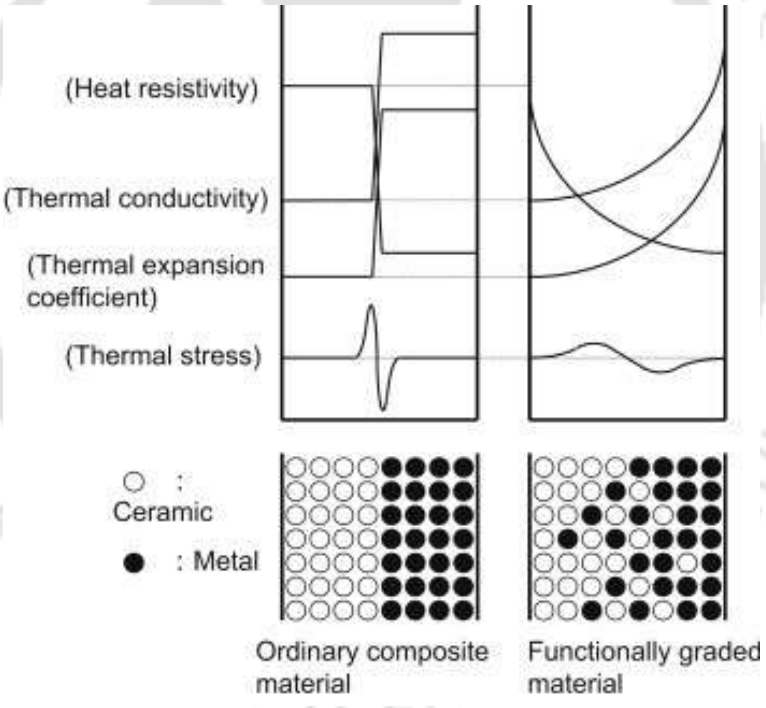

Fig. 1.3: Particle distribution in ordinary composite and FGM (Somiya [11])

in a variety of applications, such as thermal and corrosion barriers, dental implants, orthopedic implants, sensors, lightweight armor, vehicles, etc., can be found. It is also observed by many researchers [12–16] in their study is that an advanced configuration with a graded property will guide a structure to collapse in a more controlled manner and have a remarkable energy-absorbing efficiency compared with traditional uniform structures and materials. Li et al. [17] analyzed that a

TH-3234_176103111

functionally graded tube with a graded wall thickness possesses a high geometric efficiency and energy absorption capacity than a tapered and straight uniform tube under oblique impact loadings. Thus, in automobiles, materials properties and dimensions with a gradient are provided for a better energy absorbing capacity, which improves the crashworthiness performance. Moreover, it is also possible to make a high-performance adaptive structure by combining FGM substrate with piezoelectric sensors and actuators. The FGMs offer several advantages over other materials in various engineering applications. Some of the key properties that make FGMs useful and advantageous over other materials are shown below in Table 1.1.

Table 1.1: Comparison Between FGMs and Other Materials

Sl. no.	Basis	FGMs	Isotropic Material	Composite Material
1	Composition	Gradual variation of properties	Uniform	Two or more materials
2	Properties variation	Tailored to meet specific needs	Constant properties	Combination of properties
3	Performance	Improved performance in gradients	Consistent performance	Tailored performance
4	Interface properties	Smooth transition at material interfaces	Sharp interfaces	Discontinuities at interfaces
5	Manufacturing	Complex processing techniques	Simple manufacturing	Requires mixing or bonding
6	Cost	Higher cost	Standard cost	Varies with requirement
7	Applications	Aerospace, implants, thermal barriers, etc.	General engineering	Automotive, sports equipment, etc.

1.3.2 Classification of FGMs

The overall properties of FGMs are unique and distinct from the constituting materials that form it. FGMs majorly classified into three broad categories, which are illustrated below as:

(a) Based on the variation of material in FGMs: The variation of the constituent in the FGM can be continuous or step-wise. In the continuous variation, the gradation of the constituents phase changes continuously, whereas in the case of stepwise, the constituents phase changes in a discontinuous manner, such as in steps or layer-by-layer.

(b) Based on the fabrication process: FGMs can be fabricated either in bulk form (large volume of material) or as a thin film of coating (applied over the surface). Bulk forms of FGMs can

TH-3234_176103111

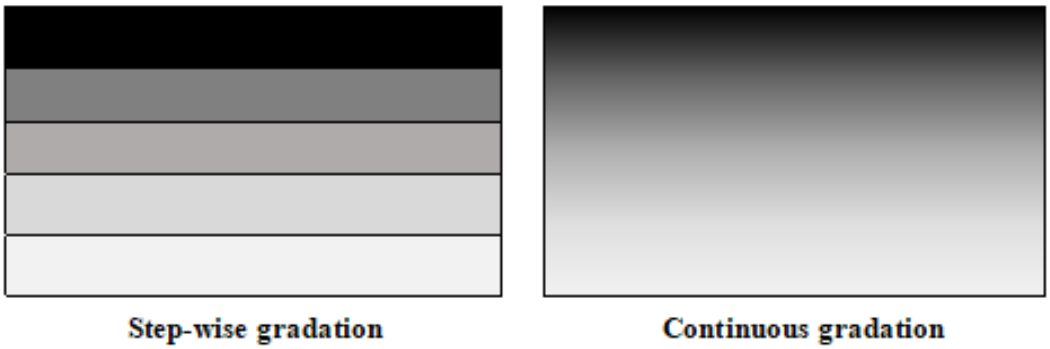

Fig. 1.4: Variation of material in FGMs

be prepared by powder metallurgy, centrifugal casting, solid freeform technique, etc., whereas thin FGMs are prepared by thermal spraying, physical deposition, chemical deposition method, etc.

(c) Based on the gradient of FGMs: FGMs are divided into three major categories on the basis of gradient, which are as follows:

i. Chemical composition gradient FGMs: In such types of FGMs, the chemical composition of the constituents, either in single-phase or multi-phase, varies gradually according to the spatial position in the material.

ii. Porosity gradient FGMs: In this variety of FGMs, porosity in the material changes according to the spatial location. Based on the requirements, the shape and size of the pores in the material can be designed and varied. These types of FGMs are commonly used in biomedical applications because porosity helps in the healing of implants, improves the strength of implant materials, reduces the bio-implant density, etc.

iii. Microstructure gradient FGMs: This type of FGMs graded in such a way that the different microstructures can produce gradually and can achieve the final required characteristics in the material. The controlled heat treatment process can prepare this type of FGMs, which can be applied where material with hard surface properties is needed (e.g., bearings, shafts, cams, gears, etc.).

1.3.3 Fabrication Methods of FGMs

FGMs can apply in the form of a coating over the surface or used as a bulk form of material. The FGMs coating is used over the surface to improve the surface properties, whereas, the bulk form

TH-3234_176103111

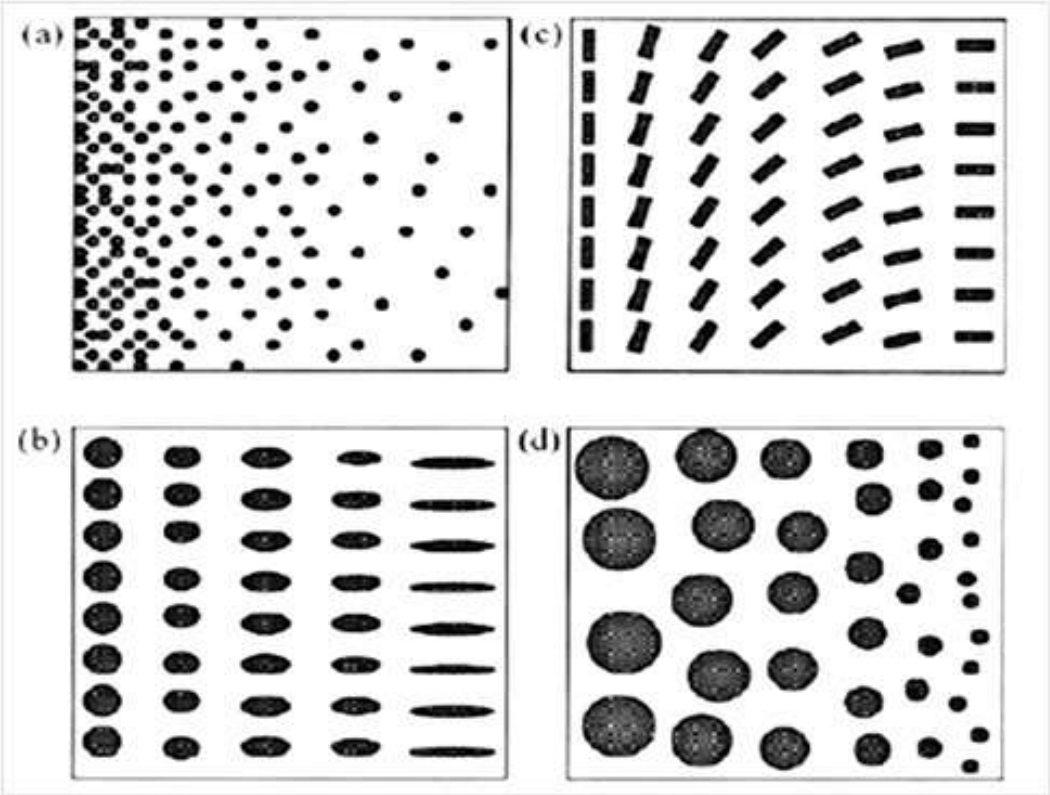

Fig. 1.5: Showing different gradient of FGMs based on: (a) fraction (b) shape (c) orientation and (d) size (El-Wazery and El-Desouky [18])

of FGMs has been designed with varying microstructure, compositions, and, properties across the volume. Based on the materials, their applications, and feasibility, various physical and chemical methods are available to fabricate the FGMs. Material property variation in FGMs much depends on the fabrication techniques and process parameters. Some updated processing techniques are illustrated as below:

i. Physical Vapor Deposition (PVD): This process is employed for the fabrication of vaporization-based thin-film coating. In this process, the solid material used to condensed into atomized vapor form, and that vaporized material is deposited over the surface, which needs to be coated [19]. There are many methods of vaporization for solid material, such as evaporation-based PVD, sputtering-based PVD, plasma spray PVD system, chemical vapor deposition (CVD), ion beam assisted deposition (IBAD), self-propagating high-temperature synthesis (SHS), etc. Above mentioned process gives a very excellent microstructure and material properties of the surface.

Advantages: Provides better coating and microstructure on the surface, conductor material in

electronic circuits can be deposited, easy to use, low operating cost, etc.

Disadvantages: Not preferred for bulk FGMs manufacturing, mainly used for thin-film coating, the vacuum chamber is required in some processes, which increases the operation cost, etc.

ii. Centrifugal Casting Method: This is also a bulk FGMs fabrication method. In this method, FGMs manufactured by spinning the mold using gravitational forces. The molten material with another reinforced material (molten or solid) is poured inside a rotating die. This rotation develops a centrifugal force, which helps to separate the lighter material from heavier material due to density difference [20]. The compositional gradient is created due to this density difference in FGMs.

Advantages: FGMs part with continuous gradation can produce, the best method for making cylindrical objects suitable for mass production, homogenous distribution, etc.

Disadvantages: Can produce only cylindrical sections, gradation affected by the densities of constituent materials because it depends on centrifugal force, etc.

iii. Powder Metallurgy: It is a prevalent and widely used process to fabricate bulk FGMs. This process includes a series of operations, first preparation of the powder (weighing, mixing, gradation, etc.), stacking and compaction of powder, and finally, sintering process [21]. Powder of metals, alloys, ceramics, polymers, etc., are prepared by various means, such as atomization, grinding, pulverization, etc. Then as per the service requirement of FGMs, these powders are mixed in appropriate proportion and with tolerable particle size. After mixing, these mixed powders are stacked in a die and compacted using a ram under adequate pressure. Then, this rammed sample (green part) is processed under high temperature (below melting temperature) in a furnace or an oven, known as sintering.

Advantages: Low operational cost, easy handling process, variety of FGMs with different shapes can manufacture, good for porous FGM, step stacking is possible, etc.

Disadvantages: Processed part has limited strength, complex shapes can not be manufactured, the material powder can be used only, etc.

iv. Tape Casting Method: A FGMs tape having constant thickness can be produced by this method. In this process, the slurry mixture (powder mixture, organic solvent, binders, and

TH-3234_176103111

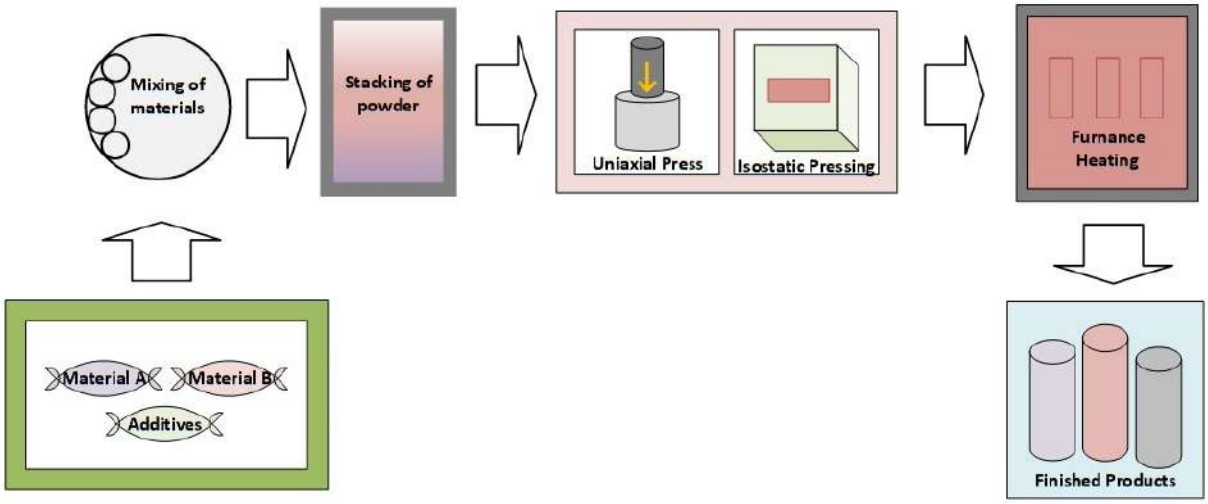

Fig. 1.6: Powder metallurgy processing steps

plasticizers) spreads on the moving belt, and this moving belt passes under the blade edge. A thin and thick film FGMs tape (thickness of microns to mm range) can be cast from this slurry by varying the blade edge. Further, these tapes can stack together under suitable temperature and pressure, so that stepped FGMs of different configurations can be prepared.

Advantages: Suitable for making FGMs tape, high-resolution FGMs can produce, etc.

Disadvantages: Part has limited strength because it depends on the sintering temperature and pressure, etc.

v. Solid Freeform Fabrication (SFF) Method: This is the most popular method to produce a physical shape of an object with the help of a computer-assisted program like Auto-CAD, Solid Edge, etc. It consists of five basic steps: generation of object data with CAD, conversion of CAD data to Standard Triangulation Languages (STL) file, Slicing the STL file into a 2-D cross-section profile, the layer-wise building of components, and finishing of the object. This fabrication can be done by various methods, such as the Laser-based SFF method, Laser cladding-based method, Selective laser sintering (SLS), 3-D printing, Selective laser melting (SLM), etc. By these methods, the intrinsic material properties and compositions of an object can be varied.

Advantages: Fully dense components can be manufactured, less energy consumption, a time-saving process, almost negligible wastage of materials, complex shapes can produce, etc.

Disadvantages: High set-up cost, required skilled operator, high operation cost, etc.

TH-3234_176103111

1.3.4 Applications of FGMs

Due to the novel characteristics of FGMs over composites, it is used majorly in various areas. Some of the fields are discussed below as: a) *Aerospace*: FGMs innovated for thermal barrier applications mainly in space because it can withstand a high thermal gradient. So the FGMs are used to make parts like space-shuttle bodies, rocket engine components, turbine wheels, solar panels, nose caps, etc.

b) *Automobiles*: Due to the high cost of FGMs, their use in this industry is minimal. So in the automobile sectors, only very delicate parts such as spark plugs, cylinder liners, combustion chambers, shock absorbers, drive-shafts, etc., are made by FGMs.

c) *Biomedicals*: FGMs are immensely used in the biomedical field, mainly for making dental implants, skeletal implants, hip implants, etc.

d) *Defence*: FGMs favored for defense applications due to their high strength-to-weight ratio and penetration resistance. In this area, mainly armor plates, bullet-proof jackets, some parts of army vehicles, etc., are manufactured.

e) *Sports*: Many sports equipment, such as golf clubs, tennis rackets, skis, etc., have been made by FGM.

f) *Optoelectronics*: FGMs used in this field as a graded refractive index material, optical fiber materials, lens material, magnetic storage media, etc., for production.

g) *Marine*: FGMs also used in marine and sub-marine fields for making parts like propeller shafts, sonar domes, cylindrical pressure hulls, diving cylinders, etc.

h) *Others*: FGMs are used widely in many areas, such as energy, power plant, nuclear plant, production engineering, etc.

The detailed literature on FGM processing techniques can be found in the review articles on FGM manufacturing, presented by Saleh et al. [9], Kieback et al. [22] and Suresh and Mortensen [23]. A variety of FGMs used in different sectors are shown in the Fig. 1.7.

TH-3234_176103111

Fig. 1.7: Applications of FGM in various sectors (Saleh et al. [9])

1.4 SMART STRUCTURES

Smart structures are systems that incorporate smart materials and sensors to monitor and control their behavior in response to changes in their environment or external stimuli. Smart materials, such as shape memory alloys, piezoelectric materials, and electroactive polymers, are used to change the mechanical, electrical, or magnetic properties of the structure in response to an external stimulus [24]. Sensors, such as strain gauges and accelerometers, are used to monitor the behavior of the structure and provide feedback to the control system. The control system then uses this feedback to adjust the properties of the smart materials and optimize the performance of the structure. Smart structures have the ability to adapt their shape, stiffness, and damping properties in real-time to optimize their performance or enhance their functionality [25].

Several types of smart materials and their unique characteristics are discussed below:

Shape memory alloys (SMAs): SMAs are metals that have the ability to "remember" their original shape and return to it when heated. This property makes them useful for applications such as self-healing structures and actuation systems.

Piezoelectric materials: Piezoelectric materials are materials that generate an electric charge when subjected to mechanical stress or deformation. This property makes them useful for applications such as vibration sensing, energy harvesting, and actuation.

Magnetostrictive materials: Magnetostrictive materials are materials that change their shape in response to a magnetic field. This property makes them useful for applications such as position sensing and actuation.

Electroactive polymers (EAPs): EAPs are materials that change their shape or properties in response to an electric field. This property makes them useful for applications such as artificial muscles and actuators.

Smart structures have numerous advantages over traditional structures. They are often lighter, more durable, and more energy-efficient than their non-smart counterparts. They can also be designed to be self-monitoring and self-repairing, which can reduce maintenance costs and improve safety.

TH-3234_176103111

Applications of smart structures: Smart materials and structures have numerous applications in many fields, including aerospace, civil engineering, robotics, and biomedical engineering [26]. In aerospace, they can be used in aircraft wings and fuselages to improve their performance and reduce their weight. It can also be used to monitor the health of aircraft structures and detect damage or fatigue. In civil engineering, smart structures are used in buildings, bridges, and other infrastructure to monitor their structural health and prevent damage from earthquakes and other natural disasters. In robotics, smart structures are used to create new types of flexible and adaptive robots that can move and manipulate objects in complex environments. In biomedical engineering, smart structures are used in prosthetic devices and artificial organs that can respond to changes in the body and improve their functionality.

1.5 MOTIVATION

Axially joined multi-segmented structures are extensively used in automobile chassis, lower wing panels, cargo doors of airplanes, bridges, etc., to reduce weight and improve the strength & structural design. These structures possess joints or interfaces. So, solutions need to be developed to predict the stresses and displacements more precisely at the interfaces. The FGM structural components, such as wings, strut bars, turbine blades, gears, concrete bars, prosthetic limbs, etc., are graded along the length (axially graded) for better performance. For real-time application and commercialization, a processing technique can be implemented to fabricate such axially segmented structures.

TH-3234_176103111

Chapter 2

Literature Review

In this chapter, a detailed literature review has been presented on different theoretical, analytical and numerical analysis techniques for multi-material and functionally graded (FG) structures and smart structures in Sec. 2.1. In the succeeding sections Sec. 2.2 and Sec. 2.3, literature survey is also presented on the various FGMs fabrication techniques and evaluation of effective material properties of the FGMs, respectively. The objectives of this work are presented in Sec. 2.4 and organization of the thesis is described in Sec. 2.5.

2.1 REVIEW FOR ANALYSIS OF MULTI-MATERIAL, FGM AND SMART STRUCTURES

Multi-material structures have gained attention in recent years as a promising approach to improving the overall performance of structural materials. This literature review will explore the current state of research on the analysis and design of multi-material, FGM and smart structures. This section presents a detailed literature review of various analysis techniques in the view of theoretical, numerical and experimental analysis points.

2.1.1 Static and Dynamic Solutions for Multi-material and FGM Structures

Structural parts are usually made with a variety of materials, which further may be lap or butt joined together. Such structural joints may behave differently under various mechanical loadings and support conditions. In this section, literature is presented for various (theoretical, analytical, numerical, etc.) methods employed by researchers to get the static and dynamic solutions for such structures.

TH-3234_176103111

2.1.2 Based on Elasticity Solution

Theoretical elasticity-based methods have been used for a long decades for structural analysis due to their simplicity. In the early 1950s, composite materials began to gain popularity in the aerospace industry. Hence, the theoretical elasticity approach, such as classical laminate theory and shear deformation theory of composite structures, started to emerge for analysis. In the 1970s and 1980s, composite and sandwich structures expanded into other fields such as marine, automotive, and civil engineering [27]. The literature available on the elasticity-based solution for the bending analysis of multi-joined and functionally graded beams, panels, plates, etc., is presented here.

Ratwani [28] analyzed stress distribution in lap-joined plates through the elasticity approach by assuming a generalized plane stress condition. After that, they extended their work for stress analysis of the sandwich plate with a composite core and metal base [29]. Delale et al. [30] implemented the classical plate theory approach to solve a single-lap joined plate under different loadings. Sankar [31] developed an elasticity solution for simply-supported FG beams subjected to sinusoidal transverse loading. Further, exact thermoelasticity solutions were developed to determine the thermal stresses in FG beams [32] and sandwich beams [33], considering an exponential variation of thermoelastic properties across the thickness. Xiao and Zhang [34] presented a solution of a simply-supported FG beam subjected to arbitrary transverse loads with exponential gradation across the thickness. Yu et al. [35] studied the flexural behavior of hybrid FRP-concrete-steel from a theoretical technique that was based on the plane section assumption and the fiber element approach. For different types of material gradation, thermo-elastic stresses were obtained for a three-layered composite beam with FGM core [36]. For an anisotropic FG beam, a series of elasticity solutions under various loading and boundary conditions were obtained using Airy's stress function considering the body force [37]. Ying et al. [38] obtained exact solutions for bending and free vibration of FG beams resting on Winkler-Pasternak elastic foundations based on the two-dimensional theory of elasticity.

The effect of sandwich panel with FG core on the stress and displacement fields under five different loading conditions (uniformly distributed, patch, point, hydrostatic, and line) [39] and

TH-3234_176103111

transverse loading configurations [40] were examined. The detailed analysis of FGM beams has been presented to estimate the capability of various classical and advanced theories [41, 42]. The transverse deformation along the thickness of FG beam is shown in Figs. 2.1 and 2.2.

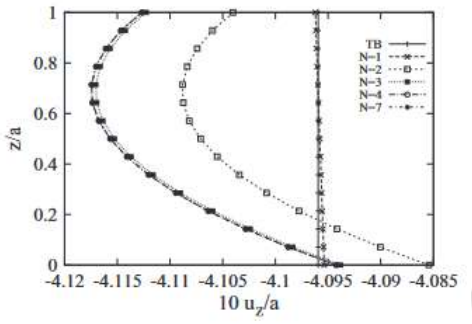

Fig. 2.1: FG beam under bending for different approximation numbers (Giunta et al. [41])

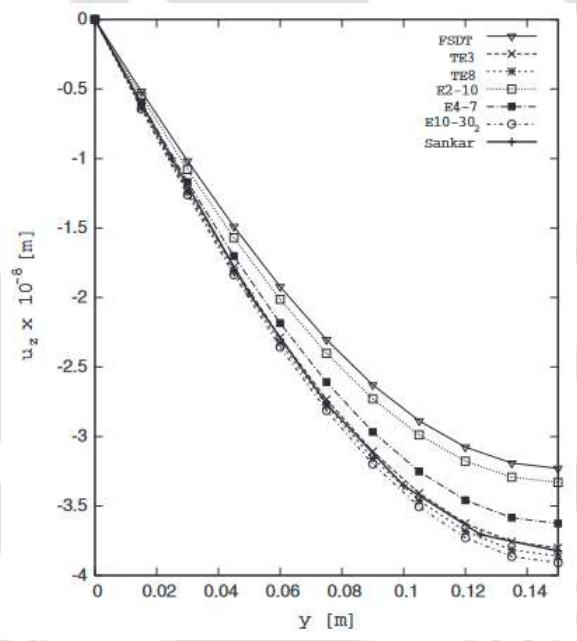

Fig. 2.2: Showing variation of transverse displacement for FG beam using different theories (Filippi et al. [42])

Xu and Zhou [43] developed the two-dimensional thermoelastic analysis for simply-supported beams with variable thickness under the thermo-mechanical loading condition. Using Airy's stress function, the solutions were developed for the beam with varying density subjected to uniform load [44]. Xu et al. [45] presented the two-dimensional elasticity solutions for bending of simply-supported FG beams with varying thicknesses under static loading. Chu et al. [46] developed a novel approach for solving the elasticity problems of the FG beam under simple uniaxial tension and

TH-3234_176103111

bending cases. In this work, the governing equations based on a two-dimensional theory of elasticity were derived using the Airy stress function in conjunction with the strain compatibility equation. Zhao and Ye [47] presented the elasticity solutions for stress and displacement of bi-modulus beams under combined loads. Alibeigloo and Liew [48] studied the bending and free vibrational behavior of FG carbon nanotube-reinforced composite beam embedded in piezoelectric layers based on the theory of elasticity. The solution based on the theory of elasticity for a simply-supported functionally graded two-layer beam subjected to transverse loading was developed [49]. Further, Benguediab et al. [50] developed a plane elasticity solution utilizing the semi-inverse method for an exponentially graded beam. He et al. [51] obtained an elasticity solution of the FG beam under uniformly distributed loads. The beam was assumed to have different moduli in tension and compression.

Zhong and Yu [52] utilized the semi-inverse method to develop a plane elasticity solution for a cantilever FG beam subjected to different loads. Shahsiah et al. [53] presented one-dimensional elasticity solutions for thermal buckling of an FG beam under uniform temperature rise and axial temperature difference. Huang et al. [54] analyzed the bending behavior of an FG anisotropic cantilever beam under a linearly distributed load. The stress function used for solving the problem was again used for other boundary conditions. Later, using a semi-inverse method, a plane elasticity solution was developed for a cantilever FG beam subjected to a linearly distributed load [55]. Nasr et al. [56] obtained a closed-form solution for stress distributions and displacements using the 2-D theory of elasticity of an FG curved beam under shear force at its free end. The influence of inhomogeneity on stress distributions was investigated. Wang and Liu [57] presented an elasticity solution for a laminated FG curved cantilever beam through the Airy stress function method under uniform loading. Arefi [58] developed the elastic solution using the linear theory of elasticity for the different shapes of FG curved beams under a pure bending case. Furthermore, the stress behavior for positive and negative values of the nonhomogeneity index was investigated. Further, the influence of gradation, boundary conditions, and lay-up configuration was investigated. In recent work, Kang et al. [59] developed a theoretical model based on a three-dimensional elasticity solution for a hybrid-core sandwich plate to evaluate the free vibration natural frequency under arbitrary boundary conditions. The literature review on various elastic theories can also be found

for FGM plates and shells [60].

Based on the above literature review, it is observed that the elasticity-based approach is simple and easy to implement for layered structures and can predict stresses for individual layers. However, analysis of a complex structure by the elasticity approach becomes complicated and could not predict results accurately [61]. Therefore, for accurate estimation, these elasticity-based approaches are later extended to an analytical approach, in which the problems are expressed into mathematical equations and solved with analytical techniques. Researchers used various analytical methods for the analysis, such as Pagano's approach, Plevako method, Peano-Baker series method, extended Kantorovich method (EKM), and state-space method. In the succeeding subsections, the literature available on these methods are presented. Additionally, most of the works are available for the FG structures having gradation along the thickness direction. The work on the analysis of piece-wise segmented structures are not found.

2.1.3 Based on Analytical Solution

This subsection presents the literature on 1-D analytical solutions for bending analysis using various approximate theories.

Pickett and Hollaway [62] used a non-linear analysis method to evaluate the composite bonded joint configurations. They studied the performance of single-lap, double-lap, and tubular joints through analytical and finite-element models considering non-linear material behavior. Yang and Pang [63] derived analytical models by using classical laminated plate theory with first-order shear deformation to analyse symmetric and asymmetric single-lap joints subjected to tensile and bending loading. Jiang and Ding [64] presented analytical solutions using the superposition principle and the trial-and-error method for FG cantilever beams. Benatta et al. [65] obtained the displacement and stresses by applying high-order flexural theories for short FG symmetric beams under three-point bending. Li [66] proposed a new unified approach, considering rotary inertia and shear deformation to analyze the static and dynamic behavior of FG beams. Later, in the extension of their work, an analytical solution based on higher-order shear deformation beam theory subjected to a transverse uniform load for static bending of simply-supported FG hybrid beams had been presented [67].

TH-3234_176103111

Pendhari et al. [68] developed a simple mixed semi-analytical model for 2-D stress elasticity-based problem and simultaneously presented a solution based on FSDT, higher order shear normal theory. It was observed that the new method could predict results accurately and efficiently. A similar type of work using the higher-order shear deformation theory had been performed for FG beams [69], for sigmoid FG beams [70], bi-directional FGM beam [71] and sandwich FG beams [72] under static loading. Further, Thai and Vo [73] studied bending and vibration analysis of FG beams based on various higher-order shear deformation beam theories. Navier-type closed-form solutions were obtained for the bending and vibration of FG beams, and it was found that these beam theories are free from the shear-locking effect. Bouremana [74] presented the bending and free vibration analysis of FG beams using a new first-order shear deformation theory (FSDT) of beam based on the neutral surface position. For the bending behavior analysis of FGM Timoshenko beams [75, 76] had been presented under arbitrary transverse loading. Naderi and Saidi [77] used a refined first-order displacement field to present the effects of bending and stretching on moderately thick FG anisotropic wide beams of various boundary conditions. Yang et al. [78] obtained a two-dimensional analytical solution for a bilayer FG cantilever beam subjected to a concentrated load at the free end. Nie et al. [79] presented an analytical solution by the displacement function method for an orthotropic FG beam with arbitrary-graded material properties. Nguyen [80] presented the analytical solutions for the static analysis of the transversely of the AFG beam having a tapered cross-section. Whereas, the dynamic analysis was presented by using several higher-order and classical theories for three-dimensional FGM beams [81]. Meradjah et al. [82] proposed a novel shear and normal deformation beam theory for bending and vibration analysis, including the stretching effect. Furthermore, the effects of gradients, thickness stretching, and thickness-to-length ratios on the bending and vibration of FG beams were analyzed. Hadji and his team developed an n^{th}-order beam theory for bending and free vibration analysis of Navier type FG beams based on neutral surface position [83]. Wang et al. [84] developed an analytical method to study the free vibration analysis of FG Euler-Bernoulli beams. The beam was assumed to follow a power-law gradation of the material mass density and elastic modulus along the beam length and in the beam thickness direction for an exponential gradation. The natural frequencies were obtained for FG cantilever

and simply-supported beams. A hyperbolic shear deformation theory was implemented for the bending analysis of FG beams based on a neutral surface position in conjunction with the Navier method [85]. Pyadh and Sabale [86] developed an analytical model for the flexure of bi-directional FG circular beams based on the classical hairbrush hypothesis. Najafi et al. [87] presented a noncentral low-velocity impact analysis using Reddy's higher-order shear deformation beam theory of simply-supported FG beams resting on a Winkler-Pasternak elastic foundation. Magnucki et al. [88] solved analytically for the beam's bending, buckling and free vibration problems with unsymmetrically varying mechanical properties in the depth direction along with FEM. Chaabane et al. [89] used a hyperbolic shear deformation theory (HySDT) to analyze the static and dynamic behavior of FG beams. Li et al. [90] investigated the non-linearized bending characteristics of a two-dimensional FG beam based on the Euler–Bernoulli beam kinematic theory. The material gradation was assumed to follow the exponential distribution function along the length, whereas the power function is assumed in the thickness direction. In a recent study, Cao et al. [91] analyzed the free vibration behavior of the AFG beams using two analytical approaches, i.e., the asymptotic perturbation and the Meijer G-function method for a continuously varying cross-section beam under different boundary conditions. Chen et al. [92] investigated the vibration problem of axially FGM beam having a variable thickness by isogeometric analysis (IGA). Alimoradzadeh [93] proposed a non-linear vibration analysis of a simply-supported axially functionally graded (AFG) beam subjected to a moving harmonic load. The analytical approach has a few advantages, i.e., it provides fast, stable, and exact solutions, parameter dependencies can be expressed explicitly, etc., and limitations, i.e., restricted to special types of problems, modeling assumptions, differ from the reality, etc. [94].

Apart from the above analytical approaches, semi-analytical EKM approach was also successfully used to develop closed-form solutions for arbitrarily supported beams, panels, plates and shells [95]. Most of the solutions were developed using the two-dimensional theories until it was extended by Kapuria and Kumari [96] to develop solutions based on three-dimensional elasticity. Later, this technique was applied to analyse the piezoelectric plates [97] and functionally graded beams [98]. Kumari and Susant [99] developed a three-dimensional free vibration solution for Levy-type lam-

TH-3234_176103111

inated plate. Apart from the application of regular plate and shell problems, this method has been applied to solve the problem of skew-symmetric plates [100, 101], sector plates [102], stepped plates [103]. Awrejcewicz et al. [104] presented a review cum research paper on the topic of various techniques which reduces nonlinear partial differential equations to an ordinary differential or algebraic equation. It has been proved that EKM is a better approach to getting the analytical solution. Singh and Kumari [98], for the first time, developed a two-dimensional elasticity solution for arbitrarily supported AFG beam having linear gradation along the axis and solved through the EKM approach. Iman Joodaky and Amin Joodaky [105] presented a solution for bending composite edge bonded plates with dissimilar dimensions, materials, foundation, and loading conditions using EKM. For the first time, the EKM procedure is modified by applying the coordinate of an arbitrary shared point on the shared edge of the two plates to the shared boundary conditions. The solution was based on the classical theory of plates.

The above literature review shows that the majority of work is available on 1-D bending solutions of FG structures. But, for the exact prediction, a two-dimensional bending solution is always needed, and EKM shows its effectiveness for various structural configurations. The analytical study on the axially joined structure is not reported till now.

2.1.4 Based on Numerical Solution

Theoretical analysis of hybrid structures became more sophisticated, incorporating new materials and advanced numerical techniques such as FEA and boundary element method. This section discusses literature based on numerical methods such as the FEM, shooting method, Ritz method, meshless method, differential quadrature method (DQM), etc.

Finite element modeling has become the main research tool to study and analyse the complex design of similar or dissimilarly joined structures. Numerous studies are reported to obtain numerical solutions for the single-lap bonded [106–108] and double-lap bonded [109–111] structures through FEM. Rastogi et al. [112] studied three-dimensional thermal stress distributions in aluminum-to-composite, symmetric, double-lap joints under uniform temperature loads. They found that the joint corners are critical regions for debonding initiation. Zou et al. [113] used classical laminate

TH-3234_176103111

plate theory to model single-lap and single-strap metal and CFRP balanced and symmetric joints subjected to tensile and/or bending moment as well as transverse shear loading and verified with FEM results. Kim et al. [114, 115] analyzed the composite adhesive joint using FE and experimentally. Castro et al. [116] presented the effect of rivet hole under fatigue on lap joined panels through FEM. The numerical FEM technique is also employed by Kapuria et al. [117] to investigate the static and dynamic bending response for the layered FG beams to validate the zigzag theory and later, it was extended for the composite panels [118]. Şimcsek [119] applied the Ritz method within the framework of Timoshenko and the higher-order shear deformation theory (HSDT) to estimate the static analysis of a simply-supported FG beam subjected to a uniformly distributed load. Taeprasartsit [120] analyzed the FG beams by employing the ANSYS BEAM3 element and found that the BEAM3 element is able to deal with any arbitrary linear temperature gradient through-thickness. Using the non-linear FE model, Kocatürk et al. [122] studied the static response of a

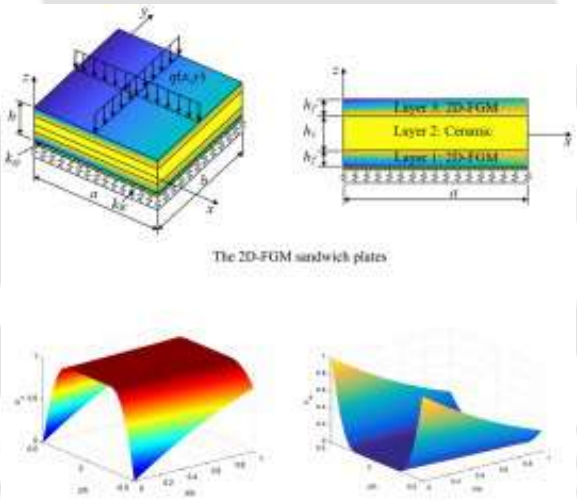

Fig. 2.3: Showing static FE analysis of bi-directional functionally graded sandwich plates under thermal loading (Nguyen et al. [121])

cantilever FG beam under transversal uniformly distributed load. Filippi et al. [123] analyzed the static behavior of FG beams by using Carrera's one-dimensional unified formulation. Further, the governing equations in a weak form were derived employing the principle of virtual displacements and solved by the FEM approach. Chen et al. [124] employed the Timoshenko beam theory in conjunction with the Ritz method for the elastic buckling and static bending of FG porous beams.

TH-3234_176103111

Frikha et al. [125] proposed a new mixed finite element for the FG beam based on the HSDT. Further, the effectiveness of the element was checked through static analysis of cantilevered and simply supported beams. Further, De Pietro and his team [126] derived a family of one-dimensional FE through a unified formulation and applied it on the FG beam for thermoelastic analysis. Malik and Kadoli [127] presented a geometric nonlinear thermo-elastic analysis using a two-dimensional Lagrangian rectangular finite element of a thin FGM beam subjected to various heat loads. The nonlinear thermoelastic deflection and thermal stresses were evaluated for different structural and thermal boundary conditions.

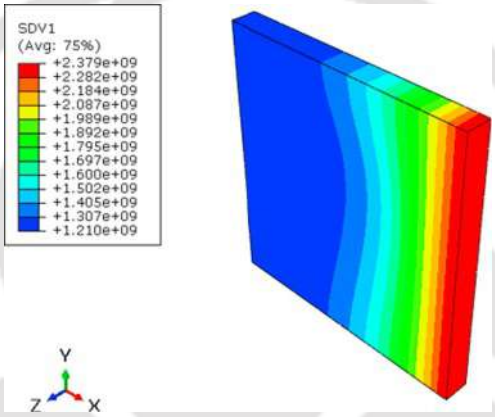

Fig. 2.4: Showing variation of Young's modulus through FE analysis of FG plate (Amirpour et al. [128])

Recently, Nam et al. [129] developed a new finite element beam model to study the static bending, free vibration, and buckling behavior of the FG beams having a variable thickness. Anna [130] studied the strength of similar and dissimilar adhesive lap joints of aluminum alloy, carbon composite, and aramid composite used in aviation. Lucas and Louta [131] explored the challenges and issues that arise in the fatigue crack growth characterization of dissimilar joints due to multiple crack formations. Recently, the stress field in adhesively bonded lap and butt joined steel structures is predicted by employing an analytical approach with the 2-D FEM [132]. Ramahi et al. [133] presented a numerical study for the double-lap adhesive joint of metal-metal and composite-composite type joint subjected to tensile and thermal loads. In a recent study, interface formation mechanisms and bonding performance of CFRP/Ti stacks were analyzed through numerical modeling and experimental techniques [134]. Zhang et al. [135] presented a very detailed review of the numerical

simulation of hybrid joints (HJs) and the future of the designing of HJs. The study also revealed that the analytical closed-form solutions are easier to implement, more accurate, and can handle stress singularity and boundary layer effects more effectively than numerical method [136, 137]. However, the numerical method has several merits over the analytical method e.g., can be used for complex geometries, solve the non-linear problem, etc. [138].

Based on the above literature review it is observed that, the analytical and numerical solutions for static analysis of multi-material and axially segmented structures does not exist. The numerical technique requires more computational effort and large computer memory. Therefore, it is necessary to develope a 2-D analytical solution for the understanding the behavior of arbitrarly supported segmented structures.

2.1.5 2-D Solutions for Smart Structures

In recent years, piezoelectric materials have been substantially used for developing smart or intelligent structures. In this field, Vel and Batra [139] presented an analytical solution based on elasticity for the cylindrical bending of the laminated plates with distributed and segmented piezoelectric actuators. Further, they obtained analytical results for the static cylindrical bending of laminated plates embedded with piezoelectric actuators under mechanical and electrical loading [140]. Qing et al. [141] developed a mathematical model for the static and dynamic analysis of a plate having PZT and PVDF piezoelectric patches. Shi et al. [142] obtained piezoelectric composite cantilever beam results based on the 2D linear theory of piezoelasticity. Xiang and Shi [143] presented an analytical solution based on the Airy stress function method for multi-layered piezoelectric beams. Behjat et al. [144] presented FEM based numerical solution for the bending and free vibration analysis of a curved functionally graded piezoelectric panel made of PZT4/PZT-5H. Nazargah et al. [145] used the FE model to analyze the static and dynamic response for a through-thickness graded piezoelectric beam. Kapuria and Kumari [146] presented a 3-D piezoelasticity solution using the EKM approach for piezoelectric laminated plates under coupled electromechanical loading. Furthermore, analytical solutions for free vibration cases using the EKM approach have been obtained for piezoelectric plates [97, 147–149], piezoelectric beam [150], axially functionally graded beam

TH-3234_176103111

integrated with piezoelectric [151]. In a recent study, Çömez [152] developed a 2-D solution based on elasticity for bending of FG piezoelectric beam. However, recent works were also presented for through thickness graded panels [153, 154] and plates [155–158].

The reported study indicates that a majority of works were presented for through-thickness graded piezoelectric structures. The analytical and numerical work on segmented piezoelectric structures are unavailable. Therefore, work in this direction can be carried out for further development.

2.2 REVIEW ON FABRICATION METHODS OF FGMs

In this section, an extensive literature study has been reported on the methods used by the researchers for the FGM fabrication.

2.2.1 Powder Metallurgy

Powder metallurgy is a manufacturing process that involves the production of metal powders and their subsequent consolidation into solid parts or components. It is one of the oldest method for the fabrication of bulk FGMs. The earliest recorded use of powder metallurgy dates back to the Bronze Age, when metal powders were used in the production of objects such as jewelry, weapons, and tools. The ancient Egyptians, for example, used a powder metallurgy process to produce gold jewelry by mixing gold powder with a binder and shaping the mixture into the desired form [159]. However, in the modern era, powder metallurgy began to develop as a distinct field of study in the early 1900s. In 1910, William Pfann invented a process for producing tungsten filaments by compressing and sintering tungsten powder. This process was later refined by the German chemist Fritz Pfleumer in the 1920s, who used the method to produce tungsten wires for use in incandescent lamps [160]. During world war-II, powder metallurgy became a critical technology for the production of military equipment. The technique was used to produce components for tanks, airplanes, and other military vehicles, as well as for the production of bearings and other mechanical parts [161]. After the war, powder metallurgy continued to grow as a field of study and a manufacturing process. Advances in technology and materials science led to the development of new

TH-3234_176103111

powder metallurgy techniques, including hot isostatic pressing and metal injection molding [162]. In recent days, powder metallurgy is a widely used manufacturing process that is used to produce a wide range of products, from simple mechanical parts to complex aerospace FGM components.

Many authors reported their work on the fabrication and characteristics assessments of powder metallurgy based metal-ceramic FGMs, which were graded along the thickness direction [163–169]. In 1993, Takahashi et al. [163] developed a tungsten(W)/copper(Cu)-based graded material by sintering and infiltration technique. Watanabe et al. [164] fabricated a SiC-AlN/Mo based functionally gradient material for thermal barrier application. From the thermo-mechanical tests, they observed that the SiC-AlN composites simultaneously showed considerable fracture strength at elevated temperature and superior heat-insulating properties. Zhu et al. [170] synthesised ZrO_2-Ni based FGM system and it's microstructure characteristics was analysed using XRD, electron probe microanalysis, and TEM. Further, in 2001, Zhu and his team extended their work and developed ZrO_2-NiCr based functionally graded material had a stepwise gradation along the thickness direction [171]. They observed that the mechanical properties of ZrO_2-NiCr system strongly depend on the constitutional variation. A five-layered metal-ceramics based FGM system of Ti-TiB_2 was fabricated [172]. From the test, it was found that compared to the conventional monolithic TiB_2 ceramics, the fabricated FGM system can possess 50% more fracture toughness. In succeeding year, Jin et al. [173] fabricated Mullite/Mo based FGM and Gelbstein et al. [174] fabricated lead-tin-telluride-based compounds (Pb_xSn_xTe) for various $x = 0.1$, 0.25, 0.5, 0.6 and 0.7 values mainly for the thermoelectric applications. Two types of multilayered FGM beams i.e. for Al/SiC and Ni/Al_2O_3 systems were designed, synthesised, and characterized considering 10, 20, 30 and 40 vol.% ceramic concentrations [175]. Further, a thermal shock test was conducted on FGMs and monolithic mullite. They observed that the FGM specimens had better thermal shock resistance than monolithic mullite. The Al/SiC systems were also fabricated for testing of armor-piercing impact test [176] and micro-hardness effect [177–179].

Moreover, a variety of FGMs systems such as Al/Al_2O_3 based [166, 180, 181], Ni/Al_2O_3 based [175], Al-B_4C based [167], Inco600 and zirconia [182], etc. were developed for structural applications. Futhermore, Efe et al. [183] fabricated and characterized the Cu/SiC based specimens to study

TH-3234_176103111

it's mechanical and electrical behavior. An improvement in relative density, hardness and electrical conductivity of the Cu/SiC based FGMs were observed with the increasing of SiC particle size [177]. The dispersion of fine SiC particles into Cu matrix improves the strength through restricting the dislocation movement [184]. The inclusion of SiC particles prevent the grain growth of Cu matrix at high temperature so that it can maintain relatively high strength at elevated temperature [185]. Recently, Al and Cu based FGM was fabricated with the gradation along thickness direction and it's micro-structural behavior is characterized [186]. Tripathy et al. [181] fabricated a six layerd Al/Al_2O_3 based FGM with a gradation along the thickness to study the effect of Al_2O_3 volume fraction on the microstructure and mechanical properties. The powder metallurgy is also used in the bio-medical industries for the fabrication of biological implant. In this field, Chenglin et al. [187] developed functionally-graded biosystem of hydroxyapatite (HAP)-titanium (Ti) by an optimized powder metallurgical process. Xiong et al. [188] designed the W-Mo-Ti-TiAl-Al-based graded material system with a density gradient and the sintering behavior of W, W-Mo, and Mo-Ti alloys were studied at low temperature. Further, Shahrjerdi et al. [189] presented a pressure-less powder metallurgy procedure as a fabrication technique for an HAP/Ti based functionally graded cylinder using an optimum experimental heat sintering. Further, for the validation of results, shrinkage, SEM, EDX, and Vicker's micro-hardness methods were employed. Sazesh et al. [190] fabricated FGM of Ti/nano-HAP as dental implant. Then using the experimental and numerical methods their biocompatibility, static strength and fatigue characteristics for different volume fraction exponents were investigated.

The literature survey reveals that this method is successfully used to develope a variety of FGMs which has gradation along the thickness direction. However, a few works are also avaliable on fabrication of axially graded. Hence, the powder metallurgy method shows its design flexibility at a lower laboratory set-up cost.

2.2.2 Spark Plasma Sintering (SPS)

This is a rapid consolidation technique that uses a high current and low voltage to create a spark between the powder particles, leading to rapid heating and densification. Using the SPS method, the

TH-3234_176103111

FGM implant made of Ti/HAP [191] and TiN/HAP [192] were fabricated by sintering it at a temperature of 950°C and pressure of 40 MPa. Watanabe et al. [193] fabricated HAP/β-Tricalcium Phosphate (β-TCP)/TiH-2 FGMs and the effects of composition layer on the bending strength, elastic modulus, thermal expansion coefficient, and crack generation behavior had been evaluated. Further, a variety of FGMs based on Ti-NaCl [194], Ni-Cu [195] and Ti/HAP [196] were fabricated and it's microstructure analysis had been performed. Tang et al. [197] synthesized three-layered W/Cu based FGM, i.e., (W-25Cu/W-50Cu/W-75Cu, by volume fraction) at different temperatures for 5 minutes under a pressure of 40 MPa. The effect of varying sintering temperature on relative density, hardness, thermal conductivity and microstructure at various layers of sintered samples were investigated. Wazery et al. [198] fabricated FGM in the form of a layered structure consisting of yttria-stabilized zirconia and nickel. The relative density, linear shrinkage, and Vickers hardness of each layer of graded materials were measured. Futhermore, multi-layered W-Cu based FGMs [199, 200] were fabricated for nuclear fusion components. The effect of sintering temperature on the physical, mechanical, and surface properties were investigated. This method was also employed for the fabrication of other types of multi-layered FGMs systems, such as Cu/Al_2O_3 [201], Ni/Al_2O_3 [202], stainless steel 316L/Al_2O_3 [203], Ti/Al_2O_3 [204] and Al/Al_2O_3 [205]. The microstructural, physical and mechanical tests were further performed.

The literature survey reveals that, the work on axially graded specimens were not carried out so far using this method. The work were done mainly for the FGMs having through thickness gradation.

2.2.3 Laser Metal Deposition (LMD)

LMD is a 3D printing technology that uses a laser as the heat source to melt and deposit metal powder or wire onto a substrate, building up a part layer by layer. Based on this method, Graf et al. [206] fabricated and repaired the cracks of stainless steel and titanium alloys (Ti6-Al4-V) based FGMs. Mahamood et al. [207] produced functionally graded titanium alloy composite using optimized process parameters and the samples were characterized through metallurgical, mechanical, and tribological studies. Reichardt [208] used a multi-hopper laser deposition system to manu-

TH-3234_176103111

facture Ti6-Al4-V to 304L stainless steel-based functionally graded components with a Vanadium interlayer. Further, a thin FGM sample was made of Ti6-Al4-V to SS316 and microstructure characterization & composition distribution analyses were performed [209]. Yan et al. [210] used this method to join titanium aluminide (Ti-48Al-2Cr-2Nb) and commercially pure titanium. Sharman et al. [211] fabricated crack-free TiAl parts using the laser-engineered net shaping (LENS) method and the characterization of samples was performed. Zhang et al. [212] manufactured Ti6-Al4-V/TiC based FGMs by direct laser deposition using Ti6-Al4-V and TiC powder and investigated the effect of process parameters and TiC composition on microstructure, Vickers hardness, and mechanical properties. Karnati et al. [213] prepared and characterized a graded material with deposits of 70 wt.% Cu-30 wt.% Ni to 100 wt.% Ni, and vice versa. Very recently, Chen et al. [214] successfully made the FGM, having the constitution varying from 100% 316L stainless steel to 100% Inconel625 alloy. The literature survey shows that, this method is more suitable for the through-thickness-graded FGMs, mainly made with metal powders. The set-up cost is very high and uneconomical for laboratory level testings.

2.3 EVALUATION OF EFFECTIVE MATERIAL PROPERTIES

An accurate estimation of the material properties of the FGM specimens is essential for a better design and precise analysis of FGM structures. The effective material properties can be assumed to have a known grading variation like a power law, exponential, etc., or estimated by the rule of mixture [215–217], micromechanical techniques [218–222], experimentation, etc. The rule of mixtures approach assumes that the composite material is a homogeneous mixture of its constituent materials and uses their respective properties to estimate the overall properties of the composite [215]. However, the micromechanical modeling approach involves modeling the individual reinforced and matrix material within the FGM and using this information to estimate the overall properties of the FGM [218]. Therefore, for this approximate estimation, various analytical approaches such as Mori-Tanaka [223, 224], mixed rule of mixture [225], Sasaki–Kerner [226], Wakashima Tsukamoto [227], self-consistent method [228], etc. are also used by the researchers. Finally, the experimentation techniques are used to estimate the properties of a composite and

TH-3234_176103111

FGMs accurately. Nakamura et al. [229] proposed an experimental approach for evaluating FGM properties through instrument indentation and inverse analysis. This approach establishes a continuous record of the variation of indentation depth as a load function to determine the specimen's elastic property. Tsukamoto [230] evaluated the indentation properties for ZrO_2/Ti based FGMs fabricated by SPS technique. Similarly, using this technique material properties for glass-alumina FGM [231], zirconia-based ceramics [232], mullite/Mo based FGM [233], Ti/HAP and Ti/SiO_2 based FGM [234], etc. were successfully evaluated.

Apart from above, a non-destructive experimental technique is also implemented for the estimation. A detailed literature study on the non-destructive impulse excitation technique is presented here. This experimentation technique is extensively used to evaluate the effective elastic and damping properties of metals, composites, alloys, FGMs, etc. [235]. Wkeglewski et al. [236] determined Young's modulus of Cr–Al_2O_3 metal-ceramic composites by RFDA and compared with FEM results. Campbell and Eckhart [237] presented a technical report on the estimation of the dynamic elastic moduli of graphite and ceramic specimens. Furthermore, the material properties were also evaluated for powder metallurgy-based ductile aluminum foam (AlMg1Si0.6) [238], orthopedic implant [239] and TiAl6V4 implant [240]. Bone-like porous monolithic HAP and HAP-ZrO_2 nanocomposite material properties estimated at a room temperature to 650°C temperature [241]. Similar work on the temperature-based mechanical properties estimation had been carried out for glass-ceramics [242], tin-copper alloy [243], alumina ceramics [244], zirconium titanate-zirconia composite [245], piezoceramics [246], etc. Recently, Hönig et al. [247] evaluated the dynamic modulus for carbon/carbon-SiC composites at different temperatures. Gain and Zhang [248] estimated temperature-dependent elastic properties of Al-12Si alloy manufactured by SLM technique. The survey shows that the impulse excitation technique is simple, easy to use, reliable, and can accurately predict the elastic and thermo-elastic properties of various types of specimens.

Based on the above literature review it is observed that,

1. The combination of metal-ceramic systems is found widely used as a structural material.

2. Experimental work for axially graded beam type specimen is not available.

TH-3234_176103111

3. The powder metallurgy is found more suitable processing method for the fabrication of such stepped gradient FGMs due to its operational flexibility and cost effectiveness.

4. The microstructure analysis of the samples is essential to predict the behavior of metal-ceramic bonding in each layer and at the interface.

5. A suitable prediction of the mechanical properties of the fabricated specimens are found more vital when it is to be applied in actual working conditions.

6. The non-destructive impulse excitation technique is suitable to estimate the effective elastic properties of specimens.

2.4 OBJECTIVES OF THE PRESENT WORK

Based on the literature survey, the following objectives were identified for the present research work:

1. To develop a two-dimensional analytical model for multi-segmented beams and panels under mechanical loading.

2. To extend the multi-segmented 3-D elasticity formulation for 3-D piezoelectricity to develop solutions for piezoelectric panels.

3. To investigate the effect of boundary layer stress and stress singularity at the interfaces for different lay-ups.

4. To fabricate Cu/SiC based axially graded system with step-wise variation of material property, using powder metallurgy.

5. To carry out characterizations of mechanical and physical properties of the system.

6. To estimate the system's elastic property and natural frequency through experimentation and 3-D FE validation.

TH-3234_176103111

2.5 ORGANISATION OF THE THESIS

The complete work presented in this thesis work has been organized into eight chapters.

Chapter 1 establishes the motivation behind the presently conducted research work. An overview has been presented on multi-material, FGM and smart structures and its growing application in various sectors. Chapter 2 devoted to the literature survey and proposed objectives for the present work. An overview of the contents of the remaining six chapters is presented below.

The two-dimensional closed-form solutions based on multi-term EKM for the static bending of edge-bonded dissimilar beams with arbitrary numbers of segments along the longitudinal (x) direction has been presented in Chapter 3. In this chapter, the results are presented for four types of configurations under various boundary conditions. The developed method is more versatile and can tackle any kind of material property variation (power law, exponential, arbitrary) along the length. The segments are assumed to have a constant material property and are perfectly bonded along the x-axis. Reissner's type mixed variational principle has been applied to derive the weak form of governing equations where stresses and displacement field variables are considered as primary variables. After that, multi-term extended Kantorovich approach is employed to transform the governing equation into two sets of algebraic-ordinary differential equations (ODEs), one along in-plane (x) and other along with the thickness (z) direction, respectively. The analytical EKM results are thoroughly validated with the FE results. It is observed that the EKM converges more rapidly and predicts the outcomes more accurately near boundary edges. The current development will act as a benchmark to assess the one-dimensional beam theories. This work can be further extended for dissimilar plates and more complex cases.

In Chapter 4, a closed-form bending solution of the multi-segmented panels is presented for various support conditions.The developed analytical solution is very unique, in which any type of material variation from one segment to the next segment can be easily tackled. The results are obtained for four types of panel configurations having dissimilar material properties with different segment length. The multi-term EKM results for all the cases are successfully validated with the FE results. Additionally, an effect of ply-angle variation on the stresses and displacements

TH-3234_176103111

have been presented for two equally segmented Al/Gr-Ep panel. This work will be very useful for the researchers to study the behavior of the piece-wise homogeneous panel type structures under in-plane loads.

The analytical solutions for the bending of segmented piezoelectric panels under various boundary conditions has been presented in Chapter 5. Reissner's type mixed variational principle has been applied to derive the weak form of governing equations where stresses, displacements, electric potential, and electric displacement field variables are considered as primary variables. The multi-term EKM solutions are developed for three piezoelectric-panel configurations. A study on the four equal segmented piezoelectric panel with a step-wise varying piezoelectric strain coefficient has been also presented. These ODEs are solved in closed-form manner which ensures the same order of accuracy for all the variables (stresses, displacements, and electric variables) by satisfying the boundary and continuity equations in exact manner. The accuracy and efficacy of the present method have been established by comparing the present numerical results with the results available in the literature and with the 2-D FE results of ABAQUS. The presented 2-D analytical solution will be helpful in the assessment of various 1-D theories and numerical methods. This work will be also very helpful to analyze the behavior of two longitudinally stacked piezoelectric strips in aerospace industries.

Chapter 6 contains the fabrication of a metal-ceramic-based axially graded beam by stacking powder in a step-wise manner using the powder metallurgy route. A detailed processing procedure of three segmented Cu/SiC (100/0, 90/10 and 80/20) beam has been presented for the first time. The characterization for the initial ball-milled powders and FGM specimens has been studied using powder-XRD, FESEM, TEM, and EDS analysis. The effect of the ball mill on the crystallite size and lattice strain of copper powder is well reported & explained using the Williamson-Hall method and Scherrer's equations. It is observed that the hardness increases with the increase in SiC content; however, the metal-ceramic bonds weaken and form voids. This work will motivate to fabrication of axially graded gas turbine blades, gears, bearings, and orthopedic implants for futuristic applications.

The experimental investigation to evaluate the elastic properties using the non-destructive tech-

TH-3234_176103111

nique for the fabricated specimen has been presented in Chapter 7. The cylindrical-shaped samples are prepared using the powder metallurgy method discussed in the previous chapter. The resonant frequency dynamic analyzer (RFDA) is used to obtain the elastic property and record the corresponding tapped resonant frequency. For the repeatability of the experiment, a minimum of five trials have been performed on each specimen. The average value of the experiment has been taken to validate and analyze the natural frequency through FEA. For FEA, a 3-D model of the specimen is modeled with the experimently recorded elastic property in ABAQUS, and the natural frequency is obtained under the free-free case. The FE natural frequencies are found to be in good agreement with the experimental values.

Finally, the major summary and conclusions of this work with suggestions for future research are summarized in Chapter 8.

TH-3234_176103111

Chapter 3

Two-Dimensional Bending Solutions for the Multi-Segmented Dissimilar Beams

3.1 INTRODUCTION

Structures are becoming bulkier due to the rise in demand for integrating several functions into a single system. Hence, combining lightweight metals like aluminum with high-strength composites like Graphite-Epoxy, Carbon-Epoxy, etc., is widely used to lighten structures. Moreover, prosthetic limbs, concrete bars, FG shafts, etc., are also designed to have varying materials along the length. The above problems can not be analysed using FG theories/concepts. In theory, material properties vary linearly, exponentially, or power-law-like along x-values; however, the material property does not follow a particular variation for the above cases. Producing or manufacturing components with very smooth variations along the length is not always practical. Therefore, it is crucial to develop a solution for accurately predicting the deflection and bending stresses under various loadings and support conditions. In real working conditions, these structural members may behave as beam, panel or plate. In this Chapter, a two-dimensional analytical solution is developed for the static bending of edge-bonded multi-segmented dissimilar beams under uniformly distributed loading conditions. The beam with equal and unequal segments is assumed to be perfectly bonded along x-direction. The segment with gradually varying material properties is also considered, which can mimic the behaviour of an axially graded beam under various boundary conditions. A flowchart of the solution methedology used for a beam model is shown in Fig. 3.1.

TH-3234_176103111

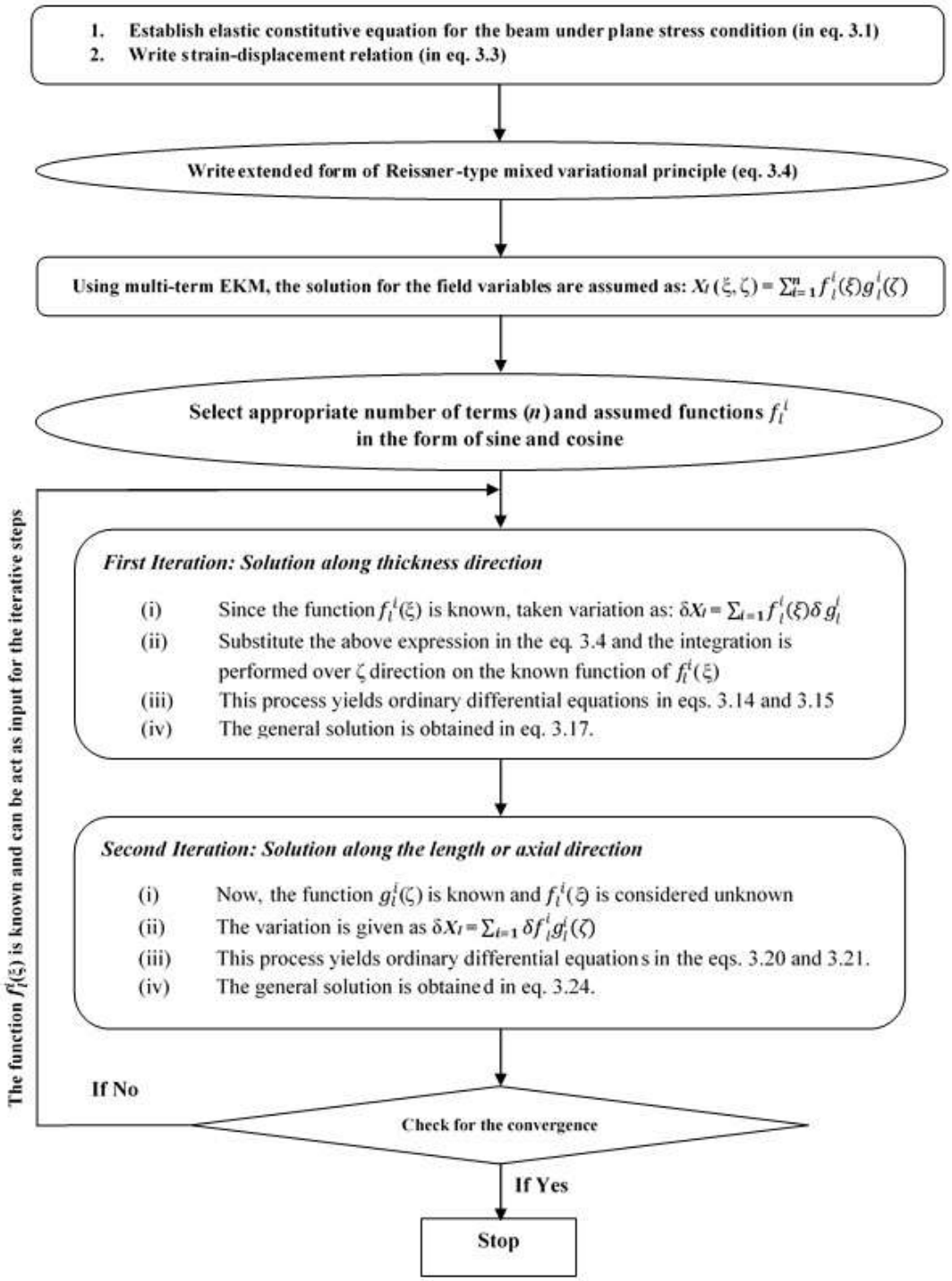

Fig. 3.1: A flowchart of EKM approach for edge bonded beam

The details about theoretical geometry, assumptions made, Reissner-type mixed-form of governing equations development, and mathematical formulation for the segmented beam are discussed in Sec. 3.2. The multi-term EKM is developed in Sec. 3.3 to solve the governing equations. A set of ODEs with constant coefficients are obtained along the z-direction using the EKM, which is solved

TH-3234_176103111

analytically in closed form, as explained in Sec. 3.3.1. Another set of ODEs with varying coefficients obtained along the x-direction is discussed in Sec. 3.3.2. The numerical results are presented for various configurations, aspect ratio, and boundary conditions under static bending in Sec. 3.4. The present EKM results are validated by comparing them with the finite element results obtained from ABAQUS. The benchmark results for static analysis are presented for various cases, which can be used to validate approximate one-dimensional and 2-D numerical solutions. At last, the conclusive summary of the present work has been summarised in Sec. 3.5.

3.2 THEORETICAL FORMULATION

A single layered beam with span length a along x-direction and total thickness h along z-direction, as shown in Fig. 3.2 is considered for the present study. It can have different boundary conditions at $x = 0$ and a and is subjected to a uniformly distributed pressure load of q_1 and q_2 applied on the bottom and top surfaces, respectively. Beam has S segments along x axis as shown in Fig 3.2. The following assumptions are made:

- Each segment may have a different isotropic or orthotropic material.
- It is not necessary to follow a particular material variation from one segment to another segment.
- Material property in each segment is constant.
- Each segment is perfectly bonded along x-axis.
- The continuity condition is exactly satisfied at each segment interface.
- Segment length may or may not be same. For a typical segment P, length is denoted by a^p.

The beam is made of S perfectly bonded segments of materials with the principal material axis x_1 oriented along the x-direction. The length of the P_{th} segment is a^p, and the x-coordinate of its left surface is denoted as x_{p-1}. The interface between the P_{th} and the $(P+1)_{th}$ segment is named as the P_{th} interface. The segment superscript is omitted unless needed for clarity.

TH-3234_176103111

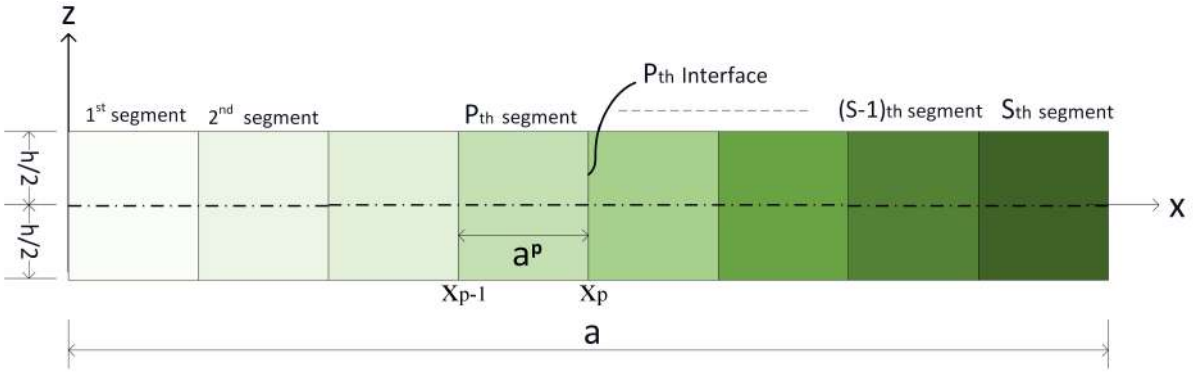

Fig. 3.2: Geometry of the axially segmented beam

Since the width is very small along y-direction, the displacement u and w considered along x-axis and z-axis, respectively, are independent of y coordinate. Therefore, stresses $\sigma_y, \tau_{yz}, \tau_{xy}$ becomes zero. For such plane stress condition, constitutive equations of an orthotropic lamina, when transformed from the material coordinate system (x_1, x_2, x_3) to the rectangular coordinate system (x, y, z) can be written for beam as,

$$\begin{bmatrix} \varepsilon_x \\ \varepsilon_z \\ \gamma_{zx} \end{bmatrix} = \begin{bmatrix} \bar{s}_{11} & \bar{s}_{13} & 0 \\ \bar{s}_{13} & \bar{s}_{33} & 0 \\ 0 & 0 & \bar{s}_{55} \end{bmatrix} \begin{bmatrix} \sigma_x \\ \sigma_z \\ \tau_{zx} \end{bmatrix} \tag{3.1}$$

The $\bar{s}_{ij}$ are transformed elastic compliances, whose expressions in terms of the engineering properties, namely, Young's moduli (Y_i), shear moduli (G_{ij}) can be referred from Ref [98]. To ensure numerical stability in the solution process, all entities are expressed in non-dimensional forms in such a way that, on substitution of dimensionless entities, the form of all governing equations remains unchanged.

$$\begin{aligned} &S = a/h; \quad h = h/a; \quad (\sigma_x^*, \sigma_z^*, \tau_{zx}^*) = (\sigma_x, \sigma_z, \tau_{zx})/SY_0 \\ &\bar{s}_{ij}^* = \bar{s}_{ij} Y_0; \quad (\varepsilon_x^*, \varepsilon_z^*, \gamma_{zx}^*) = (\varepsilon_x, \varepsilon_z, \gamma_{zx})/S \\ &(u^*, w^*) = (u, w)/h; \quad (G_{ij}^*, Y_i^*) = (G_{ij}, Y_i)/Y_0 \end{aligned} \tag{3.2}$$

where Y_0 is the value of the Young's modulus used for non-dimensionalization. In subsequent mathematical equations, the above dimensionless forms of the entities are used where the superscript * is dropped for simplicity.

TH-3234_176103111

The strain-displacement relations are,

$$\varepsilon_x = u_{,x}\,; \qquad \gamma_{zx} = w_{,x} + u_{,z}\,; \qquad \varepsilon_z = w_{,z} \tag{3.3}$$

where a subscript comma denotes differentiation.

The Reissner-typed mixed principle of virtual work [98], without any body force and unit width along y-direction, can be used for the bending analysis of the beam. It can be expressed as,

$$\int_V [\delta u(\sigma_{x,x} + \tau_{xz,z}) + \delta w(\tau_{zx,x} + \sigma_{z,z}) + \delta\sigma_x(\varepsilon_x - u_{,x}) + \delta\sigma_z(\varepsilon_z - w_{,z}) + \delta\tau_{zx}(\gamma_{zx} - u_{,z} - w_{,x})]\,\mathrm{d}V = 0, \quad \forall\ \delta u_i,\ \delta\sigma_i,\ \delta\tau_{ij} \tag{3.4}$$

where V denotes the volume of beam for per unit width along the y-direction. More details about the method can be found in Ref. [98]

Now, substituting the expressions of strain components ε_x, ε_z and γ_{zx} from Eq. (3.1) into Eq. (3.4) yields

$$\int_a \int_h [\delta u\{\sigma_{x,x} + \tau_{xz,z}\} + \delta w\{\tau_{zx,x} + \sigma_{z,z}\} + \delta\sigma_x\{\bar{s}_{11}\,\sigma_x + \bar{s}_{13}\,\sigma_z - u_{,x}\} + \delta\sigma_z\{\bar{s}_{13}\,\sigma_x + \bar{s}_{33}\,\sigma_z - w_{,z}\} + \delta\tau_{zx}\{\bar{s}_{55}\,\tau_{zx} - u_{,z} - w_{,x}\}]\,\mathrm{d}z\,\mathrm{d}x = 0 \tag{3.5}$$

Dimensionless in-plane coordinates ξ^p for P_{th} segment and a local thickness coordinate ζ are introduced, which varies from 0 to 1.

$$\xi^p = (x - x_{p-1})/a^p\,; \qquad \zeta = (z - z_0)/h \tag{3.6}$$

The bottom & top surfaces of the beam are assumed to be free from the shear traction and subjected to uniformly distributed pressure q_1 & q_2, respectively. The support conditions at the top ($z = h/2$) and bottom ($z = z_0 = -h/2$) surfaces of the beam can be expressed as,

$$\begin{aligned} &\text{at} \quad z = -h/2: \quad \sigma_z = -q_1; \quad \tau_{zx} = 0; \\ &\text{at} \quad z = h/2: \quad \sigma_z = -q_2; \quad \tau_{zx} = 0; \end{aligned} \tag{3.7}$$

For perfect bonding at each segment, the interface continuity conditions must be satisfied at the

P_{th} interface,

$$[(u,\, w,\, \sigma_x,\, \tau_{zx})|_{\xi=1}]^{(p)} = [(u,\, w,\, \sigma_x,\, \tau_{zx})|_{\xi=0}]^{(p+1)} \tag{3.8}$$

The beam can have different combinations of mechanical support at x=0 and x=a, such as,

$$\begin{aligned} &\text{Simply supported (S) :} && w = 0, && \sigma_x = 0 \\ &\text{Clamped (C) :} && u = 0, && w = 0 \\ &\text{Free (F) :} && \tau_{xz} = 0, && \sigma_x = 0 \end{aligned} \tag{3.9}$$

3.3 THE GENERALIZED MULTI-TERM EKM

The five field variables, which comprise of displacements and stress entities that need to be solved are given in $\mathbf{X}$, which is considered as a set of primary variables where its l^{th} component can be presented as: $\mathbf{X_l}=[\,u \quad w \quad \sigma_x \quad \sigma_z \quad \tau_{zx}\,]^{\mathrm{T}}$

Using the multi-term EKM [98], these field variables for the P_{th} segment are expressed in n-term series. It consist the products of separable functions of ξ and ζ, as,

$$\mathbf{X_l} = \sum_{i=1}^{n} f_l^i(\xi) g_l^i(\zeta) + \delta_{l4}[q_a + z q_d], \qquad l = 1, 2, \ldots 5 \tag{3.10}$$

where, $g_l^i(\zeta)$ and $f_l^i(\xi)$ are the unknown functions of ζ and ξ, respectively. The number of terms in solution is represented by n and the repeated index l does not mean summation here. To satisfy the compatibility condition for σ_z as given in Eq. (3.8), an additional term ($\delta_{l4}[q_a+zq_d]$) is superimposed to the above solution for σ_z. Where, δ_{l4} is Kroneckor's delta, $\delta_{l4} = 1$ for $l = 4$ and else $\delta_{l4} = 0$, $q_a = -(q_1 + q_2)/2$ and $q_d = -(q_2 - q_1)/h$.

The functions $g_l^i(\zeta)$ is valid for the thickness, and $f_l^i(\xi)$ functions are dependent on the P_{th} segment. These unknown functions (g and f) of ζ and ξ are to be solved in two iterative steps by satisfying all homogenous support conditions.

3.3.1 First Iteration Step

In first step, x-direction functions $f_l^i(\xi)$ are assumed as known, while functions $g_l^i(\zeta)$ need to be solved. In the EKM, the initial trail functions are not required to satisfy the prescribed support conditions. Hence, to start the iterative process f_l^i are assumed as, $f_2^i(\xi)$=$f_3^i(\xi)$=$f_4^i(\xi)$=$\sin i\pi\xi$ and

$f_1^i(\xi)$=$f_5^i(\xi)$=$\cos i\pi\xi$. Therefore, the variation δX_i is given as,

$$\delta X_l = \sum_{i=1}^{n} f_l^i(\xi)\delta g_l^i, \qquad l = 1, 2, \ldots 5 \tag{3.11}$$

Functions $g_l^i(\zeta)$ are segregated into two column vectors $\bar{\mathbf{G}}$ and $\hat{\mathbf{G}}$. Where $\bar{\mathbf{G}}$ contains those particular $4n$ primary variables which are specified at the support along z-direction. Where, $\hat{\mathbf{G}}$ contains the remaining $1n$ dependent variables:

$$\bar{\mathbf{G}} = [\, g_1^1 \ldots g_1^n \quad g_2^1 \ldots g_2^n \quad g_4^1 \ldots g_4^n \quad g_5^1 \ldots g_5^n \,]^{\mathrm{T}}$$
$$\hat{\mathbf{G}} = [\, g_3^1 \ldots g_3^n \,]^{\mathrm{T}} \tag{3.12}$$

Now, Eqs. (3.10) and (3.11) are substituted into Eq. (3.5).

where, the f_l^i are known functions and integration along x-direction are performed. Since the variations for δg_l^i are arbitrary, the coefficients of δg_l^i must vanish (equal to zero), which generates the following set of $4n$ first order ODEs and $1n$ linear algebraic equations for each layer:

$$\mathbf{M}\bar{\mathbf{G}}_{,\zeta} = \bar{\mathbf{A}}\bar{\mathbf{G}} + \hat{\mathbf{A}}\hat{\mathbf{G}} + \bar{\mathbf{Q}}_{\mathbf{p}}^{\mathbf{m}} \tag{3.13}$$

$$\mathbf{K}\hat{\mathbf{G}} = \tilde{\mathbf{A}}\bar{\mathbf{G}} + \tilde{\mathbf{Q}}_{\mathbf{p}}^{\mathbf{m}} \tag{3.14}$$

where, $\mathbf{M}_{4n\times 4n}$, $\bar{\mathbf{A}}_{4n\times 4n}$, $\hat{\mathbf{A}}_{4n\times 1n}$, $\mathbf{K}_{1n\times 1n}$ and $\tilde{\mathbf{A}}_{1n\times 4n}$ are known matrices.

Non-zero elements of the matrices are given below:

$$\begin{aligned}
&M_{i_1j_1} = M_{j_4i_4} = \langle f_5^i f_1^j\rangle_a,\ M_{i_2j_2} = M_{j_3i_3} = \langle f_4^i f_2^j\rangle_a \\
&\bar{A}_{i_1j_2} = \tfrac{-t}{a}\langle f_5^i f_{2,\xi}^j\rangle_a, \qquad \bar{A}_{i_1j_4} = t\bar{s}_{55}\langle f_5^i f_5^j\rangle_a \\
&\bar{A}_{i_2j_3} = t\bar{s}_{33}\langle f_4^i f_4^j\rangle_a, \qquad \hat{A}_{i_2j_1} = t\bar{s}_{13}\langle f_4^i f_3^j\rangle_a \\
&\bar{A}_{i_3j_4} = \tfrac{-t}{a}\langle f_2^i f_{5,\xi}^j\rangle_a, \qquad \hat{A}_{i_4j_1} = \tfrac{-t}{a}\langle f_1^i f_{3,\xi}^j\rangle_a \\
&K_{i_1j_1} = \bar{s}_{11}\langle f_3^i f_3^j\rangle_a, \qquad \tilde{A}_{i_1j_1} = \tfrac{1}{a}\langle f_3^i f_{1,\xi}^j\rangle_a \\
&\tilde{A}_{i_1j_3} = -\bar{s}_{13}\langle f_3^i f_4^j\rangle_a
\end{aligned} \tag{3.15}$$

where, $i_c = (c-1)n + i$ and $j_d = (d-1)n + j$ for $c, d = 1, 2, \ldots, 4$.

$\bar{\mathbf{Q}}_{\mathbf{p}}, \tilde{\mathbf{Q}}_{\mathbf{p}}$ are load vectors of size $4n$, and $1n$, respectively, whose non-zero terms are given by

$$\bar{Q}_{p_{i3}} = -t\langle f_2^i\rangle_a q_d, \qquad \bar{Q}_{p_{i2}} = t\bar{s}_{33}\langle f_4^i\rangle_a\,(q_a + \zeta t q_d)$$

$$\tilde{Q}_{p_{i1}} = -\bar{s}_{13}\langle f_3^i \rangle_a \, (q_a + \zeta t q_d) \tag{3.16}$$

Here, the notation $\langle \ldots \rangle_a = \sum_{p=1}^{S} a^p \int_0^1 (\ldots)^p \, d\xi$, represents integration over the span length a and $q_a = q_a + q_d z_0$.

Since the functions f_l^i are known functions, elements of the matrices defined in Eqs. (3.15),(3.16) have been evaluated in the closed form. $\hat{\mathbf{G}}$ is obtained from Eq. (3.14) and put into Eq. (3.13) which yields a set of $4n$ first-order homogeneous ODEs as:

$$\bar{\mathbf{G}}_{,\zeta} = \mathbf{A}\bar{\mathbf{G}} + \mathbf{Q_p} \tag{3.17}$$

where $\mathbf{A} = \mathbf{M}^{-1}[\bar{\mathbf{A}} + \hat{\mathbf{A}}\mathbf{K}^{-1}\tilde{\mathbf{A}}]$, $\mathbf{Q_p} = \mathbf{M}^{-1}[\bar{\mathbf{Q}}_\mathbf{p}^\mathbf{m} + \hat{\mathbf{A}}\mathbf{K}^{-1}\tilde{\mathbf{Q}}_\mathbf{p}^\mathbf{m}]$.

Above Eq. (3.17) represent a system of $4n$ non-homogeneous first order ODEs with constant coefficient. This can be solved using the approach discussed in Ref. [96].

3.3.2 Second Iteration Step

Now $g_l^i(\zeta)$ is known from the first step, whereas $f_l^i(\xi)$ is considered unknown. So, in this step, arbitrary variation is considered in f_l^i functions. Therefore, variation for this case is written from Eq. (3.11) as:

$$\delta X_l^i = \sum_{i=1}^{n} g_l^i(\zeta)\delta f_l^i \quad \text{for} \quad l = 1, 2, \ldots, 5 \tag{3.18}$$

Similarly, like the first step, $f_l^i(\xi)$ are segregated into two column vectors $\bar{\mathbf{F}}$ and $\hat{\mathbf{F}}$. Where $\bar{\mathbf{F}}$ carries those particular $4n$ primary variables which come in the support conditions at edges $x = 0, 1$ and $\hat{\mathbf{F}}$ contains the remaining $1n$ variables,

$$\bar{\mathbf{F}} = [\, f_1^1 \ldots f_1^n \quad f_2^1 \ldots f_2^n \quad f_3^1 \ldots f_3^n \quad f_5^1 \ldots f_5^n \,]^{\mathrm{T}}$$
$$\hat{\mathbf{F}} = [\, f_4^1 \ldots f_4^n \,]^{\mathrm{T}} \tag{3.19}$$

Now, substituting Eq. (3.10) and Eq. (3.18) in Eq. (5.16), performing integration over ζ direction on the known functions of ζ, applying integration by parts wherever necessary, and equating the coefficient of δf_l^i to zero individually, yields the following system of differential-algebraic equations

for f_l^i:

$$\mathbf{N}\bar{\mathbf{F}}_{,\xi} = \bar{\mathbf{B}}\bar{\mathbf{F}} + \hat{\mathbf{B}}\hat{\mathbf{F}} + \bar{\mathbf{P}} \tag{3.20}$$

$$\mathbf{L}\hat{\mathbf{F}} = \tilde{\mathbf{B}}\bar{\mathbf{F}} + \tilde{\mathbf{P}} \tag{3.21}$$

where, $\mathbf{N}_{4n\times 4n}$, $\bar{\mathbf{B}}_{4n\times 4n}$, $\hat{\mathbf{B}}_{4n\times 1n}$, $\mathbf{L}_{1n\times 1n}$ and $\tilde{\mathbf{B}}_{1n\times 4n}$ are known matrices. Similarly, $\bar{\mathbf{P}}_{\mathbf{m}}$ and $\tilde{\mathbf{P}}_{\mathbf{m}}$ are $4n \times 1$ and $1n \times 1$ column vectors comprising of the loading terms.

Non-zero elements of the matrices are given below,

$$\begin{aligned}
&N_{i_1j_1} = N_{j_3i_3} = \langle g_3^i g_1^j\rangle_h, && N_{i_2j_2} = N_{j_4i_4} = \langle g_5^i g_2^j\rangle_h \\
&\bar{B}_{i_1j_3} = \langle \bar{s}_{11} g_3^i g_3^j\rangle_h, && \hat{B}_{i_1j_1} = \langle \bar{s}_{13} g_3^i g_4^j\rangle_h \\
&\bar{B}_{i_2j_1} = -\langle g_5^i \tfrac{g_{1,\zeta}^j}{t}\rangle_h, && \bar{B}_{i_2j_4} = \langle \bar{s}_{55} g_5^i g_5^j\rangle_h \\
&\hat{B}_{i_4j_1} = -\langle g_2^i \tfrac{g_{4,\zeta}^j}{t}\rangle_h && \bar{B}_{i_3j_4} = -\langle \tfrac{g_{5,\zeta}^j}{t} g_1^i\rangle_h \\
&\tilde{B}_{i_1j_3} = -\langle \bar{s}_{13} g_4^i g_3^j\rangle_h && L_{i_1j_1} = \langle \bar{s}_{33} g_4^i g_4^j\rangle_h \\
&\tilde{B}_{i_1j_2} = \langle g_4^i \tfrac{g_{2,\zeta}^j}{t}\rangle_h
\end{aligned} \tag{3.22}$$

Similarly, non-zero elements of the pressure loading vector are given as,

$$\begin{aligned}
&\bar{P}_{m_{i1}} = \langle \bar{s}_{13} g_3^i (q_a + q_d t\zeta)\rangle_h, && \bar{P}_{m_{i4}} = -q_d \langle g_2^i\rangle_h \\
&\tilde{P}_{m_{i1}} = -\langle \bar{s}_{33} g_4^i (q_a + q_d t\zeta)\rangle_h
\end{aligned} \tag{3.23}$$

where, $\langle \ldots \rangle_h = h\int_0^1 (\ldots) d\zeta$

Since $g^i(\zeta)$ are known in close-form from the previous step, substituting algebraic equations (3.21) into Eq. (3.20) yields the following set of first-order ODEs with constant coefficients for $\bar{\mathbf{F}}$,

$$\bar{\mathbf{F}}_{,\xi} = \mathbf{B_0}\bar{\mathbf{F}} + \mathbf{P_0} \tag{3.24}$$

where, $B_0 = N^{-1}[\bar{B} + \hat{B}L^{-1}\bar{B}]$, $P_0 = N^{-1}[\hat{B}L^{-1}\tilde{P} + \bar{P}]$.

Above Eq. (3.24) represent a system of $4n$ non-homogeneous first order ODEs with constant coefficient. This can be solved using the approach discussed in Ref. [96].

3.4 NUMERICAL RESULTS AND DISCUSSIONS

The numerical results are presented and discussed for four types of beam as shown in Fig. 3.3. Beam (a) has two equal segments, the first and second segments are made of Aluminium (Al) and

Graphite-Epoxy (Gr-Ep), respectively. Beam (b) has two unequal segments, the first segment is $0.3L$ while the second is $0.7L$. Beam (c) is made of steel and Gr-Ep of unequal segment. Beam (d) has four equal segments. The first segment is made of pure aluminium, 2^{nd}, 3^{rd}, and 4^{th} contain the material properties corresponding to the varying ratio of Al and SiC. The thickness of all beams is taken as h. If a beam is subjected to clamped support at x=0 and free at edge x=a, then it is designated as CF. The material properties considered here are presented in Table 4.1.

Table 3.1: Material Properties

Sl no.	Material	Young's Modulus (Y) in GPa	Shear Modulus (G) in GPa	Poisson's Ratio (ν)
1	Aluminium (Al)	68	25.76	0.32
2	Steel	200	76.90	0.30
3	Al/SiC [90/10 layer]	70.20	26.53	0.323
4	Al/SiC [80/20 layer]	72.40	27.30	0.326
5	Al/SiC [70/30 layer]	74.60	28.066	0.329

		Y_1	Y_2	Y_3	G_{12}	G_{13}	G_{23}	ν_{12}	ν_{13}	ν_{23}
6	Graphite-Epoxy (Gr-Ep) [249]	181	10.30	10.30	7.17	7.17	2.87	0.28	0.28	0.33

Y_i and G_{ij} are in GPa

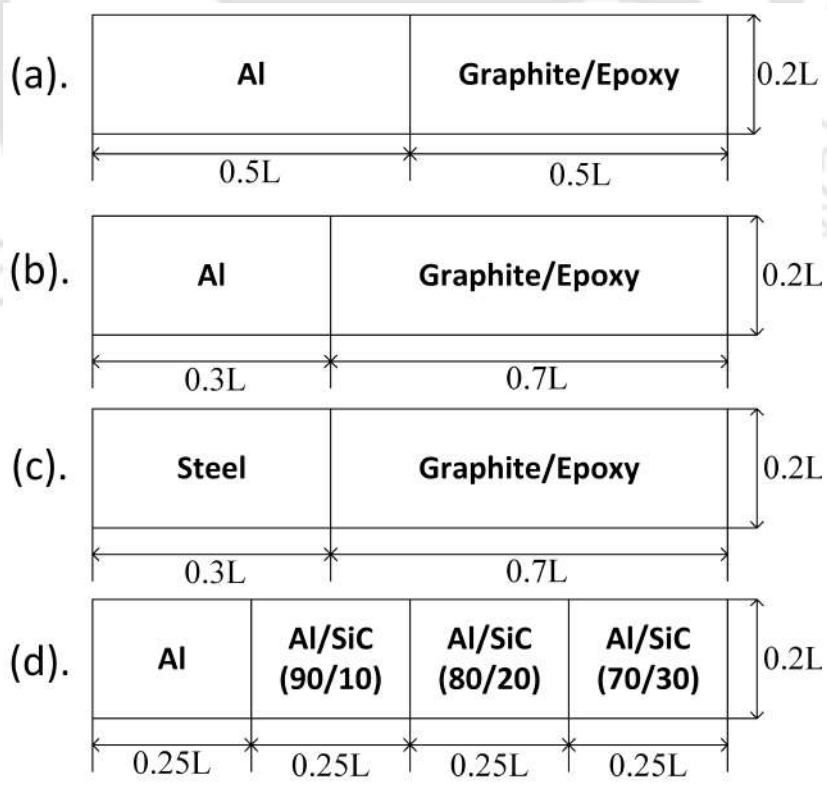

Fig. 3.3: Configuration lay up for beams (S= 5)

The beams are subjected to a uniform pressure q_2=q_0 at the top surface and q_1= 0 at the bottom

TH-3234_176103111

surface. The present numerical results are non-dimensionalized with $S = a/h$, q_0=1, Y_0= 10.3 GPa (for beam configuration a, b), 200 GPa (for beam c), and 74.60 GPa (for beam d) as:

$$(\bar{u}, \bar{w}) = 100(u, w/S)Y_0/p_0 h S^3;\ (\bar{\sigma}_x, \bar{\tau}_{zx}) = (\sigma_x, S\tau_{zx})/p_0 S^2$$

The 2D exact or closed-form solution is not available in the literature for other types of support conditions. Therefore, the present results are compared with 2D FE results for other combinations of boundary conditions. Since it is a beam with a small width, the plane stress element of ABAQUS [250] can be used. The 2D plane beam with length a along x-direction and thickness h along z-direction is modeled in ABAQUS using the eight-noded quadratic plane stress element type CPS8R with a mesh size of 100 (length) × 20 (thickness). The modeled beam with meshing is shown in Fig. 3.4. The converged results of FE are presented in figures along with 2D EKM results.

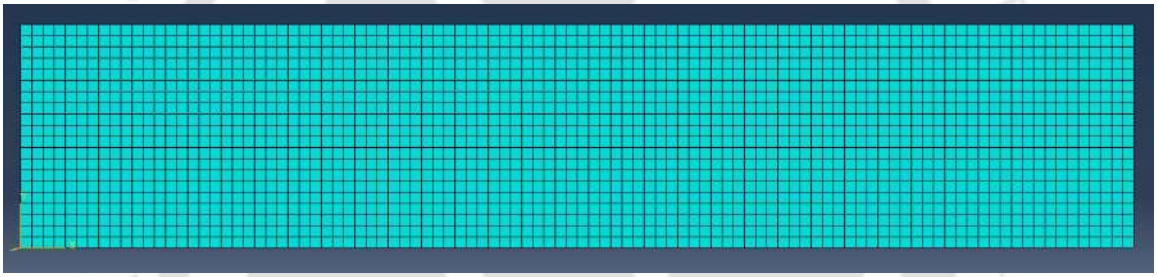

Fig. 3.4: Showing meshed beam

Longitudinal variation of $\bar{u}, \bar{w}, \bar{\sigma}_{xx}$ and $\bar{\tau}_{zx}$ is presented in Fig. 3.5 for thick (S=5) beam (a). The results are presented for clamped-clamped (CC) and clamped-free (CF) support conditions. Present EKM results with single-term (n=1) and two-term (n=2) with at least two iterations are presented to show the convergence, accuracy, and efficacy of the method. The in-plane displacement is asymmetric, and the Al section has a deeper curve than the Gr-Ep section. Similarly, transverse deflection has also shifted its maximum location, and a very steep slope is observed. The in-plane stress $\bar{\sigma}_{xx}$ has shown a rise in stress value and increases very rapidly near the boundary. Transverse shear stress $\bar{\tau}_{zx}$ also shows a sharp kink at the junction and boundary effects near the clamped supports. The EKM results for two terms are found in good match with FE results rather than a single term.

Longitudinal variation of $\bar{u}, \bar{w}, \bar{\sigma}_{xx}$ and $\bar{\tau}_{zx}$ is presented in Fig. 3.6 for beam (b). For unequal

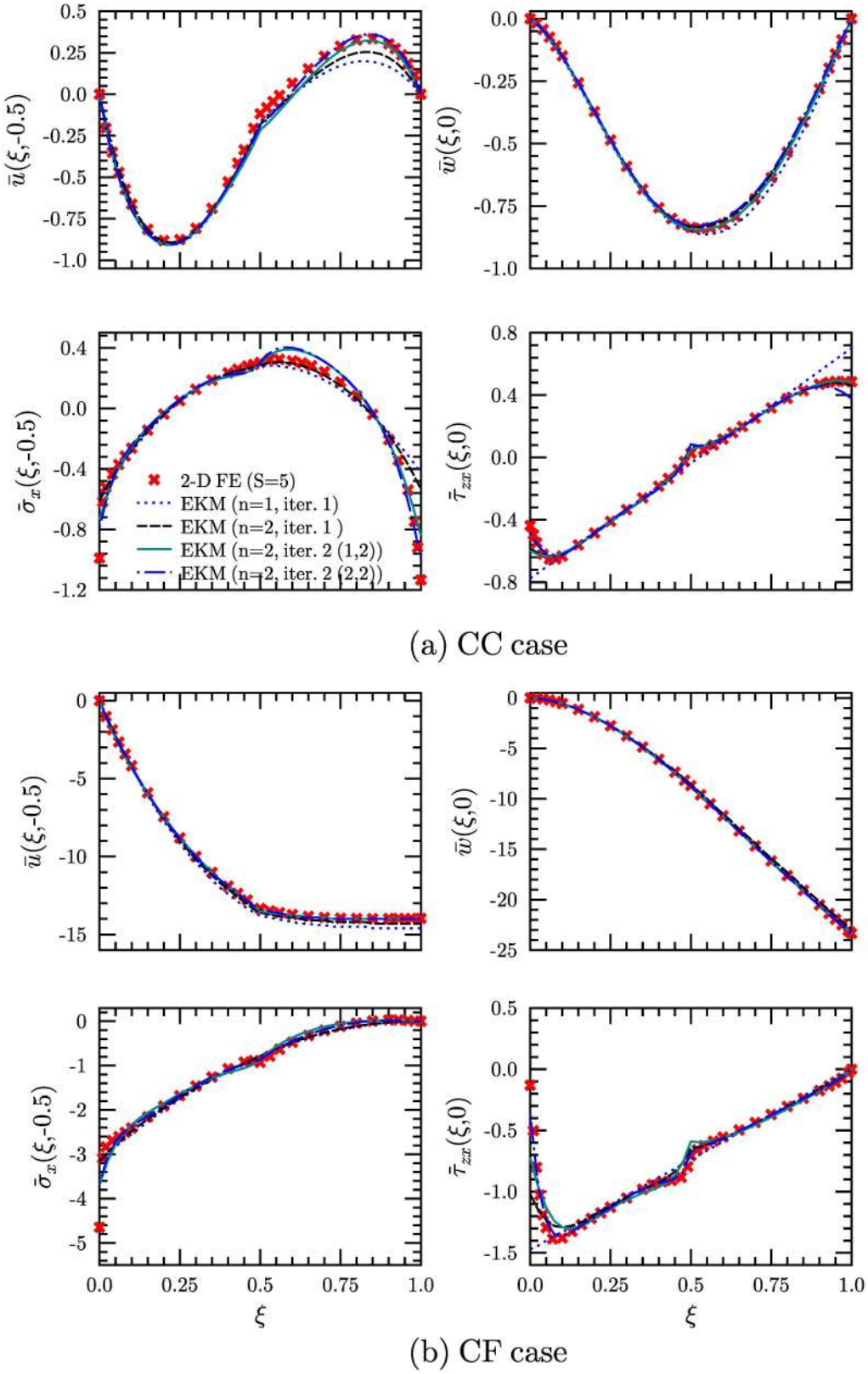

Fig. 3.5: Variation of deflections and stresses for Al/Gr-Ep beam (a) with S=5

TH-3234_176103111

segment, the variation is stronger than equally segmented beam (a). Specifically, a hook formation is observed in the variation of transverse shear stress. It is observed that for the CF case, a deeper and bigger hook is observed as compared to the CC case. Just near the interface, there is a surge in transverse shear stress, which may lead to fail the joint. This effect can not be captured by 1D theories of beam. In order to understand this effect more deeply, another beam (c) which has a strong material, steel and Gr-Ep, is considered for study. The longitudinal variations are presented in Fig. 3.7 for thick (S=5) beam (c). The results are presented for simply-supported (SS), CC, and CF cases. There is not much significant variation is observed for the SS case, while, under CC and CF cases, the effects are clearly visible for all the variables.

Longitudinal variation of shear stress $\bar{\tau}_{zx}$ is presented in Fig. 3.8 for beam (c). It is observed that there is no hook for the SS case, but the hook formation is observed under CC and CF cases. However, in the CF case, the hook is found to be more prominent and deeper than the CC case. It is to be noted that present results are in good agreement with 2D FE results except at the very edge. This mismatch is observed because the FE solution could not accurately capture the structure behavior due to stress singularities at the clamped boundary. Therefore, in the close vicinity of the clamped end, the accuracy of FE becomes questionable. This disagreement at the very clamped support is well reported and discussed in literature [96–99].

In recent work [251], an axially graded beam type specimen of Al/SiC having step-wise variation of material properties was fabricated. The beam had segments of varying properties which were joined longitudinally, is considered here for the study. The material properties of each segment is calculated using the rule of mixture and presented in Table 4.1. The longitudinal variation of $\bar{u}, \bar{w}, \bar{\sigma}_{xx}$ are presented in Fig. 3.9 for thick (S=5) beam (d) under SS, CC and CF cases. The effect of S is also studied in this analysis. It is observed that for SS and CF cases, there is no significant variation is observed with an increment of S. While the transverse displacement ($\bar{w}$) variation shows a significant difference under CC and CS cases. It shows the transverse displacement is decreasing with a decrease in beam thickness. Transverse shear stress $\bar{\tau}_{zx}$ is plotted in Fig. 3.10. The present results are in good agreement with 2D FE.

Figure 3.11 presents the through-thickness variation of in-plane stress for beam (c) at segment

TH-3234_176103111

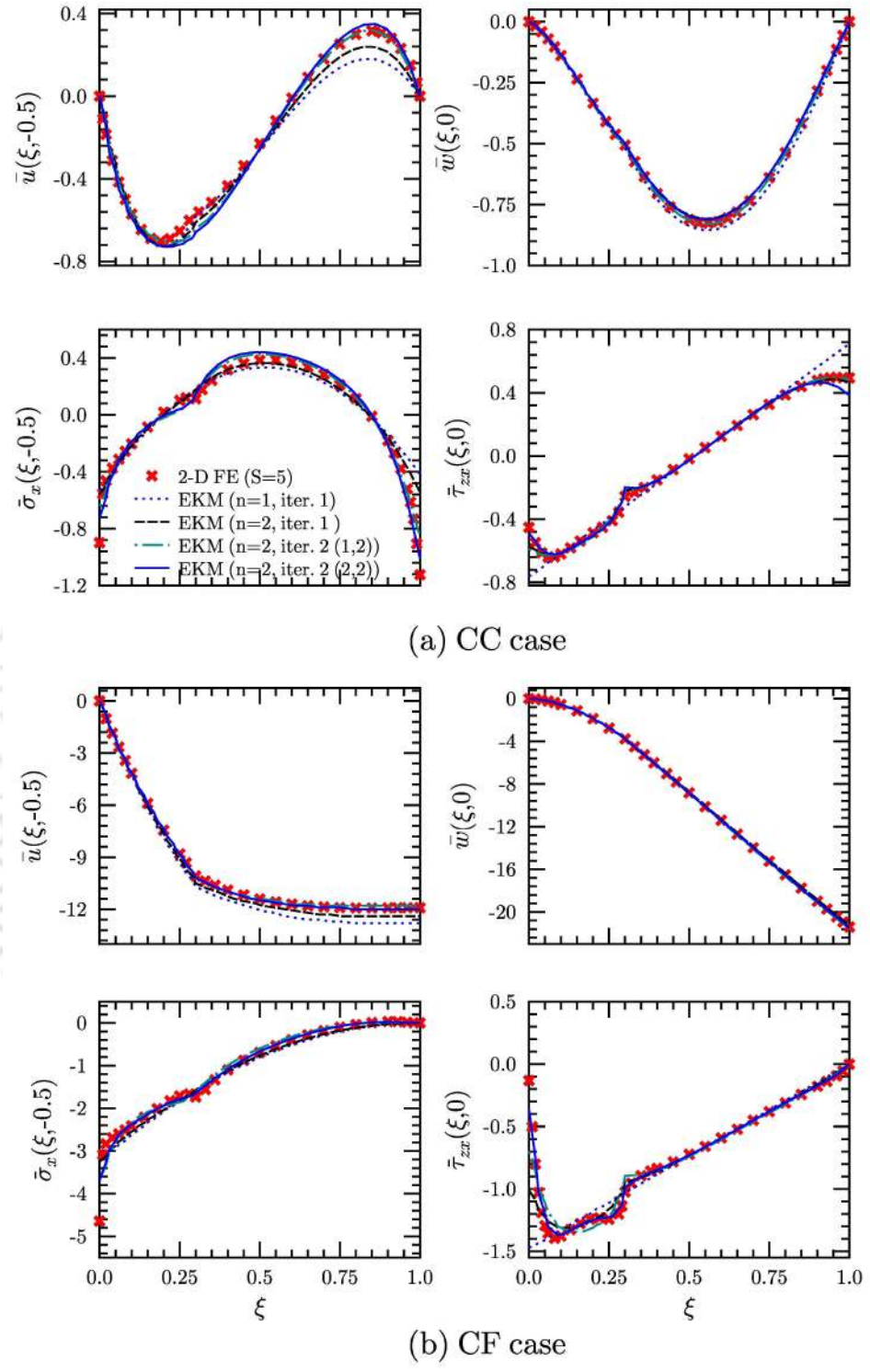

Fig. 3.6: Variation of deflections and stresses for Al/Gr-Ep beam (b) with S=5

junction (x=0.3) and near the junction (x=0.28). The present results are also compared with 2D FE, and found in good agreement for SS and CF cases. However, under the CC case, at the interface (x=0.3) a disagreement between EKM and FE can be observed. Through-thickness variations of

TH-3234_176103111

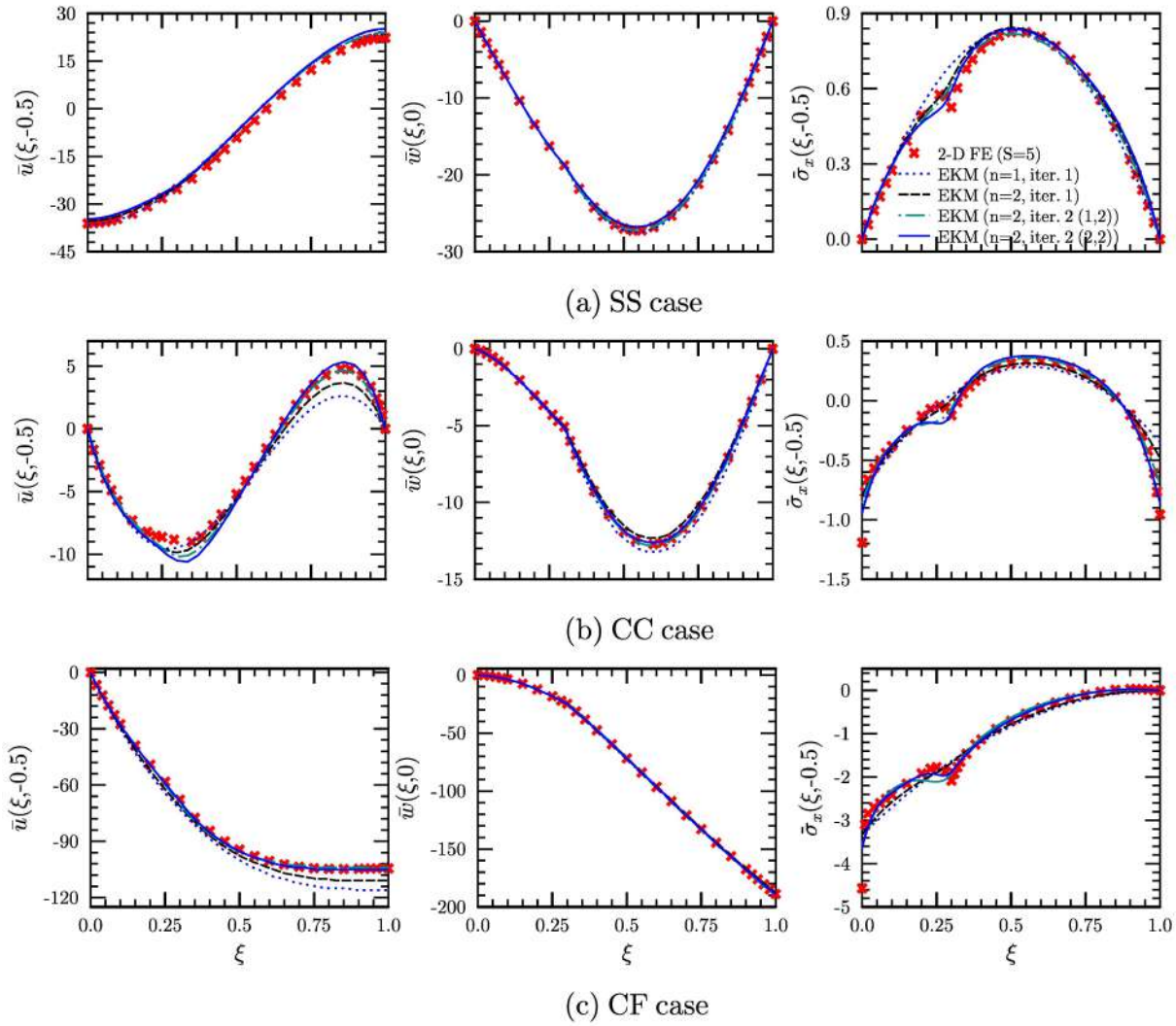

Fig. 3.7: Variation of deflections and stresses for Steel/Gr-Ep beam (c) with S=5

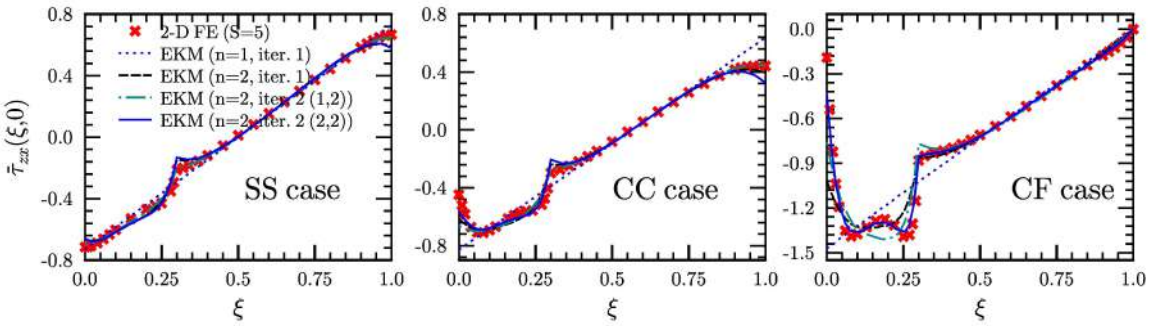

Fig. 3.8: Variation of shear stresses for Steel/Gr-Ep beam (c) with S=5

transverse shear stress at different locations, i.e. near the clamped edge and junction are presented in Fig. 3.12. For this case also present results show a good match with 2D FE. The contour plot of 2D FE is presented in Fig. 3.13. The stress variation in the steel section does not follow traditional

TH-3234_176103111

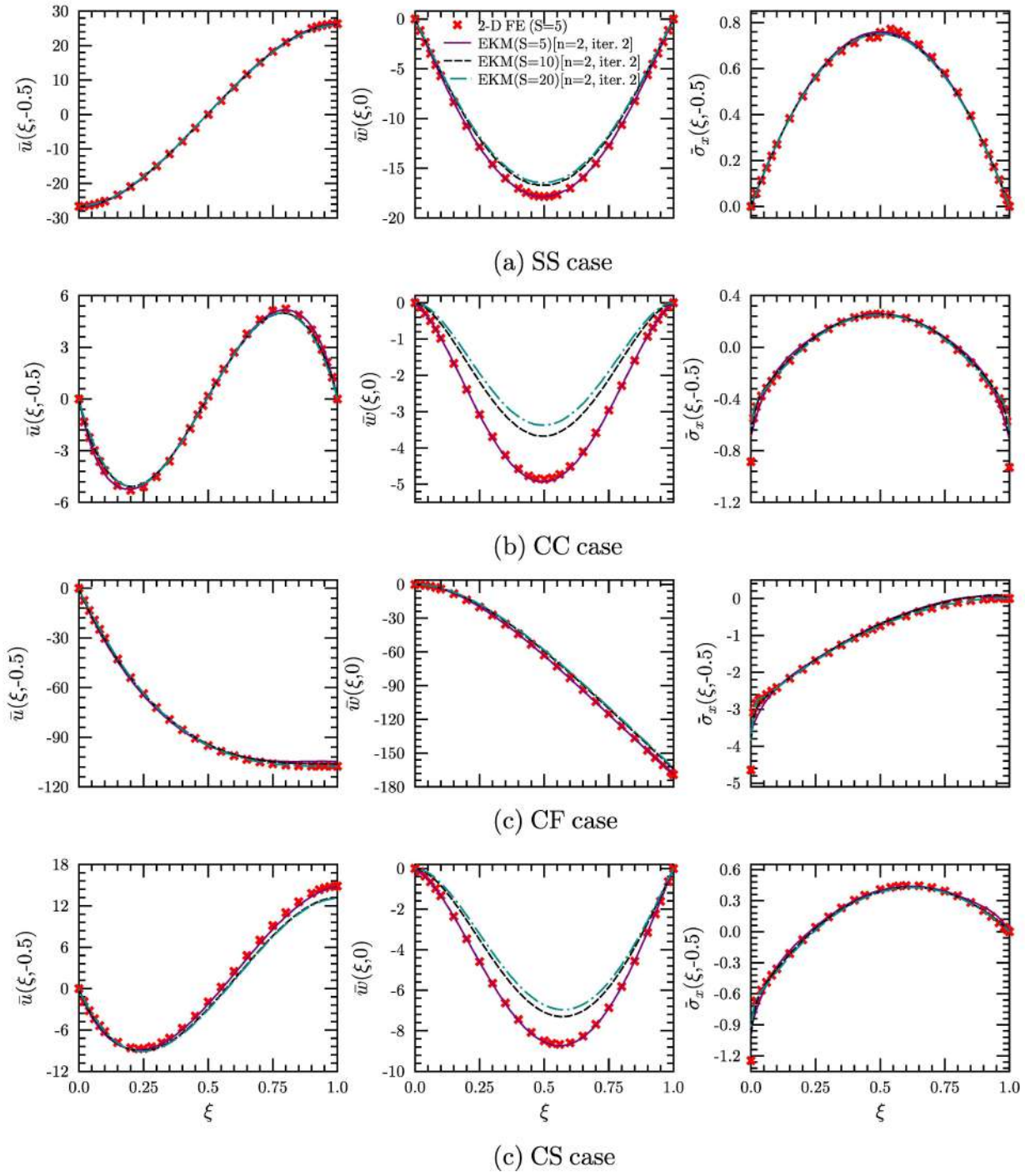

Fig. 3.9: Variation of deflections and stresses for four segmented Al/Sic beam (d) with S=5, 10 and 20

variation, while in the Gr-Ep section, it is more or less usual. Therefore, one-dimensional beam theories will not predict this behavior. The variation is significantly affected by the boundary conditions (in Fig. 3.8).

TH-3234_176103111

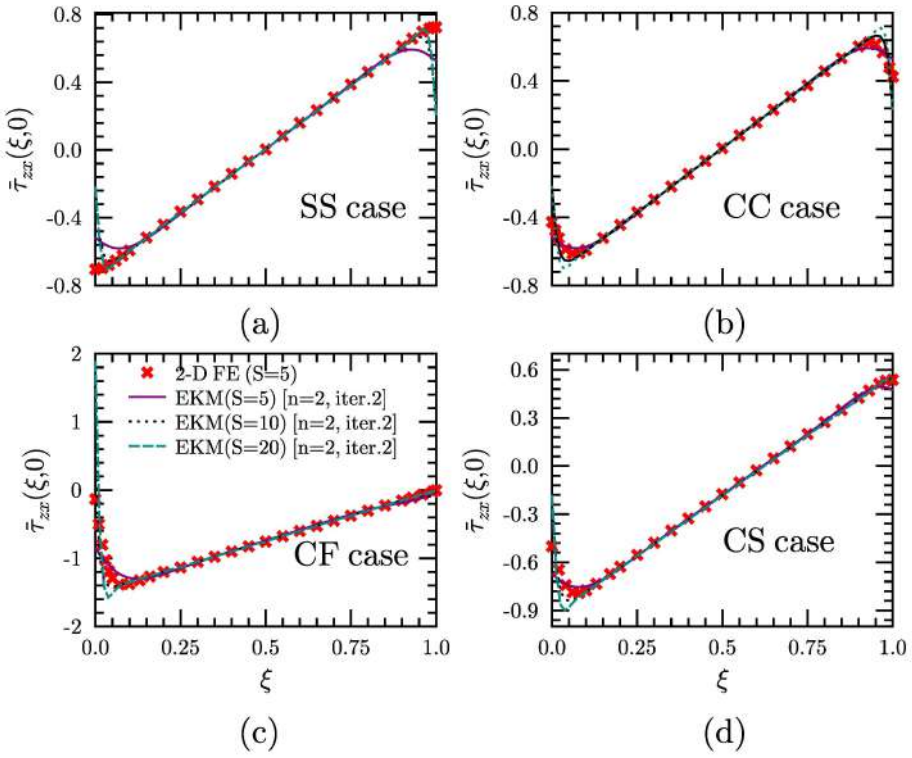

Fig. 3.10: Variation of shear stresses for four segmented Al/Sic beam (d) with S=5, 10 and 20

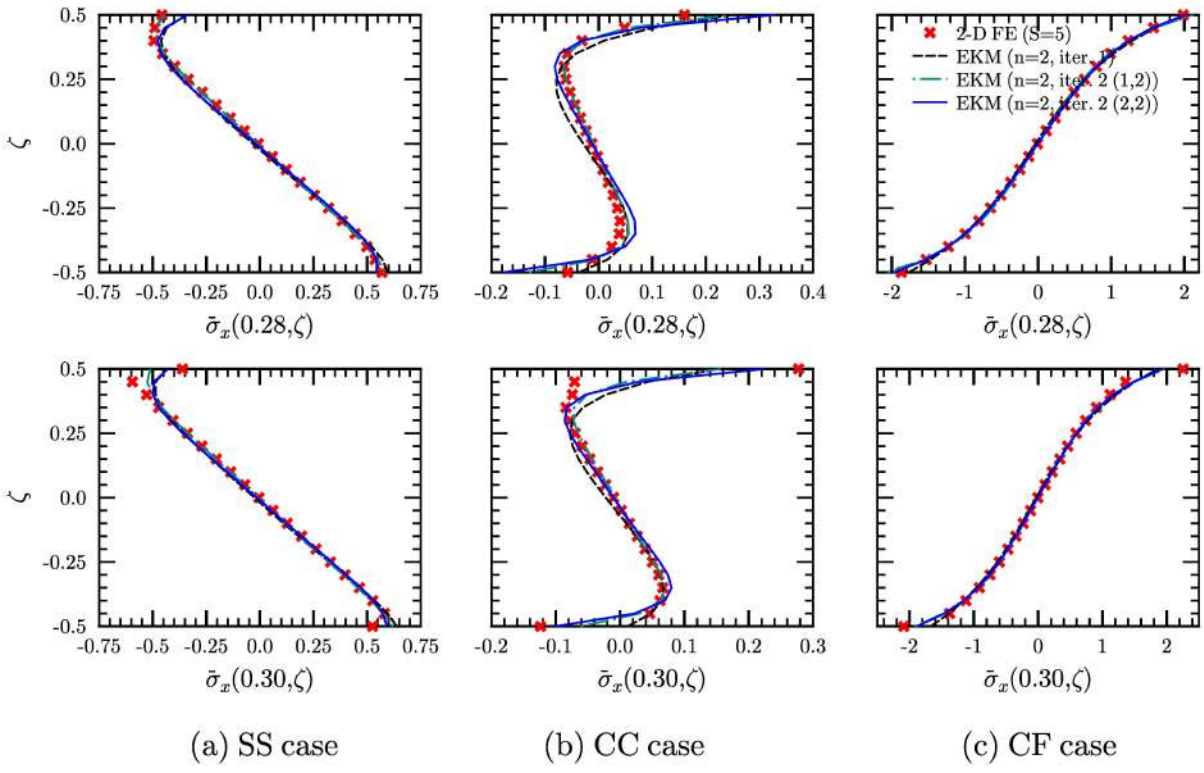

Fig. 3.11: Variation of stresses for Steel/Gr-Ep beam (c) with S=5

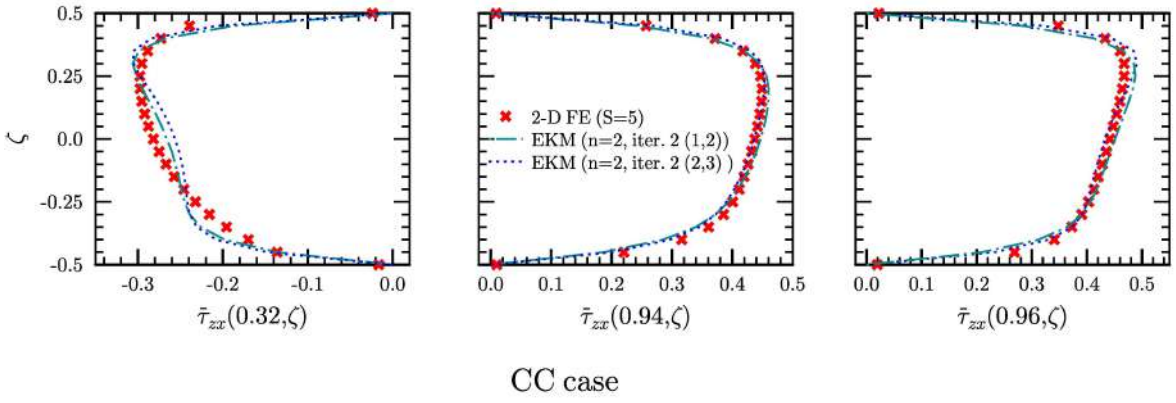

Fig. 3.12: Variation of shear stresses for Steel/Gr-Ep beam (c) with S=5

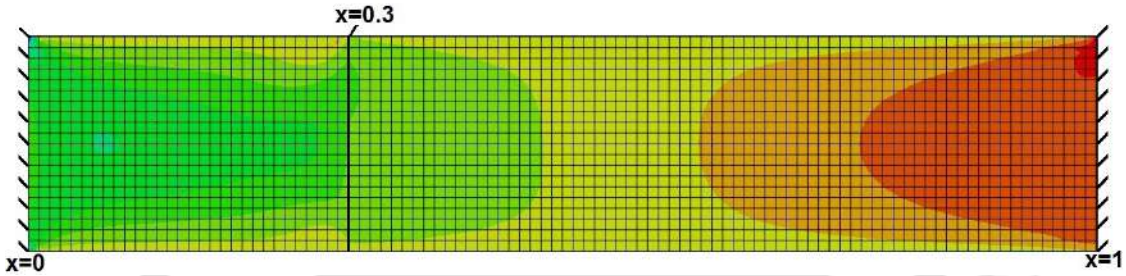

Fig. 3.13: Variation of shear stresses for Steel/Gr-Ep beam in ABAQUS under CC case

3.5 SUMMARY

For the first time, a two-dimensional analytical solution using the EKM approach is developed for a multi-segmented dissimilar beam based on elasticity. The interfaces along x-direction are satisfied exactly. Numerical results are presented for four different lay-ups. The present technique is found to be more versatile and can handle any material combination along the length. This approach is also able to manage any kind of variation in material property (power law, exponential, arbitrary) along the length. From the study of beam (d), it is clear that this method is capable enough to analyze the behavior of axially graded beams. The EKM results converge very fast i.e., within two iterations and show a good match with FE results. The longitudinal variation of shear stress is found to be more prominent at the clamped edges. A very significant effect on the shear stress is observed near the junction, and the effect of boundary conditions play a significant role. An increase in S for beam (d) shows a decrease in deflection under CC and CS cases. This development will lead to the development of multi-material step beam and plate problems.

TH-3234_176103111

Chapter 4

2-D Analytical Solutions for the Bending of Multi-Segmented Panels

4.1 INTRODUCTION

The analytical results for the multi-segmented beams are successfully obtained and validated with FE results in Chapter 3. Now, in this Chapter, the analysis is extended for the multi-segmented panels. A two-dimensional closed-form solution is developed for static bending analysis of multi-segmented panels. The panels with different segment materials and lengths are considered. A panel with gradually varying properties is also considered, which mimics the axially graded panel under different support cases. A flowchart showing the solution methedology involved for an elastic panel through EKM approach is shown in Fig. 4.1. The Reissner-type mixed-form of governing equations as developed in Chapter 3 for the beams, is now extended for the flat panels and described in Sec. 4.2. The multi-term extended Kantorovich approach, as developed in Chapter 3, is extended and applied to solve the governing equations in Sec. 4.3. The use of EKM to generate a set of ODEs with constant coefficient along the z-direction is explained in Sec. 4.3.1. Further, the equations are solved analytically in closed form. An additional set of ordinary differential equations (ODEs) with varying coefficients are obtained along the x-direction discussed in Sec. 4.3.2. The numerical results are reported in Sec. 4.4 for various configurations, aspect ratios, ply-angles, and boundary conditions of panels. The present method is validated by comparing the results with the 3-D FE (ABAQUS). Finally, the work presented in this Chapter is concluded, and a summary of it is reported in Sec. 4.5.

TH-3234_176103111

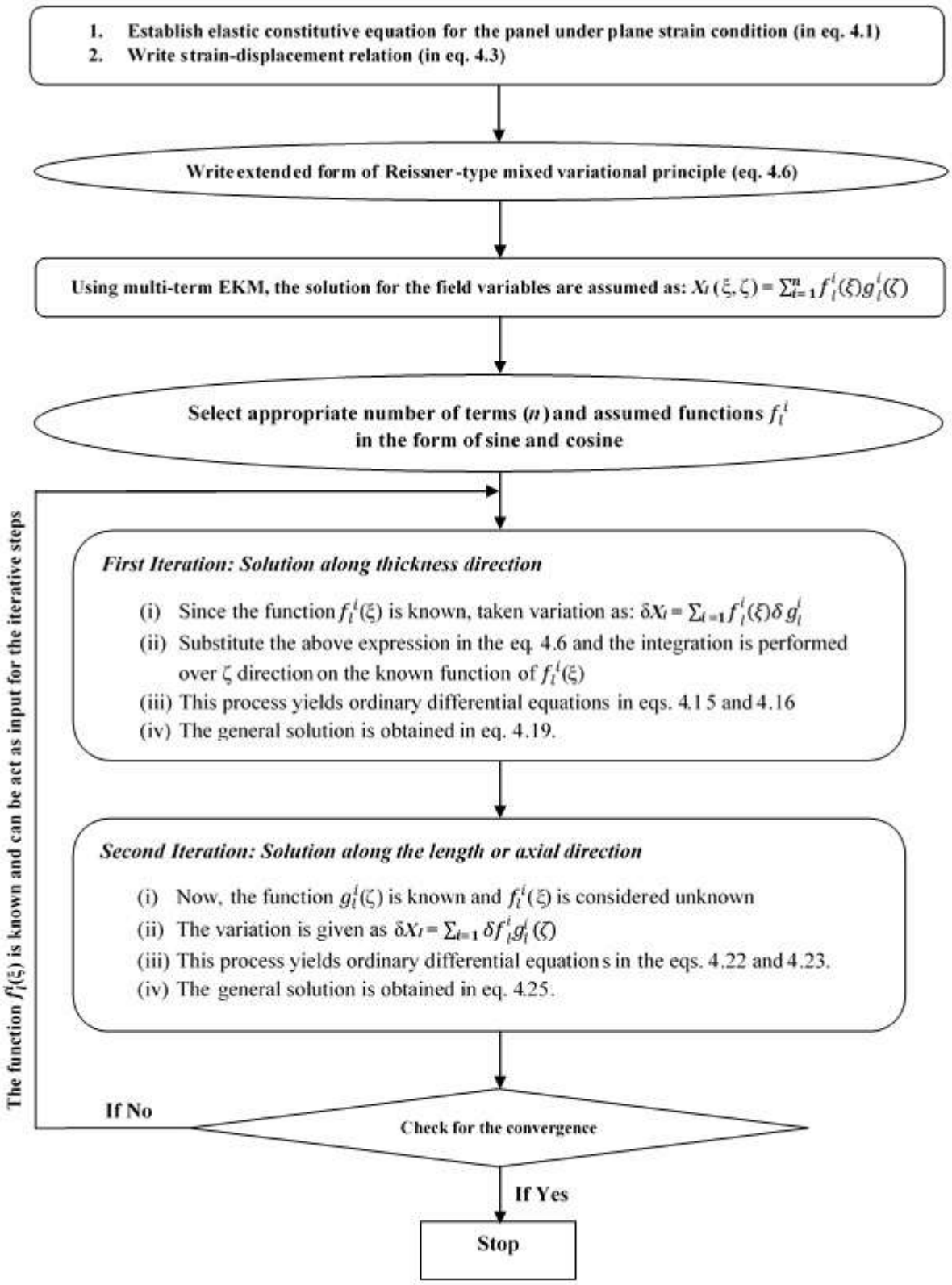

Fig. 4.1: A flow chart of EKM approach for multi-segmented panel

4.2 THEORETICAL FORMULATION

A single-layered panel as shown in Fig. 4.2 having span length (a) and total thickness (h) along the x-direction and z-direction respectively is considered for the study. The panel can have different boundary condition at $x = 0$ and a, and on the bottom and top surfaces a uniformly distributed pressure loads of q_1 and q_2 have been applied, respectively. The panel as shown in Fig. 4.2 consists of S segments along x-axis. For the panel analysis, similar assumptions are made as for the beam in Chapter 3. The panel is constructed with S perfectly bonded segments of materials with the principal material axis x_1, which is aligned in the x-direction. The p_{th} segment is having a length $a^{(p)}$, and its left surface is denoted as x_{p-1} along the x-coordinate. The interface between the p_{th} and the $(p+1)_{th}$ segment is named as the p_{th} interface. The segment superscript is omitted unless needed for clarity.

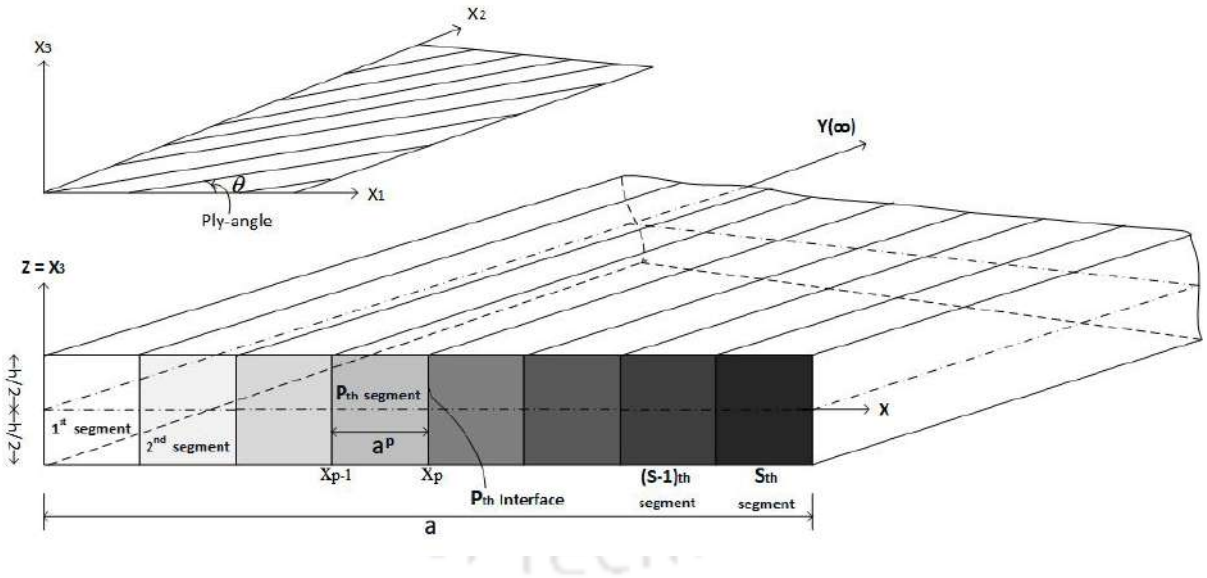

Fig. 4.2: The multi-segmented panel geometry.

Since the width is extremly long along y-direction that represents a generalized plain strain problem of cylindrical bending, where all entities are independent of y direction [252]. Whereas, the displacement u, v and w are considered along x-axis, y-axis and z-axis, respectively which is independent of y-coordinate. For such plane strain condition, the constitutive equations for an blue angle-ply orthotropic lamina from the material coordinate system (x_1, x_2, x_3) to the rectangular

TH-3234_176103111

coordinate system (x, y, z) after transformation for a panel can be written as [252],

$$\begin{bmatrix} \varepsilon_x \\ \varepsilon_y \\ \varepsilon_z \\ \gamma_{yz} \\ \gamma_{zx} \\ \gamma_{xy} \end{bmatrix} = \begin{bmatrix} \bar{s}_{11} & \bar{s}_{12} & \bar{s}_{13} & 0 & 0 & \bar{s}_{16} \\ \bar{s}_{12} & \bar{s}_{22} & \bar{s}_{23} & 0 & 0 & \bar{s}_{26} \\ \bar{s}_{13} & \bar{s}_{23} & \bar{s}_{33} & 0 & 0 & \bar{s}_{36} \\ 0 & 0 & 0 & \bar{s}_{44} & \bar{s}_{45} & 0 \\ 0 & 0 & 0 & \bar{s}_{54} & \bar{s}_{55} & 0 \\ \bar{s}_{16} & \bar{s}_{26} & \bar{s}_{36} & 0 & 0 & \bar{s}_{66} \end{bmatrix} \begin{bmatrix} \sigma_x \\ \sigma_y \\ \sigma_z \\ \tau_{yz} \\ \tau_{zx} \\ \tau_{xy} \end{bmatrix} \tag{4.1}$$

The $\bar{s}_{ij}$ are transformed elastic compliances, whose expressions in terms of the engineering properties, namely, Young's modulus Y_i, shear modulus G_{ij} and major poisson's ratio ν_{ij} can be taken from Ref. [98]. All entities are expressed in non-dimensional forms to provide numerical stability during the solution process in such a way that, on the substitution of dimensionless entities do not alter the form of all governing equations.

$$\begin{gathered} S = a/h; \quad \bar{s}^*_{ij} = \bar{s}_{ij} Y_0; \quad h^* = h/a \\ (\sigma^*_x, \sigma^*_y, \sigma^*_z, \tau^*_{xy}, \tau^*_{yz}, \tau^*_{zx}) = (\sigma_x, \sigma_y, \sigma_z, \tau_{xy}, \tau_{yz}, \tau_{zx})/SY_0 \\ (\epsilon^*_x, \epsilon^*_y, \epsilon^*_z, \gamma^*_{xy}, \gamma^*_{yz}, \gamma^*_{zx}) = (\epsilon_x, \epsilon_y, \epsilon_z, \gamma_{xy}, \gamma_{yz}, \gamma_{zx})/S \\ (u^*, v^*, w^*) = (u, v, w)/h; \quad (G^*_{ij},\, Y^*_i) = (G_{ij},\, Y_i)/Y_0 \end{gathered} \tag{4.2}$$

where, Y_0 is the Young's modulus value used for the non-dimensionalization. The above dimensionless form of the entities are used in subsequent mathematical equations. For the simplicity, the superscript * is dropped. The strain-displacement relations are presented as,

$$\begin{gathered} \epsilon_x = u_{,x}; \quad \epsilon_y = 0; \quad \epsilon_z = w_{,z} \\ \gamma_{zx} = w_{,x} + u_{,z}; \quad \gamma_{yz} = v_{,z}; \quad \gamma_{xy} = v_{,x} \end{gathered} \tag{4.3}$$

Using Eq. (4.3) and Eq. (4.1), σ_y can be obtained as

$$\sigma_y = -(\bar{s}_{12}/\bar{s}_{22})\sigma_x - (\bar{s}_{23}/\bar{s}_{22})\sigma_z - (\bar{s}_{26}/\bar{s}_{22})\tau_x y \tag{4.4}$$

and the same is eliminated from Eq. (4.1) to yield

$$\begin{aligned} \epsilon_x &= p_{11}\sigma_x + p_{13}\sigma_z + p_{16}\tau_{xy} \\ \epsilon_z &= p_{31}\sigma_x + p_{33}\sigma_z + p_{36}\tau_{xy} \\ \gamma_{xy} &= p_{61}\sigma_x + p_{63}\sigma_z + p_{66}\tau_{xy} \end{aligned} \tag{4.5}$$

where, $p_{ij} = \bar{s}_{ij} - \bar{s}_{2i}\bar{s}_{2j}/\bar{s}_{22}$

The Reissner-type mixed variational principle for cylindrical bending analysis of the panel, without any body force and unit width along y-direction, can be expressed as [98],

$$\begin{aligned}\int_V [\delta u(\sigma_{x,x} + \tau_{xz,z}) + \delta v(\tau_{xy,x} + \tau_{yz,z}) + \delta w(\tau_{zx,x} + \sigma_{z,z}) \\ +\delta\sigma_x(\epsilon_x - u_{,x}) + \delta\sigma_z(\epsilon_z - w_{,z}) + \delta\tau_{yz}(\gamma_{yz} - v_{,z}) \\ +\delta\tau_{zx}(\gamma_{zx} - u_{,z} - w_{,x}) + \delta\tau_{xy}(\gamma_{xy} - v_{,x})]\, dV = 0, \quad \forall \delta u_i, \delta v_i, \delta w_i, \delta\sigma_i, \delta\tau_{ij}\end{aligned} \tag{4.6}$$

where, V stands for the volume of panel having unit width along the y-direction. Now, the expressions of strain components ϵ_x, ϵ_z, γ_{xy}, γ_{yz} and γ_{zx} are substituted from Eq. (4.1), Eq. (4.5) into Eq. (4.6), which yields

$$\begin{aligned}\int_V [\delta u(\sigma_{x,x} + \tau_{xz,z}) + \delta v(\tau_{xy,x} + \tau_{yz,z}) + \delta w(\tau_{zx,x} + \sigma_{z,z}) + \\ \delta\sigma_x(\bar{s}_{11}\,\sigma_x + \bar{s}_{13}\,\sigma_z + \bar{s}_{16}\,\tau_{xy} - u_{,x}) + \\ \delta\sigma_z(\bar{s}_{13}\sigma_x + \bar{s}_{33}\sigma_z + \bar{s}_{36}\,\tau_{xy} - w_{,z}) + \delta\tau_{yz}(\bar{s}_{44}\tau_{yz} + \bar{s}_{45}\tau_{zx} - v_{,z}) + \\ \delta\tau_{zx}(\bar{s}_{45}\tau_{yz} + \bar{s}_{55}\tau_{zx} - u_{,z} - w_{,x}) + \delta\tau_{xy}(\bar{s}_{16}\sigma_x + \bar{s}_{66}\tau_{xy} + \bar{s}_{36}\sigma_z - v_{,x})]\, dV = 0,\end{aligned} \tag{4.7}$$

The dimensionless in-plane coordinates ξ^p and a local thickness coordinate ζ are introduced for p_{th} layer, which varies from 0 to 1.

$$\xi^p = (x - x_{p-1})/a^{(p)}\,; \qquad \zeta = (z - z_0)/h \tag{4.8}$$

A uniformly distributed pressure q_1 and q_2 are applied on the bottom & top surfaces of the panel, respectively. Whereas, top and bottom surfaces of the panel are assumed to be free from the shear traction. Therefore support conditions at the top ($z = h/2$) and bottom ($z = -h/2$) surfaces of the panel can be expressed as,

$$\begin{aligned}\text{at} \quad z = -h/2: \quad \sigma_z = -q_1; \quad \tau_{zx} = 0; \quad \tau_{yz} = 0 \\ \text{at} \quad z = h/2: \quad \sigma_z = -q_2; \quad \tau_{zx} = 0; \quad \tau_{yz} = 0\end{aligned} \tag{4.9}$$

For the perfect bonding of each segment, the interface continuity conditions must be satisfied at the p_{th} interface,

$$[(u,\, v,\, w,\, \sigma_x,\, \tau_{yz},\, \tau_{zx})|_{\xi=1}]^{(p)} = [(u,\, v,\, w,\, \sigma_x,\, \tau_{yz},\, \tau_{zx})|_{\xi=0}]^{(p+1)} \tag{4.10}$$

Various type of mechanical supports combination can be applied at x=0 & x=a of the panel and the support conditions are as,

$$\begin{aligned} \text{Simply supported (S)}: &\quad w=0, \quad \tau_{xy}=0, \quad \sigma_x=0 \\ \text{Clamped (C)}: &\quad u=0, \quad v=0, \quad w=0 \\ \text{Free (F)}: &\quad \sigma_x=0, \quad \tau_{xz}=0, \quad \tau_{xy}=0 \end{aligned} \tag{4.11}$$

4.3 THE GENERALIZED MULTI-TERM EKM

The eight field variables to be solved are $\mathbf{X} = [\,u \quad v \quad w \quad \sigma_x \quad \sigma_z \quad \tau_{xy} \quad \tau_{yz} \quad \tau_{zx}\,]^{\mathrm{T}}$. These field variables for the p_{th} lamina are expressed in n-term series using the multi-term EKM [98], which contain the products of separable functions of ξ, ζ and time, as,

$$X_l(\xi,\zeta) = \sum_{i=1}^{n} f_l^i(\xi) g_l^i(\zeta) + \delta_{l5}[q_a + z q_d] \qquad \text{for} \qquad l = 1, 2, \ldots 8 \tag{4.12}$$

where, $g_l^i(\zeta)$ and $f_l^i(\xi)$ are the unknown functions of ζ and ξ, respectively. Here, n is the number of terms in solution and the repeated index l does not mean summation here. The nonhomogeneous boundary conditions for σ_z as given in Eq. (4.10) has been satisfied by superimposing an additional term ($\delta_{l5}[q_a + z q_d]$) into the above solution for σ_z. Where, δ_{l5} is Kroneckor's delta, $\delta_{l5} = 1$ for $l = 5$ and else $\delta_{l5} = 0$, $q_a = -(q_1 + q_2)/2$ and $q_d = -(q_2 - q_1)/h$. Using similar procedure as for the beam, the functions (g and f) of ζ and ξ are solved in two iterative steps.

4.3.1 First Iteration Step

In first step, the functions $g_l^i(\zeta)$ need to be solved, while functions $f_l^i(\xi)$ in the x-direction are assumed as known. In the EKM, it is not necessary for the initial trail functions to satisfy the required support conditions. Hence, to initiate the iteration process functions f_l^i are assumed as, $f_1^i(\xi)$=$f_2^i(\xi)$=$f_7^i(\xi)$=$f_8^i(\xi)$=$\cos i\pi\xi$ and $f_3^i(\xi)$=$f_4^i(\xi)$=$f_5^i(\xi)$=$f_6^i(\xi)$=$\sin i\pi\xi$. Now, the functions f_l^i are known and the variation δX_i is given as,

$$\delta X_l = \sum_{i=1}^{n} f_l^i(\xi) \delta g_l^i, \qquad l = 1, 2, \ldots 8 \tag{4.13}$$

TH-3234_176103111

The functions $g_l^i(\zeta)$ are seperated into two column vectors $\bar{\mathbf{G}}$ and $\hat{\mathbf{G}}$. The specific $6n$ primary variables that are specified at the support along z-direction are contained in $\bar{\mathbf{G}}$ vector. whereas the remaining $2n$ dependent variables are contained in the $\hat{\mathbf{G}}$ vector.

$$\bar{\mathbf{G}} = [\, g_1^1 \dots g_1^n \quad g_2^1 \dots g_2^n \quad g_3^1 \dots g_3^n \quad g_5^1 \dots g_5^n \quad g_7^1 \dots g_7^n \quad g_8^1 \dots g_8^n \,]^T$$

$$\hat{\mathbf{G}} = [\, g_4^1 \dots g_4^n \qquad g_6^1 \dots g_6^n \,]^T \tag{4.14}$$

here, the f_l^i are known functions integration along x-direction are evaluated. Since the change in δg_l^i is arbitrary, the coefficients of δg_l^i must be equal to zero. It results a set of $6n$ first order ODEs and $2n$ linear algebraic equations for each segment, as following:

$$\mathbf{M}\bar{\mathbf{G}}_{,\zeta} = \bar{\mathbf{A}}\bar{\mathbf{G}} + \hat{\mathbf{A}}\hat{\mathbf{G}} + \bar{\mathbf{Q}}_{\mathbf{p}} \tag{4.15}$$

$$\mathbf{K}\hat{\mathbf{G}} = \tilde{\mathbf{A}}\bar{\mathbf{G}} + \tilde{\mathbf{Q}}_{\mathbf{p}} \tag{4.16}$$

where, $\mathbf{M}_{6n\times 6n}$, $\bar{\mathbf{A}}_{6n\times 6n}$, $\hat{\mathbf{A}}_{6n\times 2n}$, $\mathbf{K}_{2n\times 2n}$ and $\tilde{\mathbf{A}}_{2n\times 6n}$ are known matrices. The matrices contains non-zero elements are written below as,

$$M_{i_1j_1} = \langle f_8^i f_1^j \rangle_a, \quad M_{i_2j_2} = \langle f_7^i f_2^j \rangle_a, \quad M_{i_3j_3} = \langle f_5^i f_3^j \rangle_a$$

$$M_{i_1j_1} = M_{j_6i_6}, \quad M_{i_2j_2} = M_{j_5i_5}, \quad M_{i_3j_3} = M_{j_4i_4}$$

$$\bar{A}_{i_1j_3} = \tfrac{-t}{a}\langle f_8^i f_{3,\xi}^j \rangle_a,\ \bar{A}_{i_1j_5} = t\bar{s}_{45}\langle f_8^i f_7^j \rangle_a,\ \bar{A}_{i_1j_6} = t\bar{s}_{55}\langle f_8^i f_8^j \rangle_a$$

$$\bar{A}_{i_2j_5} = t\bar{s}_{44}\langle f_7^i f_7^j \rangle_a,\ \bar{A}_{i_2j_6} = t\bar{s}_{45}\langle f_7^i f_8^j \rangle_a,\ \bar{A}_{i_3j_4} = tp_{33}\langle f_5^i f_5^j \rangle_a$$

$$\hat{A}_{i_3j_1} = tp_{31}\langle f_5^i f_4^j \rangle_a,\ \hat{A}_{i_3j_2} = tp_{36}\langle f_5^i f_6^j \rangle_a,\ \bar{A}_{i_4j_6} = \tfrac{-t}{a}\langle f_3^i f_{8,\xi}^j \rangle_a \tag{4.17}$$

$$\hat{A}_{i_5j_2} = \tfrac{-t}{a}\langle f_2^i f_{6,\xi}^j \rangle_a,\ \hat{A}_{i_6j_1} = \tfrac{-t}{a}\langle f_1^i f_{4,\xi}^j \rangle_a,\ K_{i_1j_1} = p_{11}\langle f_4^i f_4^j \rangle_a$$

$$K_{i_1j_2} = p_{16}\langle f_4^i f_6^j \rangle_a,\ K_{i_2j_2} = p_{66}\langle f_6^i f_6^j \rangle_a,\ K_{i_2j_1} = K_{i_1j_2}$$

$$\tilde{A}_{i_1j_1} = \tfrac{1}{a}\langle f_4^i f_{1,\xi}^j \rangle_a, \quad \tilde{A}_{i_2j_2} = \tfrac{1}{a}\langle f_6^i f_{2,\xi}^j \rangle_a$$

$$\tilde{A}_{i_1j_4} = -p_{13}\langle f_4^i f_5^j \rangle_a,\ \tilde{A}_{i_2j_4} = -p_{63}\langle f_6^i f_5^j \rangle_a$$

where $i_c = (c-1)n + i$ and $j_d = (d-1)n + j$ for $c, d = 1, 2, \ldots, 8$. $\bar{Q}_p, \tilde{Q}_p$ are load vectors of size $6n$, and $2n$, respectively, whose non-zero elements are given by

$$\begin{aligned} \bar{Q}_{p_{i4}} &= -tq_d \langle f_3^i \rangle_a \qquad \bar{Q}_{p_{i3}} = tp_{33} \langle f_5^i \rangle_a \, (q_a + \zeta t q_d) \\ \tilde{Q}_{p_{i1}} &= -p_{13} \langle f_4^i \rangle_a \, (q_a + \zeta t q_d) \qquad \tilde{Q}_{p_{i2}} = -p_{63} \langle f_6^i \rangle_a \, (q_a + \zeta t q_d) \end{aligned} \tag{4.18}$$

where, the notation $\langle \ldots \rangle_a = \sum_{p=1}^{S} a^{(p)} \int_0^1 (\ldots)^{(p)} \, d\xi$ depicts the integration over the span length a and $q_a = q_a + q_d z_0$. Since the functions f_l^i are known functions, elements of the matrices defined in Eqs. (4.17) and Eq. (4.18) have been evaluated in close form. $\hat{\mathbf{G}}$ is obtained after solving Eq. (4.16) and it further substituted into Eq. (4.15), which results

$$\bar{\mathbf{G}}_{,\zeta} = \mathbf{A}\bar{\mathbf{G}} + \mathbf{Q_p} \tag{4.19}$$

where, $\mathbf{A} = \mathbf{M}^{-1}[\bar{\mathbf{A}} + \hat{\mathbf{A}}\mathbf{K}^{-1}\tilde{\mathbf{A}}]$, $\mathbf{Q_p} = \mathbf{M}^{-1}[\bar{\mathbf{Q}}_\mathbf{p} + \hat{\mathbf{A}}\mathbf{K}^{-1}\tilde{\mathbf{Q}}_\mathbf{p}]$.

Above Eq. (4.19) shows a system of $6n$ non-homogeneous first order ODEs with constant coefficient. This set of equations can be solved by using the approach as discussed in Ref. [96].

4.3.2 Second Iteration Step

Now from the first step function $g_l^i(\zeta)$ is known, whereas $f_l^i(\xi)$ are assumed as unknown. So an arbitrary variation of the functions f_l^i is considered in this step. Therefore, from equation Eq. (4.12) the variation for this case can be written as:

$$\delta X_l = \sum_{i=1}^{n} g_l^i(\zeta) \delta f_l^i \quad \text{for} \quad l = 1, 2, \ldots, 8 \tag{4.20}$$

Similarly, like the previous step, $f_l^i(\xi)$ are seperated into two column vectors namely $\bar{\mathbf{F}}$ and $\hat{\mathbf{F}}$. Where, $\bar{\mathbf{F}}$ contains those particular $6n$ primary variables which come in the support conditions at edges $x = 0, 1$ and $\hat{\mathbf{F}}$ holds the remaining $2n$ variables,

$$\begin{aligned} \bar{\mathbf{F}} &= [\, f_1^1 \ldots f_1^n \quad f_2^1 \ldots f_2^n \quad f_3^1 \ldots f_3^n \quad f_4^1 \ldots f_4^n \quad f_6^1 \ldots f_6^n \quad f_8^1 \ldots f_8^n \,]^T \\ \hat{\mathbf{F}} &= [\, f_5^1 \ldots f_5^n \qquad f_7^1 \ldots f_7^n \,]^T \end{aligned} \tag{4.21}$$

Substituting the Eq. (4.20) into Eq. (4.7) and integrating it over ζ direction on the known func-

tions of ζ. Wherever needed the integration by parts is performed, and the coefficient of δf_l^i is equated individually to zero. This yields a system of differential-algebraic equations for f_l^i as following:

$$\mathbf{N}\bar{\mathbf{F}}_{,\xi} = \bar{\mathbf{B}}\bar{\mathbf{F}} + \hat{\mathbf{B}}\hat{\mathbf{F}} + \bar{\mathbf{P}}_\mathbf{p} \tag{4.22}$$

$$\mathbf{L}\hat{\mathbf{F}} = \tilde{\mathbf{B}}\bar{\mathbf{F}} + \tilde{\mathbf{P}}_\mathbf{p} \tag{4.23}$$

where, $\mathbf{N}_{6n\times 6n}$, $\bar{\mathbf{B}}_{6n\times 6n}$, $\hat{\mathbf{B}}_{6n\times 2n}$, $\mathbf{L}_{2n\times 2n}$ and $\tilde{\mathbf{B}}_{2n\times 6n}$ are known matrices. Similarly, $\bar{\mathbf{P}}_\mathbf{p}$ and $\tilde{\mathbf{P}}_\mathbf{p}$ are the column vectors of $6n\times 1$ and $2n\times 1$ respectively, which contains the loading terms. The matrices contains non-zero elements are written below as,

$$\begin{gathered}
N_{i_1j_1} = \langle g_4^i g_1^j\rangle_h, \quad N_{i_2j_2} = \langle g_6^i g_2^j\rangle_h, \quad N_{i_3j_3} = \langle g_8^i g_3^j\rangle_h \\
N_{i_1j_1} = N_{j_4i_4}, \quad N_{i_2j_2} = N_{j_5i_5}, \quad N_{i_3j_3} = N_{j_6i_6} \\
\bar{B}_{i_1j_4} = \langle p_{11} g_4^i g_4^j\rangle_h, \quad \bar{B}_{i_1j_5} = \langle p_{16} g_4^i g_6^j\rangle_h, \quad \hat{B}_{i_1j_1} = \langle p_{13} g_4^i g_5^j\rangle_h \\
\bar{B}_{i_2j_4} = \langle p_{61} g_4^i g_6^j\rangle_h, \quad \bar{B}_{i_2j_5} = \langle p_{66} g_6^i g_6^j\rangle_h, \quad \hat{B}_{i_2j_1} = \langle p_{63} g_6^i g_5^j\rangle_h \\
\bar{B}_{i_3j_1} = \langle g_8^i \tfrac{g_{1,\zeta}^j}{t}\rangle_h, \quad \bar{B}_{i_3j_6} = \langle \bar{s}_{55} g_8^i g_8^j\rangle_h, \quad \hat{B}_{i_3j_2} = \langle \bar{s}_{45} g_8^i g_7^j\rangle_h \\
\bar{B}_{i_4j_6} = \langle g_8^j \tfrac{g_{1,\zeta}^i}{t}\rangle_h, \quad \hat{B}_{i_5j_2} = \langle g_7^j \tfrac{g_{2,\zeta}^i}{t}\rangle_h, \quad \hat{B}_{i_6j_1} = \langle g_3^i \tfrac{g_{5,\zeta}^j}{t}\rangle_h \\
\bar{L}_{i_1j_1} = \langle p_{33} g_5^i g_5^j\rangle_h, \quad \bar{L}_{i_2j_2} = \langle \bar{s}_{44} g_7^i g_7^j\rangle_h, \quad \tilde{B}_{i_1j_3} = \langle g_5^i \tfrac{g_{3,\zeta}^j}{t}\rangle_h \\
\tilde{B}_{i_1j_4} = -\langle p_{31} g_5^i g_4^j\rangle_h, \; \tilde{B}_{i_1j_5} = -\langle p_{36} g_5^i g_6^j\rangle_h, \; \tilde{B}_{i_2j_2} = \langle g_7^i \tfrac{g_{2,\zeta}^j}{t}\rangle_h \\
\tilde{B}_{i_2j_6} = -\langle \bar{s}_{45} g_7^i g_8^j\rangle_h
\end{gathered} \tag{4.24}$$

Similarly, pressure loading vector contains non-zero elements are given as,

$$\begin{aligned}
\bar{P}_{p_{i6}} &= -q_d\langle g_3^i\rangle_h; \qquad \bar{P}_{p_{i2}} = p_{63}\langle g_6^i(q_a + \zeta t q_d)\rangle_h \\
\bar{P}_{p_{i1}} &= p_{13}\langle g_4^i(q_a + \zeta t q_d)\rangle_h; \qquad \tilde{P}_{p_{i1}} = p_{33}\langle g_5^i(q_a + \zeta t q_d)\rangle_h
\end{aligned} \tag{4.25}$$

where, $\langle\ldots\rangle_h = h\int_0^1(\ldots)d\zeta$ Since the function $g^i(\zeta)$ in closed-form is known from the previous step. Now, substituting the Eq. (4.23) into Eq. (4.22). It gives a set of the first order ODEs with constant

coefficients for $\bar{F}$,

$$\bar{\mathbf{F}}_{,\xi} = \mathbf{B_0}\bar{\mathbf{F}} + \mathbf{P_0} \tag{4.26}$$

where, $\mathbf{B_0} = \mathbf{N^{-1}}[\bar{\mathbf{B}} + \hat{\mathbf{B}}\mathbf{L^{-1}}\tilde{\mathbf{B}}]$, $\mathbf{P_0} = \mathbf{N^{-1}}[\hat{\mathbf{B}}\mathbf{L^{-1}}\tilde{\mathbf{P}}_\mathbf{p} + \bar{\mathbf{P}}_\mathbf{p}]$. The equation shown above is a $6n$ non-homogeneous first order ODEs system with the constant coefficient. This equation can be solved using the approach discussed in [96].

4.4 NUMERICAL RESULTS AND DISCUSSIONS

In this work, four types of panel configurations as shown in Fig. 4.3 are taken into consideration and the numerical results are presented & discussed. The panel (a) consits of two equal segment which first and second segment is composed of Al and Gr-Ep, respectively. Whereas, the panel (b) made with unequal segment of Al and Gr-Ep, first segment of Al is $0.3L$ and Gr-Ep segment is of $0.7L$. Similar to panel (b), the panel (c) with a stronger material is considered which composed with steel and Gr-Ep segment. A four equally segmented panel (d) has been considerd for the study, in which the first segment consist of pure Al.

While the 2^{nd}, 3^{rd} and 4^{th} segments contain the material properties corresponding to different ratios of Al and SiC. The panel thickness is represented by h. A panel is said to be in the SS case, if it has a simply-support at x=0 and a free edge at x=a. The ply angle (θ) is representing the fiber orientation about z-axis from top to bottom of the Gr-Ep composite, as shown in Fig. 4.3. The material properties considered here are presented in the Table **??**.

Table 4.1: Material Properties

Sl no.	Material	Young's Modulus (Y) in GPa	Shear Modulus (G) in GPa	Poisson's Ratio (ν)
1	Aluminium (Al)	68	25.76	0.32
2	Steel	200	76.90	0.30
3	Al/SiC [90/10 layer]	70.20	26.53	0.323
4	Al/SiC [80/20 layer]	72.40	27.30	0.326
5	Al/SiC [70/30 layer]	74.60	28.066	0.329

		Y_1	Y_2	Y_3	G_{12}	G_{13}	G_{23}	ν_{12}	ν_{13}	ν_{23}
6	Graphite-Epoxy (Gr-Ep) [249]	181	10.3	10.3	7.17	7.17	2.87	0.28	0.28	0.33

Y_i and G_{ij} are in GPa

A uniform pressure $q_2 = q_0$ at the top surface and $q_1 = 0$ at the bottom surface are applied

TH-3234_176103111

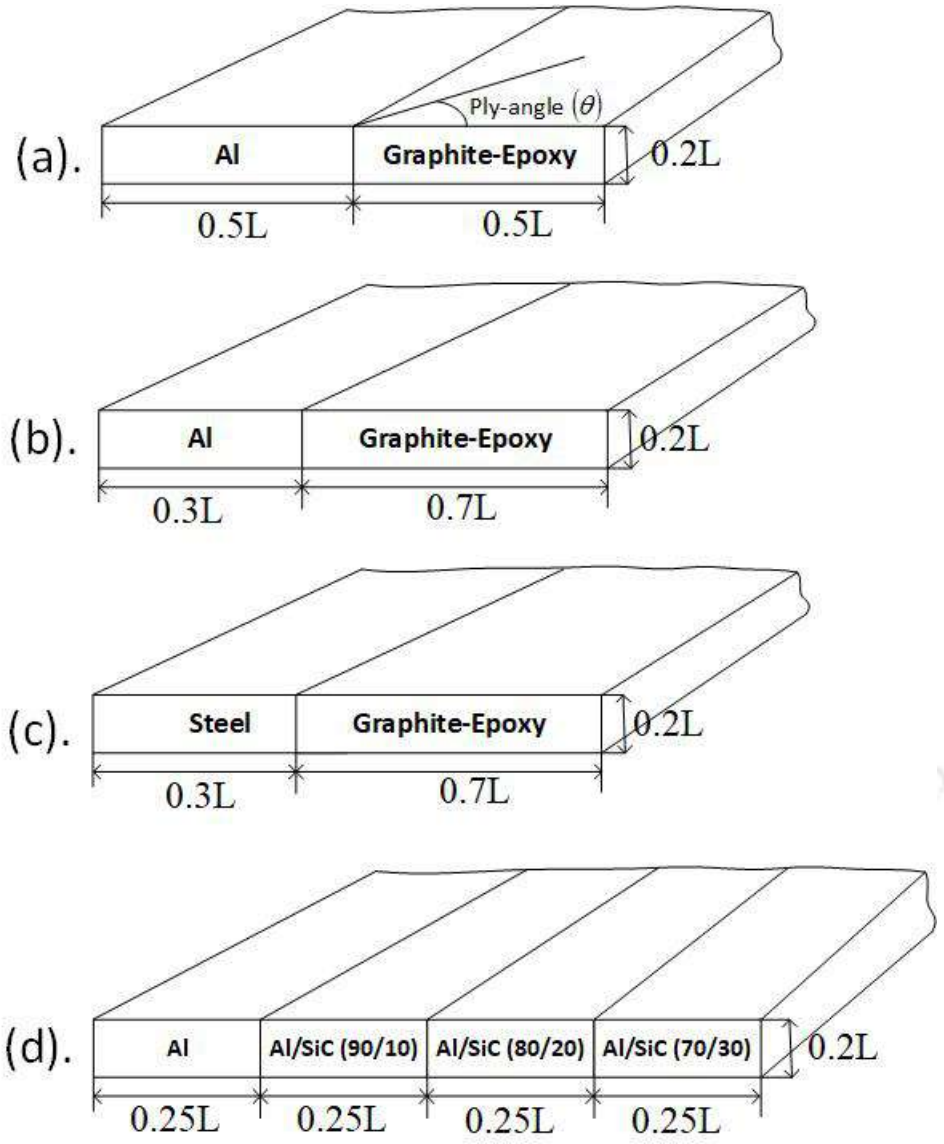

Fig. 4.3: Panel configurations

on the panel. The currently obtained numerical results are non-dimensionalized with $S = a/h$, $Y_0 = 10.3$ GPa (for panel configuration a, b), 200 GPa (for panel c) & 74.6 GPa (For panel d) and $q_0 = 1$ as:

$$(\bar{u}, \bar{w}) = 100(u, w/S)Y_0/q_0 h S^3;\ (\bar{\sigma}_x, \bar{\sigma}_y, \bar{\sigma}_z, \bar{\tau}_{zx}) = (\sigma_x, \sigma_y, q_0 S^2 \sigma_z, S\tau_{zx})/q_0 S^2.$$

Since there are not any 2-D exact or closed-form solutions are available for other kinds of support conditions in the literatures for the panel. Therefore, the current results are compared with 3-D finite element (FE) results for different combinations of boundary conditions.

For this study, panel (a) having Gr-Ep with 30 and 45 degree ply-angles have been modeled

TH-3234_176103111

and the numerical results are presented. For the comparison and validation, 3-D FE solutions are obtained from the FE software ABAQUS. Here, for the modelling of angle ply panel in ABAQUS plain strain element can not be used [252]. Hence, a plate with the y-direction length (b) to span (a) ratio of 20 is modeled for $a/h = 5$ to simulate the generalized plane strain condition. The 20-noded quadratic serendipity hexahedral element (C3D20R) with reduced integration is used [253]. The model is meshed with a mesh size of 40 (length) $\times$ 50 (width) $\times$ 16 (thickness) for the panel. The meshed panel is shown in Fig. 4.4. The converged 3-D FE results are presented at the mid-section along y-direction for the angle ply panels. The FE results are not satisfying the interface continuity conditions as in EKM. Therefore, an average of the stressess values are taken at the interface locations. The converged FE results are presented along with the EKM results for all panel configurations.

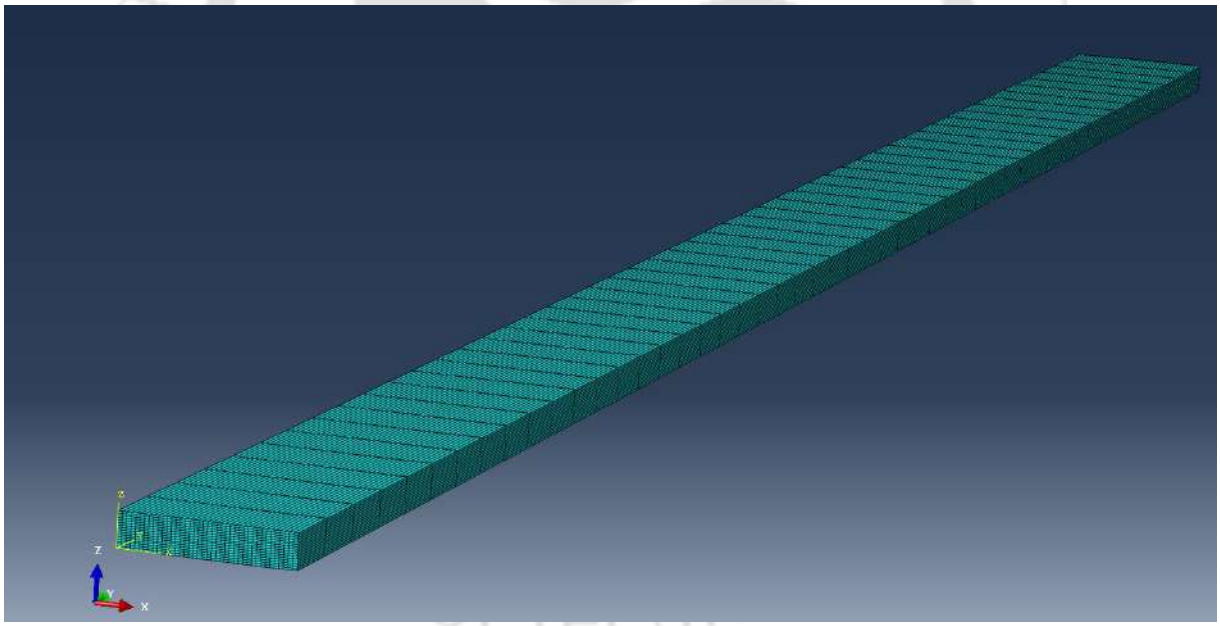

Fig. 4.4: Meshed panel geometry

For the thick (S=5) case of panel (a), change in $\bar{u}, \bar{w}, \bar{\sigma}_x$ and $\bar{\tau}_{zx}$ along x-axis are presented in Fig. 4.5. The outcomes for the panel with CC and CF support conditions are presented. For demostrating the convergence, accuracy, and effectiveness of this approach, current results (EKM) with single term (n=1) and two term (n=2) with at least two iterations are shown. From the findings, it can be seen that the Al section has a deeper curvature than Gr-Ep section and the

TH-3234_176103111

in-plane displacement ($\bar{u}$) is asymmetric. Similar to in-plane displacement, the maximum location of deflection ($\bar{w}$) is also moved and a very steep slope is observed. A gradual rise in stress value of in-plane stress $\bar{\sigma}_x$ can be seen for both the cases. However, near the boundary the in-plane stress increases very rapidly. In both cases, the transverse shear stress ($\bar{\tau}_{zx}$) is showing a sharp kink at the segmental interface and a effect of boundary near the clamped supports. Further, the effect of boundary conditions on the stresses $\bar{\sigma}_y$ and $\bar{\sigma}_z$ have been presented for panel (a) configuration in Fig. 4.6. The results are presented for the stresses along the longitudinal and through the thickness directions. The through-thickness results near the edges (at x=0.2) are shown in Figs. 4.6 (a, b, c) for $\bar{\sigma}_z$. The EKM results are found in good agreement with the FE solutions. The Figs. 4.6 (d) & 4.6 (e) present through-thickness results of $\bar{\sigma}_z$ for CF case at x=0 (clamped) and x=0.5 (interface). The EKM results are not in agreement with FE at these locations. It can also be seen that the FE results do not satisfy the boundary conditions i.e. (at z=-h/2, σ_z=0 & at z=h/2, σ_z=1) while EKM satisfies. The effect of various boundary conditions on the longitudinal variation of $\bar{\sigma}_z$ is presented in the Fig. 4.6 (f). Here, a significant jump near the edges (at x=0) is observed, but, at the opposite edge (at x=1) no such effect is observed. The through thickness variation of stress $\bar{\sigma}_y$ is presented near the clamped edge (at x=0.1) in Fig. 4.6 (g). A good agreement of the FE and EKM results can be observed for the stress variable. Further, the longitudinal variation of σ_y has been presented in Fig. 4.6 (h). The FE solution is not matching with EKM result at the interface. It may be due to dissatifaction of boundary and the interface continuity conditions by 3D FE. It is also observed that FE overestimates the stresses near the clamped edge. Theoretically, τ_{xy} should be zero at the interfaces and σ_z at the bottom of the panel. But there is non -zero values are obseved and presented in Fig. 4.6 (i) for better clarity. For thick (S=5) case of panel (b), the variation of $\bar{u}, \bar{w}, \bar{\sigma}_x$ and $\bar{\tau}_{zx}$ along the length are presented in Fig. 4.7 for thick (S=5) case. In contrast to an equal-segmented panel, an unequal-segmented panel shows a stronger variation. In particular, a hook development is seen in the transverse shear stress variation. It has been noted that a deeper and larger hook is obtained in the CF case as compared to the CC case. The increase in transverse shear stress ($\bar{\tau}_{zx}$) near the interface is noticed, which could cause the collapse of the joints. The 1-D theories are not able to capture this effect. Another panel (c), which is

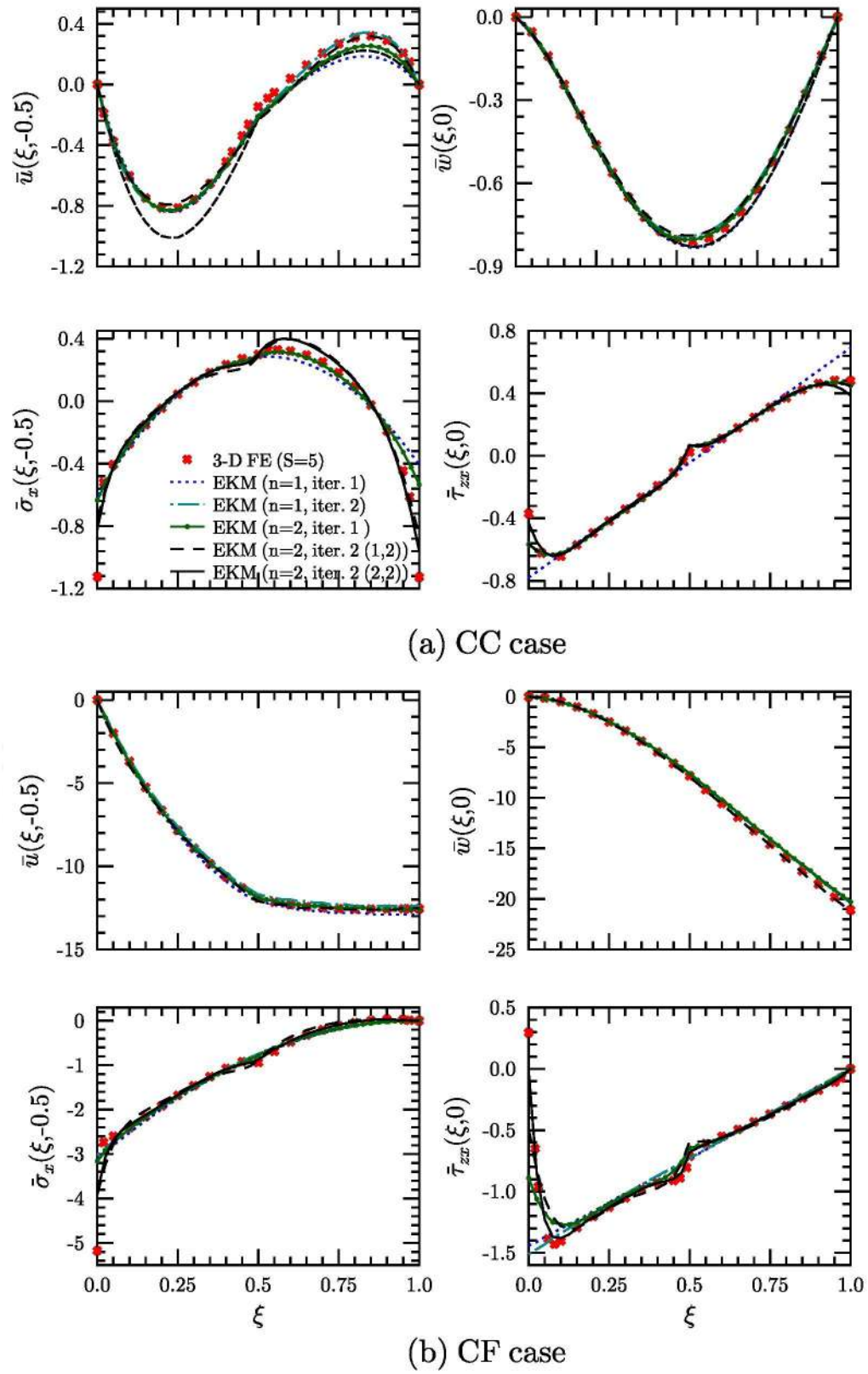

Fig. 4.5: Variation of deflections and stresses along the length for panel (a) with S=5

TH-3234_176103111

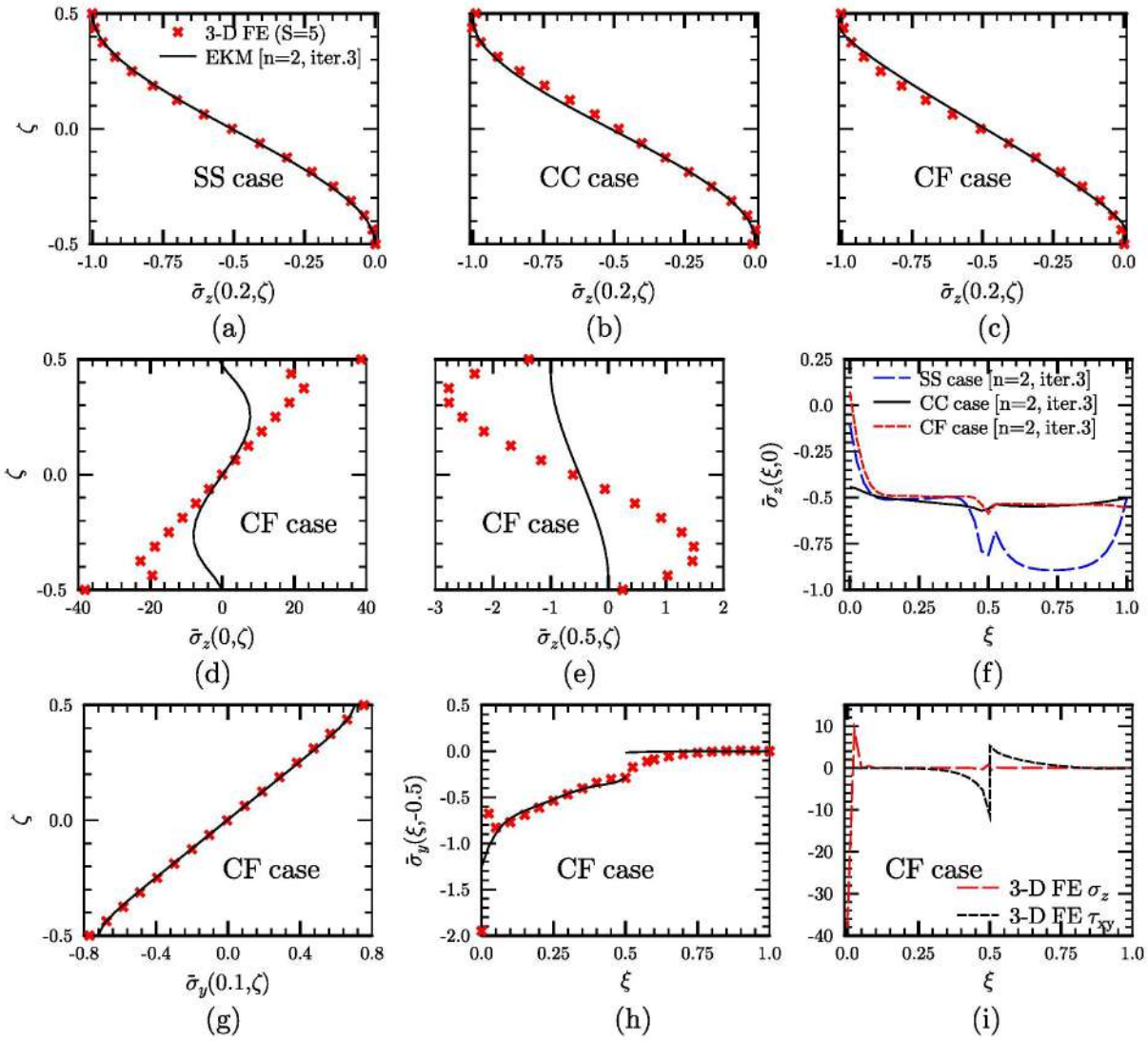

Fig. 4.6: Variation of stresses along the length and thickness for panel (a) with S=5

made of more stronger than Al i.e. steel and Gr-Ep is taken into consideration to gain a deeper understanding of this effect. For the thick (S=5) case of panel (c), longitudinal variation of $\bar{u}, \bar{w}$ and $\bar{\sigma}_x$ are shown in Fig. 4.8. The findings are reported for the SS, CC and CF cases. For the simply supported case negligible variation in the stresses are observed while for the CC and CF cases, the effect of support condition is clearly visible for all the entities. Whereas in Fig. 4.9, the longitudinal change of shear stress $\bar{\tau}_{zx}$ has been also presented for thick (S=5) case of panel (c). From the results, it is noticed that for SS case no hook formation is initiated but for the CC and CF cases a hook shape formation is observed. However, this hook shape is found more deeper for the CF case. It should be emphasised that, the current results are in good agreement with the

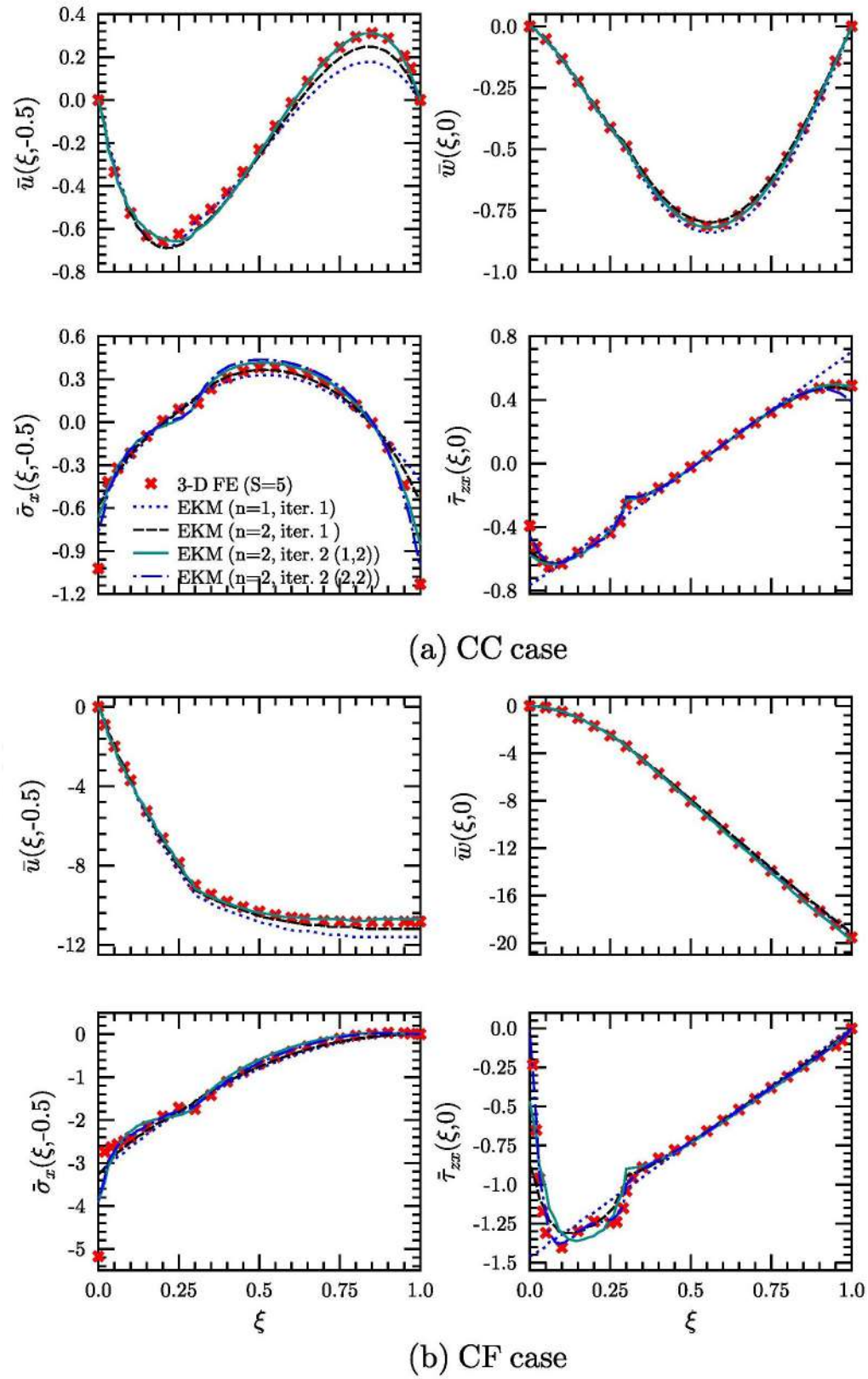

Fig. 4.7: Variation of deflections and stresses for panel (b) with S=5

TH-3234_176103111

3-D FE except near to the edge. This disagreement at the very clamped support is well reported and discussed in literatures [96–99]. Sometimes, the axially graded panel with step-wise variation in the material properties is also used in the structural applications. Such type of panels made of Al/SiC, as shown in panel (d) is considered here for the study. Using the rule of mixture, the material properties of each segment are determined [251] and shown in the Table **??**. For thick (S=5) case, the longitudinal change in $\bar{u}, \bar{w}$ and $\bar{\sigma}_x$ are shown in Fig. 4.10 for SS, CC and CF cases. The impact of S on the panel is also studied through these results. For the SS and CF cases, it is observed that the increase in S has no appreciable effect on the variables. Whereas, the transverse shear stress $\bar{\tau}_{zx}$ for panel (d) is plotted in Fig. 4.11. From the observations, the current findings and 3-D FE are in good accord.

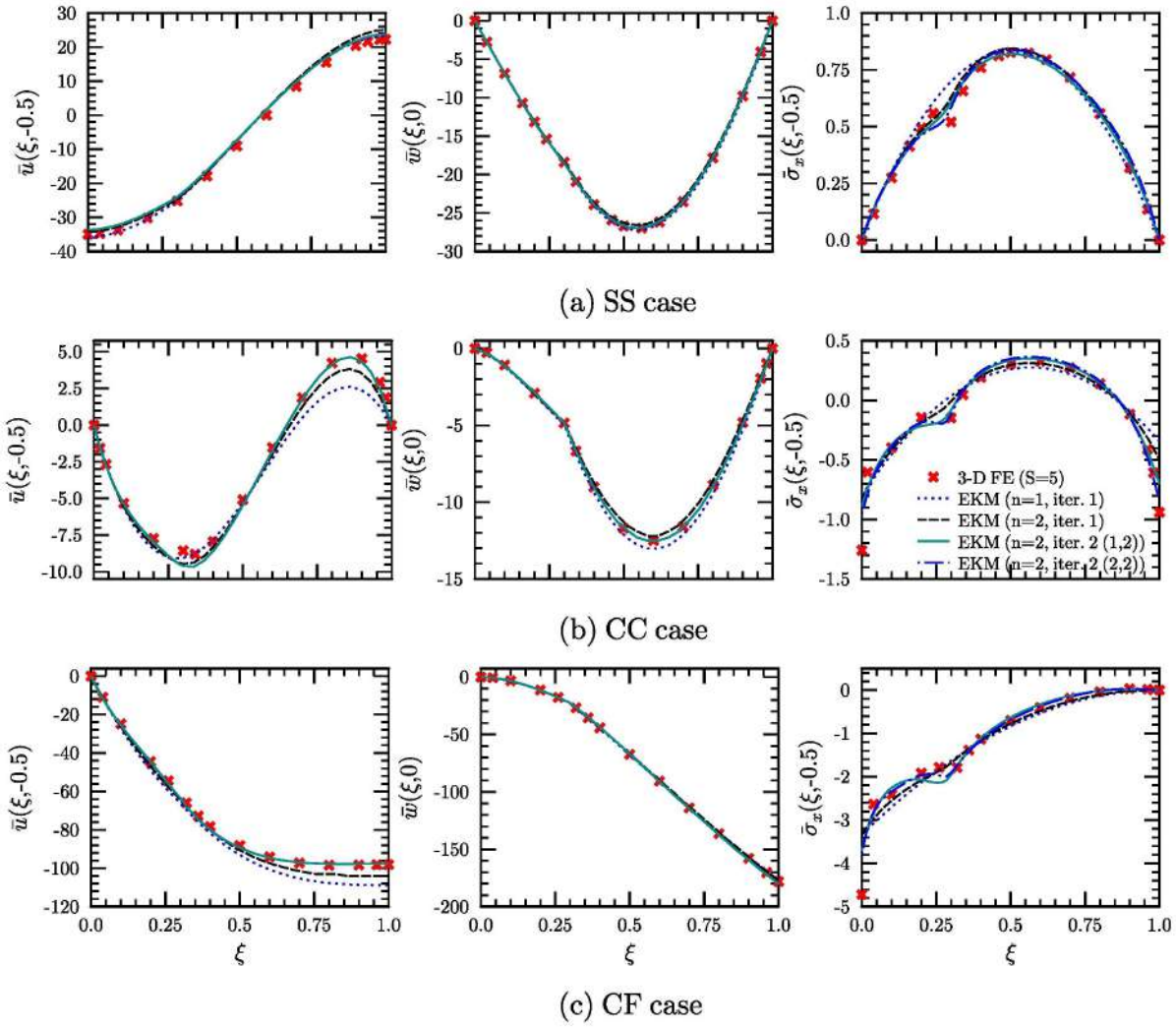

Fig. 4.8: Variation of deflections and stresses along the length for panel (c) with S=5

TH-3234_176103111

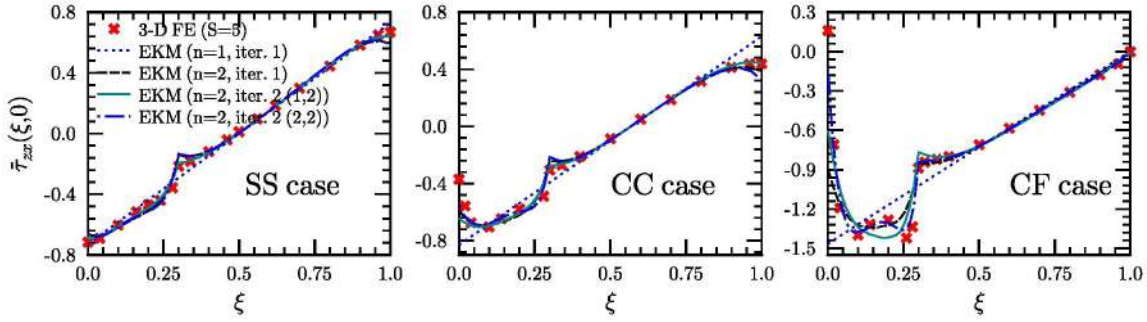

Fig. 4.9: Variation of shear stresses along the length for panel (c) with S=5

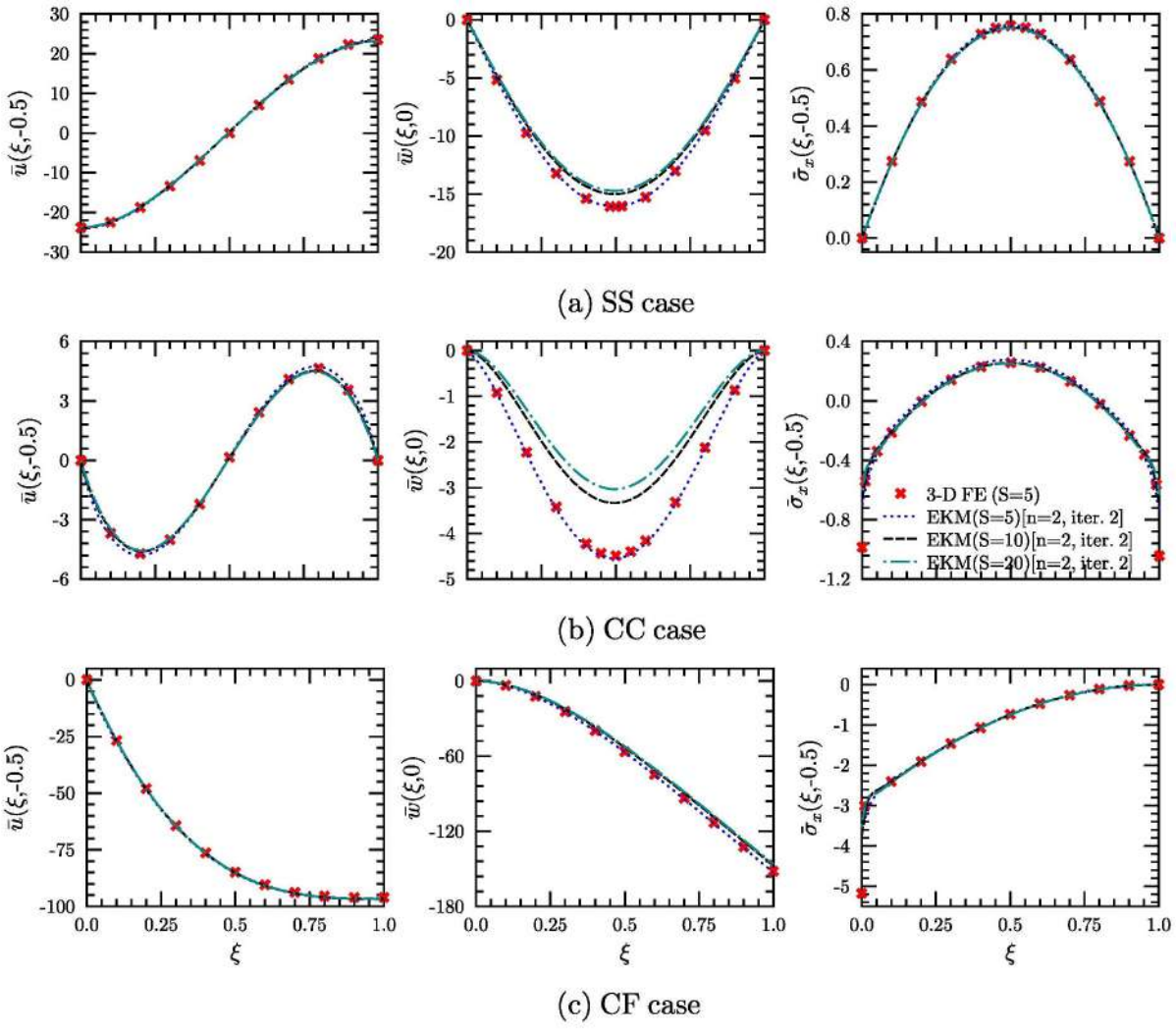

Fig. 4.10: Variation of deflections and stresses along the length for panel (d)

The composite materials panel segment with different fiber angle may be used for joining. So, for study the effect of ply-angle the longitudinal variation of $\bar{u}, \bar{w}, \bar{\sigma}_x$ and $\bar{\tau}_{zx}$ are presented for thick (S=5) panel (a) having 30 and 45 degree ply angle in Fig. 4.12 and Fig. 4.13 respectively. The

TH-3234_176103111

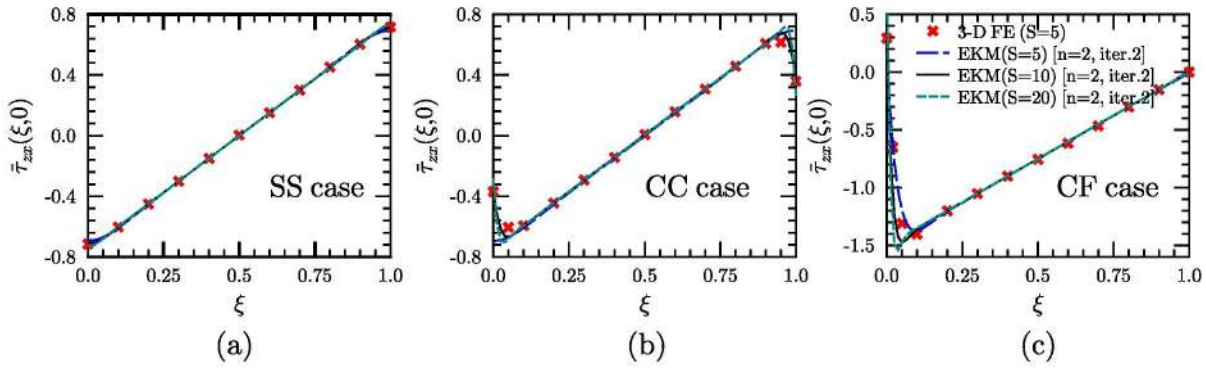

Fig. 4.11: Variation of shear stresses along the length for panel (d)

multi-term EKM results are presented and validated with the 3-D FE for the CC, SS and CF cases. The presented EKM results are found in good agreement with the FE results for all the cases. The effect on the stresses of the increase in ply-angle is presented for SS, CF and CC cases in Fig. 4.14. The EKM results for two terms are obtained after two iterations are presented for 0, 30, 45 degree (for SS and CF case) and 0, 30, 45 and 90 degree ply angles (for CC case). It is observed that, with the increase of ply-angle, the $\bar{\sigma}_x$ value is slightly reduced in the Gr-Ep section for SS case and causes no change for CF case. Whereas, for the CC case a reduction in $\bar{\sigma}_x$ value is observed at the segment interface and clamped edge of Gr-Ep segment. But, the $\bar{\sigma}_x$ value is also increasing simultaneously at the very clamped edges of the Al segment. This increase in stress indicates that at very clamped edges of the Al segment, it may need more robust support. However, the increase in ply-angle for the SS and CF cases shows no significant changes in the variation of $\bar{\tau}_{zx}$. For the CC case, the $\bar{\tau}_{zx}$ value is decreasing at the interface of the segments (zoomed view is shown), but a deep hook formation at the very clamp edge at the Al segment side is clearly observed. So, with the increase in ply-angle, the edge effect is clearly observed in the CC case.

TH-3234_176103111

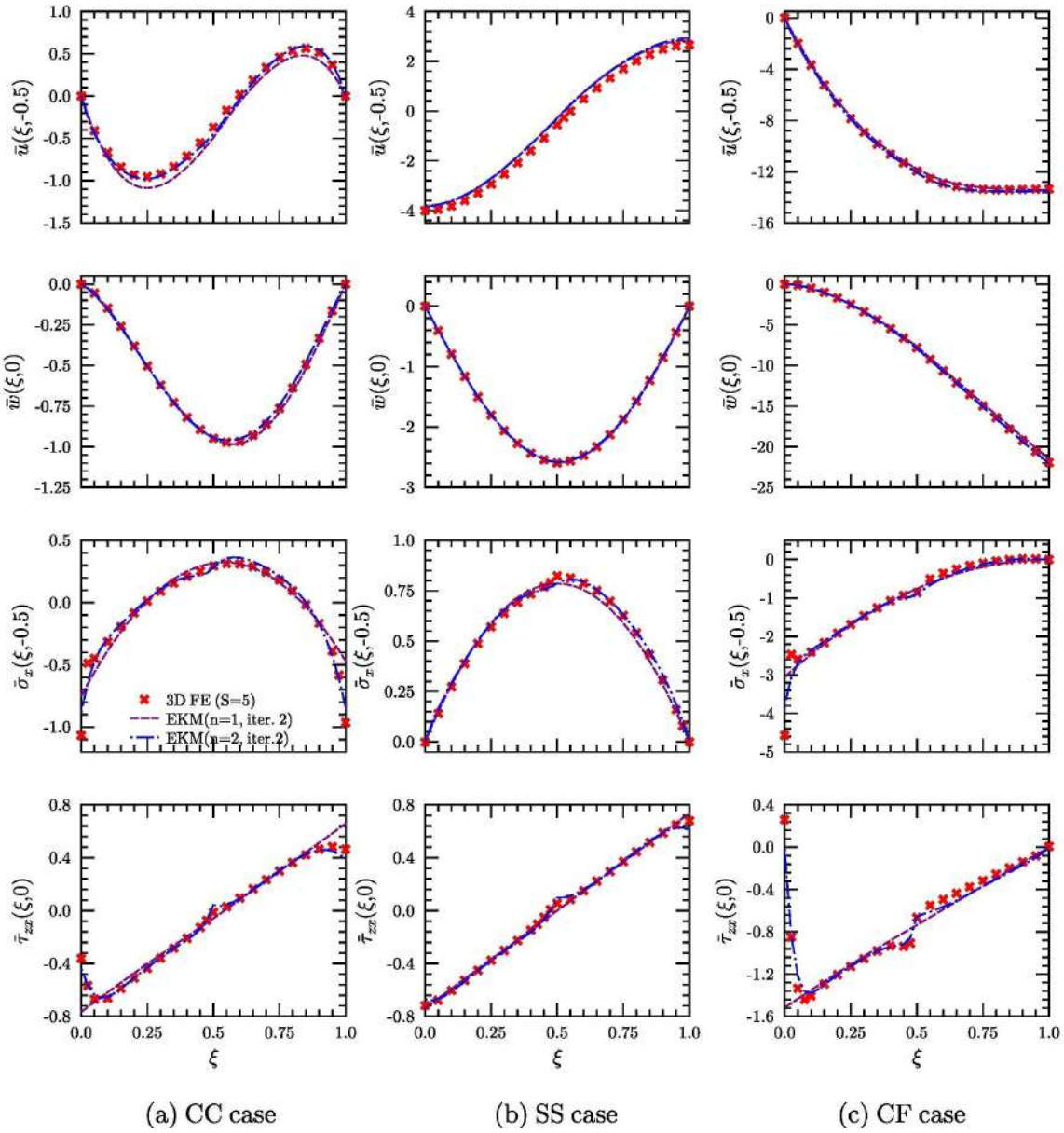

Fig. 4.12: Variation of deflections and stresses along the length for 30 degree angle-ply panel (a) with S=5

TH-3234_176103111

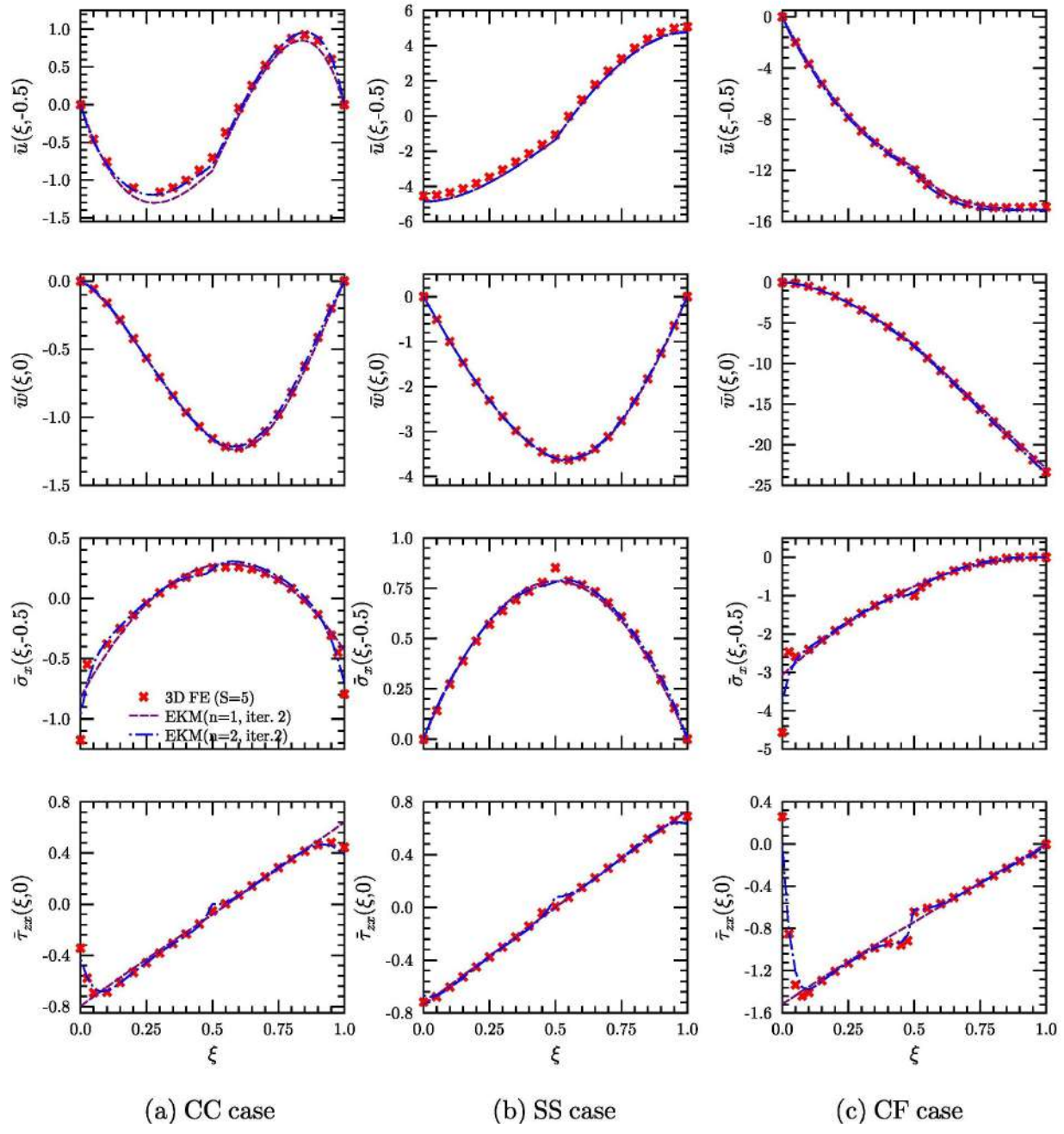

Fig. 4.13: Variation of deflections and stresses along the length for 45 degree angle-ply panel (a) with S=5

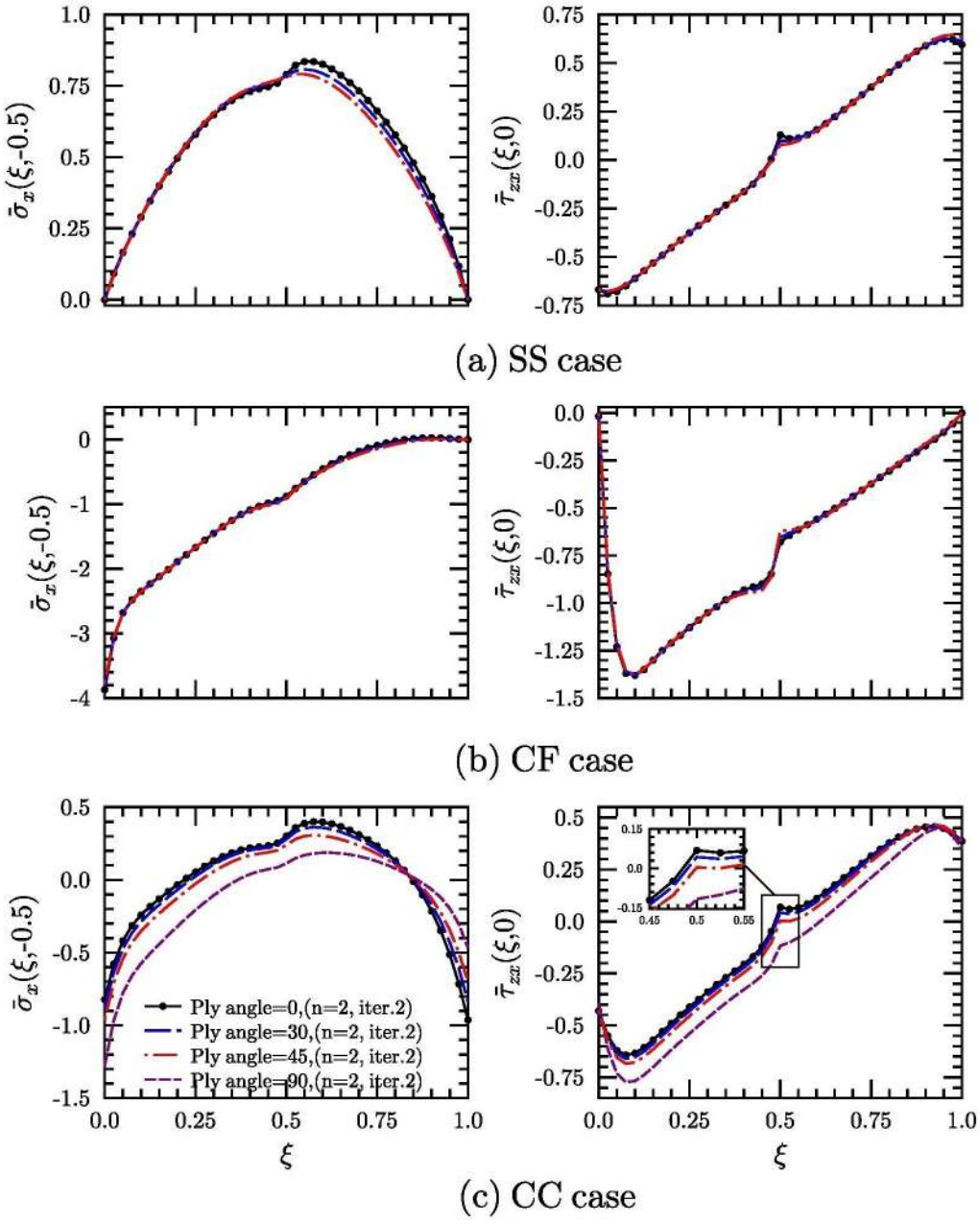

Fig. 4.14: Effect of ply-angles on the stresses for panel (a) with S=5

4.5 SUMMARY

First time, analytical 2-D solution based on elasticity for a multi-segmented panel subjected to arbitrary boundary conditions is presented. Four lay-ups are considered for the present numerical study. The segment with lighter and heavier material with the Gr-Ep for equal & unequal length and it's effect on the variables are investigated. A deeper hook formation shows a high shear stress generation at the very clamped edge in the CF case than CC case for panel (b). For panel (c), high shear stress has been generated at the clamped edge compared to panel (b) under CF support case. For the panel (d), a change in S has negligible effect on the deflection and stresses for the SS and CF compared to CC cases. In the CC case, a higher magnitude of $\bar{w}$ has been observed for $S = 5$. If the S is doubled i.e. $S = 10$ then approximately 26% reduction in the magnitude of $\bar{w}$ has been observed. Whereas if it is increased by four times, then about 32% reduction in the magnitude of $\bar{w}$ from the initial value is observed. It depict that an increase in S cause a significant reduction in the panel deflection under the CC case. The boundary conditions have a substantial impact on the shear stress near the edges for panel (d). At the boundary and interfaces, present results and 3-D FE results are not in good agreement. It has been observed that 3-D FE solution does not satisfy the interface continuity and boundary conditions at the edges and at the interfaces. The effect of ply-angles on the stresses are also studied. It is observed that, the stress $\bar{\sigma}_x$ start decreasing with an increase in ply-angle. The present developed technique is very novel and more flexible to handle any material combination along the panel length. This work also useful for the researchers to study the behavior of the piece-wise homogeneous panel type structures under in-plane loads. The presented results can also be used as the benchmark for the development of plate problems under different loading and support conditions.

TH-3234_176103111

Chapter 5

Two-Dimensional Bending Solutions for the Multi-Segmented Dissimilar Piezoelectric Panels

5.1 INTRODUCTION

Piezoelectric materials have been substantially used to develop smart or intelligent structures that can control, sense, and actuate the signals. In many sensing applications, the piezoelectric materials are morphed or joined edge to edge or axially stacked together within the smart structures for better suitability. Moreover, during the operations, the piezoelectric materials are exposed to various loading environments. Therefore, for a better structural design and performance, it is important to accurately estimate the material behaviour under this environment. In this Chapter, a 2-D analytical solution has been presented for the bending of segmented smart panels. In Sec. 5.2, the details about the piezoelectric panel geometry, constitutive equations, and governing equations have been presented. The Reissner-type mixed variational principle approach is applied to derive the weak form of governing equations for the piezoelectric panel. The stresses, displacements, electric potential, and electric displacement field variables are considered here as primary variables. The boundary conditions and interface bonding imposed for the panels are explained in Sec. 5.3. Thereafter, in Sec. 5.4 multi-term extended Kantorovich approach is employed to transform the governing equation into two sets of algebraic-ordinary differential equations (ODEs), one along in-plane (x) and the other along the thickness (z) direction, respectively. These ODEs are solved in a closed-form manner, ensuring the same order of accuracy for all the variables (stresses, dis-

TH-3234_176103111

placements, and electric variables) by satisfying the boundary and continuity equations in exact manners. In Sec. 5.5, the numerical results are reported for various configurations of piezoelectric panels under different sets of boundary conditions. The numerical results are observed in excellent agreement with the analytical results. The presented 2-D analytical solutions will be helpful in the assessment of various 1-D theories and numerical methods. The present development can be extended to develop segmented piezoelectric plate problems. A flowchart of the solution methodology used for this segmented piezoelectric panel is shown in Fig. 5.1.

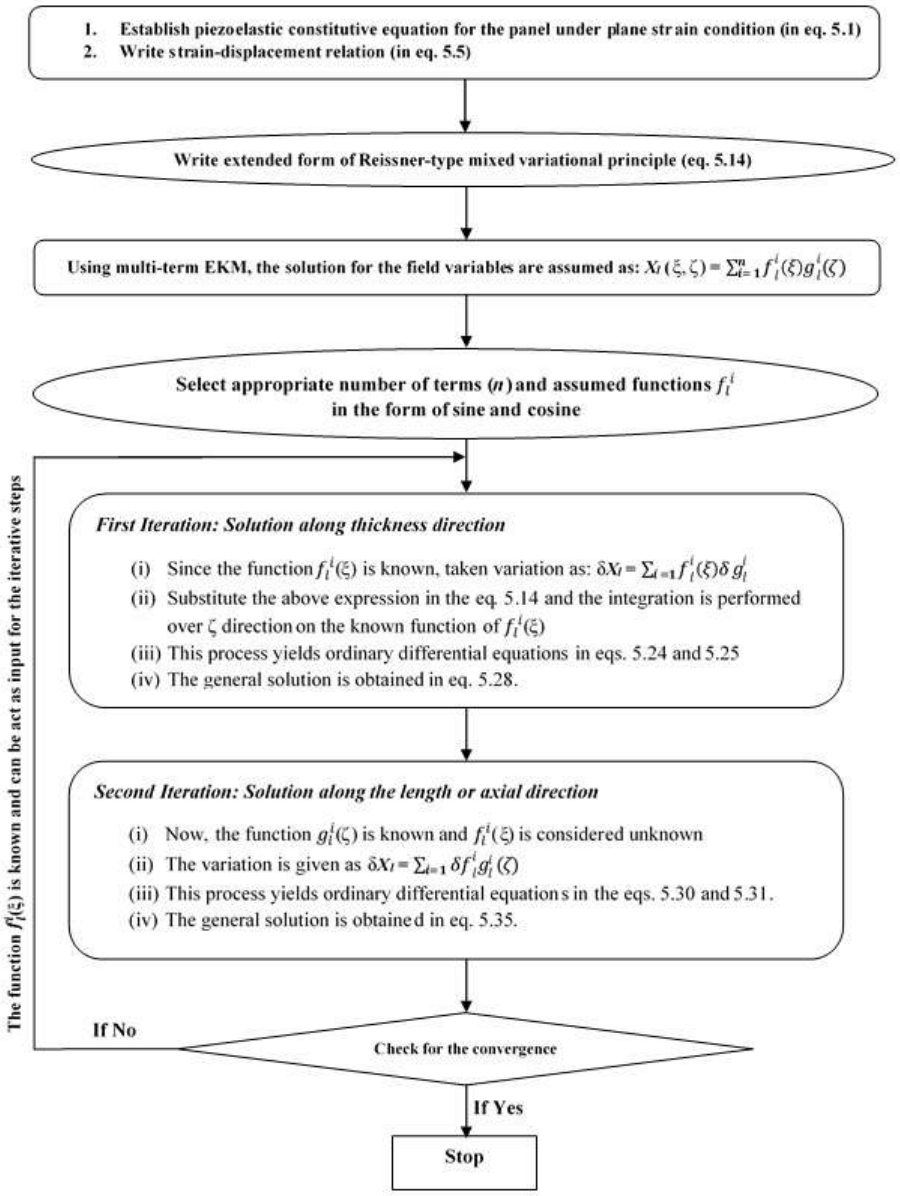

Fig. 5.1: A flowchart of EKM approach for segmented piezoelectric panel

TH-3234_176103111

5.2 THEORETICAL FORMULATION

A single layered infinitely long piezoelectric panel, which is made of S perfectly bonded segments along x-axis, has been considered as shown in Fig. 5.2. It has span length (a) along x direction and total thickness (h) along z direction. The piezoelectric materials are assumed to have a class mm^2 symmetry concerning the principal axis of material x_1, x_2 and x_3. The axis x_1 and x_3 are oriented along the x and z directions, respectively. An arbitrary segment J from the panel is considered, and the length of this is denoted as a^J. The left and right coordinates of the segment is denoted as x_{J-1} and x_J respectively along the x-axis. The interface between the J_{th} and $(J+1)_{th}$ segment is denoted as J_{th} interface. For the mathematical formulation, similar assumptions are made as in Chapter 3.

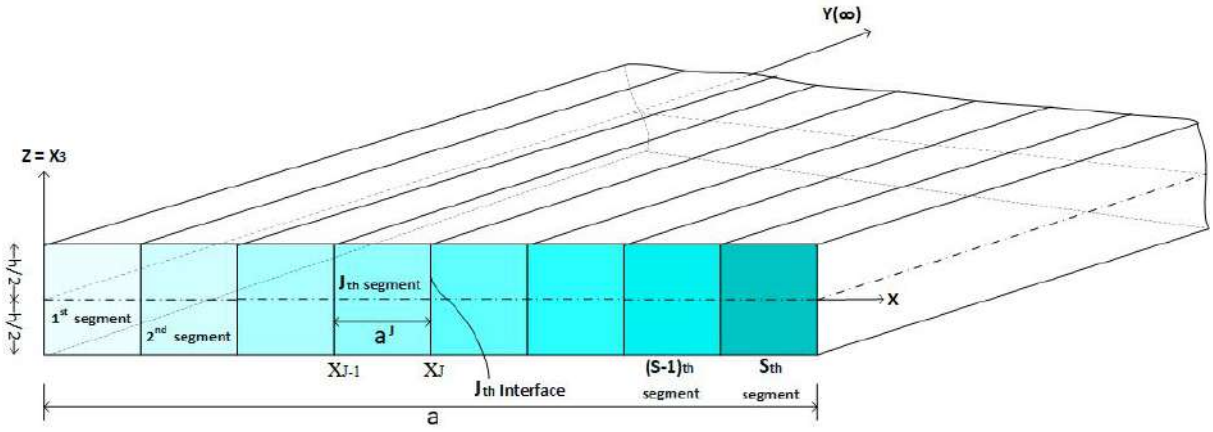

Fig. 5.2: Geometry of the piezoelectric panel

For clarity, the segment superscript is omitted. All variables of this generalized plane strain problem are independent of y. The transformed 3-D piezoelasticity constitutive equations can be expressed in a compressed form in Eq. (5.2) and (5.3). It relates the stress components (σ_i and τ_{ij}), electric field components (E_i) to their respective strain components (ε_i and γ_{ij}) and electric displacement components (D_i) with the structural coordinate system (x, y , z) [146],

$$[\varepsilon] = [\bar{s}][\sigma] + [\bar{d}]^T[E], [D] = [\bar{d}][\sigma] + [\bar{\epsilon}][E] \tag{5.1}$$

TH-3234_176103111

where, the terms are as

$$[\varepsilon] = \begin{bmatrix} \varepsilon_x \\ \varepsilon_y \\ \varepsilon_z \\ \gamma_{yz} \\ \gamma_{zx} \\ \gamma_{xy} \end{bmatrix}, [\bar{s}] = \begin{bmatrix} \bar{s}_{11} & \bar{s}_{12} & \bar{s}_{13} & 0 & 0 & \bar{s}_{16} \\ \bar{s}_{21} & \bar{s}_{22} & \bar{s}_{23} & 0 & 0 & \bar{s}_{26} \\ \bar{s}_{31} & \bar{s}_{23} & \bar{s}_{33} & 0 & 0 & \bar{s}_{36} \\ 0 & 0 & 0 & \bar{s}_{44} & \bar{s}_{45} & 0 \\ 0 & 0 & 0 & \bar{s}_{54} & \bar{s}_{55} & 0 \\ \bar{s}_{61} & \bar{s}_{62} & \bar{s}_{63} & 0 & 0 & \bar{s}_{66} \end{bmatrix}, [\sigma] = \begin{bmatrix} \sigma_x \\ \sigma_y \\ \sigma_z \\ \tau_{yz} \\ \tau_{zx} \\ \tau_{xy} \end{bmatrix}, [E] = \begin{bmatrix} E_x \\ E_y \\ E_z \end{bmatrix}, \tag{5.2}$$

$$[D] = \begin{bmatrix} D_x \\ D_y \\ D_z \end{bmatrix}, [\bar{d}] = \begin{bmatrix} 0 & 0 & 0 & \bar{d}_{14} & \bar{d}_{15} & 0 \\ 0 & 0 & 0 & \bar{d}_{24} & \bar{d}_{25} & 0 \\ \bar{d}_{31} & \bar{d}_{32} & \bar{d}_{33} & 0 & 0 & \bar{d}_{36} \end{bmatrix}, [\bar{\epsilon}] = \begin{bmatrix} \bar{\epsilon}_{11} & \bar{\epsilon}_{12} & 0 \\ \bar{\epsilon}_{21} & \bar{\epsilon}_{22} & 0 \\ 0 & 0 & \bar{\epsilon}_{33} \end{bmatrix} \tag{5.3}$$

where, $\bar{s}_{ij}$ are transformed elastic compliances, $\bar{d}_{ij}$ are piezoelectric strain constants and $\bar{\epsilon}_{ij}$ are dielectric permittivities at constant stress field.

All variables are non-dimensionalized in such a way that the non-dimensional forms of the governing equation should not alter the original equations as in Ref. [146].

$$\begin{gathered} S = a/h, \quad \bar{s}^*_{ij} = \bar{s}_{ij} Y_0, \quad h^* = h/a \\ (\sigma^*_x, \sigma^*_y, \sigma^*_z, \tau^*_{xy}, \tau^*_{yz}, \tau^*_{zx}) = (\sigma_x, \sigma_y, \sigma_z, \tau_{xy}, \tau_{yz}, \tau_{zx})/SY_0 \\ (\epsilon^*_x, \epsilon^*_y, \epsilon^*_z, \gamma^*_{xy}, \gamma^*_{yz}, \gamma^*_{zx}) = (\epsilon_x, \epsilon_y, \epsilon_z, \gamma_{xy}, \gamma_{yz}, \gamma_{zx})/S \\ (u^*, v^*, w^*) = (u, v, w)/h, \quad (G^*_{ij},\, Y^*_i) = (G_{ij},\, Y_i)/Y_0 \\ (D^*_x, D^*_y, D^*_z) = (D_x, D_y, D_z)S/Y_0 d_0, \quad \epsilon^*_{ij} = \epsilon_{ij}/Y_0 d_0^2 \\ (\phi^*) = (\phi) d_0/h, \quad (E^*_x, E^*_y, E^*_z) = (E_x, E_y, E_z) d_0 S \end{gathered} \tag{5.4}$$

where, Y_0 is the value of Young's modulus and d_0 of piezoelectric constant.

For simplicity, the superscript * is dropped from the dimensionless entities. Assuming that the entities are independent of y i.e., generalised plane strain case of cylindrical bending, the strain-displacement and electric field-potential relations can be simplified as

$$\begin{bmatrix} \varepsilon_x \\ \varepsilon_y \\ \varepsilon_z \end{bmatrix} = \begin{bmatrix} u_{,x} \\ 0 \\ w_{,z} \end{bmatrix}; \begin{bmatrix} \gamma_{yz} \\ \gamma_{zx} \\ \gamma_{xy} \end{bmatrix} = \begin{bmatrix} v_{,z} \\ w_{,x} + u_{,z} \\ v_{,x} \end{bmatrix} and \begin{bmatrix} E_x \\ E_y \\ E_z \end{bmatrix} = \begin{bmatrix} -\phi_{,x} \\ 0 \\ -\phi_{,z} \end{bmatrix} \tag{5.5}$$

Here, the subscript comma denotes differentiation. Now, E_z can be expressed in terms of D_z

from Eq. (5.1) using Eq. (5.2) and Eq. (5.3) as

$$E_z = \frac{1}{\bar{\epsilon}_{33}} D_z - \bar{C}'_{31}\sigma_x - \bar{C}'_{32}\sigma_y - \bar{C}'_{33}\sigma_z - \bar{C}'_{36}\tau_{xy} \tag{5.6}$$

where $\bar{C}'_{ij} = \bar{d}_{ij}/\bar{\epsilon}_{33}$. Now, ε_y from Eq. (5.5) and Eq. (5.6) substituted into Eq. (5.1), then σ_y is obtained as

$$\sigma_y = -1/\bar{t}'_{22}[\bar{t}'_{12}\sigma_x - \bar{t}'_{26}\tau_{xy} - \bar{t}'_{23}\sigma_z - \bar{C}'_{32}D_z] \tag{5.7}$$

where $\bar{t}'_{ij} = \bar{s}_{ij} - \bar{d}_{3i}\bar{d}_{3j}/\bar{\epsilon}_{33}$.

The entities σ_y and E_z can be eliminated from Eqs. (5.1) and Eq. (5.6) by using Eqs. (5.6) and (5.7),

$$\begin{bmatrix} \varepsilon_x \\ \varepsilon_z \\ \gamma_{xy} \\ E_z \end{bmatrix} = \begin{bmatrix} n_{11} & n_{16} & n_{13} & n_{18} \\ n_{31} & n_{36} & n_{33} & n_{38} \\ n_{61} & n_{66} & n_{63} & n_{68} \\ -n_{81} & -n_{86} & -n_{83} & -n_{88} \end{bmatrix} \begin{bmatrix} \sigma_x \\ \tau_{xy} \\ \sigma_z \\ D_z \end{bmatrix} \tag{5.8}$$

where,

$$\begin{aligned} n_{ij} &= \bar{t}'_{ij} - \bar{t}'_{2i}\bar{t}'_{2j}/\bar{t}'_{22}, & n_{88} &= -1/\bar{\epsilon}_{33} - \bar{C}'^2_{32}/\bar{t}'_{22} \\ n_{i8} &= n_{8i} = \bar{C}'_{3i} - \bar{t}'_{2i}\bar{C}'_{32}/\bar{t}'_{22}, & \text{for} \quad (i,j) &= 1,3,6 \end{aligned} \tag{5.9}$$

Similarly, the entities γ_{zx}, γ_{yz} and E_x can be represented in terms of τ_{zx}, τ_{yz} and D_x from Eqs. (5.1) as

$$\gamma_{yz} = n_{44}\tau_{yz} + n_{45}\tau_{zx} + n_{47}D_x \tag{5.10}$$

$$\gamma_{zx} = n_{54}\tau_{yz} + n_{55}\tau_{zx} + n_{57}D_x \tag{5.11}$$

$$E_x = -n_{74}\tau_{yz} - n_{75}\tau_{zx} + n_{77}D_x \tag{5.12}$$

where,

$$\begin{aligned} n_{ij} &= \bar{s}_{ij} - \bar{d}_{1i}\bar{d}_{1j}/\bar{\epsilon}_{11}, \quad \text{for} \quad (i,j) = (4,5), & n_{47} &= \bar{d}_{14}/\bar{\epsilon}_{11} \\ n_{74} &= n_{47}, & n_{77} &= 1/\bar{\epsilon}_{11}, & n_{57} &= n_{75} = \bar{d}_{15}/\bar{\epsilon}_{11} \end{aligned} \tag{5.13}$$

For the cylindrical bending case, without any body force and internal charge source the extended Reissner-type mixed variational principle for the piezoelectric case can be written as [146]

$$\int_V [\delta u(\tau_{xz,z} + \sigma_{x,x}) + \delta v(\tau_{yz,z} + \tau_{xy,x}) + \delta w(\sigma_{z,z} + \tau_{zx,x}) + \delta\phi(D_{z,z} + D_{x,x}) + \delta\sigma_x(\varepsilon_x - u_{,x})$$

TH-3234_176103111

$$+\delta\sigma_z(\varepsilon_z - w_{,z}) + \delta\tau_{yz}(\gamma_{yz} - v_{,z}) + \delta\tau_{zx}(\gamma_{zx} - u_{,z} - w_{,x}) + \delta\tau_{xy}(\gamma_{xy} - v_{,x}) - \delta D_x(E_x + \phi_{,x})$$

$$-\delta D_z(E_z + \phi_{,z})]dV = 0, \ \ \forall\ \delta u_i,\ \delta\sigma_i,\ \delta\tau_{ij},\ \delta\phi,\ \delta D_i \tag{5.14}$$

where V represents the volume of panel per unit width along y axis. Equation (5.14) implies that the associated variationally consistent boundary conditions, as stated below, are to be satisfied exactly.

The expressions of strains (ε_x, ε_z, γ_{xy}, γ_{yz} and γ_{zx}) and electric field components (E_z & E_x) from Eqs. (5.8) and (5.10)-(5.12) substituted into Eq. (5.14), it yields

$$\int_V [\delta u(\sigma_{x,x} + \tau_{xz,z}) + \delta v(\tau_{xy,x} + \tau_{yz,z}) + \delta w(\tau_{zx,x} + \sigma_{z,z}) + \delta\phi(D_{z,z} + D_{x,x})$$

$$+\delta\sigma_x(n_{11}\sigma_x + n_{16}\tau_{xy} + n_{13}\sigma_z + n_{18}D_z - u_{,x}) - \delta\sigma_z(w_{,z} - n_{31}\sigma_x - n_{36}\tau_{xy} - n_{33}\sigma_z - n_{38}D_z)$$

$$-\delta\tau_{yz}(v_{,z} - n_{44}\tau_{yz} - n_{45}\tau_{zx} - n_{47}D_x) - \delta\tau_{zx}(u_{,z} + w_{,x} - n_{54}\tau_{yz} - n_{55}\tau_{zx} - n_{57}D_x)$$

$$+\delta\tau_{xy}(n_{61}\sigma_x + n_{66}\tau_{xy} + n_{63}\sigma_z + n_{68}D_z - v_{,x}) - \delta D_x(\phi_{,x} - n_{74}\tau_{yz} - n_{75}\tau_{zx} + n_{77}D_x)$$

$$-\delta D_z(\phi_{,z} - n_{81}\sigma_x - n_{86}\tau_{xy} - n_{83}\sigma_z - n_{88}D_z)]dV = 0 \tag{5.15}$$

5.3 INTERFACE AND BOUNDARY CONDITIONS

A non-dimensional in-plane co-ordinate ξ^J for J_{th} segment and a local thickness co-ordinate ζ have been introduced, it varies from 0 to 1. For the panel, it can be written as

$$\xi^J = (x - x_{J-1})/a^J\,; \qquad \zeta = (z - z_0)/h \tag{5.16}$$

A uniformly distributed pressure of q_1 and q_2 is applied to the bottom and top surfaces of the panel, respectively. While it is assumed that both of the surfaces of the panel are free from shear traction. These surfaces may be subject to either a prescribed transverse electric displacement (charge density) D_α or a transverse electric potential ϕ_α, both of which are uniformly distributed over x. Therefore, at the top (z=h/2) and bottom (z=-h/2) surfaces of the panel, required support

TH-3234_176103111

conditions can be expressed as,

$$\begin{aligned} &\text{at bottom}: \quad \sigma_z = -q_1, \quad \tau_{zx}, \tau_{yz} = 0, \quad D_z = D_1 \ \text{ or } \ \phi = \phi_1 \\ &\text{at top}: \quad \sigma_z = -q_2, \quad \tau_{zx}, \tau_{yz} = 0, \quad D_z = D_2 \ \text{ or } \ \phi = \phi_2 \end{aligned} \tag{5.17}$$

The perfect bonding at the J_{th} interface of the panel segment is achieved by satisfying following conditions,

$$[(u,\, v,\, w,\, \sigma_x,\, \tau_{zx},\, \tau_{xy},\, \phi,\, D_x)|_{\xi=1}]^{(J)} = [(u,\, v,\, w,\, \sigma_x,\, \tau_{zx},\, \tau_{xy},\, \phi,\, D_x)|_{\xi=0}]^{(J+1)} \tag{5.18}$$

The piezo-panel may be subjected under any mechanical support combination at x=0 and a, such as,

$$\begin{aligned} &\text{Simply Supported (S)}: \quad w, \sigma_x, \tau_{xy} = 0 \\ &\text{Clamped (C)}: \quad u, v, w = 0 \\ &\text{Free (F)}: \quad \sigma_x, \tau_{xz}, \tau_{xy} = 0 \end{aligned} \tag{5.19}$$

The support ends may be subjected to open circuit ($D_x = 0$) or closed circuit conditions with recommended electrical potential.

5.4 THE GENERALISED EKM

The solutions for the field variables $\mathbf{X} = [\, u \quad v \quad w \quad \sigma_x \quad \sigma_z \quad \tau_{xy} \quad \tau_{yz} \quad \tau_{zx} \quad \phi \quad D_x \quad D_z \,]^{\mathrm{T}}$ is obtained by applying multi-term EKM [254]. These field variables are expressed in n-term series for the J_{th} segment, which consists the products of separable functions for ξ, ζ and time, as,

$$X_l(\xi, \zeta) = \sum_{i=1}^{n} f_l^i(\xi) g_l^i(\zeta) + \delta_{l5}[q_a + z q_d] + \delta_{l9}\bar{g}_9 \qquad \text{for} \qquad l = 1, 2, \ldots 11 \tag{5.20}$$

wherein two unknown univariate functions $f_l^i(\xi)$ and $g_l^i(\zeta)$ of ξ and ζ respectively need to be obtained iteratively by gratifying all homogenous boundary conditions. The repeated index l does not represent summation here. δ_{lm} is Kronecker's delta, $q_a = -(q_1 + q_2)/2$ and $q_d = -(q_2 - q_1)/h$.

TH-3234_176103111

The solution $\bar{g}_9$ for single layer non-homogeneous boundary condition of ϕ is given by

$$\bar{g}_9 = \begin{cases} -\phi_1 & \text{for} \quad z = -h/2 \\ -\phi_2 & \text{for} \quad z = h/2 \end{cases} \tag{5.21}$$

While function $g_l^i(\zeta)$ is defined for the panel layer and function $f_l^i(\xi)$ depends on the segment. Both unknown functions (f and g) of ξ and ζ, respectively will be obtained in two iterative steps by fulfilling all homogenous support conditions.

5.4.1 First Iteration Step

In the first step, functions $f_l^i(\xi)$ are considered as known in x-direction, while functions $g_l^i(\zeta)$ need to be solved. In the EKM, it is not necessary to satisfy the prescribed support conditions by the initial trail functions. Hence, to initiate the iterative process f_l^i are assumed as, $f_1(\xi) = f_2(\xi) = f_7(\xi) = f_8(\xi) = f_{10}(\xi) = \cos i\pi\xi$ and $f_3(\xi) = f_4(\xi) = f_5(\xi) = f_6(\xi) = f_9(\xi) = f_{11}(\xi) = \sin i\pi\xi$. Hence, f_l^i are known, the variation δX_i is given as,

$$\delta X_l = \sum_{i=1}^{n} f_l^i(\xi)\delta g_l^i, \qquad l = 1, 2, \ldots 11 \tag{5.22}$$

Now, the functions $g_l^i(\zeta)$ are partitioned into a column vector $\bar{\mathbf{G}}$ that consists all those eight variables which appear in the interface & boundary conditions (5.17) and (5.18), and a column vector $\hat{\mathbf{G}}$ of remaining three variables:

$$\bar{\mathbf{G}} = [\, g_1^1 \ldots g_1^n \quad g_2^1 \ldots g_2^n \quad g_3^1 \ldots g_3^n \quad g_5^1 \ldots g_5^n \quad g_7^1 \ldots g_7^n \quad g_8^1 \ldots g_8^n \quad g_9^1 \ldots g_9^n \quad g_{11}^1 \ldots g_{11}^n \,]^{\mathrm{T}}$$

$$\hat{\mathbf{G}} = [\, g_4^1 \ldots g_4^n \quad g_6^1 \ldots g_6^n \quad g_{10}^1 \ldots g_{10}^n \,]^{\mathrm{T}} \tag{5.23}$$

Now, substituting Eqs. (5.20) and (5.22) in Eq. (5.15), integrating over ξ direction and assuming that the variations δg_l^i are arbitrary, the coefficients of δg_l^i ($l = 1, \ldots, 11$; $i = 1, 2, \ldots, n$) are equated to zero individually. It gives a set of 8n $1st$ order ordinary differential equations and $3n$ linear algebraic equations for every segment as following:

$$\mathbf{M}\bar{\mathbf{G}}_{,\zeta} = \bar{\mathbf{A}}\bar{\mathbf{G}} + \hat{\mathbf{A}}\hat{\mathbf{G}} + \bar{\mathbf{Q}}_{\mathbf{p}} + \bar{\mathbf{Q}}_{\mathbf{e}} \tag{5.24}$$

$$\mathbf{K}\hat{\mathbf{G}} = \tilde{\mathbf{A}}\bar{\mathbf{G}} + \tilde{\mathbf{Q}}_{\mathbf{p}} \tag{5.25}$$

TH-3234_176103111

where $\mathbf{M}(8n\times 8n)$, $\bar{\mathbf{A}}(8n\times 8n)$, $\hat{\mathbf{A}}(8n\times 3n)$, $\mathbf{K}(3n\times 3n)$ and $\tilde{\mathbf{A}}(3n\times 8n)$ are matrices. The notation $\langle\ldots\rangle_a=\sum_{p=1}^{S} a^p \int_0^1 (\ldots)^p \, d\xi$ indicate integration across the span length (a) and $q_a = q_a + q_d z_0$. The non-zero terms of the equations are as follows:

$$
\begin{aligned}
&M_{i_1j_1} = \langle f_8^i f_1^j\rangle_a, && M_{i_2j_2} = \langle f_7^i f_2^j\rangle_a, && M_{i_3j_3} = \langle f_5^i f_3^j\rangle_a\\
&M_{i_1j_1} = M_{j_6i_6}, && M_{i_2j_2} = M_{j_5i_5}, && M_{i_3j_3} = M_{j_4i_4}\\
&M_{i_7j_7} = M_{j_8i_8} = \langle f_{11}^i f_9^j\rangle_a, && \bar{A}_{i_1j_3} = \tfrac{-t}{a}\langle f_8^i f_{3,\xi}^j\rangle_a, && \bar{A}_{i_1j_5} = tp_{45}\langle f_8^i f_7^j\rangle_a\\
&\bar{A}_{i_1j_6} = tp_{55}\langle f_8^i f_8^j\rangle_a, && \hat{A}_{i_1j_3} = tp_{57}\langle f_8^i f_{10}^j\rangle_a, && \bar{A}_{i_2j_5} = tp_{44}\langle f_7^i f_7^j\rangle_a\\
&\bar{A}_{i_2j_6} = tp_{45}\langle f_7^i f_8^j\rangle_a, && \hat{A}_{i_2j_3} = tp_{47}\langle f_7^i f_{10}^j\rangle_a, && \bar{A}_{i_3j_4} = tp_{33}\langle f_5^i f_5^j\rangle_a\\
&\bar{A}_{i_3j_8} = tp_{38}\langle f_5^i f_{11}^j\rangle_a, && \hat{A}_{i_3j_1} = tp_{31}\langle f_5^i f_4^j\rangle_a, && \hat{A}_{i_3j_2} = tp_{36}\langle f_5^i f_6^j\rangle_a\\
&\bar{A}_{i_4j_6} = \tfrac{-t}{a}\langle f_3^i f_{8,\xi}^j\rangle_a, && \hat{A}_{i_5j_2} = \tfrac{-t}{a}\langle f_2^i f_{6,\xi}^j\rangle_a, && \hat{A}_{i_6j_1} = \tfrac{-t}{a}\langle f_1^i f_{4,\xi}^j\rangle_a\\
&\bar{A}_{i_7j_4} = tp_{83}\langle f_{11}^i f_5^j\rangle_a, && \bar{A}_{i_7j_8} = tp_{88}\langle f_{11}^i f_{11}^j\rangle_a, && \hat{A}_{i_7j_1} = tp_{81}\langle f_{11}^i f_4^j\rangle_a\\
&\hat{A}_{i_7j_2} = tp_{86}\langle f_{11}^i f_6^j\rangle_a, && \hat{A}_{i_8j_3} = \tfrac{-t}{a}\langle f_9^i f_{10,\xi}^j\rangle_a, && K_{i_1j_1} = p_{11}\langle f_4^i f_4^j\rangle_a\\
&K_{i_1j_2} = p_{16}\langle f_4^i f_6^j\rangle_a, && K_{j_2i_1} = K_{i_1j_2}, && K_{i_2j_2} = p_{66}\langle f_6^i f_6^j\rangle_a\\
&K_{i_3j_3} = p_{77}\langle f_{10}^i f_{10}^j\rangle_a, && \tilde{A}_{i_1j_1} = \tfrac{1}{a}\langle f_4^i f_{1,\xi}^j\rangle_a, && \tilde{A}_{i_1j_4} = -p_{13}\langle f_4^i f_5^j\rangle_a\\
&\tilde{A}_{i_1j_8} = -p_{18}\langle f_4^i f_{11}^j\rangle_a, && \tilde{A}_{i_2j_2} = \tfrac{1}{a}\langle f_6^i f_{2,\xi}^j\rangle_a, && \tilde{A}_{i_2j_4} = -p_{63}\langle f_6^i f_5^j\rangle_a\\
&\tilde{A}_{i_2j_8} = -p_{68}\langle f_6^i f_{11}^j\rangle_a, && \tilde{A}_{i_3j_5} = p_{74}\langle f_{10}^i f_7^j\rangle_a, && \tilde{A}_{i_3j_6} = p_{75}\langle f_{10}^i f_8^j\rangle_a\\
&\tilde{A}_{i_3j_7} = \tfrac{-1}{a}\langle f_{10}^i f_{9,\xi}^j\rangle_a
\end{aligned}
\tag{5.26}
$$

here, $i_p = (p-1)n + i$ and $j_q = (q-1)n + j$ for $p, q = 1, 2, \ldots, 11$.

Whereas, the load vectors are $\bar{\mathbf{Q}}_{\mathbf{p}}(8n\times 1n)$, $\tilde{\mathbf{Q}}_{\mathbf{p}}(3n\times 1n)$ and $\bar{\mathbf{Q}}_{\mathbf{e}}(8n\times 1n)$, whose non-zero terms are given as

$$
\begin{aligned}
&\bar{Q}_{p_{i_4}} = -t\langle f_3^i\rangle_a q_d, && \bar{Q}_{p_{i_3}} = tp_{33}\langle f_5^i\rangle_a\,(q_a + \zeta t q_d)\\
&\bar{Q}_{p_{i_7}} = tp_{83}\langle f_{11}^i\rangle_a (q_a + \zeta t q_d), && \tilde{Q}_{p_{i_1}} = -p_{13}\langle f_4^i\rangle_a\,(q_a + \zeta t q_d)\\
&\tilde{Q}_{p_{i_2}} = -p_{63}\langle f_6^i\rangle_a\,(q_a + \zeta t q_d), && \bar{Q}_{e_{i_7}} = \begin{cases} \langle f_{11}^i\rangle_a \phi_1 & \text{for } z = -h/2\\ -\langle f_{11}^i\rangle_a \phi_2 & \text{for } z = h/2\\ 0 & \text{otherwise}\end{cases}
\end{aligned}
\tag{5.27}
$$

where $q_a = q_a + q_d z$. Since the functions f_l^i are known analytical functions, elements of the matrices

defined in Eqs. (5.26) and (5.27) are evaluated in close form.

5.4.2 Second Iteration Step

In the second iterative step, the obtained solution for $g_l^i(\zeta)$ from the previous step is taken and function f_l^i is assumed as unknown. In this case, the variation δX is given by

$$\delta X_l^i = \sum_{i=1}^{n} g_l^i(\zeta)\delta f_l^i \quad \text{for} \quad l = 1, 2, \ldots, 11 \tag{5.28}$$

The functions $f_l^i(\xi)$ are seperated into two vectors $\bar{\mathbf{F}}$ and $\hat{\mathbf{F}}$. $\bar{\mathbf{F}}$ contain the variables which appear in the boundary conditions (5.19) and $\hat{\mathbf{F}}$ consist the remaining variables, as given below:

$$\begin{aligned}
\bar{\mathbf{F}} &= [\, f_1^1 \ldots f_1^n \quad f_2^1 \ldots f_2^n \quad f_3^1 \ldots f_3^n \quad f_4^1 \ldots f_4^n \quad f_6^1 \ldots f_6^n \quad f_8^1 \ldots f_8^n \quad f_9^1 \ldots f_9^n \quad f_{10}^1 \ldots f_{10}^n \,]^{\mathrm{T}} \\
\hat{\mathbf{F}} &= [\, f_5^1 \ldots f_5^n \quad f_7^1 \ldots f_7^n \quad f_{11}^1 \ldots f_{11}^n \,]^{\mathrm{T}}
\end{aligned} \tag{5.29}$$

Substituting Eq. (5.28) in Eq. (5.15), performing integration across ζ direction on the known functions of ζ. Wherever needed integration by parts is applied and coefficient of δf_l^i is equated to zero seperatly. It yields a system of differential-algebraic equations for f_l^i as follows:

$$\mathbf{N}\bar{\mathbf{F}}_{,\xi} = \bar{\mathbf{B}}\bar{\mathbf{F}} + \hat{\mathbf{B}}\hat{\mathbf{F}} + \bar{\mathbf{P}}_{\mathbf{m}} \tag{5.30}$$

$$\mathbf{L}\hat{\mathbf{F}} = \tilde{\mathbf{B}}\bar{\mathbf{F}} + \tilde{\mathbf{P}}_{\mathbf{m}} \tag{5.31}$$

where $\mathbf{N}(8n \times 8n)$, $\bar{\mathbf{B}}(8n \times 8n)$, $\hat{\mathbf{B}}(8n \times 3n)$, $\mathbf{L}(3n \times 3n)$ and $\tilde{\mathbf{B}}(3n \times 8n)$ are matrices. The vectors contain loading terms are $\bar{\mathbf{P}}_{\mathbf{m}}$ and $\tilde{\mathbf{P}}_{\mathbf{m}}$ of size $8n \times 1n$ and $3n \times 1n$, respectively. Here, the expression $\langle \ldots \rangle_h = \sum_{k=1}^{L} t^{(k)} \int_0^1 (\ldots)^{(k)}\, d\zeta$ depicts integration across the thickness and the non-zero terms of the above specified matrices are given as:

$$\begin{aligned}
N_{i_1 j_1} = N_{j_4 i_4} = \langle g_4^i g_1^j \rangle_h, \;\; N_{i_2 j_2} = N_{j_5 i_5} = \langle g_6^i g_2^j \rangle_h \\
N_{i_3 j_3} = N_{j_6 i_6} = \langle g_8^i g_3^j \rangle_h, \;\; N_{i_7 j_7} = N_{j_8 i_8} = \langle g_{10}^i g_9^j \rangle_h
\end{aligned} \tag{5.32}$$

TH-3234_176103111

$$\bar{B}_{i_1j_4} = \langle \bar{p}_{11} g_4^i g_4^j \rangle_h, \quad \bar{B}_{i_1j_5} = \langle \bar{p}_{16} g_4^i g_6^j \rangle_h, \quad \hat{B}_{i_1j_1} = \langle \bar{p}_{13} g_4^i g_5^j \rangle_h, \quad \bar{B}_{i_1j_7} = -\langle \bar{p}_{18} g_4^i \tfrac{g_{9,\zeta}^j}{t} \rangle_h$$

$$\bar{B}_{i_2j_4} = \langle \bar{p}_{61} g_6^i g_4^j \rangle_h, \quad \bar{B}_{i_2j_5} = \langle \bar{p}_{66} g_6^i g_6^j \rangle_h, \quad \hat{B}_{i_2j_1} = \langle \bar{p}_{63} g_6^i g_5^j \rangle_h \quad \bar{B}_{i_2j_7} = -\langle \bar{p}_{68} g_6^i \tfrac{g_{9,\zeta}^j}{t} \rangle_h$$

$$\bar{B}_{i_3j_1} = -\langle g_8^i \tfrac{g_{1,\zeta}^j}{t} \rangle_h, \quad \bar{B}_{i_3j_6} = \langle p_{55} g_8^i g_8^j \rangle_h, \quad \hat{B}_{i_3j_2} = \langle p_{45} g_8^i g_7^j \rangle_h, \quad \bar{B}_{i_3j_8} = \langle p_{57} g_8^i g_{10}^j \rangle_h$$

$$\bar{B}_{i_4j_6} = \langle \tfrac{g_{1,\zeta}^i}{t} g_8^j \rangle_h, \quad \hat{B}_{i_5j_2} = \langle \tfrac{g_{2,\zeta}^i}{t} g_7^j \rangle_h, \quad \hat{B}_{i_6j_1} = \langle g_3^i \tfrac{g_{5,\zeta}^j}{t} \rangle_h, \quad \bar{B}_{i_7j_6} = \langle p_{75} g_{10}^i g_8^j \rangle_h$$

$$\bar{B}_{i_7j_8} = -\langle p_{77} g_{10}^i g_{10}^j \rangle_h, \; \hat{B}_{i_7j_2} = \langle p_{74} g_{10}^i g_7^j \rangle_h, \quad \hat{B}_{i_8j_3} = -\langle g_9^i \tfrac{g_{11,\zeta}^j}{t} \rangle_h, \quad L_{i_1j_1} = \langle \bar{p}_{33} g_5^i g_5^j \rangle_h \tag{5.33}$$

$$\tilde{B}_{i_1j_7} = \langle \bar{p}_{38} g_5^i \tfrac{g_{9,\zeta}^j}{t} \rangle_h, \quad L_{i_2j_2} = \langle p_{44} g_7^i g_7^j \rangle_h, \quad L_{i_3j_1} = \langle \bar{p}_{83} g_{11}^i g_5^j \rangle_h, \quad L_{i_3j_3} = \langle \bar{p}_{88} g_{11}^i g_{11}^j \rangle_h$$

$$\tilde{B}_{i_1j_3} = \langle g_5^i \tfrac{g_{3,\zeta}^j}{t} \rangle_h, \quad \tilde{B}_{i_1j_4} = -\langle \bar{p}_{31} g_5^i g_4^j \rangle_h, \quad \tilde{B}_{i_1j_5} = -\langle \bar{p}_{36} g_5^i g_6^j \rangle_h, \quad \tilde{B}_{i_2j_2} = \langle g_7^i \tfrac{g_{2,\zeta}^j}{t} \rangle_h$$

$$\tilde{B}_{i_2j_6} = -\langle p_{45} g_7^i g_8^j \rangle_h, \quad \tilde{B}_{i_2j_8} = -\langle p_{47} g_7^i g_{10}^j \rangle_h, \; \tilde{B}_{i_3j_4} = -\langle \bar{p}_{81} g_{11}^i g_4^j \rangle_h, \; \tilde{B}_{i_3j_5} = -\langle \bar{p}_{86} g_{11}^i g_6^j \rangle_h$$

$$\tilde{B}_{i_3j_7} = \langle g_{11}^i \tfrac{g_{9,\zeta}^j}{t} \rangle_h$$

$$\bar{P}_{m_{i_1}} = \langle \bar{p}_{13} g_4^i (p_a^k + p_d t\zeta) \rangle_h - \langle \bar{p}_{18} g_4^i \bar{g}_{9,\zeta} \rangle_h, \quad \bar{P}_{m_{i2}} = \langle \bar{p}_{63} g_6^i (p_a^k + p_d t\zeta) \rangle_h - \langle \bar{p}_{68} g_6^i \bar{g}_{9,\zeta} \rangle_h$$

$$\bar{P}_{m_{i6}} = -p_d \langle g_3^i \rangle_h, \qquad \tilde{P}_{m_{i1}} = -\langle \bar{p}_{33} g_5^i (p_a^k + p_d t\zeta) \rangle_h + \langle \bar{p}_{38} g_5^i \bar{g}_{9,\zeta} \rangle_h \tag{5.34}$$

$$\tilde{P}_{m_{i3}} = -\langle \bar{p}_{83} g_{11}^i (p_a^k + p_d t\zeta) \rangle_h + \langle g_{11}^i \bar{g}_{9,\zeta} \rangle_h$$

Now substituting $\hat{\mathbf{F}}$ from Eq. (5.31) into Eq. (5.30) yields the following set of first order ODEs for $\bar{\mathbf{F}}$:

$$\bar{\mathbf{F}}_{,\xi} = \mathbf{B}\bar{\mathbf{F}} + \mathbf{P_m} \tag{5.35}$$

with $\mathbf{B} = \mathbf{N}^{-1}[\bar{\mathbf{B}} + \hat{\mathbf{B}}\mathbf{L}^{-1}\tilde{\mathbf{B}}]$ and $\mathbf{P_m} = \mathbf{N}^{-1}[\bar{\mathbf{P}}_\mathbf{m} + \hat{\mathbf{B}}\mathbf{L}^{-1}\tilde{\mathbf{P}}_\mathbf{m}]$. This iteration can be repeated for each direction alternately till the convergence of results.

5.5 NUMERICAL RESULTS AND DISCUSSIONS

The numerical results are presented and discussed for three piezoelectric-panel configurations as shown in Fig. 5.3. The panel configuration details are as follows:

Panel (a): It is the single-segmented panel of PZT-5A, which has been considered for the validation of multi-term EKM and FE results.

Panel (b): It has two equal piezoelectric segments, the first and second segments are made of PFRC-2 and PZT-5A, respectively.

Panel (c): It consists of four equal piezoelectric segments, namely PZT-A, PZT-B, PZT-C, and

TH-3234_176103111

PZT-D, respectively. The material properties of each segment are similar to PZT-5A; only a variation of piezoelectric strain coefficient (d_{31}) along the x axis has been considered. This variation follows a linear step-wise variation of d_{31} along the length. The effective d_{31} values are -181.6875, -203.0625, -224.4375, and -245.8125 pm/V for segments PZT-A, PZT-B, PZT-C, and PZT-D respectively.

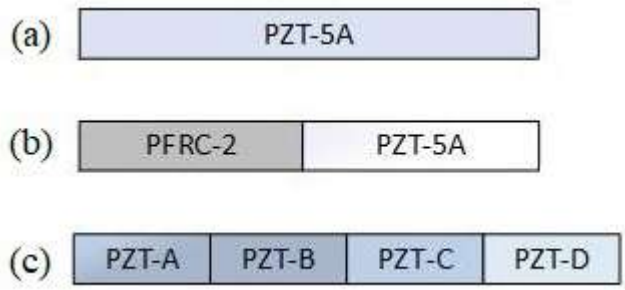

Fig. 5.3: Configuration lay-up of piezoelectric panel under S-S case

However, the thickness of all panels is considered as h. If the panel edges are subjected under the clamped support at x=0 and simply support at x=a, then it is designated as C-S. In this study, material properties considered for the analysis are presented in Table 5.1.

Table 5.1: Material Properties

Material	Y_1	Y_2	Y_3	G_{23}	G_{13}	G_{12}	ν_{12}	ν_{13}	ν_{23}
PZT-5A*	61	61	53.20	21.10	21.10	22.60	0.35	0.38	0.38
PFRC-2*	38.87	13.68	13.20	3.0148	4.3541	4.3699	0.31080	0.41796	0.20079
Material	d_{31}	d_{32}	d_{33}	d_{24}	d_{15}	η_{11}	η_{22}	η_{33}	
PZT-5A*	-171	-171	374	584	584	15.30	15.30	15	
PFRC-2*	-263	-224	485	0	0	29.769	29.769	24.403	

Units: Young's moduli Y_i and shear moduli G_{ij} in GPa; piezoelectric strain coefficients d_{ij} in pm/V; electric permittivities η_{ij} in nF/m; * [146]

The panels are subjected under uniform pressure q_2=q_0 and open circuit conditions at the top surface. In contrast, the bottom surface of the panel is subjected to closed circuit conditions and zero pressure loading q_1= 0. The support ends of the panel are assumed under closed circuit (CC)

conditions. The present numerical results are non-dimensionalized with $S = a/h$, Y_0= 61 GPa, q_0=1 and d_0=374 $\times$ 10^{-12} CN^{-1} as:

$$(\bar{u}, \bar{w}, \bar{\phi}) = 100(Su,\ w,\ 10^2\phi d_0 S^2)Y_0/p_0 h S^4$$

$$(\bar{\sigma}_x,\ \bar{\tau}_{zx}) = (\sigma_x,\ S\tau_{zx})/p_0 S^2, \qquad (\bar{D}_x,\ \bar{D}_z) = (D_x/S,\ D_z)/d_0 p_0$$

For single layer PZT-5A piezoelectric panel, the exact multi-term EKM solutions were obtained by Kapuria and Kumari [146] under the simply-support case. The present multi-term EKM solutions for three variables are validated with the existing results. Whereas for panels (b) & (c), the obtained EKM results for the variables are validated with the 2-D FE results. For the FE analysis of the current model, ABAQUS software is used. As it is a panel with a very long width along Y-direction, hence a generalized plane strain condition is assumed. The displacement and stress components along the y-direction are independent and function of x only. This results the displacement component (v) and shear stresses (τ_{zx} and τ_{zx}) to ideally be zero for cross-ply case. However, for an angle-ply case, these components have non-zero values. Therefore, for 2-D FE analysis, the plane strain element of ABAQUS [250] is used. In ABAQUS, a 2-D plane panel is modeled with length a and thickness h along x and z-directions, respectively. Thereafter, panel (a) has been meshed with a mesh size of 50 (length) $\times$ 20 (thickness), each segment of panel (b) and panel (c) are meshed with a mesh size of 25 (length) $\times$ 20 (thickness). The meshed 2-D panel model is shown in Fig. 5.4. All panel configurations are meshed with the eight-noded quadratic serendipity plain strain piezoelectric (CPE8RE) element with reduced integration. The converged results of FE under different support conditions are presented in figures, along with multi-term EKM results for thick panels (S=5). Present (EKM) results with multi-terms n=2 & 3 are presented to display the accuracy, convergence, and efficacy of the method.

For panel (a): The longitudinal variation of $\bar{w}$ and stresses ($\bar{\sigma}_x$ & $\bar{\tau}_{zx}$) have been validated from Kapuria and Kumari [146]. Additionally, the multi-term EKM results for longitudinal displacement ($\bar{u}$), electric potential ($\bar{\phi}$) and electrical displacement ($\bar{D}_z$) are presented in Fig. 5.5 and compared with the FE results. It has been observed that the obtained multi-term EKM and FE results for

TH-3234_176103111

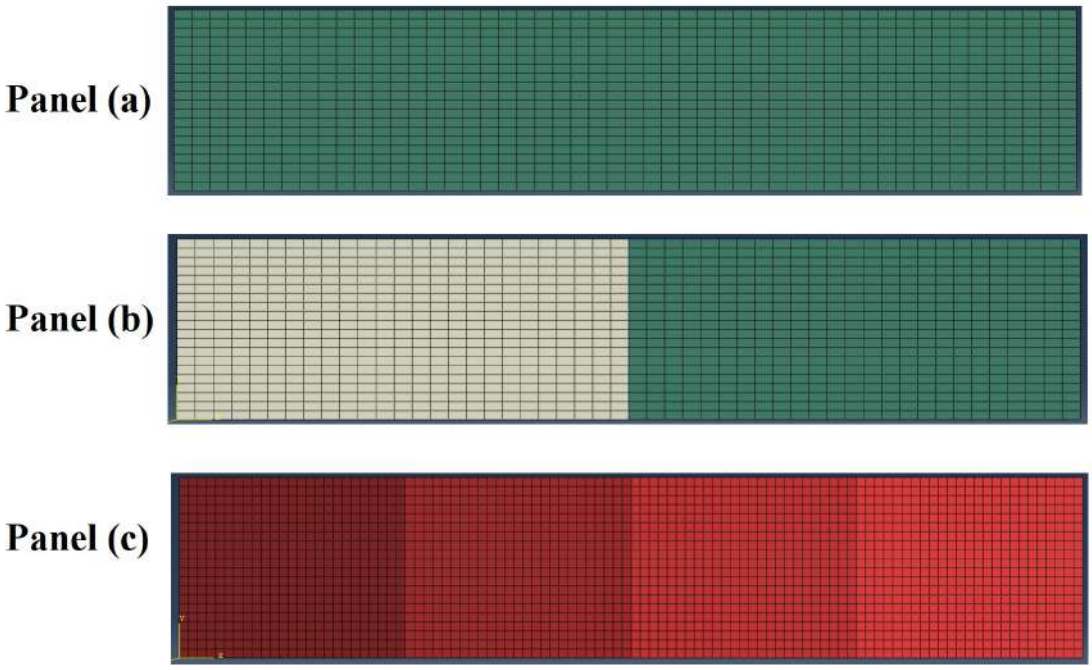

Fig. 5.4: Showing meshed panel

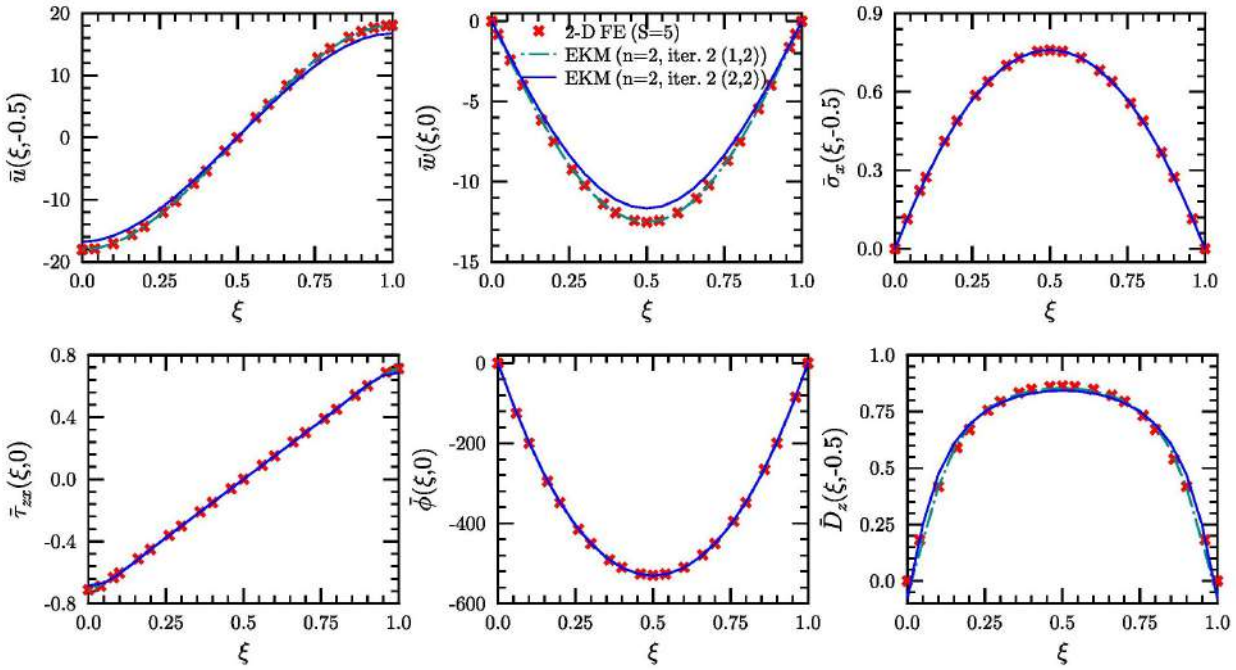

Fig. 5.5: Longitudinal variation of deflections, stresses, electric potential and $\bar{D}_z$ for single layer piezoelectric panel (a) under S-S condition

panel (a) are in good agreement for all variables under the S-S support case.

For panel (b): The longitudinal variation of $\bar{u}$, $\bar{w}$, $\bar{\sigma}_x$, $\bar{\tau}_{zx}$, $\bar{\phi}$ and $\bar{D}_z$ are presented in Fig. 5.6 & 5.7 for thick (S=5) case. The results are presented for simply support at both ends (S-S), clamped-

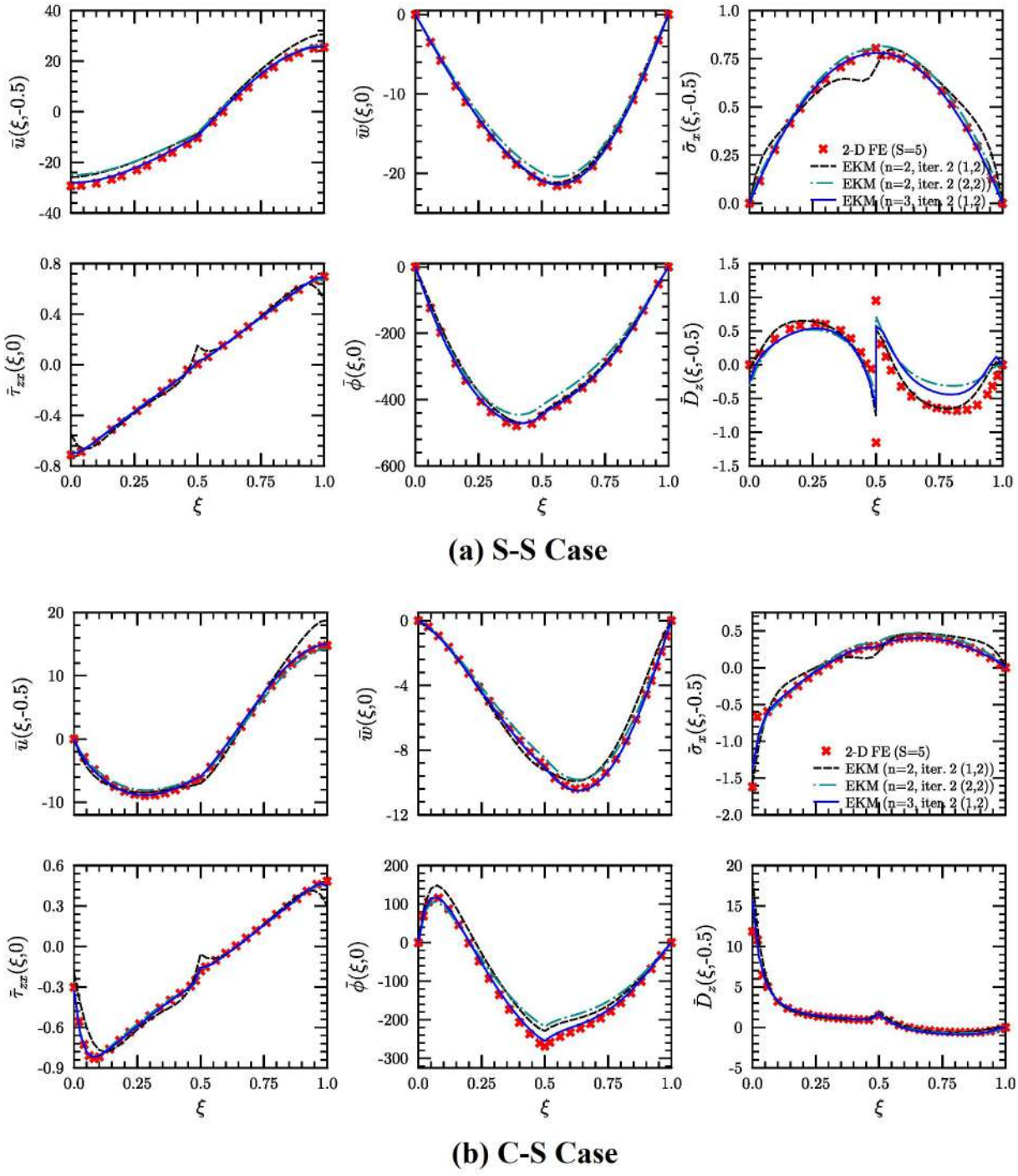

Fig. 5.6: Longitudinal variation of deflections, stresses, electric potential and $\bar{D}_z$ for two segmented piezoelectric panel (b)

simply support (C-S), clamped-free (C-F), and clamped-clamped (C-C) support conditions. From the presented results for panel (b) following major observations are made, which are as follows:

Under the S-S case, the longitudinal change of in-plane displacement ($\bar{u}$) shows a symmetric

behavior about the mid of the panel. Whereas transverse displacement $\bar{w}$ attains its peak slightly right side of the segment junction, i.e., in the PZT-5A segment. It may be due to the weaker elastic properties of PFRC-2 than PZT-5A. The shear stress $\bar{\tau}_{zx}$ varies linearly along the length, which has its maxima at the edges. However, the longitudinal variation of $\bar{D}_z$ shows a concave-convex-shaped pattern in PFRC-2 and PZT-5A segments, respectively. A sudden rise and fall of the $\bar{D}_z$ are also observed at the interface. In the C-S case, the stresses $\bar{\sigma}_x$ and $\bar{\tau}_{zx}$ show its maximum at a very clamped edge, and the converged FE results show a good agreement with the EKM (for n=3) results. Whereas for $\bar{D}_z$, the FE results are showing disagreement with the EKM results only at the clamped edge

From Fig. 5.7 under the C-F case, the in-plane and transverse displacement attain their maximum at the free edge. However, at a very clamped edge, the shear stress $\bar{\tau}_{zx}$ shows a hook shape formation at the clamped edge and interface. It depicts the generation of high-shear stress near the clamped edge. Additionally, the longitudinal variation of the $\bar{\phi}$ shows a significant rise of electric potential in the PFRC-2 segment and gradually settles to zero at the free end of PZT-5A. The longitudinal variation of $\bar{D}_z$ for the C-C case again shows a disagreement between FE and EKM results at the clamped edges.

For panel (c): The longitudinal variation of all variables is presented in Fig. 5.8 & 5.9 for thick (S=5) case under S-S, C-S, C-F, and C-C support conditions. It is observed that the presented results for panel (c) show an excellent agreement between FE and EKM with three terms. The longitudinal variation of $\bar{D}_z$ under the S-S case shows a unique saw-tooth behavior with a sudden jump at each segmental interface. While in C-S and C-F cases, $\bar{D}_z$ shows a minimal jump at the interface and a bathtub type of pattern under the C-C case. However, there is no discernible difference for other variables is observed.

TH-3234_176103111

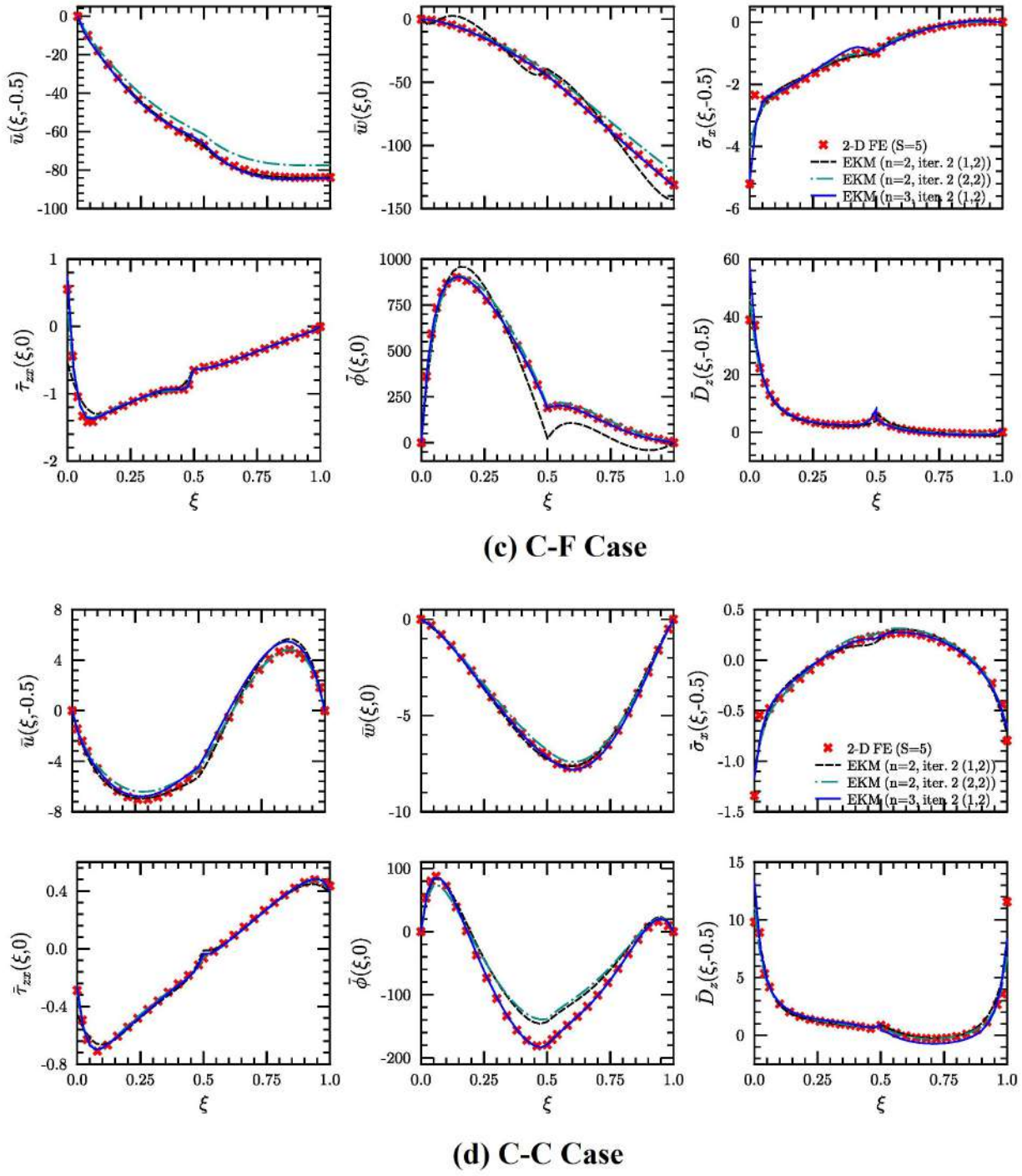

Fig. 5.7: Longitudinal variation of deflections, stresses, electric potential and $\bar{D}_z$ for two segmented piezoelectric panel (b)

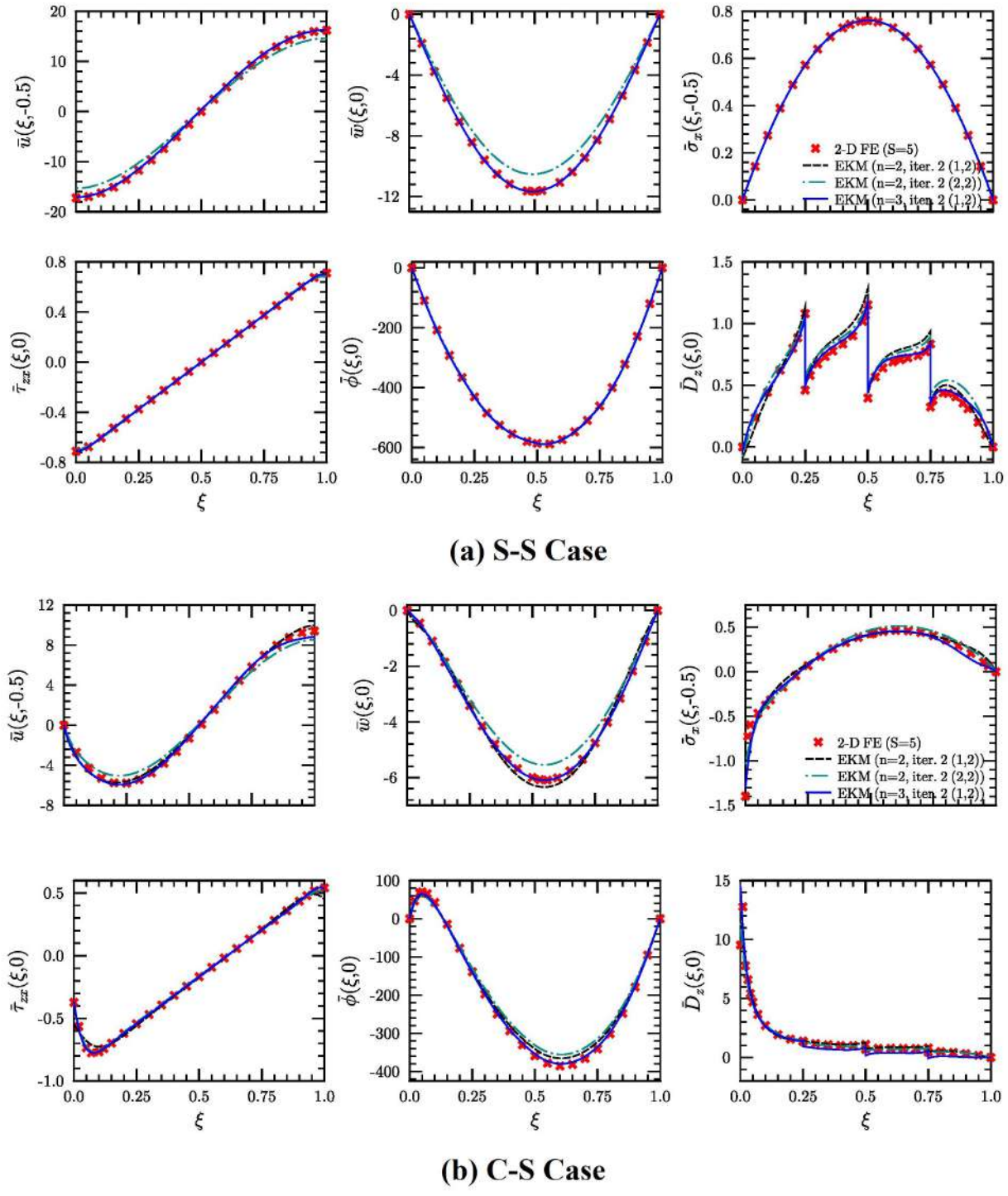

Fig. 5.8: Longitudinal variation of deflections, stresses, electric potential and $\bar{D}_z$ for four segmented piezoelectric panel (c)

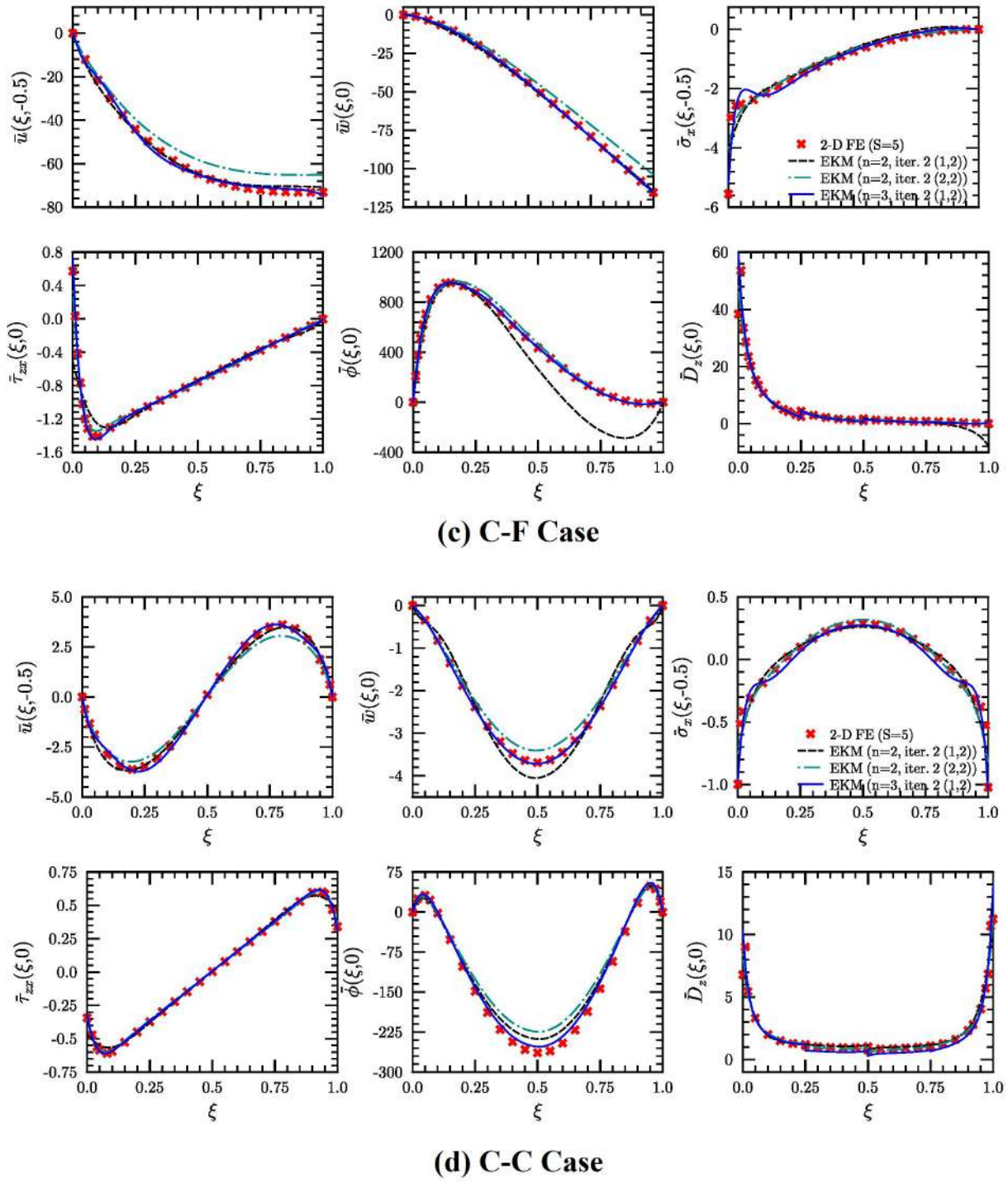

Fig. 5.9: Longitudinal variation of deflections, stresses, electric potential and $\bar{D}_z$ for four segmented piezoelectric panel (c)

5.6 SUMMARY

Two-dimensional analytical solutions have been developed using a multi-term EKM for piezoelectric panels having multiple segments along the x-axis. The accuracy and effectiveness of this method are established by comparing it with the 2-D FE results. By using the mixed approach in EKM solution, all boundary conditions at the point and the interface conditions along x-direction are satisfied exactly, and results good accuracy of all the variables. The analytical and numerical results are presented for three different types of lay-ups, which are in excellent agreement with each other. The multi-term EKM and FE solutions for panel (a) are validated with the existing results. A few additional results are also included for a better understanding of the panel behavior under S-S case. For panel (a), the EKM results after two terms and two iterations show convergence and accurately match the FE results. For panels (b) and (c), the EKM results after three terms and two iterations closely match the FE results. The EKM results shows a rapid convergance, because the maximum number of iteration did not exceed more than two for any panel configuration. The solutions obtained from the EKM requires much less effort than the numerical FE solutions, because a major portion of the computation is done analytically. An increase in segment numbers requires more number of terms and iteration in EKM solution, which may delay the convergance. In the case of panel (b), a disagreement of the EKM and FE results for $\bar{D}_z$ are seen at the very clamped edge under C-C, C-F, and C-S cases. Under the S-S case, a change in piezoelectric material and the number of segments do not significantly affect the normal and shear stress variation. This work can be extended to develop the solutions for multi-material piezoelectric beam and plate problems under various mechanical and electromechanical loading conditions using multi-term EKM. This work can also be used as a benchmark for solving an axially graded piezoelectric panel having a step gradient.

TH-3234_176103111

Chapter 6

Fabrication and Characterization of Cu/SiC Based Axially Functionally Graded Beam

6.1 INTRODUCTION

The metal-ceramics based FGMs are intensively used in various industries such as in aerospace, automobiles, electronics etc. for structural and thermal applications. The Cu/SiC metal-ceramic based system consists good mechanical and physical properties such as high thermal conductivity, high strength, a stable ceramic bonding at high working temperature, corrosion resistance, low cost etc. On the other hand, the SiC has very high working temperature, high hardness and high wear resistance. A three-layered Cu/SiC (100/0, 90/10, and 80/20) FGM beam having gradation along the length is fabricated using the powder metallurgy method for the first time. The details of material properties, powder specifications and processing of powders to fabricate the specimens are elaborated in Sec. 6.2. Further, the details are presented for the preparation of powder mixture in Sec. 6.2.2, machines used in Sec. 6.2.3, compaction of powders in Sec. 6.2.4 and sintering of specimens in Sec. 6.2.5. A detailed characterization of the powders using powder XRD, TEM and FESEM techniques have been carried out before the compaction, which are discussed in Sec. 6.3. The effect of ball-milling on the peak broadening, lattice strain and crystallite size of the copper powder are studied in Sec. 6.3.1.1 using Williamson-Hall method and Sherrer's equations. The TEM analysis of the ball-milled copper powder is discussed in Sec. 6.3.1.2. In Sec. 6.3.2, a detailed discussion on the FESEM and EDS analysis of the Cu/SiC specimens are reported. Apart from it,

TH-3234_176103111

a Vicker's micro-hardness tests of the specimens are also performed which is discussed in Sec. 6.3.3. Further, at last a conclusive summary on the work has been reported in Sec. 6.4.

6.2 EXPERIMENTATION

6.2.1 Material System

From a wide range of combinations of metal-ceramic based material system here Cu-SiC based system is chosen. This metal-ceramics based FGMs material system is choosen on the basis of thermo-mechanical properties (high thermal conductivity, good strength, good ceramic bonding, etc.) of the Cu over other metals. Moreover, this material system based FGMs also gives a superior ductility & toughness of copper, high strength & high modulus of SiC reinforced particles [255]. The detailed material properties used in this fabrication process are shown in Table 6.1.

Table 6.1: Properties of FGM constituents (Metal-ceramic and binders)

Sl no.	Material	Particle size (μm)	Melting point (°C)	Density (kg/m^3)	Manufacturer
1	Cu (99.5% pure)	< 450	1083.4	8940	Sigma Aldrich
2	SiC (97.5% pure)	<36	2700	3220	Sigma Aldrich
3	PVA (99% pure)	-	200	1190	Akshar Chem

Here, PVA is used as an organic binder for both material system, because, it left significantly less carbon residue after the sintering. The Zinc Stearate powder [Research-lab fine chem industries, Mumbai] is used as die lubricant during uni-axial die compaction [256].

6.2.2 Preprocessing of Raw Materials

In the powder metallurgy process, the first operation is separation of fine particles of powder from the coarse particles. Numerous methods are available to measure the particle size of the powder, i.e. test sieve, laser particle size analyzer, scanning electron microscopy etc. Here, test sieves are used for the particle size separation and it's measurement, because of it's easiness in operation. The powders are sieved using different coarse and finer sets of sieves (300, 150, 75, 50 and 37 μm) on a table top sieve shaker as shown in Fig. 6.1(a and b). The Cu powder of particle's size between

TH-3234_176103111

(37-50μm) and the SiC powder of size less than 37μm are used for the fabrication of the FGM specimens.

After the particle's size separation, the coarse particles (more than 50μm) are processed into fine particles. For this processing, the coarse powders are ball milled using planetary mono ball milling machine [make: FRITSCH, model- PULVERISETTE 6 classic line] as shown in Fig. 6.1(c). The powders are milled in a 500ml zirconium oxide jar using the spherical zirconia balls of diameter 10 & 12 mm. The ball to powder ratio is maintained at 10:1 during the milling process. The milling is carried out continuously at 250 r.p.m. for 8 hrs, provided the cooling of machine for 10 minutes at each one hour interval [257]. After the ball-milling of pure Cu powder, it is sieved and the fine particles are separated. Then, the sieved Cu powder (50-37μm) is mixed with initial SiC powder in the metal-ceramic wt% ratios of 90/10 and 80/20. This mixed powders are separately ball milled at 250 r.p.m for 4 hrs. After that, this ball-milled mixed powders are sieved and the fine mixed powders are separated for the fabrication of FGM as shown in Fig. 6.1(f).

6.2.3 Powder Blending or Mixing

In this step, metal powder, ceramic powder and binders are mixed in required proportion. Here, for 100/0 layer the pure Cu powder is mixed with 3% aquas PVA solution for 15 minutes inside the blender. Whereas, for 90/10 and 80/20 layers, the mixed Cu/SiC powder is added with 4% aquas PVA solution and blended separately for 20 minutes. The PVA solution is prepared by the mixing of 20% PVA powder with 80% water at a temperature of 80° on magnetic stirrer for 30 minutes with 300 r.p.m. [258].

6.2.4 Powder Compaction

In this step, the blended powders are stacked and pressed under high pressure. Here, the powders are first compacted uni-axially inside a stainless steel die cavity ($l \times b \times h = 11.5 \times 11.5 \times 90$ mm) at UTM [make: BISS, model-MEDIAN 250] followed by CIP [make: American Isostatic Presses, inc.] for the fabrication of FGM beam.

The pure Cu (100/0 layer) and Cu/SiC mixed powders (for 90/10 & 80/20 layers) are filled layer by layer inside the die cavity. The stainless steel die and punch is lubricated with the zinc

TH-3234_176103111

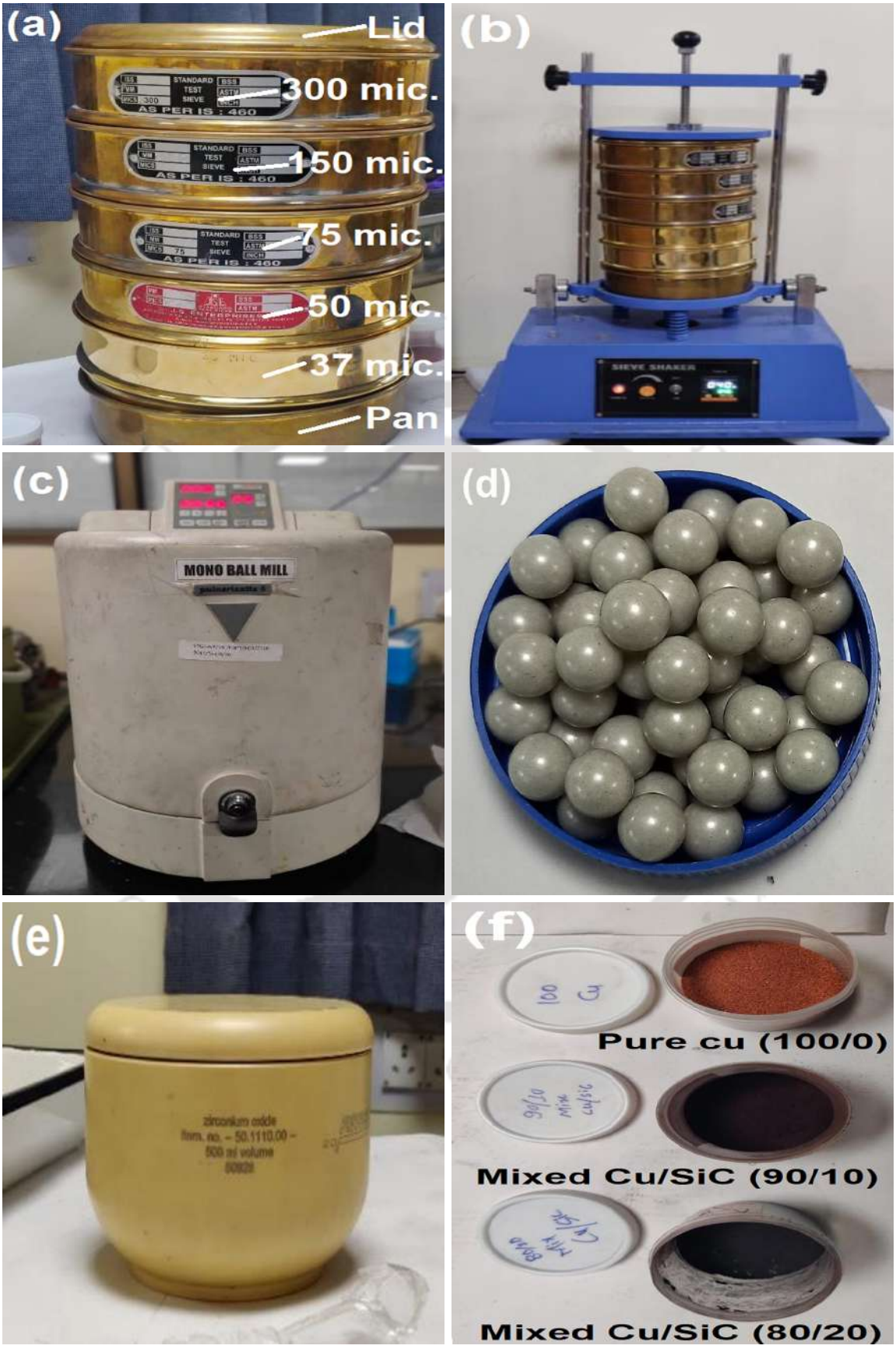

Fig. 6.1: (a) Test sieves (b) Sieve shaker (c) Mono-ball milling machine (d) Zirconia balls (e) Grinding jar and (f) Intial Cu powder and ball-milled mixed Cu/SiC

Fig. 6.2: (a) Uni-axial compaction at UTM (zoomed view) (b) Rubber molds (c) Sealed rubber mold for compaction (d) CIP unit (e) Cu/SiC green specimen (f) Sintered and polished specimen

stearate powder before each compaction. The compaction load gradually increased up-to a set load of 100 kN at UTM and the load is hold for 2 minutes as shown in Fig. 6.2(a). After that, the compacted green specimen is ejected from the die and it's dimensions are measured. Then, this green specimen is kept inside a rectangular shaped rubber mold as shown in Fig. 6.2(b and c). Now, after the sealing of rubber molds it kept inside the compaction chamber of CIP unit as shown in Fig. 6.2(d). The compression pressure is gradually increased up-to a set pressure of 250 MPa and the specimens are kept under this pressure for 2 minutes. Further, the specimens are taken out from the CIP unit and it's dimensions & weight are measured as shown in Fig. 6.2(e).

6.2.5 Sintering

After the compaction, the green specimens are further sintered inside the muffle furnace. For the sintering, the specimens are kept at 900°C for 120 minutes and allow to cool the specimens inside the furnace. Then after, the specimens are taken out from the furnace for the weighing and measuring. From the measurement, no distortion and a marginal reduction in the weight of the specimens are observed. However, a layer of oxide formation is also observed on the specimens it is due to reaction of oxygen with Cu at high temperature.

6.3 RESULTS AND DISCUSSION

6.3.1 Powder Characterization

After the pre-processing of powders, the powder characterization has been carried out using the powder XRD, TEM and FESEM techniques. In the powder XRD analysis, the diffraction angle (2θ) Vs intensity plot is obtained for Cu (before and after milling), ball-milled Cu/SiC mixture, initial SiC powder. Whereas, in the FESEM analysis the morphology of Cu powder (before and after the ball milling) and initial SiC powder is analyzed.

6.3.1.1 Powder XRD results

The powder XRD has been carried out for all the initial and ball-milled powders on [make: Rigaku, model- Smartlab X-ray diffractrometer], step width at 0.02°, CuK_α radiation, a wavelength of 1.5418Å and a scan speed of 21.6746° per minute. The obtained XRD plots are shown in Fig. 6.3.

The results are obtained for a 2θ range from 30°-90° for the initial Cu, ball-milled Cu and mixed Cu/SiC (90/10) powder and 20°-70° for initial SiC powder.

From the obtained results for the copper powder at initial state and after the ball milling the peak of maximum intensity for both the powders are found when the diffraction angle is at near 43.28° for (1,1,1) plane [259]. The diffraction pattern also shows peaks at near 50.45°, 74.17° and 89.9°for the planes (2,0,0), (2,2,0) and (311), respectively. These patterns matches with the Joint Committee on Powder Diffraction Standards (JCPDS), having the card no. 00-004-0836 of cubic copper crystal. While, it is also observed that the initially sharp diffraction lines are considerably broadened after the ball milling in Fig. 6.3(a and b). It is may be due to an increase in internal lattice strains and crystallite size [260]. The maximum intensity for SiC at it's initial state are found when the diffraction angle is near to 35.46° in Fig. 6.3(c).

However, for the ball-milled Cu/SiC mixture, a formation of the very small peak intensity at near 35° in Fig. 6.3(d) is visible for the Cu/Sic (90/10) mixture, which is may be due to mixing a low wt% of SiC with Cu. Moreover, this peak considerably big for the 80/20 ball-milled mixture at near 35° and appearance of a new peak of SiC at near 60° can be observed as shown in Fig. 6.3(e), it is due to presence of relatively high SiC contents in the mixture. The maximum intensity for the PVA powder is observed at 19.8° in Fig. 6.3(f). Further, by using this diffraction data the crystallite size from the Scherrer method and intrinsic strain using uniform deformation model (UDM) of the Williamson's-Hall (W-H) approach have been calculated.

1. Scherrer method

   The X-ray diffraction peaks broadening usually happens due to the crystalline size effect and intrinsic lattice strain effect. This peak broadening basically consists of two parts i.e. instrument and physical broadening of the sample [261, 262]. The instrumental broadening can be corrected corresponding to each diffraction peak of Cu and ball-milled Cu powder using the relation:

$$\beta_d^2 = \beta_m^2 - \beta_i^2 \tag{6.1}$$

TH-3234_176103111

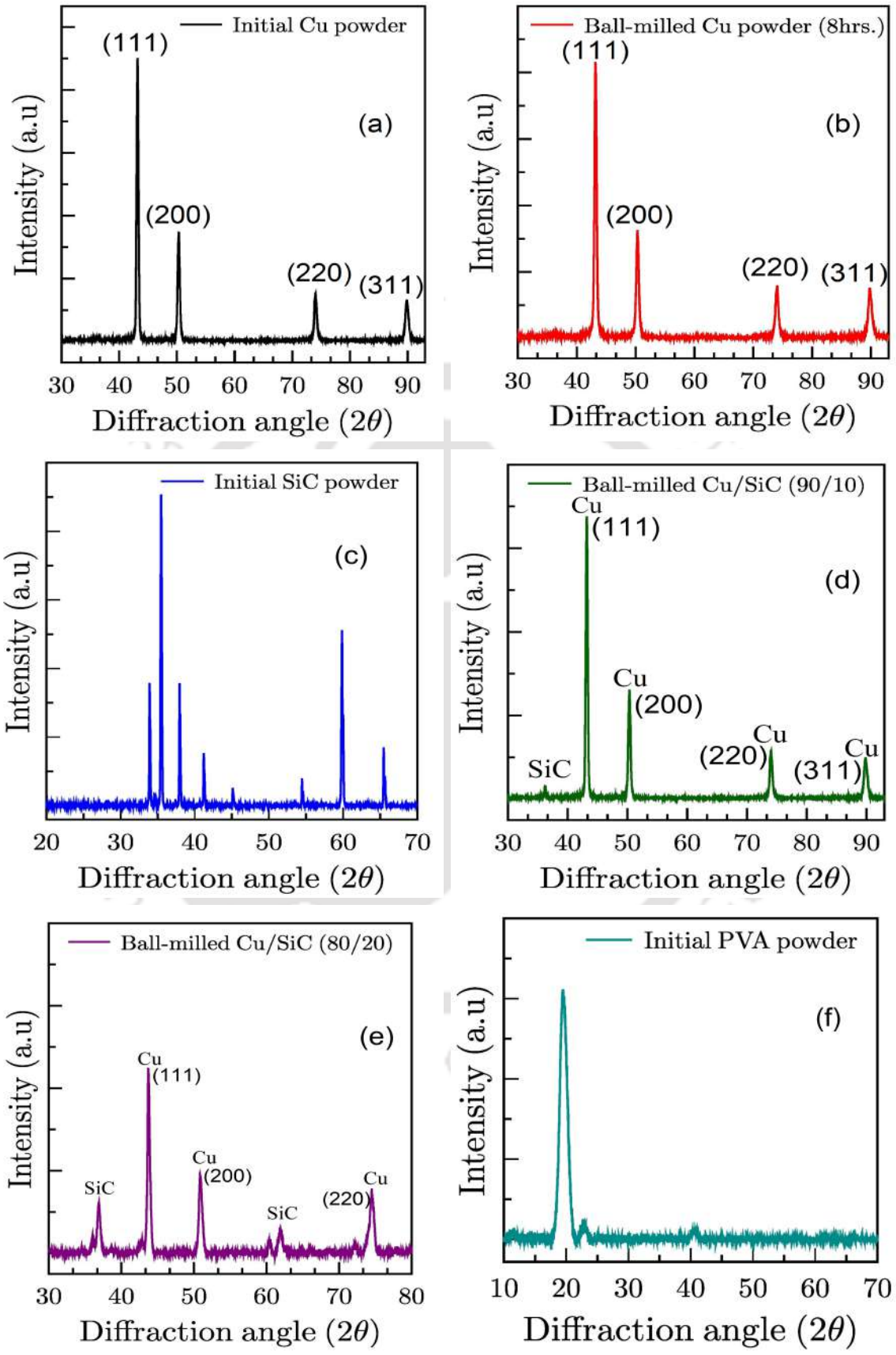

Fig. 6.3: Powder XRD plots

TH-3234_176103111

Where, β_m, β_i and β_d are measured, instrumental and corrected broadening. The β_m and β_i are measured as full width at half maximum (FWHM). Then, the average crystalline size is calculated using the corrected physical broadening through the Debye-Scherrer's equation [263].

$$D = K\lambda/\beta_d cos\theta \tag{6.2}$$

Where, D= Crystallite size, K= Shape factor (0.9), λ= Wavelength of CuK_α radiation. From the calculation, the average crystallite size (D) for the initial Cu powder, 8 hrs ball-milled Cu powder and the ball-milled Cu/SiC(90/10) mixed powder is obtained as 17.822 nm, 22.027 nm and 22.521 nm respectively. Further, the Eq.6.2 can be rearranged as:

$$cos\theta = \frac{K\lambda}{D}.\frac{1}{\beta_d} \tag{6.3}$$

The Scherrer plot between $1/\beta_d$ and cosθ has been plotted as shown in Fig. 6.4(a, b and c) from which the average crystallite size can be calculated from it's slope for the initial and ball-milled Cu powder.

2. Williamson-Hall method

The effect of crystallite size on the broadening of XRD peaks are only considers in the Scherrer formula, but using the Williamson-Hall method the intrinsic strain of the lattice can also be calculated. According to this method, total broadening of the peaks includes line broadening of XRD peaks due to the size and micro-strain of the crystals [264]. It can be written as:

$$\beta_{total} = \beta_{size} + \beta_{strain} \tag{6.4}$$

Now, the crystallite size and micro-strain is measured using the uniform deformation model (UDM) approach, it considers uniform strain throughout the crystallographic direction. The intrinsic strain induced peak broadening can be expressed as ,

$$\beta_{strain} = 4\epsilon tan\theta \tag{6.5}$$

TH-3234_176103111

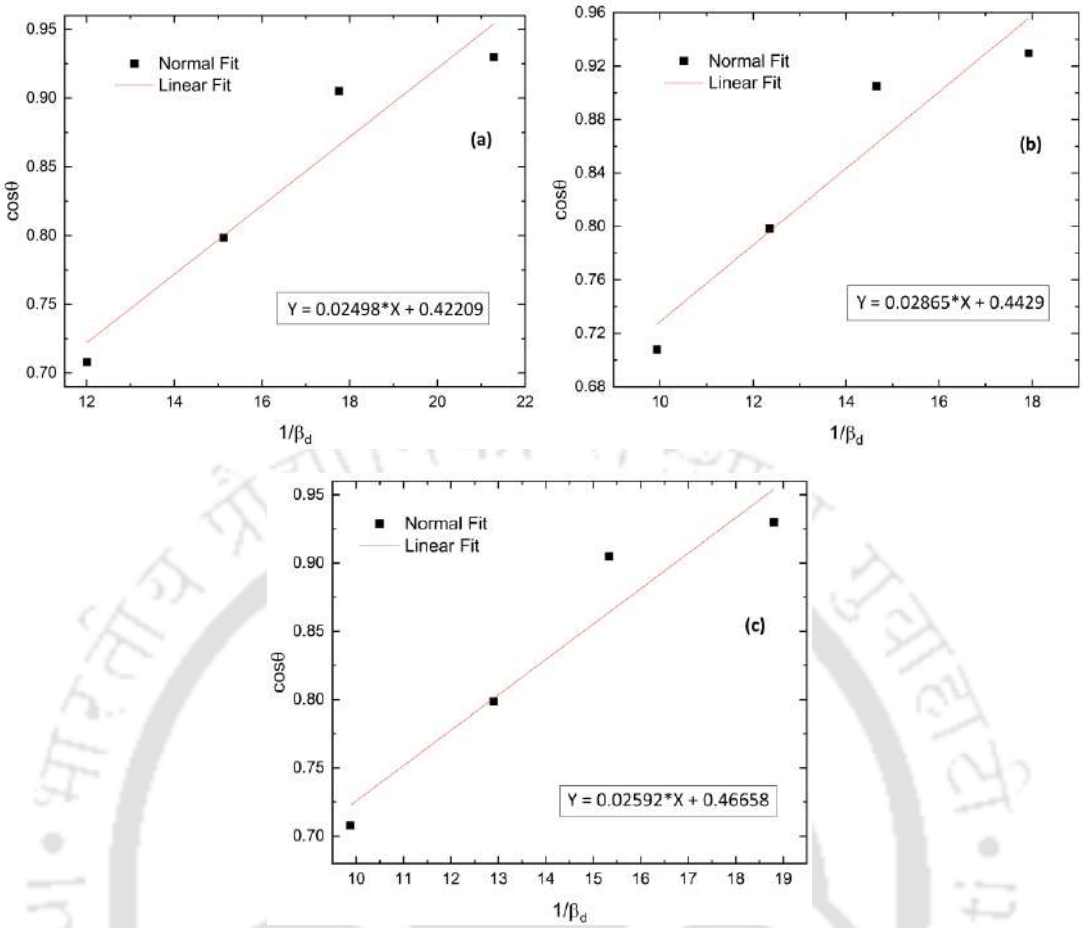

Fig. 6.4: Scherrer plots for: (a) Initial Cu powder (b) Ball-milled Cu powder and (c) Ball-milled Cu/SiC (90/10)

So, the total broadening due to strain and size in a particular peak having the *hkl* value is expressed as:

$$\beta_{hkl} = \beta_{size} + \beta_{strain} \tag{6.6}$$

Where, β_{hkl} is the full width at half of the maximum for different diffraction planes.

$$\beta_{hkl} = K\lambda/Dcos\theta + 4\epsilon tan\theta \tag{6.7}$$

After the re-arranging of the equation we can get,

$$\beta_{hkl}cos\theta = K\lambda/D + 4\epsilon sin\theta \tag{6.8}$$

TH-3234_176103111

This is an equation of straight line and also known as the uniform deformation model equation. A graph has been plotted for this equation keeping 4sinθ as X-axis and β_{hkl}cosθ as Y-axis corresponding to each XRD peaks of the initial and ball-milled Cu powder in Fig. 6.5(a, b and c). This straight line has been plotted by the linear Gauss fitting of the scattered data points, having a correlation coefficient value of $R^2 = 0.924$, 0.916 & 0.87416 for initial, ball-milled Cu powder and Cu/SiC (90/10) mixed powder respectively. Whereas the slope of this straight line gives the value of the intrinsic strain and the average crystallite size (D) is obtained from the intercept [265]. The average crystallite size obtained from this approach is 26.736 nm, 31.183 nm & 31.608 nm and the intrinsic strain is obtained as 1.65×10^{-3}, 1.29×10^{-3} & 1.91×10^{-3} for the initial, ball-milled Cu and Cu/SiC (90/10) mixed powder respectively. As the slope of the plotted line is positive and the obtained crystallite size is also increasing, it indicates the lattice expansion that produces an intrinsic strain due to the milling [266].

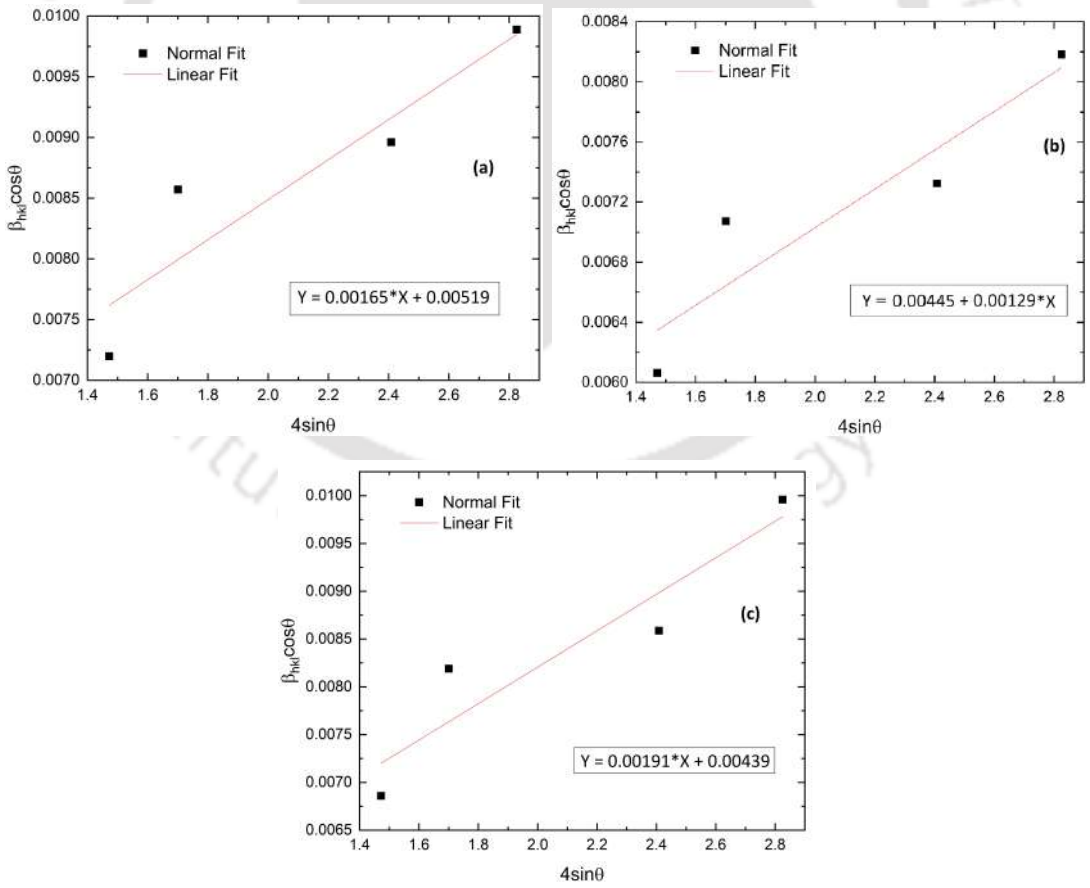

Fig. 6.5: Williamson-Hall UDM plots for: (a) Initial Cu powder (b) Ball-milled Cu powder and (c) Ball-milled Cu/SiC (90/10)

6.3.1.2 TEM results

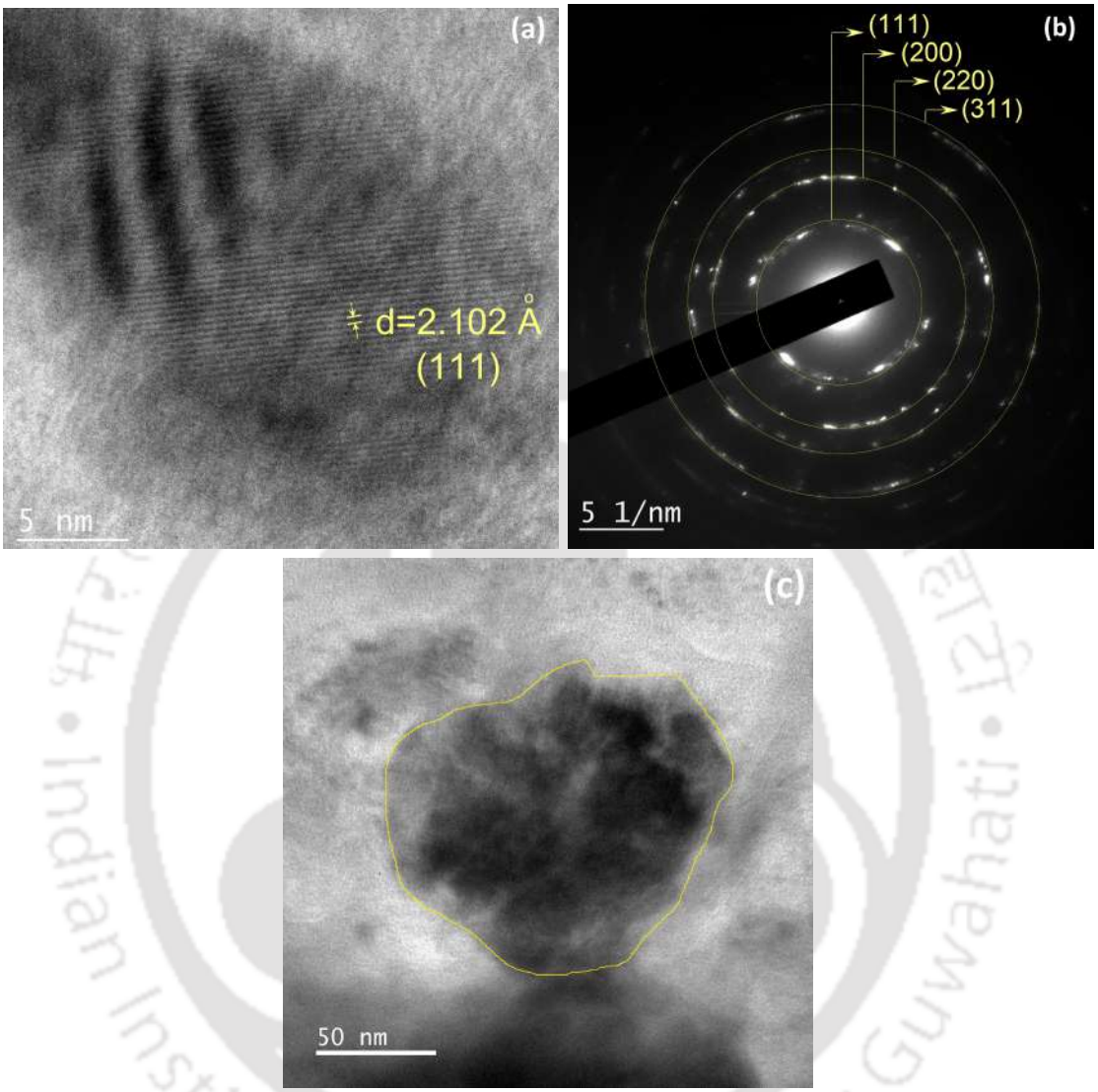

Fig. 6.6: TEM images showing: (a) Inter-planar spacing for (111) plane (b) SAED pattern and (c) Ball-milled Cu grain morphology

The crystal structure analysis of the ball-milled Cu powder has been studied by TEM [Make: JEOL, Model :2100F]. For this, the TEM sample has been prepared through the drop-casting of prolonged sonicated ball-milled powder over the Cu grid [Make: Sigma Aldrich] having 300 mesh. The high-resolution transmission electron microscope (HR-TEM) image of the ball-milled Cu powder is shown in Fig. 6.6. From the HR-TEM fringes analysis, the inter-planar spacing for the (111) reflection plane is obtained as 2.102Å, as shown in Fig. 6.6(a). The selected area electron diffraction (SAED) has been obtained in Fig. 6.6(b) for the ball-milled Cu powder. The SAED

pattern shows the bright dots connected with each other in a ring-shaped pattern that reveals the polycrystallinity of the powder. The SAED patterns also show it's consistency with the XRD patterns for different reflections of planes. This investigation of the SAED patterns has been carried out using the ImageJ software, which revealed the d_{hkl} spacing of the ball-milled powder as 2.128Å, 1.824Å, 1.305Å and 1.151Å for the (111), (200), (220) and (311) planes respectively. The obtained TEM image in the Fig. 6.6(c) shows a relatively low sphericity and angular-shaped grain. The sphericity of the powder grains is distorted due to the impact of powder particles during milling. The average crystallite size of this grain is obtained as 27.587 nm which is found near to the Williamson-Hall approach value.

6.3.1.3 FESEM results

The FESEM [make: Zeiss, model- Sigma 300] is conducted on Cu and SiC powder at it's initial state and for the ball-milled Cu powder. The obtained FESEM images are shown below in Fig. 6.7.

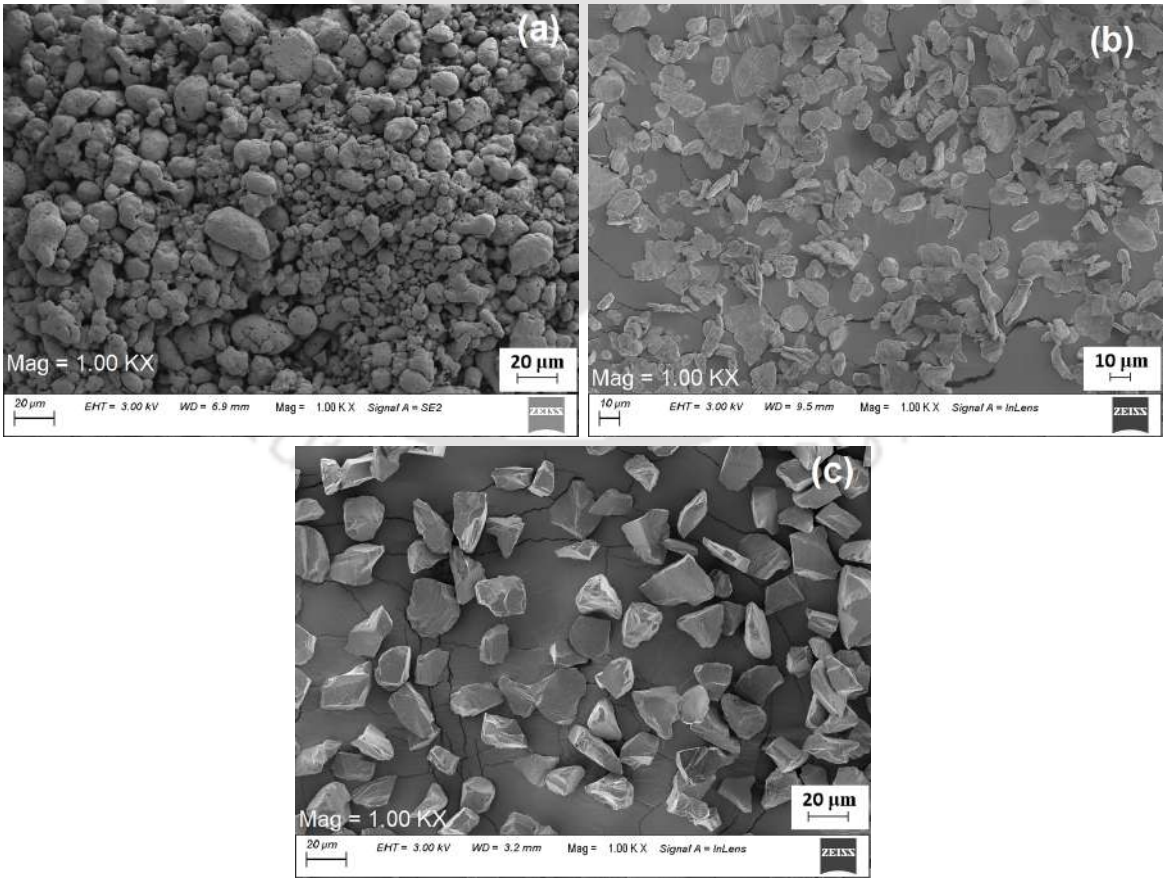

Fig. 6.7: FESEM images: (a) Initial Cu powder (b) Ball milled Cu powder and (c) Initial SiC powder

From the obtained FESEM results, it can be seen that the initial Cu powder's particles are a mixture of large and small fine-size particles, most of which have spherical shapes as shown in Fig. 6.7(a). But, after the ball milling of relatively big size Cu particles, a reduction, changing of shapes (mostly flake shaped) can be observed in Fig. 6.7(a and b). While some edges of such flakes tend to be convoluted, and few small sphere-shaped particles are stuck within the flakes [267]. The initial SiC powder shows most of the rounded and angular shape particles in Fig. 6.7(c).

6.3.2 Characterization of Cu/SiC Specimens

After the sintering, the microstructure analysis on the sintered specimens have been conducted using the optical microscope, FESEM, and EDS. For this analysis, the sintered three-layer Cu/SiC specimen is first polished using the lower to a high grade of emery paper on a polishing machine. The polished three-layer Cu/SiC specimen is shown in Fig. 6.2(f).

6.3.2.1 Optical microscope, FESEM and EDS results

The optical microscope [make: Zeiss] image for each layer of the sintered FGM specimen is shown in Fig. 6.8. From the obtained results for the 100/0 layer, it is observed that the Cu grains are well joined together along the grain boundaries. These well-joined Cu grains are due to providing sufficient compact pressure and sintering temperature during the fabrication process. Moreover, the specimens are made by the powder metallurgy process due to which some large and small size porosities are also visible in Fig. 6.8(a). For the 90/10 layer, a few SiC particle concentrations are clearly visible along with the Cu matrix which confirms the presence of a small SiC wt% within the layer in Fig. 6.8(b). For the 80/20 layer, a large no.of SiC clusters are visible and the presence of small porosities near the edges of SiC particles is observed. Moreover, this increase of SiC content in the Cu matrix also helps in to fill the large size porosities, which can be observed in Fig. 6.8(c). These images also justify an increase of SiC concentration along the length of the specimen.

The FESEM results for each layer of the sintered specimen is shown in Fig. 6.9. The result for the 100/0 layer in Fig. 6.9(a) clearly shows an absence of SiC content. However, due to powder compacted specimen, some porosities are also observed in white patches. The result for the 90/10 layer shows the presence of a high concentration of SiC contents than the 100/0 layer in Fig. 6.9(b).

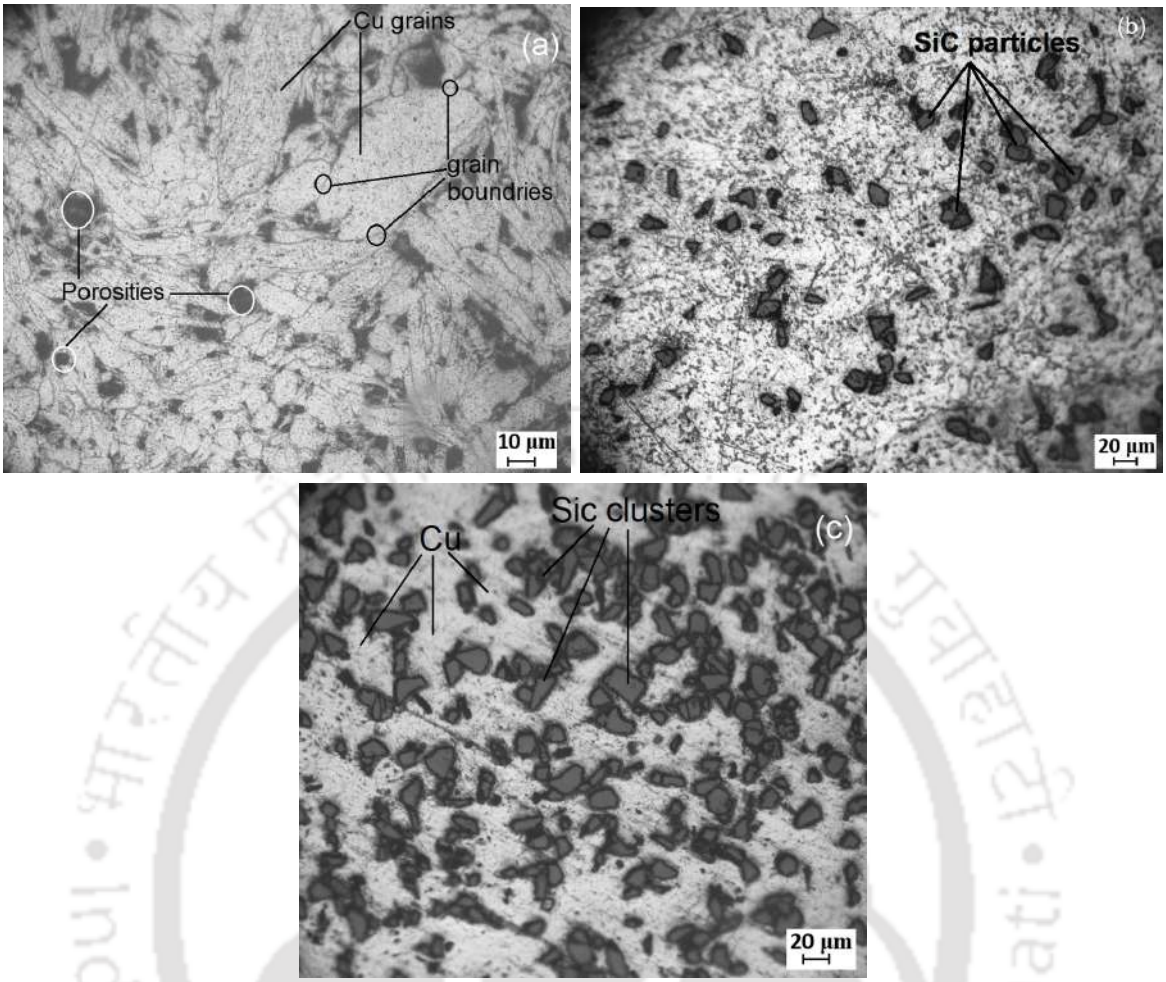

Fig. 6.8: Showing optical microscope images of the specimen (a) 100/0 layer (b) 90/10 layer (c) 80/20 layer

While a huge number of SiC clusters can be clearly seen for the 80/20 layer in Fig. 6.9(c). It justifies the presence of higher SiC concentration in the 80/20 layer than the 90/10 layer of the sintered FGM specimen. The FESEM images also justify a well-compact FGM sample with a gradual variation of SiC content along the length.

The EDS analysis of 80/20 layer of Cu/SiC specimen is conducted to analyze the presence and distribution of current elements in wt%, as shown in Fig. 6.10. Here, both point and area spectrum is taken at different locations on the specimen surface. The dark grey regions show the SiC particles and grey region shows Cu particles. The spectrum analysis of the elements are shown in the tabular form. The spectrum 1 is taken on the Cu surface, spectrum 2 on the SiC particle, spectrum 3 on the area consisting of Cu and SiC content and spectrum 4 on the Cu and SiC particle interface.

TH-3234_176103111

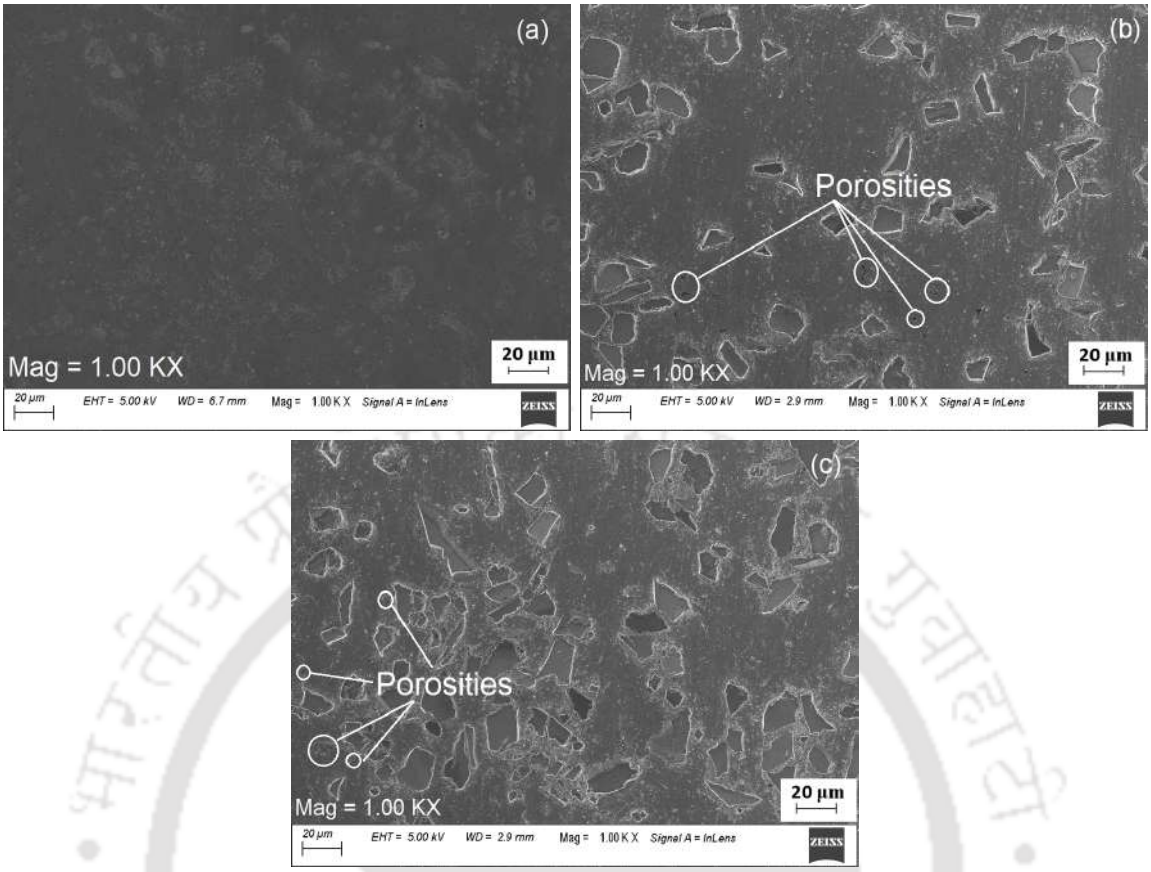

Fig. 6.9: Showing FESEM results of 3-layered sintered Cu/SiC specimen (a) 100/0 layer (b) 90/10 layer (c) 80/20 layer

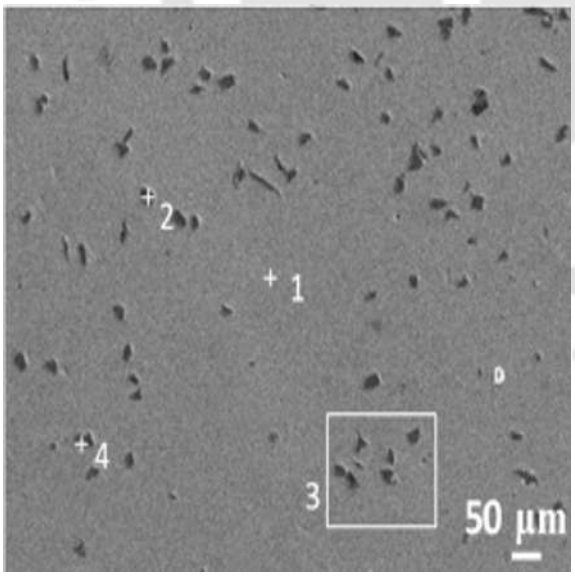

Elements (wt%)	Spectrums			
	1	2	3	4
C	-	32.6	25.1	7.9
O	0.1	0.3	3.7	1.7
Si	-	66.9	64.5	5.5
Cu	99.9	0.2	6.8	84.9

Fig. 6.10: Showing EDS results of 80/20 layer for different spectrums

Spectrum 1 shows a higher wt% of Cu, whereas spectrum 2 possesses higher Silicon (Si) content than other elements. Moreover, for spectrum 2, a relatively high wt% of carbon (C) (almost half of

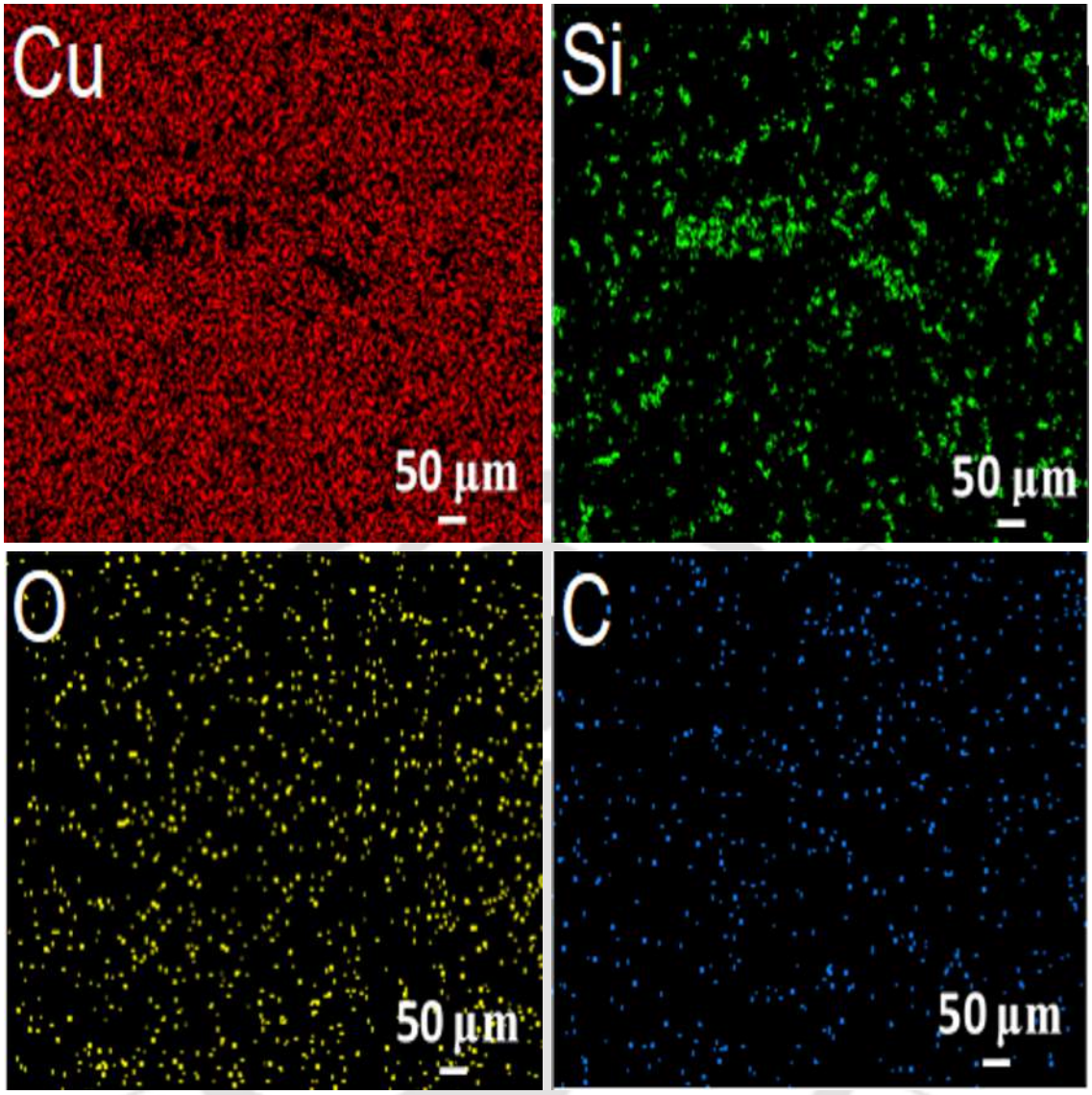

Fig. 6.11: Showing mapped EDS results for spectrum 3

Si content) and a small wt% of oxygen (O) are also observed. This avalaibility of oxygen probably results from the free surfaces of SiC particles. Spectrum 3 shows the presence of higher wt% of Si content in the selected area. It is due to the presence of higher SiC concentration than Cu in spectrum 3. Spectrum 4 shows a higher wt% of the Cu at the Cu and SiC particle interface. In addition in Fig. 6.11, a mapped EDS analysis for spectrum 3 of the 80/20 specimen is shown. The mapped results are shown with different colors for a better clarity of elemental distribution within the selected area. Here, the copper element is shown in red, silicon in green, oxygen in yellow and carbon in blue. The mapped result for Cu shows some black regions, which justifies the presence of SiC components within the matrix.

TH-3234_176103111

6.3.3 Hardness Test

The Vicker's micro-hardness test [make: Omnitech India, model- MVH-II] is conducted for each layer of the polished specimen by applying a load of 200gm with a dwell time of 20 seconds. The micro-hardness measurements for 90/10 and 80/20 layers are performed by providing homogeneous indentation on the Cu and SiC particles. The test results are obtained after taking an average of 16 measurements on each layer. For the 100/0 layer, the average micro-hardness value (HV) is 124 whereas for 90/10 and 80/20 layer it increased to 185 and 259, respectively. The increment in the hardness value increases linearly with the increase of SiC content within the Cu matrix. The fitted linear relationship of the hardness value for the sintered Cu/SiC sample is shown in Fig. 6.12. It can be estimated that Young's modulus will also decrease linearly with the increment of SiC content. This can be verified with further investigations.

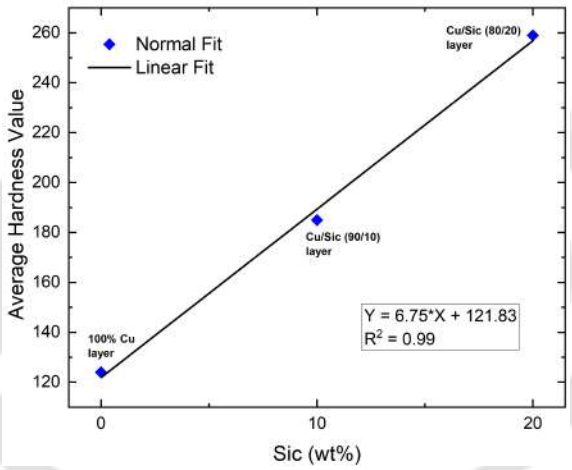

Fig. 6.12: SiC content Vs Hardness value plot of the sintered sample

6.4 SUMMARY

Generally, the FGMs made of metal and ceramics are fabricated with varying material concentrations along the thickness direction. Such FGMs are comparatively easier to manufacture by the powder metallurgy method due to of lesser compact thickness, whether the uni-axial compaction is suitable for relatively shorter axially graded specimens with a better compacted green sample due to its limited length-to-width ratio. This work can be summarized as a three-layered Cu/SiC-based axially graded FGM beam-type specimen successfully fabricated with the powder metallurgy

TH-3234_176103111

method. The powders are ball-milled, mixed, stacked layer-wise inside the die, and compacted uni-axially and iso-statically at CIP for better bonding of powders. Powder XRD analysis of the initial and ball-milled powder has been carried out. The significant effect of the ball-milling on the crystallite size and lattice strain has been studied using Sherrer's method and the Williamson-Hall approach. An increment in crystallite size confirms the broadening of XRD peaks due to the ball-milling. From TEM analysis, the reflection of planes is verified through SAED patterns and the inter-planar spacing for the (111) plane is also measured. The obtained average crystallite size obtained through the TEM is in excellent agreement with the size obtained from the Williamson-Hall approach. The FESEM analysis identifies particle sizes and morphology of the powders before and after the ball-milling. A well-compacted metal-ceramic bonding and gradation along the length are clearly observed in the study. The EDS analysis successfully justifies the presence of elements at different points and locations for the 80/20 layer. Vicker's hardness test depicts a linear increase in micro-hardness value with SiC wt% along the length. This work will help to fabricate axially graded gas turbine blades, gears, bearings, and orthopedic implants for futuristic applications.

TH-3234_176103111

Chapter 7

Evaluation of Elastic Property for Axially Graded Powder Metallurgy Specimen by RFDA

7.1 INTRODUCTION

The processing for the fabrication of axially graded beam-shaped specimens by powder metallurgy technique has been discussed thoroughly in the previous chapter. For further material design and analysis, obtaining the fabricated specimen's material properties is essential. Therefore, in this chapter, a rigorous discussion has been presented on the evaluation of the material property of the sintered Cu/SiC-based samples through a non-destructive impulse excitation technique. A dynamic modulus system, i.e., RFDA-Basic instrument from Integrated Material Control Engineering (IMCE), has been used to estimate the effective property. For this experimentation, the cylindrical-shaped specimens of pure Cu, two-layered Cu/SiC [100/0 98/2], and three-layered Cu/SiC [100/0 98/2 96/4] are prepared. The synthesis of the specimens is briefly presented in Sec. 7.2. In Sec. 7.3, a detailed working of the RFDA instrument and experimentation procedures are discussed. The elastic properties of specimens are obtained and further used for the numerical simulation on ABAQUS to validate their corresponding resonant frequencies. A detailed discussion on numerical 3-D FE results analysis is presented in Sec. 7.4. Further, a conclusive summary of the work has been presented in Sec. 7.5.

TH-3234_176103111

7.2 SYNTHESIS OF SPECIMENS

Using the similar processing technique as discussed in Chapter 6, a cylindrical-shaped Cu/SiC-based axially graded specimens have been fabricated. Three types of specimens say S1, S2 and S3 with a varying SiC wt% are considered in this experimentation. Here S1, S2 and S3 symbolically represent the pure copper [100/0], two-layered Cu/SiC [100/0 98/2] and 3-layered Cu/SiC [100/0 98/2 96/4] FGM specimens, as shown in Fig. 7.2. During the powder preparation pure Cu powder is mixed with different ratios of SiC powder, i.e., 2 % for S2, and 4 & 6 % for specimen S3. The mixed powders are further stacked layer-wise and sealed within the cylindrical shaped rubber mold for the compaction, as shown in Fig. 7.1. The compaction of the powder has been carried out on CIP at a set pressure of 250 MPa. The specimens are ejected and sintered within a muffle furnance at a temperature of 900°C for 120 minutes. The specimens are taken out from the furnance after its cooling, as shown in Fig. 7.3. Further, the weight and physical dimensions are measured for all the sintered specimens as shown in Fig. 7.2. The values are approximated upto two digits for the ease in experimentation, as shown in the Table 7.1.

Fig. 7.1: (a) Cylindrical rubber mold and (b) Sintered Specimens

7.3 WORKING OF RFDA AND EXPERIMENTATION

The schematic representation of the RFDA-Basic setup is shown in Fig. 7.3. This RFDA system includes (a) string-based specimen support with movable nylon strings to accommodate a range

TH-3234_176103111

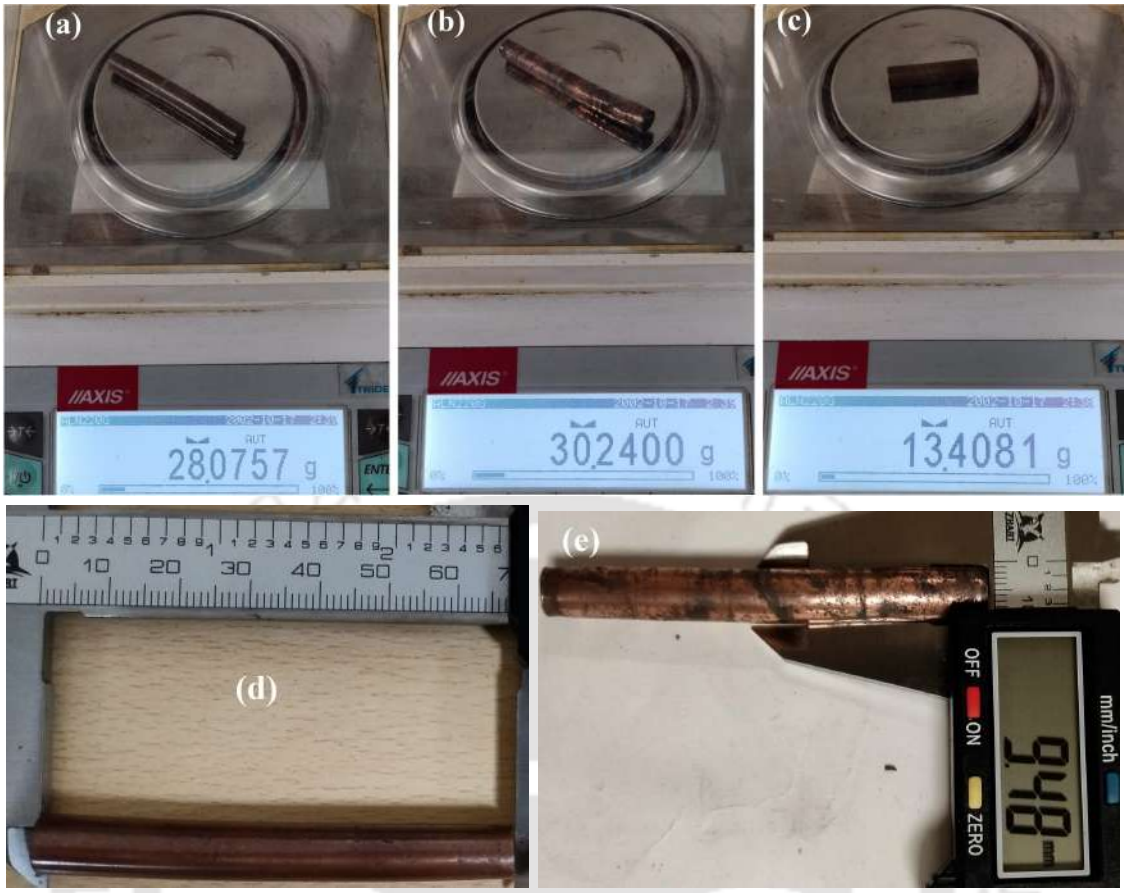

Fig. 7.2: Showing weight of (a) Specimen S1 (b) Specimen S2 (c) Specimen S3 (d) Specimen S1 length and (e) Specimen S2 diameter

Table 7.1: Specimen dimensions

Specimen	Length (mm)	Diameter (mm)	Weight (gm)	Density (Kg/m^3)
S1	68	8.60	28.08	7108.88
S2	72.50	9.48	30.24	5909.32
S3	40.56	7.90	13.41	6745.07

of specimen sizes, (b) a flexible hammer (steel ball with plastic belt), (c) a USB microphone to measure sample vibration, and (d) a computer with RFDA software to record, analyze and save the results. RFDA records acoustic signals in the time domain, then the software transforms the signal to the frequency domain and determines a first set of approximatively f_r by fast Fourier transformation (FFT) [268]. First, the file information must be provided to the software to initiate the experimentation. In this step, the specimen's details, i.e., specimen geometry, length, diameter,

and weight, are provided to the RFDA software. The specimen dimension must follow the ASTM E1876-15 standard, i.e., length/diameter ≥ 5. Based on the provided details, the software suggests the node length, usually 0.224 of the total length and node distance. The nylon strings need to slide and adjust to the recommended node length. Thereafter, the specimen is kept over nylon strings and the microphone is placed near the node position to capture the tapped acoustic signal, as shown in Fig. 7.4. The specimen is manually tapped at its center with a small flexible hammer and the recorded signal is displayed on the computer screen, as shown in Fig. 7.5 for S1. Similarly, the signals are recorded for each specimen. The experiments are repeated multiple times for the reliability of the results. Here, five measurements have been recorded for all the specimens. The measured frequency (for two modes) and Young's modulus for S1, S2, and S3 are shown in Table 7.2. The value of Poisson's ratio is assumed as 0.275 for all the experimental trials.

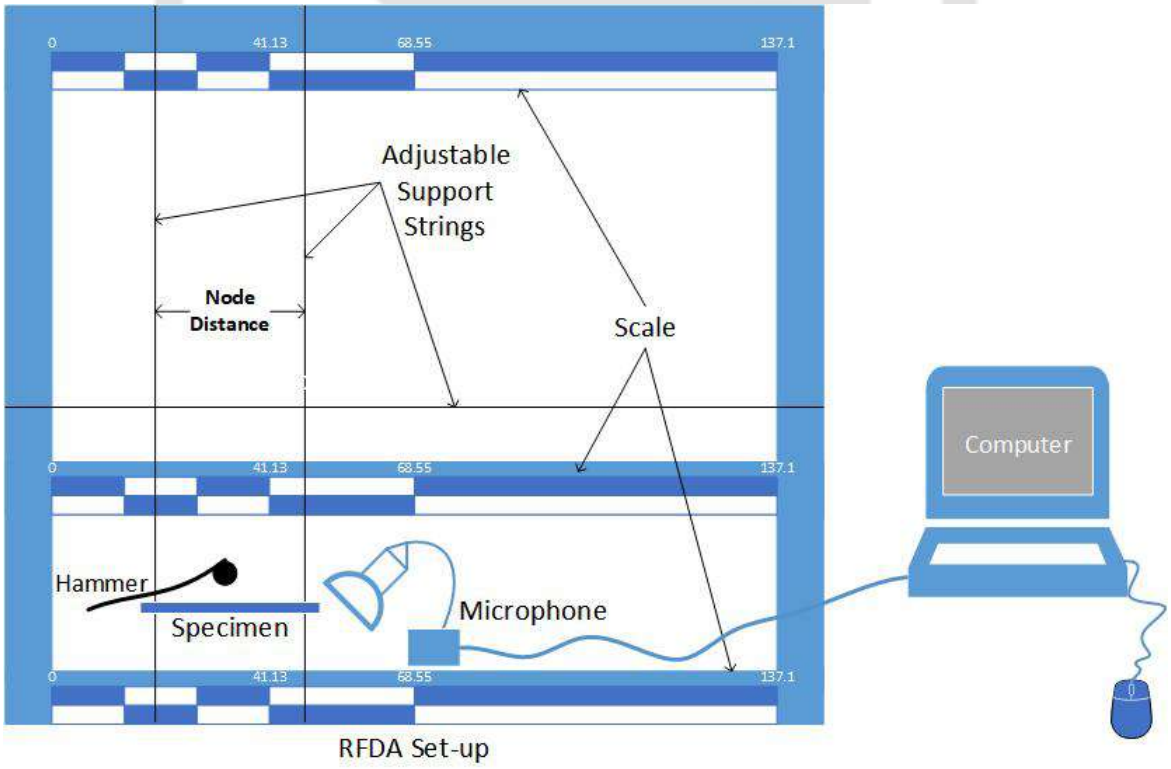

Fig. 7.3: Showing schematic diagram of RFDA working set-up

TH-3234_176103111

Fig. 7.4: RFDA in working

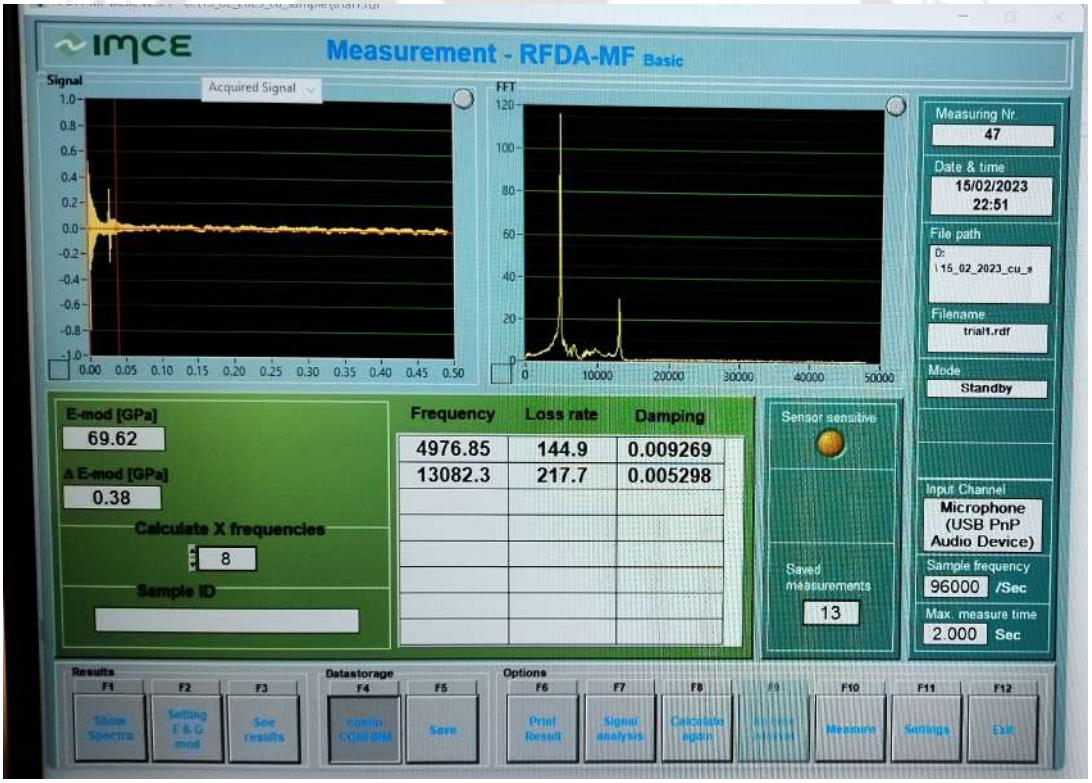

Fig. 7.5: Recorded signal for specimen S1

7.4 NUMERICAL RESULTS AND DISCUSSION

Further, the numerical FE analysis for all specimens has been conducted to validate the natural frequency for the corresponding Young's modulus of specimens. For this FE analysis, a 3-D model

Table 7.2: Experimental results for specimens S1, S2 and S3

Specimen		Trial No. 1	2	3	4	5	Average value
S1	Mode 1 (Hz)	4974.05	4976.85	4976.26	5002.65	4992.21	4984.40
	Mode 2 (Hz)	13094.40	13082.30	13086.10	13148.40	13129.40	13108.12
	Young's modulus (in GPa)	69.54	69.62	69.60	70.34	70.05	69.83
S2	Mode 1 (Hz)	3225.12	3172.22	3121.34	2987.10	3192.41	3139.64
	Mode 2 (Hz)	8498.20	8385.37	8352.60	8272.80	8332.69	8368.33
	Young's modulus (in GPa)	25.94	23.86	25.32	26.12	24.92	25.23
S3	Mode 1 (Hz)	5484.37	5877.53	5537.17	5129.13	5714.29	5548.50
	Mode 2 (Hz)	14280.80	11751.10	14330.20	14342.80	13714.29	13675.88
	Young's modulus (in GPa)	13.27	15.24	13.52	11.60	14.40	13.61

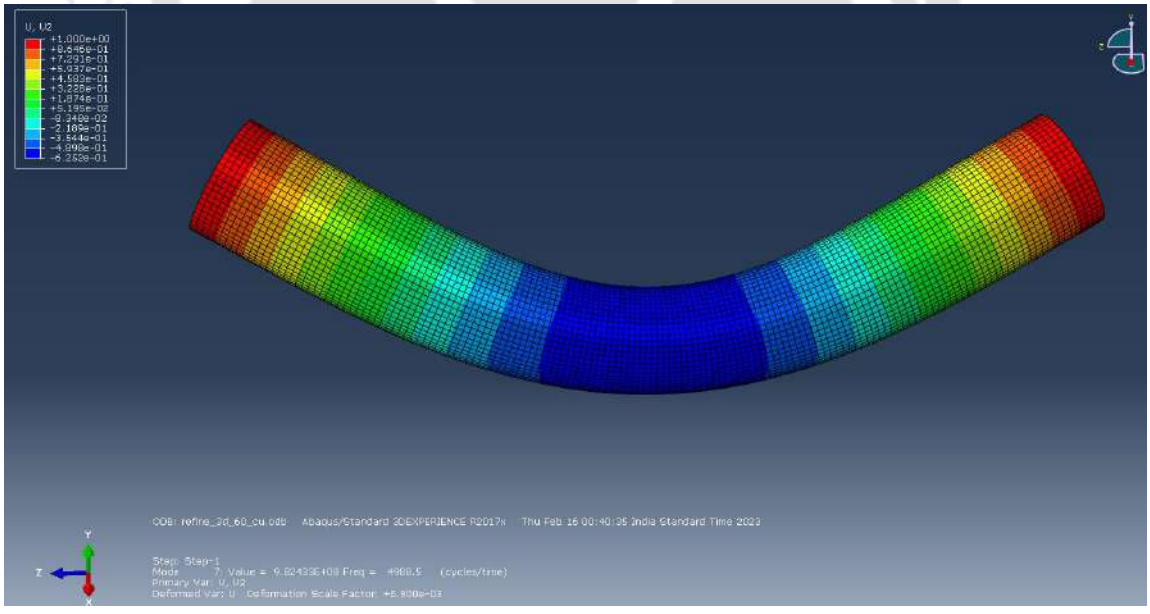

Fig. 7.6: Showing FE flexural mode shape of S1 for Mode 1

of S1, S2, and S3 has been modeled separately in ABAQUS software. The linear perturbation step is chosen to obtain the natural frequency of the specimen under the free-free (F-F) boundary

TH-3234_176103111

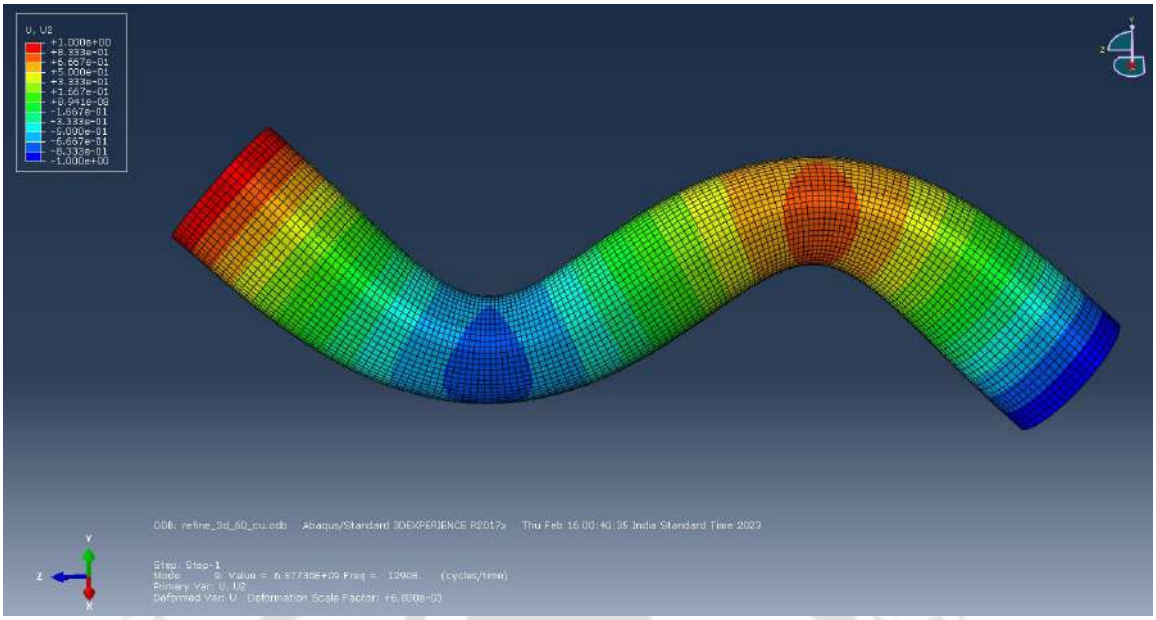

Fig. 7.7: Showing FE flexural mode shape of S1 for Mode 2

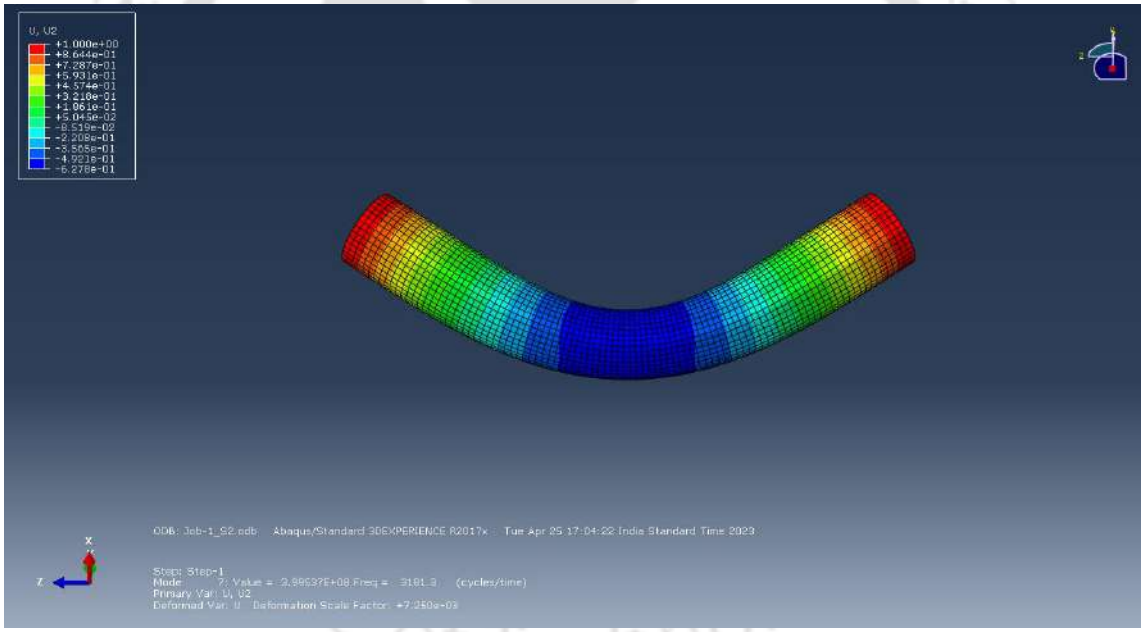

Fig. 7.8: Showing FE flexural mode shape of S2 for Mode 1

condition. The periphery of the model has been divided into 40 elements and meshed with the 3D stress 20-node quadratic brick, reduced integration C3D20R element. The obtained natural frequency for different modes is presented in Table 7.3, and the corresponding difference (in %) is calculated. The FE results under bending modes are shown for S1 in Figs 7.6 & 7.7, for S2 in Fig. 7.8 & 7.9 and for S3 in Fig. 7.10 & Fig. 7.11. It is observed that the obtained natural frequencies through the experiment and FE analysis are in good agreement with each other for all

TH-3234_176103111

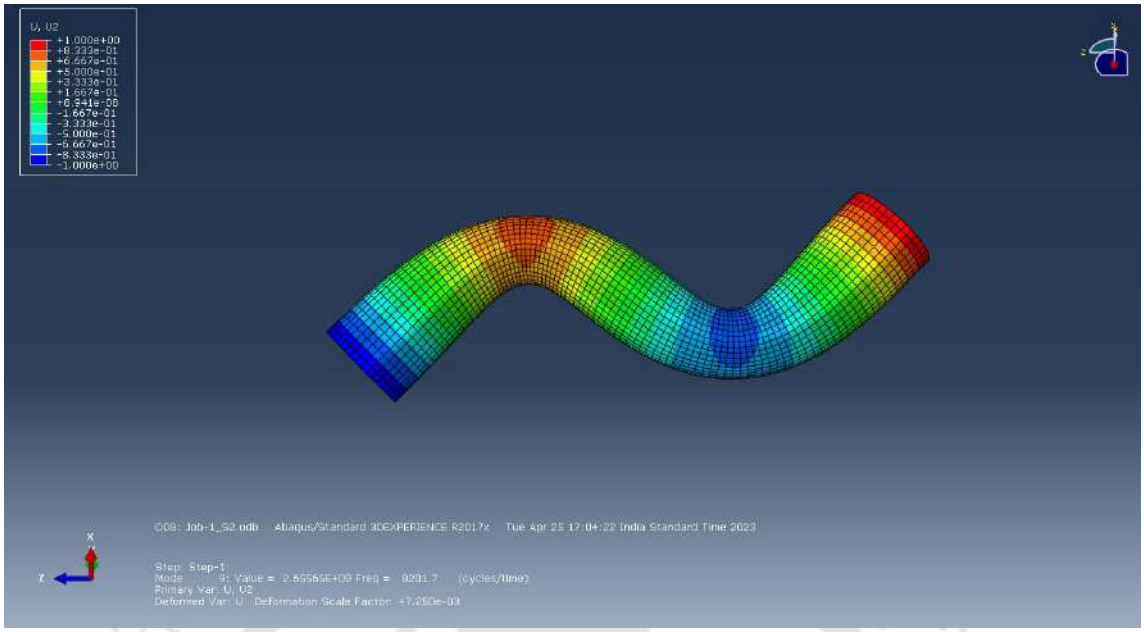

Fig. 7.9: Showing FE flexural mode shape of S2 for Mode 2

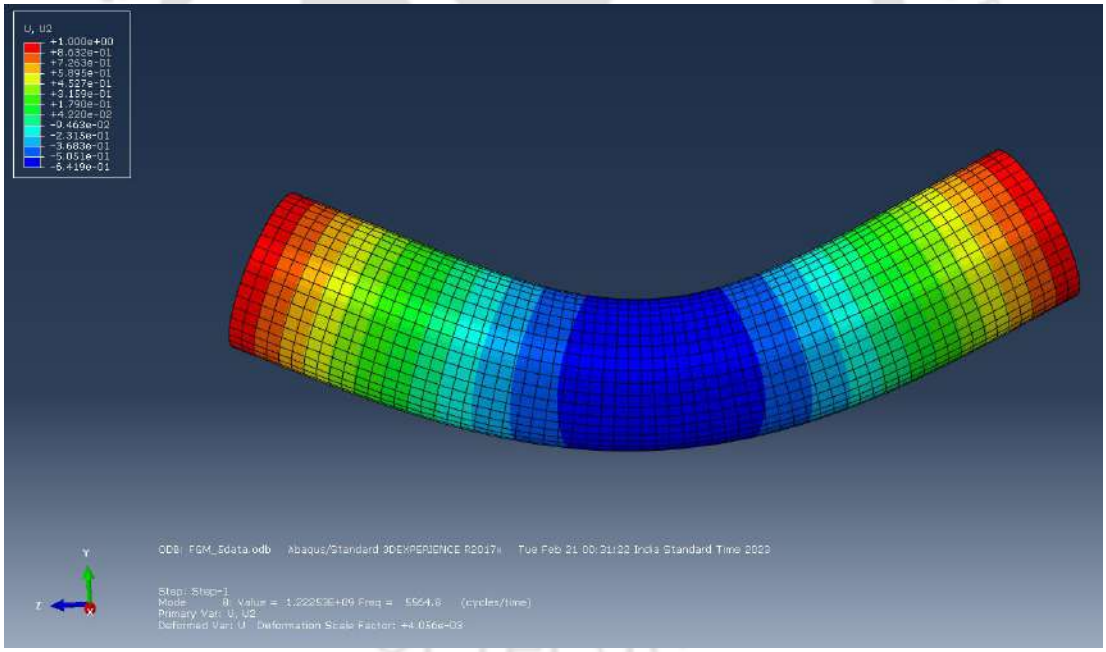

Fig. 7.10: Showing FE flexural mode shape of S3 for Mode 1

specimens. The mode 2 frequency for both specimens is less than the average experimental value.

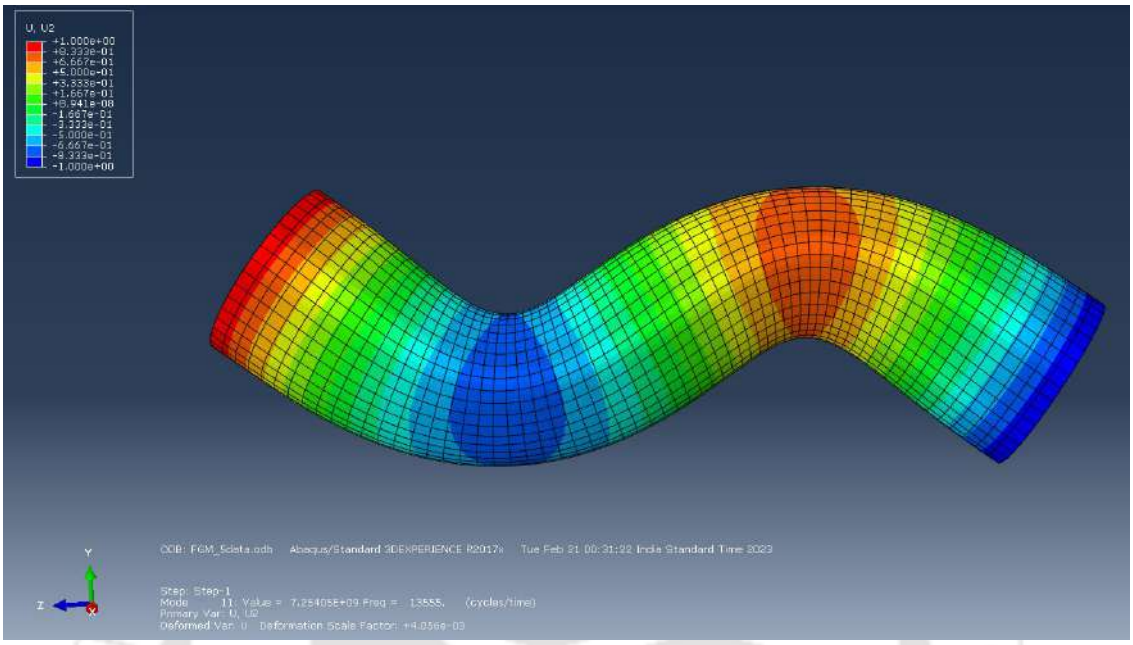

Fig. 7.11: Showing FE flexural mode shape of S3 for Mode 2

Table 7.3: % difference in natural frequencies

Specimen	Mode No.	Exp. f_n (Hz)	FEA f_n (Hz)	% Difference (FEA-Exp.)/Exp.
S1	1	4984.40	4988.50	0.0822
	2	13108.12	12908	-1.527
S2	1	3139.64	3181.30	1.327
	2	8368.33	8201.70	-1.991
S3	1	5548.50	5564.80	0.294
	2	13675.88	13555	-0.884

TH-3234_176103111

7.5 SUMMARY

The elastic property of the powder metallurgy based specimens are obtained using the RFDA technique. The natural frequencies for first two bending modes have been obtained for pure copper, two layered Cu/SiC [100/0 98/2] and three layered Cu/SiC [100/0 98/2 96/4] specimens. For the repeatability, at least five number of trials have been conducted on each specimen. Experimentally obtained elastic properties of specimens are used for FE modelling. The 3-D FE results under free-free case is obtained and validated with the experimental results. A good match between the experimental and FE results are observed for all specimens.

TH-3234_176103111

Chapter 8

Conclusions

For the first time, the elasticity-based accurate analytical solutions are presented for static bending of in-plane functionally graded composite and piezoelectric structures with stepped or piece-wise gradation along the length. The Reissner's type mixed variational principle is applied to derive the weak form of coupled governing equations in which stresses and displacements variables act as primary variables. Interface continuity and boundary conditions are satisfied in exact pointwise manners, which ensures the same order of accuracy for all the variables (stresses, displacements, and electric variables). Further, multi-term EKM, a recently developed powerful iterative technique is employed to reduce the governing equation into sets of ordinary differential equations (ODEs). These sets of ODEs are solved analytically, which is a key in the accurate prediction of free edge stresses. A detailed numerical study established excellent agreement of the present iterative series solution with existing literature results and FE results. Further, the influence of the segment material properties and segment numbers on the static response of structures is studied extensively for different support conditions and thickness ratios. The present solution is valid for thick as well as thin FGM structures (beams and panels). Benchmark results are presented for segments with both isotropic and composite materials for various configurations and different combinations of boundary conditions. The present analytical solution for step-wise functionally graded structures also serves as a benchmark in assessing the accuracy of the numerical models and 1D/2D theories. For the first time, an attempt towards the fabrication of an axially graded FGM beam using the powder metallurgy method is initiated. A three-layered Cu/SiC beam-type specimen has been fabricated. The procedures implemented for the fabrication and characterization are explained

TH-3234_176103111

in detail. A detailed analysis of the initial powder, ball-milling effect, and the FGM sample's microstructure is presented for a better understanding. Further, the effective material properties and natural frequency of the multi-layered FGM samples are successfully evaluated experimently, using the non-destructive RFDA technique. The 3-D FE model of the samples are modeled and validated with the experimental results. Further, the following novel and significant conclusions are drawn based on the present study.

8.1 CONCLUSIONS FROM THE PRESENT WORK

The major outcomes of this research work is summarized here and the major conclusions are encapsulated below.

1. A two-dimensional elasticity solution has been presented for bending analysis of segmented beams using the multi-term EKM. The influence of segment length and material properties on the static bending behaviour is studied for different boundary conditions. The detailed analytical and numerical study reveals that:

   (i) Using the mixed principle of virtual work, the governing equations are presented in weak form. The multi-term extended Kantorovich method is further implemented to solve sets of ODEs and obtain the solutions for five field variables.

   (ii) The present technique is found to be more versatile and can handle any material combination along the length. It can also easily manage any type of variation in the material property, i.e., power law, exponential or arbitrary.

   (iii) The EKM solution converges more rapidly (in just one or two terms) and predicts accurate results for all the beam configurations under static bending.

   (iv) For simply-supported case, single term (n=1, *iter*.1) gives accurate prediction for deflections and stresses. Whereas a two-term solution (n=2, *iter*.2) is required for the other boundary conditions.

   (v) A very significant effect on the shear stress near the segment junction of Al/Gr-Ep and Steel/Gr-Ep can be seen. However, a deeper hook shape is observed for the Steel/Gr-Ep

than the Al/Gr-Ep beam. The effect of boundary conditions and aspect ratio (S) also play a significant role in the stresses, and displacement is clearly observed.

(vi) For all the lay-ups, the numerical results are obtained from the ABAQUS software using plane stress elements, and it is found in good agreement with the EKM results except near the edges.

(vii) It is observed from the through-the-thickness results, slightly away from the boundary edges and segment interface, the FE and EKM results are in good agreement with each other.

(viii) From the 2-D FE contour plot, the stress variation in the Steel section is not following traditional variation, while in Gr-Ep section, it is more or less usual. Therefore, one-dimensional beam theories will not predict this behaviour. The convergence, accuracy, and efficacy of the EKM method are well presented and observed from the analysis.

(ix) Present results can be used as benchmarks to assess the one-dimensional beam theories. This development will lead to the development of multi-material step beam and plate problems.

2. The analytical 2-D solution based on elasticity for a multisegmented panel subjected to arbitrary boundary conditions is presented using the multi-term EKM. The influence of the segment length and ply angles is studied under different boundary conditions. These are some novel and significant contributions of the present work:

(i) The Reissner's-type mixed variational principle is used to obtain the weak form of governing equations. The governing equations are further solved for thickness and in-plane directions using the EKM. The solutions are obtained for eight field variables by solving a set of linear ordinary differential equations.

(ii) This method provides flexibility to take any number of segments and materials (isotropic or orthotropic) for the panel design. The continuity conditions are satisfied at the interface of each segment.

TH-3234_176103111

(iii) The longitudinal and through-the-thickness variations are presented for four types of panel configurations under different support conditions. The EKM results with two terms (n=2) are able to predict the results accurately.

(iv) An effect of change in ply-angle on the stresses has been studied for Al/Gr-Ep panel under various support conditions. An increase in ply-angle does not affect much for the SS and CF cases much, whereas a significant shift of stresses can be observed for the CC case.

(v) For the numerical results of the angle-ply panel, a 3-D model of the panel configurations with generalized plane strain condition has been modeled in ABAQUS using the C3D20R element. The 3-D FE and EKM results are found in excellent agreement except at the edges and segment interface. This disagreement in FE results can be seen from the through-thickness variation of the stress.

(vi) For the CF case, the longitudinal variation of shear stress for the heavier material (Steel/Gr-Ep) shows a deeper hook formation near the junction than the lighter material (Al/Gr-Ep).

(vii) The effect of change in panel thickness has been presented for an equally segmented panel. The results do not show any significant difference for stress variables under various support cases.

(viii) The multi-term EKM results for various ply-angles of Gr-Ep are found to be in good agreement with the FE results.

(ix) The current development can be useful for researchers to study the behaviour of the piece-wise homogeneous panel-type structures under in-plane loads. The presented results can be used as the benchmark for the development of plate problems under different loading and support conditions.

3. Two-dimensional analytical solutions have been developed using the multi-term extended Kantorovich method for piezoelectric panels having multiple segments along the x-axis. The

TH-3234_176103111

segment of soft & hard piezoelectric material are joined together under different support conditions and the study led to following conclusions:

(i) The developed method is more flexible and reliable that can care of any piezoelectric material. This approach can imitate the axially grading behaviour of piezoelectric material and can accurately predict the normal and transverse stresses at the interfaces.

(ii) From the transformed 3-D piezoelectricity constitutive equations the expression of mechanical strain and electric components are simplified. The extended Reissner type mixed variational principle is further implemented to obtain the governing equations for piezoelectric case.

(iii) A perfect bonding of segments is assumed to satisfy the mechanical and electrical continuity conditions at the interface. The panel are subjected to closed circuit condtions on the side and bottom face of the panel while an uniform pressure is applied on the top face.

(iv) The multi-term EKM solutions for eleven field variables are solved in both transverse and longitudinal directions. The accuracy and efficacy of the present method is confirmed by comparing the present result with the existent solutions in literature or with the finite element.

(v) The EKM results with two and three terms are found in good agreement with the numerical results for the single and segmented panels respectively. Under the simply-support case, two segmented piezoelectric panel behaves uniqely and electric displacement follows a saw-tooth pattern.

(vi) This development can be extended to develop the multi-material piezoelectric beam and plate problems under various mechanical and electromechanical loading conditions. This work can also be used as a benchmark for solving an axially graded piezoelectric panel having a step gradient.

4. The metal-ceramic based functionally graded beam having a step-wise linear gradation along

the length is fabricated through the powder metallurgy route. The microstructure characteristics of the specimens have been analyzed. The major observations made during the fabrication and analysis are listed below:

(i) A three-layered Cu/SiC-based axially graded FGM beam-type specimen can be successfully fabricated with the powder metallurgy method.

(ii) The powders are milled, mixed, and stacked layer-wise inside the rectangular die to compact uni-axially, followed by CIP for better bonding of powders.

(iii) The powder XRD analysis of the initial and ball-milled powder has been carried out. The ball-milling effect on the crystallite size and lattice strain is studied using Sherrer's method and Williamson-Hall's approach. An increase in crystallite size has been observed, which confirms the peak broadening of peaks due to the ball-milling.

(iv) From TEM analysis, the reflection of planes has been verified through SAED patterns, and the inter-planar spacing for the (111) plane has been measured. The obtained average crystallite size by the TEM is found to be in good agreement with the size obtained by the Williamson-Hall approach for the ball-milled Cu powder.

(v) From FESEM analysis, particle sizes and morphology of the powders are identified before and after the ball-milling. A change in the copper particles after the ball milling, i.e., from spherical to flake shape, is clearly observed.

(vi) The FESEM and optical microscopic analysis for each layer of the specimen are presented. From the observation, the presence of few porosities and the absence of SiC contents can be seen clearly for the 100/0 layer. However, a significant increase in SiC concentrations is also seen for 90/10 and 80/20 layers.

(vii) From FESEM analysis for 90/10 and 80/20 layers, it is observed that the porosities are reduced with the increment of reinforced particles. It may be due to the inclusion of reinforced precipitate within the matrix.

(viii) From the EDS analysis, the presence of various elements at different points and locations in the 80/20 layer of FGM is successfully justified.

TH-3234_176103111

(ix) The Vicker's micro-hardness test of the specimen depicts that the micro-hardness value is increasing linearly with the increase of SiC wt% concentration in the FGM layers.

(x) This type of work will be helpful to fabricate axially graded gas turbine blades, gears, bearings, and orthopedic implants for futuristic applications.

5. The effective elastic properties of the powder metallurgy-based Cu/SiC samples has been evaluated. The experimental results for the specimens are recorded and compared with the 3-D FE results. The FE results are presented for free-free cases and the study led to the following conclusions:

   (i) The overall elastic property obtained for pure copper, two-layered and three layered Cu/SiC specimens using the non-destructive RFDA technique.

   (ii) For the repeatability of the experiment minimum of five trials has been performed and the average is found satisfactory for the present analysis.

   (iii) For FE analysis, a 3-D model of the specimen is developed and natural frequency is obtained under plane stress conditions for the free-free case.

   (iv) The experimental frequencies for all the specimens closely match the 3-D FE results.

   (v) The experimental results for mode 1 are found to be lesser than the 3-D FE and vice-versa for mode-2 in all cases.

8.2 FUTURE SCOPE OF WORK

The future studies based on this work can be in following aspects:

1. The present 2-D elasticity solutions can be extended to obtain analytical solutions for the segmented plates under static loading.

2. To obtain 2D close-form solutions for axially segmented beams and panels under thermal or thermomechanical loadings.

3. To obtain analytical solutions for the segmented plates under thermomechanical loading.

TH-3234_176103111

4. Buckling and transient vibration analysis of axially segmented beams and panels can be developed using the EKM approach.

5. To develop 2D closed-form solutions for the segmented piezoelectric panels and plates under electromechanical loadings.

6. To develop 2D closed-form solutions for the segmented piezoelectric panels under thermo-electro-mechanical loadings.

7. The present fabrication technique and microstructure study can be extended for other types of material systems and for different numbers of graded segments.

8. A study for the variation of compaction pressure & sintering temperature on the specimen's microstructure and mechanical strength can be performed.

9. The mechanical and thermal testings, such as bending, compression, thermal shock analysis, etc., can be performed.

TH-3234_176103111

Bibliography

[1] Naito, J., and Suzuki, R., 2020. "Multi-material automotive bodies and dissimilar joining technology to realize multi-material". *Kobelco Technology Review*(8), pp. 32–37.

[2] Hanser, D. A., 2006. *Architecture of France*. Greenwood Publishing Group.

[3] Elssner, G., and Petzow, G., 1990. "Metal/ceramic joining". *ISIJ international,* **30**(12), pp. 1011–1032.

[4] Naebe, M., and Shirvanimoghaddam, K., 2016. "Functionally graded materials: A review of fabrication and properties". *Applied Materials Today,* **5**, pp. 223–245.

[5] Toudehdehghan, A., Lim, J., Foo, K. E., Ma'arof, M., and Mathews, J., 2017. "A brief review of functionally graded materials". In MATEC Web Conferences, Vol. 131, EDP Sciences.

[6] Bakar, W., Basri, S. N., Jamaludin, S., and Sajjad, A., 2018. "Functionally graded materials: An overview of dental applications". *World Journal of Dentistry,* **9**(2), pp. 137–144.

[7] Zhang, N., Khan, T., Guo, H., Shi, S., Zhong, W., and Zhang, W., 2019. "Functionally graded materials: An overview of stability, buckling, and free vibration analysis". *Advances in Materials Science and Engineering,* **2019**.

[8] Koizumi, M., 1997. "FGM activities in japan". *Composites Part B: Engineering,* **28**(1-2), pp. 1–4.

[9] Saleh, B., Jiang, J., Fathi, R., Al-hababi, T., Xu, Q., Wang, L., Song, D., and Ma, A., 2020. "30 years of functionally graded materials: An overview of manufacturing methods, applications and future challenges". *Composites Part B: Engineering,* **201**, p. 108376.

TH-3234_176103111

[10] Bohidar, S. K., Sharma, R., and Mishra, P. R., 2014. "Functionally graded materials: A critical review". *International Journal of Research,* **1**(4), pp. 289–301.

[11] Somiya, S., 2013. *Handbook of advanced ceramics: materials, applications, processing, and properties.* Academic press.

[12] Ajdari, A., Nayeb-Hashemi, H., and Vaziri, A., 2011. "Dynamic crushing and energy absorption of regular, irregular and functionally graded cellular structures". *International Journal of Solids and Structures,* **48**(3-4), pp. 506–516.

[13] Cui, L., Kiernan, S., and Gilchrist, M. D., 2009. "Designing the energy absorption capacity of functionally graded foam materials". *Materials Science and Engineering: A,* **507**(1-2), pp. 215–225.

[14] Xu, F., Zhang, X., and Zhang, H., 2018. "A review on functionally graded structures and materials for energy absorption". *Engineering Structures,* **171**, pp. 309–325.

[15] Chen, D., Kitipornchai, S., and Yang, J., 2018. "Dynamic response and energy absorption of functionally graded porous structures". *Materials & Design,* **140**, pp. 473–487.

[16] Qi, D., Lu, Q., He, C., Li, Y., Wu, W., and Xiao, D., 2019. "Impact energy absorption of functionally graded chiral honeycomb structures". *Extreme Mechanics Letters,* **32**, p. 100568.

[17] Li, G., Xu, F., Sun, G., and Li, Q., 2015. "A comparative study on thin-walled structures with functionally graded thickness (FGT) and tapered tubes withstanding oblique impact loading". *International Journal of Impact Engineering,* **77**, pp. 68–83.

[18] El-Wazery, M., and El-Desouky, A., 2015. "A review on functionally graded ceramic-metal materials". *Journal of Materials and Environmental Science,* **6**(5), pp. 1369–1376.

[19] Jamaludin, S. N. S., Mustapha, F., Nuruzzaman, D. M., and Basri, S. N., 2013. "A review on the fabrication techniques of functionally graded ceramic-metallic materials in advanced composites". *Scientific Research and Essays,* **8**(21), pp. 828–840.

TH-3234_176103111

[20] Besisa, D. H., and Ewais, E. M., 2016. "Advances in functionally graded ceramics- processing, sintering properties and applications". *Ebrahimini F, ed*, pp. 1–31.

[21] Mahamood, R. M., Akinlabi, E. T., Shukla, M., and Pityana, S., 2012. "Functionally graded material: An overview". *Proceedings of the World Congress on Engineering,* **3**, pp. 1593–1597.

[22] Kieback, B., Neubrand, A., and Riedel, H., 2003. "Processing techniques for functionally graded materials". *Materials Science and Engineering: A,* **362**(1–2), pp. 81 – 106.

[23] Suresh, S., and Mortensen, A., 1998. *Fundamentals of Functionally Graded Materials: Processing and Thermomechanical Behaviour of Graded Metals and Metal-ceramic Composites.* IOM Communications Limited.

[24] Gandhi, M. V., and Thompson, B., 1992. *Smart materials and structures.* Springer Science & Business Media.

[25] Cao, W., Cudney, H. H., and Waser, R., 1999. "Smart materials and structures". *Proceedings of the National Academy of Sciences,* **96**(15), pp. 8330–8331.

[26] Ghareeb, N., and Farhat, M., 2018. "Smart materials and structures: State of the art and applications". *Nano Res. Appl,* **4**, pp. 1–5.

[27] Hyer, M. W., and White, S. R., 2009. *Stress analysis of fiber-reinforced composite materials.* DEStech Publications, Inc.

[28] Erdogan, F., and Ratwani, M., 1971. "Stress distribution in bonded joints". *Journal of composite materials,* **5**(3), pp. 378–393.

[29] Erdogan, F., and Arin, K., 1972. "A sandwich plate with a part-through and a debonding crack". *Engineering Fracture Mechanics,* **4**(3), pp. 449–458.

[30] Delale, F., Erdogan, F., and Aydinoglu, M., 1981. "Stresses in adhesively bonded joints: a closed-form solution". *Journal of Composite Materials,* **15**(3), pp. 249–271.

TH-3234_176103111

[31] Sankar, B. V., 2001. "An elasticity solution for functionally graded beams". *Composites Science and Technology,* **61**(5), pp. 689–696.

[32] Sankar, B., and Tzeng, J., 2002. "Thermal stresses in functionally graded beams". *AIAA Journal,* **40**(6), pp. 1228–1232.

[33] Venkataraman, S., and Sankar, B., 2003. "Elasticity solution for stresses in a sandwich beam with functionally graded core". *AIAA Journal,* **41**(12), pp. 2501–2505.

[34] Xiao, J., and Zhang, D., 2005. "Plane elasticity analysis for simply-supported functionally graded beams". *Xibei Gongye Daxue Xuebao/Journal of Northwestern Polytechnical University,* **23**(2), pp. 189–192.

[35] Yu, T., Wong, Y., Teng, J., Dong, S., and Lam, E., 2006. "Flexural behavior of hybrid FRP-concrete-steel double-skin tubular members". *Journal of Composites for Construction,* **10**(5), pp. 443–452.

[36] Nirmala, K., Upadhyay, P., Prucz, J., and Lyons, D., 2006. "Thermo-elastic stresses in composite beams with functionally graded layer". *Journal of Reinforced Plastics and Composites,* **25**(12), pp. 1241–1254.

[37] Ding, H., Huang, D., and Chen, W., 2007. "Elasticity solutions for plane anisotropic functionally graded beams". *International Journal of Solids and Structures,* **44**(1), pp. 176–196.

[38] Ying, J., Lü, C., and Chen, W., 2008. "Two-dimensional elasticity solutions for functionally graded beams resting on elastic foundations". *Composite Structures,* **84**(3), pp. 209–219.

[39] Woodward, B., and Kashtalyan, M., 2011. "3d elasticity analysis of sandwich panels with graded core under distributed and concentrated loadings". *International journal of mechanical sciences,* **53**(10), pp. 872–885.

[40] Kashtalyan, M., and Menshykova, M., 2009. "Three-dimensional elasticity solution for sandwich panels with a functionally graded core". *Composite structures,* **87**(1), pp. 36–43.

TH-3234_176103111

[41] Giunta, G., Belouettar, S., and Carrera, E., 2010. "Analysis of fgm beams by means of classical and advanced theories". *Mechanics of Advanced Materials and Structures,* **17**(8), pp. 622–635.

[42] Filippi, M., Carrera, E., and Zenkour, A., 2015. "Static analyses of fgm beams by various theories and finite elements". *Composites Part B: Engineering,* **72**, pp. 1–9.

[43] Xu, Y., and Zhou, D., 2012. "Two-dimensional thermoelastic analysis of beams with variable thickness subjected to thermo-mechanical loads". *Applied Mathematical Modelling,* **36**(12), pp. 5818–5829.

[44] Daneshmehr, A. R., Momeni, S., and Akhloumadi, M. R., 2012. "Exact elasticity solution for the density functionally gradient beam by using Airy stress function". In Applied Mechanics and Materials, Vol. 110, Trans Tech Publ, pp. 4669–4676.

[45] Xu, Y., Yu, T., and Zhou, D., 2014. "Two-dimensional elasticity solution for bending of functionally graded beams with variable thickness". *Meccanica,* **49**(10), pp. 2479–2489.

[46] Chu, P., Li, X.-F., Wu, J.-X., and Lee, K., 2015. "Two-dimensional elasticity solution of elastic strips and beams made of functionally graded materials under tension and bending". *Acta Mechanica,* **226**(7), pp. 2235–2253.

[47] Zhao, H., and Ye, Z., 2015. "Analytic elasticity solution of bi-modulus beams under combined loads". *Applied Mathematics and Mechanics,* **36**(4), pp. 427–438.

[48] Alibeigloo, A., and Liew, K., 2015. "Elasticity solution of free vibration and bending behavior of functionally graded carbon nanotube-reinforced composite beam with thin piezoelectric layers using differential quadrature method". *International Journal of Applied Mechanics,* **7**(01), p. 1550002.

[49] Çömez, İ., 2016. "Elasticity solution for a functionally graded two-layer beam with simple supported edges". *Turkish Journal of Engineering and Environmental Sciences,* **38**(3), pp. 373–381.

TH-3234_176103111

[50] Benguediab, S., Tounsi, A., Abdelaziz, H., and Meziane, M., 2017. "Elasticity solution for a cantilever beam with exponentially varying properties". *Journal of Applied Mechanics and Technical Physics,* **58**(2), pp. 354–361.

[51] He, X.-T., Li, W.-M., Sun, J.-Y., and Wang, Z.-X., 2018. "An elasticity solution of functionally graded beams with different moduli in tension and compression". *Mechanics of Advanced Materials and Structures,* **25**(2), pp. 143–154.

[52] Zhong, Z., and Yu, T., 2007. "Analytical solution of a cantilever functionally graded beam". *Composites Science and Technology,* **67**(3-4), pp. 481–488.

[53] Eslami, M. R., Shahsiah, R., and Nikbin, K., 2009. "Thermal buckling of functionally graded beams". *Iranian Journal of Mechanical Engineering Transactions of the ISME,* **10**(2), pp. 65–81.

[54] Huang, D., Ding, H., and Chen, W., 2009. "Analytical solution and semi-analytical solution for anisotropic functionally graded beam subject to arbitrary loading". *Science in China, Series G: Physics, Mechanics and Astronomy,* **52**(8), pp. 1244–1256.

[55] Daouadji, T. H., Henni, A. H., Tounsi, A., and El Abbes, A. B., 2013. "Elasticity solution of a cantilever functionally graded beam". *Applied Composite Materials,* **20**(1), pp. 1–15.

[56] Nasr, A., Atashipour, S. R., and Fadaee, M., 2010. "An elasticity solution for static analysis of functionally graded curved beam subjected to a shear force". *International Journal of Engineering. Transactions B: Applications,* **23**(2), pp. 169–178.

[57] Wang, M., and Liu, Y., 2013. "Elasticity solutions for orthotropic functionally graded curved beams". *European Journal of Mechanics-A/Solids,* **37**, pp. 8–16.

[58] Arefi, M., 2015. "Elastic solution of a curved beam made of functionally graded materials with different cross sections". *Steel Compos. Struct,* **18**(3), pp. 659–672.

[59] Kang, R., Shen, C., and Lu, T. J., 2022. "A three-dimensional theoretical model of free vibra-

TH-3234_176103111

tion for multifunctional sandwich plates with honeycomb-corrugated hybrid cores". *Composite Structures,* **298**, p. 115990.

[60] Thai, H.-T., and Kim, S.-E., 2015. "A review of theories for the modeling and analysis of functionally graded plates and shells". *Composite Structures,* **128**, pp. 70–86.

[61] Kapania, R. K., 1989. "A Review on the Analysis of Laminated Shells". *Journal of Pressure Vessel Technology,* **111**(2), pp. 88–96.

[62] Pickett, A., and Hollaway, L., 1985. "The analysis of elastic-plastic adhesive stress in bonded lap joints in FRP structures". *Composite Structures,* **4**(2), pp. 135–160.

[63] Yang, C., and Pang, S.-S., 1996. "Stress-strain analysis of single-lap composite joints under tension". *Journal of Engineering Materials and Technology,* **118**(2), pp. 247–255.

[64] Jiang, A.-M., and Ding, H.-J., 2005. "Analytical solutions for orthotropic cantilever beams (ii): Solutions for density functionally graded beams". *Journal of Zhejiang University: Science,* **6 A**(3), pp. 155–158.

[65] Benatta, M., Mechab, I., Tounsi, A., and Adda Bedia, E., 2008. "Static analysis of functionally graded short beams including warping and shear deformation effects". *Computational Materials Science,* **44**(2), pp. 765–773.

[66] Li, X.-F., 2008. "A unified approach for analyzing static and dynamic behaviors of functionally graded Timoshenko and Euler-Bernoulli beams". *Journal of Sound and Vibration,* **318**(4-5), pp. 1210–1229.

[67] Benatta, M., Tounsi, A., Mechab, I., and Bachir Bouiadjra, M., 2009. "Mathematical solution for bending of short hybrid composite beams with variable fibers spacing". *Applied Mathematics and Computation,* **212**(2), pp. 337–348.

[68] Pendhari, S., Kant, T., Desai, Y., and Venkata Subbaiah, C., 2010. "On deformation of functionally graded narrow beams under transverse loads". *International Journal of Mechanics and Materials in Design,* **6**(3), pp. 269–282.

TH-3234_176103111

[69] Li, X.-F., Wang, B.-L., and Han, J.-C., 2010. "A higher-order theory for static and dynamic analyses of functionally graded beams". *Archive of Applied Mechanics,* **80**(10), pp. 1197–1212.

[70] Ben-Oumrane, S., Abedlouahed, T., Ismail, M., Mohamed, B., Mustapha, M., and El Abbas, A., 2009. "A theoretical analysis of flexional bending of Al/Al_2O_3 S-FGM thick beams". *Computational Materials Science,* **44**(4), pp. 1344–1350.

[71] Giunta, G., Belouettar, S., and Carrera, E., 2010. "Analysis of FGM beams by means of classical and advanced theories". *Mechanics of Advanced Materials and Structures,* **17**(8), pp. 622–635.

[72] Giunta, G., Crisafulli, D., Belouettar, S., and Carrera, E., 2011. "Hierarchical theories for the free vibration analysis of functionally graded beams". *Composite Structures,* **94**(1), pp. 68–74.

[73] Thai, H.-T., and Vo, T., 2012. "Bending and free vibration of functionally graded beams using various higher-order shear deformation beam theories". *International Journal of Mechanical Sciences,* **62**(1), pp. 57–66.

[74] Bouremana, M., Houari, M., Tounsi, A., Kaci, A., and Bedia, E., 2013. "A new first shear deformation beam theory based on neutral surface position for functionally graded beams". *Steel and Composite Structures,* **15**(5), pp. 467–479.

[75] Li, S.-R., Cao, D.-F., and Wan, Z.-Q., 2013. "Bending solutions of fgm timoshenko beams from those of the homogenous Euler-Bernoulli beams". *Applied Mathematical Modelling,* **37**(10-11), pp. 7077–7085.

[76] Hadi, A., Daneshmehr, A., Mehrian, S. N., Hosseini, M., and Ehsani, F., 2013. "Elastic analysis of functionally graded Timoshenko beam subjected to transverse loading". *Technical Journal of Engineering and Applied Sciences,* **3**(13), pp. 1246–1254.

[77] Naderi, A., and Saidi, A., 2013. "Bending-stretching analysis of moderately thick functionally graded anisotropic wide beams". *Archive of Applied Mechanics,* **83**(9), pp. 1359–1370.

TH-3234_176103111

[78] Yang, Q., Zheng, B., Zhang, K., and Zhu, J., 2013. "Analytical solution of a bilayer functionally graded cantilever beam with concentrated loads". *Archive of Applied Mechanics,* **83**(3), pp. 455–466.

[79] Nie, G., Zhong, Z., and Chen, S., 2013. "Analytical solution for a functionally graded beam with arbitrary graded material properties". *Composites Part B: Engineering,* **44**(1), pp. 274–282.

[80] Nguyen, D. K., 2014. "Large displacement behaviour of tapered cantilever Euler–Bernoulli beams made of functionally graded material". *Applied Mathematics and Computation,* **237**, pp. 340 – 355.

[81] Giunta, G., Koutsawa, Y., Belouettar, S., and Calvi, A., 2014. "A dynamic analysis of three-dimensional functionally graded beams by hierarchical models". *Smart Structures and Systems,* **13**(4), pp. 637–657.

[82] Meradjah, M., Kaci, A., Houari, M., Tounsi, A., and Mahmoud, S., 2015. "A new higher order shear and normal deformation theory for functionally graded beams". *Steel and Composite Structures,* **18**(3), pp. 793–809.

[83] Hadji, L., Daouadji, T., Tounsi, A., and Bedia, E., 2015. "A n-order refined theory for bending and free vibration of functionally graded beams". *Structural Engineering and Mechanics,* **54**(5), pp. 923–936.

[84] Wang, Z.-H., Wang, X.-H., Xu, G.-D., Cheng, S., and Zeng, T., 2016. "Free vibration of two-directional functionally graded beams". *Composite Structures,* **135**, pp. 191–198.

[85] Zouatnia, N., Hadji, L., and Kassoul, A., 2017. "A refined hyperbolic shear deformation theory for bending of functionally graded beams based on neutral surface position". *Structural Engineering and Mechanics,* **63**(5), pp. 683–689.

[86] Pydah, A., and Sabale, A., 2017. "Static analysis of bi-directional functionally graded curved beams". *Composite Structures,* **160**, pp. 867–876.

TH-3234_176103111

[87] Najafi, F., Shojaeefard, M., and Saeidi Googarchin, H., 2017. "Nonlinear dynamic response of FGM beams with Winkler-Pasternak foundation subject to noncentral low velocity impact in thermal field". *Composite Structures,* **167**, pp. 132–143.

[88] Magnucki, K., Lewinski, J., Magnucka-Blandzi, E., and Kedzia, P., 2018. "Bending, buckling and free vibration of a beam with unsymmetrically varying mechanical properties". *Journal of Theoretical and Applied Mechanics,* **56**.

[89] Chaabane, L. A., Bourada, F., Sekkal, M., Zerouati, S., Zaoui, F. Z., Tounsi, A., Derras, A., Bousahla, A. A., and Tounsi, A., 2019. "Analytical study of bending and free vibration responses of functionally graded beams resting on elastic foundation". *Structural Engineering and Mechanics,* **71**(2), pp. 185–196.

[90] Li, L., Li, X., and Hu, Y., 2018. "Nonlinear bending of a two-dimensionally functionally graded beam". *Composite Structures,* **184**, pp. 1049–1061.

[91] Cao, D., Wang, B., Hu, W., and Gao, Y., 2019. "Free vibration of axially functionally graded beam". In *Mechanics of Functionally Graded Materials and Structures*. IntechOpen, DOI: 10.5772/intechopen.85835.

[92] Chen, M., Jin, G., Zhang, Y., Niu, F., and Liu, Z., 2019. "Three-dimensional vibration analysis of beams with axial functionally graded materials and variable thickness". *Composite Structures,* **207**, pp. 304–322.

[93] Alimoradzadeh, M., Salehi, M., and Esfarjani, S. M., 2019. "Nonlinear dynamic response of an axially functionally graded (AFG) beam resting on nonlinear elastic foundation subjected to moving load". *Nonlinear Engineering,* **8**(1), pp. 250–260.

[94] Marschik, C., Roland, W., Löw-Baselli, B., and Steinbichler, G., 2020. "Application of hybrid modeling in polymer processing". *SPE ANTEC Technical Papers*.

[95] Singhatanadgid, P., and Singhanart, T., 2019. "The Kantorovich method applied to bending,

TH-3234_176103111

buckling, vibration, and 3D stress analyses of plates: A literature review". *Mechanics of advanced materials and structures,* **26**(2), pp. 170–188.

[96] Kapuria, S., and Kumari, P., 2012. "Multiterm Extended Kantorovich Method for Three-Dimensional Elasticity Solution of Laminated Plates". *Journal of Applied Mechanics,* **79**(6), 09. 061018.

[97] Kumari, P., Behera, S., and Kapuria, S., 2016. "Coupled three-dimensional piezoelasticity solution for edge effects in levy-type rectangular piezolaminated plates using mixed field extended Kantorovich method". *Composite Structures,* **140**, pp. 491–505.

[98] Singh, A., and Kumari, P., 2018. "Two-dimensional elasticity solution for arbitrarily supported axially functionally graded beams". *Journal of Solid Mechanics,* **10**(4), pp. 719–733.

[99] Kumari, P., and Behera, S., 2017. "Three-dimensional free vibration analysis of levy-type laminated plates using multi-term extended Kantorovich method". *Composites Part B: Engineering,* **116**, pp. 224–238.

[100] Joodaky, A., Joodaky, I., Hedayati, M., Masoomi, R., and Farahani, E. B., 2013. "Deflection and stress analysis of thin fgm skew plates on Winkler foundation with various boundary conditions using extended Kantorovich method". *Composites Part B: Engineering,* **51**, pp. 191–196.

[101] Joodaky, A., and Joodaky, I., 2015. "A semi-analytical study on static behavior of thin skew plates on Winkler and Pasternak foundations". *International Journal of Mechanical Sciences,* **100**, pp. 322–327.

[102] Fereidoon, A., Mohyeddin, A., Sheikhi, M., and Rahmani, H., 2012. "Bending analysis of functionally graded annular sector plates by extended Kantorovich method". *Composites Part B: Engineering,* **43**(5), pp. 2172–2179.

[103] Singhatanadgid, P., and Taranajetsada, P., 2016. "Vibration analysis of stepped rectangu-

TH-3234_176103111

lar plates using the extended Kantorovich method". *Mechanics of Advanced Materials and Structures,* **23**(2), pp. 201–215.

[104] Awrejcewicz, J., Krysko-Jr, V., Kalutsky, L., Zhigalov, M., and Krysko, V., 2021. "Review of the methods of transition from partial to ordinary differential equations: From macro-to nano-structural dynamics". *Archives of Computational Methods in Engineering*, pp. 1–33.

[105] Joodaky, I., and Joodaky, A., 2019. "Bending of edge-bonded dissimilar rectangular plates". *Meccanica,* **54**(3), pp. 565–572.

[106] Harris, J., and Adams, R., 1984. "Strength prediction of bonded single lap joints by non-linear finite element methods". *International journal of adhesion and adhesives,* **4**(2), pp. 65–78.

[107] Tsai, M., and Morton, J., 1994. "An evaluation of analytical and numerical solutions to the single-lap joint". *International Journal of Solids and Structures,* **31**(18), pp. 2537–2563.

[108] Her, S.-C., 1999. "Stress analysis of adhesively-bonded lap joints". *Composite structures,* **47**(1-4), pp. 673–678.

[109] Bogdanovich, A., and Kizhakkethara, I., 1999. "Three-dimensional finite element analysis of double-lap composite adhesive bonded joint using submodeling approach". *Composites Part B: Engineering,* **30**(6), pp. 537–551.

[110] Adams, R. D., Adams, R. D., Comyn, J., Wake, W. C., and Wake, W., 1997. *Structural adhesive joints in engineering.* Springer Science & Business Media.

[111] Xiong, Y., and Bedair, O., 1999. "Analytical and finite element modeling of riveted lap joints in aircraft structure". *AIAA journal,* **37**(1), pp. 93–99.

[112] Boss, J., Ganesh, V., and Lim, C., 2003. "Modulus grading versus geometrical grading of composite adherends in single-lap bonded joints". *Composite Structures,* **62**(1), pp. 113–121.

[113] Zou, G., Shahin, K., and Taheri, F., 2004. "An analytical solution for the analysis of symmetric composite adhesively bonded joints". *Composite Structures,* **65**(3-4), pp. 499–510.

TH-3234_176103111

[114] Kim, K.-S., Yoo, J.-S., Yi, Y.-M., and Kim, C.-G., 2006. "Failure mode and strength of uni-directional composite single lap bonded joints with different bonding methods". *Composite structures,* **72**(4), pp. 477–485.

[115] Kim, K.-S., Yi, Y.-M., Cho, G.-R., and Kim, C.-G., 2008. "Failure prediction and strength improvement of uni-directional composite single lap bonded joints". *Composite structures,* **82**(4), pp. 513–520.

[116] De Castro, P., De Matos, P., Moreira, P., and Da Silva, L., 2007. "An overview on fatigue analysis of aeronautical structural details: open hole, single rivet lap-joint, and lap-joint panel". *Materials Science and Engineering: A,* **468**, pp. 144–157.

[117] Kapuria, S., Bhattacharyya, M., and Kumar, A., 2008. "Bending and free vibration response of layered functionally graded beams: A theoretical model and its experimental validation". *Composite Structures,* **82**(3), pp. 390–402.

[118] Kapuria, S., and Kumari, P., 2011. "Extended Kantorovich Method for Three-Dimensional Elasticity Solution of Laminated Composite Structures in Cylindrical Bending". *Journal of Applied Mechanics,* **78**(6).

[119] Şimşek, M., 2009. "Static analysis of a functionally graded beam under a uniformly distributed load by Ritz method". *International Journal of Engineering & Applied Sciences,* **1**(3), pp. 1–11.

[120] Taeprasartsit, S., 2010. "Using a homogeneous beam element to analyse functionally graded beams". *Proceedings of the Institution of Mechanical Engineers, Part C: Journal of Mechanical Engineering Science,* **224**(4), pp. 789–795.

[121] Nguyen, V.-C., Tran, H.-Q., and Pham, V.-V., 2023. "Nonlinear static analysis of bi-directional functionally graded sandwich plates in thermal environments by a higher-order finite element model". *Thin-Walled Structures,* **188**, p. 110819.

[122] Kocatürk, T., Şimşek, M., and Akbaş, Ş., 2011. "Large displacement static analysis of a

TH-3234_176103111

cantilever Timoshenko beam composed of functionally graded material". *Science and Engineering of Composite Materials,* **18**(1-2), pp. 21–34.

[123] Filippi, M., Carrera, E., and Zenkour, A., 2015. "Static analyses of FGM beams by various theories and finite elements". *Composites Part B: Engineering,* **72**, pp. 1–9.

[124] Chen, D., Yang, J., and Kitipornchai, S., 2015. "Elastic buckling and static bending of shear deformable functionally graded porous beam". *Composite Structures,* **133**, pp. 54–61.

[125] Frikha, A., Hajlaoui, A., Wali, M., and Dammak, F., 2016. "A new higher order C_0 mixed beam element for FGM beams analysis". *Composites Part B: Engineering,* **106**, pp. 181–189.

[126] De Pietro, G., Hui, Y., Giunta, G., Belouettar, S., Carrera, E., and Hu, H., 2016. "Hierarchical one-dimensional finite elements for the thermal stress analysis of three-dimensional functionally graded beams". *Composite Structures,* **153**, pp. 514–528.

[127] Malik, P., and Kadoli, R., 2017. "Thermo-elastic response of SUS316-Al_2O_3 functionally graded beams under various heat loads". *International Journal of Mechanical Sciences,* **128-129**, pp. 206–223.

[128] Amirpour, M., Bickerton, S., Calius, E., Das, R., and Mace, B., 2019. "Numerical and experimental study on deformation of 3d-printed polymeric functionally graded plates: 3D-digital image correlation approach". *Composite Structures,* **211**, pp. 481–489.

[129] Nam, V. H., Vinh, P. V., Chinh, N. V., Thom, D. V., Hong, T. T., et al., 2019. "A new beam model for simulation of the mechanical behaviour of variable thickness functionally graded material beams based on modified first order shear deformation theory". *Materials,* **12**(3), p. 404.

[130] Rudawska, A., 2019. "Comparison of the adhesive joints' strength of the similar and dissimilar systems of metal alloy/polymer composite". *Applied Adhesion Science,* **7**(1), pp. 1–17.

[131] Adamos, L., and Loutas, T., 2021. "Challenges in the fatigue crack growth characterization of

TH-3234_176103111

metal/composite joints: A compliance-based investigation of a Ti/CFRP joint". *International Journal of Fatigue,* **148**, p. 106233.

[132] Bahrami, B., Ayatollahi, M., Alavi, S., and da Silva, L., 2022. "On the prediction of the stress field in adhesive joints using a combined analytical-numerical method". *International Journal of Adhesion and Adhesives,* **116**, p. 103151.

[133] Al-Ramahi, N. J., Joffe, R., and Varna, J., 2021. "Numerical analysis of stresses in double-lap adhesive joint under thermo-mechanical load". *Engineering Structures,* **233**, p. 111863.

[134] Zhou, Y., Zhang, P., and Ning, F., 2023. "Joining of carbon fiber reinforced polymer/titanium stacks using directed energy deposition additive manufacturing". *Composite Structures,* **310**, p. 116775.

[135] Zhang, H., Zhang, L., Liu, Z., Qi, S., Zhu, Y., and Zhu, P., 2021. "Numerical analysis of hybrid (bonded/bolted) FRP composite joints: a review". *Composite Structures*, p. 113606.

[136] Wu CP, L. Y., 2016. "A review of semi-analytical numerical methods for laminated composite and multilayered functionally graded elastic/piezoelectric plates and shells". *Compos Struct,* **147**, pp. 1–15.

[137] Mittelstedt, C., and Becker, W., 2007. "Free-edge effects in composite laminates". *Applied Mechanics Reviews,* **60**(5), pp. 217–245.

[138] Sharma, H., Patil, M., and Woolsey, C., 2020. "A review of structure-preserving numerical methods for engineering applications". *Computer Methods in Applied Mechanics and Engineering,* **366**, p. 113067.

[139] Vel, S. S., and Batra, R., 2000. "Cylindrical bending of laminated plates with distributed and segmented piezoelectric actuators/sensors". *AIAA journal,* **38**(5), pp. 857–867.

[140] Vel, S. S., and Batra, R., 2001. "Exact solution for the cylindrical bending of laminated plates with embedded piezoelectric shear actuators". *Smart Materials and Structures,* **10**(2), p. 240.

TH-3234_176103111

[141] Qing, G., Qiu, J., and Liu, Y., 2006. "A semi-analytical solution for static and dynamic analysis of plates with piezoelectric patches". *International journal of solids and structures,* **43**(6), pp. 1388–1403.

[142] Shi, Z., Xiang, H., and Spencer, B., 2006. "Exact analysis of multi-layer piezoelectric/composite cantilevers". *Smart Materials and Structures,* **15**(5), p. 1447.

[143] Xiang, H., and Shi, Z., 2008. "Static analysis for multi-layered piezoelectric cantilevers". *International Journal of Solids and Structures,* **45**(1), pp. 113–128.

[144] Behjat, B., Salehi, M., Sadighi, M., Armin, A., and Abbasi, M., 2009. "Static, dynamic, and free vibration analysis of functionally graded piezoelectric panels using finite element method". *Journal of Intelligent Material Systems and Structures,* **20**(13), pp. 1635–1646.

[145] Lezgy-Nazargah, M., Vidal, P., and Polit, O., 2013. "An efficient finite element model for static and dynamic analyses of functionally graded piezoelectric beams". *Composite Structures,* **104**, pp. 71–84.

[146] Kapuria, S., and Kumari, P., 2013. "Extended kantorovich method for coupled piezoelasticity solution of piezolaminated plates showing edge effects". *Proceedings of the Royal Society A: Mathematical, Physical and Engineering Sciences,* **469**(2151), p. 20120565.

[147] Kumari, P., and Shakya, A. K., 2017. "Two-dimensional solution of piezoelectric plate subjected to arbitrary boundary conditions using extended Kantorovich method". *Procedia engineering,* **173**, pp. 1523–1530.

[148] Behera, S., and Kumari, P., 2019. "Analytical piezoelasticity solution for natural frequencies of Levy-type piezolaminated plates". *International Journal of Applied Mechanics,* **11**(03), p. 1950023.

[149] Behera, S., and Kumari, P., 2020. "Free vibration analysis of levy-type smart hybrid plates using three-dimensional extended Kantorovich method". In *Structural Integrity Assessment.* Springer, pp. 467–477.

TH-3234_176103111

[150] Singh, A., Kumari, P., and Bind, P., 2020. "2D free vibration solution of the hybrid piezoelectric laminated beams using extended Kantorovich method". *Journal of The Institution of Engineers (India): Series C,* **101**(1), pp. 1–12.

[151] Singh, A., and Kumari, P., 2020. "Two-dimensional free vibration analysis of axially functionally graded beams integrated with piezoelectric layers: An piezoelasticity approach". *International Journal of Applied Mechanics,* **12**(04), p. 2050037.

[152] Çömez, İ., Aribas, U. N., Kutlu, A., and Omurtag, M. H., 2022. "Two-dimensional solution of functionally graded piezoelectric-layered beams". *Journal of the Brazilian Society of Mechanical Sciences and Engineering,* **44**(3), p. 101.

[153] Li, L., Ren, Y., and Jin, Q., 2023. "Wave propagation in piezoelectric doubly-curved panels considering thermal effects: Piezoelectricity-based synergistic effect analysis". *Acta Astronautica,* **204**, pp. 331–347.

[154] Meuyou, H., Ntamack, G., and Azrar, L., 2023. "Three-dimensional semi-analytical solutions of arbitrary functionally graded piezoelectric doubly curved shell panel under thermo-electric load". *Journal of Thermal Stresses*, pp. 1–24.

[155] Singh, A., Naskar, S., Kumari, P., and Mukhopadhyay, T., 2023. "Viscoelastic free vibration analysis of in-plane functionally graded orthotropic plates integrated with piezoelectric sensors: Time-dependent 3d analytical solutions". *Mechanical Systems and Signal Processing,* **184**, p. 109636.

[156] Tran, H.-Q., Vu, V.-T., and Tran, M.-T., 2023. "Free vibration analysis of piezoelectric functionally graded porous plates with graphene platelets reinforcement by pb-2 ritz method". *Composite Structures,* **305**, p. 116535.

[157] Kumar, V., Singh, S., Saran, V., and Harsha, S., 2023. "Vibration response of the exponential functionally graded material plate with variable thickness resting on the orthotropic pasternak foundation". *Mechanics Based Design of Structures and Machines*, pp. 1–28.

TH-3234_176103111

[158] Kenanda, M. A., Hammadi, F., Belabed, Z., and Meliani, M. H., 2023. "Free vibration analysis of porous functionally graded plates using a novel quasi-3d hyperbolic high order shear deformation theory.". *Frattura e Integrita Strutturale*(64).

[159] Upadhyaya, G. S., 1997. *Powder metallurgy technology.* Cambridge Int Science Publishing.

[160] Datta, B. K., 2014. *Powder metallurgy: an advanced technique of processing engineering materials.* PHI Learning Pvt. Ltd.

[161] Dobrzański, L. A., 2017. *Powder Metallurgy: Fundamentals and Case Studies.* BoD–Books on Demand.

[162] Samal, P., and Newkirk, J., 2015. "Powder metallurgy methods and applications". *ASM handbook of powder metallurgy,* **7**.

[163] Takahashi, M., Itoh, Y., Miyazaki, M., Takano, H., and Okuhata, T., 1993. "Fabrication of tungsten/copper graded material". *International Journal of Refractory Metals and Hard Materials,* **12**(5), pp. 243–250.

[164] Watanabe, R., Kawasaki, A., Tanaka, M., and Li, J.-F., 1993. "Fabrication of SiC-AlN/Mo functionally gradient material for high temperature use". *International Journal of Refractory Metals and Hard Materials,* **12**(4), pp. 187–193.

[165] Nemat-Alla, M., Ata, M., Ragab, M., and Khair-Eldeen, W., 2011. "Powder metallurgical fabrication and microstructural investigations of aluminum/steel functionally graded material". *Mater Sci Appl,* **2**, pp. 1708–1718.

[166] Sanuddin, A., Ali, A., and Hanim, M., 2012. "Fabrication of Al/Al_2O_3 FGM rotating disc". *International Journal of Automotive and Mechanical Engineering (IJAME),* **5**, pp. 622–629.

[167] Canakci, A., Varol, T., Özkaya, S., and Erdemir, F., 2014. "Microstructure and properties of Al-B_4 C functionally graded materials produced by powder metallurgy method". *Universal Journal of Materials Science,* **2**(5), pp. 90–95.

TH-3234_176103111

[168] Efe, G. F. C., Ipek, M., Zeytin, S., and Bindal, C., 2016. "Fabrication and properties of sic reinforced copper-matrix-composite contact material". *Materials and technology,* **50**(4), pp. 585–590.

[169] Srinivas, P. N. S., Balakrishna, B., et al., 2020. "Microstructural, mechanical and tribological characterization on the Al based functionally graded material fabricated powder metallurgy". *Materials Research Express,* **7**(2), p. 026513.

[170] Zhu, J., Yin, Z., and Lai, Z., 1996. "Fabrication and microstructure of ZrO_2-Ni functional gradient material by powder metallurgy". *Journal of materials science,* **31**(21), pp. 5829–5834.

[171] Zhu, J., Lai, Z., Yin, Z., Jeon, J., and Lee, S., 2001. "Fabrication of ZrO_2-NiCr functionally graded material by powder metallurgy". *Materials chemistry and physics,* **68**(1-3), pp. 130–135.

[172] Ma, J., He, Z., and Tan, G., 2002. "Fabrication and characterization of Ti-TiB_2 functionally graded material system". *Metallurgical and Materials Transactions A,* **33**(3), pp. 681–685.

[173] Jin, G., Takeuchi, M., Honda, S., Nishikawa, T., and Awaji, H., 2005. "Properties of multi-layered mullite/Mo functionally graded materials fabricated by powder metallurgy processing". *Materials Chemistry and Physics,* **89**(2-3), pp. 238–243.

[174] Gelbstein, Y., Dashevsky, Z., and Dariel, M., 2007. "Powder metallurgical processing of functionally graded p-$Pb_{1-x}Sn_xTe$ materials for thermoelectric applications". *Physica B: Condensed Matter,* **391**(2), pp. 256–265.

[175] Bhattacharyya, M., Kumar, A. N., and Kapuria, S., 2008. "Synthesis and characterization of Al/SiC and Ni/Al_2O_3 functionally graded materials". *Materials Science and Engineering: A,* **487**(1-2), pp. 524–535.

[176] Übeyli, M., Balci, E., Sarikan, B., Öztaş, M. K., Camuşcu, N., Yildirim, R. O., and Keleş,

TH-3234_176103111

Ö., 2014. "The ballistic performance of SiC-AA7075 functionally graded composite produced by powder metallurgy". *Materials & Design (1980-2015),* **56**, pp. 31–36.

[177] Efe, G. C., İpek, M., Zeytin, S., and Bindal, C., 2012. "An investigation of the effect of SiC particle size on Cu–SiC composites". *Composites Part B: Engineering,* **43**(4), pp. 1813–1822.

[178] Kumar, R., and Chandrappa, C., 2014. "Synthesis and characterization of Al-SiC functionally graded material composite using powder metallurgy techniques". *International Journal of Innovative Research in Science, Engineering and Technology,* **3**(8).

[179] Erdemir, F., Canakci, A., and Varol, T., 2015. "Microstructural characterization and mechanical properties of functionally graded Al2024/SiC composites prepared by powder metallurgy techniques". *Transactions of Nonferrous Metals Society of China,* **25**(11), pp. 3569–3577.

[180] Çalıskan, F., Cömert, S., and Kocaman, E., 2017. "Fabrication of functional graded Al2124 composite reinforced with Al_2O_3 particles.". *Acta Physica Polonica, A.,* **131**(3).

[181] Tripathy, A., Sarangi, S. K., Chaubey, A. K., and Mohanty, U. K., 2020. "Fabrication of Al/Al_2O_3 functionally graded material using powder metallurgy route". In Applications of Robotics in Industry Using Advanced Mechanisms, Springer International Publishing, pp. 377–387.

[182] Gillia, O., and Caillens, B., 2011. "Fabrication of a material with composition gradient for metal/ceramic assembly". *Powder technology,* **208**(2), pp. 355–366.

[183] Efe, G. C., Yener, T., Altinsoy, I., İpek, M., Zeytin, S., and Bindal, C., 2011. "The effect of sintering temperature on some properties of Cu–SiC composite". *Journal of Alloys and Compounds,* **509**(20), pp. 6036–6042.

[184] Zhu, J., Liu, L., Hu, G., Shen, B., Hu, W., and Ding, W., 2004. "Study on composite electroforming of Cu/SiCp composites". *Materials Letters,* **58**(10), pp. 1634–1637.

[185] Kang, H.-K., and Kang, S. B., 2006. "Thermal decomposition of silicon carbide in a plasma-

TH-3234_176103111

sprayed Cu/SiC composite deposit". *Materials Science and Engineering: A,* **428**(1-2), pp. 336–345.

[186] Chauhan, P. K., and Khan, S., 2020. "Microstructural examination of aluminium-copper functionally graded material developed by powder metallurgy route". *Materials Today: Proceedings,* **25**, pp. 833–837.

[187] Chenglin, C., Jingchuan, Z., Zhongda, Y., and Shidong, W., 1999. "Hydroxyapatite-Ti functionally graded biomaterial fabricated by powder metallurgy". *Materials Science and Engineering: A,* **271**(1-2), pp. 95–100.

[188] Xiong, H., Zhang, L., Chen, L., Hirai, T., and Yuan, R., 2000. "Design and fabrication of W-Mo-Ti-TiAl-Al system functionally graded material". *Metallurgical and Materials Transactions A,* **31**(9), pp. 2369–2376.

[189] Shahrjerdi, A., Mustapha, F., Bayat, M., Sapuan, S., and Majid, D., 2011. "Fabrication of functionally graded hydroxyapatite-titanium by applying optimal sintering procedure and powder metallurgy". *International Journal of Physical Sciences,* **6**(9), pp. 2258–2267.

[190] Sazesh, S., Ghassemi, A., Ebrahimi, R., and Khodaei, M., 2019. "Fabrication and characterization of nHA/titanium dental implant". *Materials Research Express,* **6**(4), jan, p. 045060.

[191] Miyao, R., Omori, M., Watari, F., Yokoyama, A., Matsuno, H., Hirai, T., and Kawasaki, T., 2000. "Fabrication of functionally graded implants by spark plasma sintering and their properties". *Funtai Oyobi Fummatsu Yakin/Journal of the Japan Society of Powder and Powder Metallurgy,* **47**(11), pp. 1239–1242.

[192] Kondo, H., Yokoyama, A., Omori, M., Ohkubo, A., Hirai, T., Watari, F., Uo, M., and Kawasaki, T., 2004. "Fabrication of titanium nitride/apatite functionally graded implants by spark plasma sintering". *Materials Transactions,* **45**(11), pp. 3156–3162.

[193] Watanabe, T., Yamamoto, S., Matsuda, N., Hukase, Y., Izui, H., and Okano, M., 2008. "Processing of FGM with five concentric layers by spark plasma sintering and analysis by

TH-3234_176103111

the finite element method - the fabrication of TiH_2-(SHA_{p-100}+β-TCP) functionally graded material (FGM)". *Funtai Oyobi Fummatsu Yakin/Journal of the Japan Society of Powder and Powder Metallurgy,* **55**(5), pp. 365–372.

[194] Watanabe, Y., Iwasa, Y., Sato, H., Teramoto, A., Abe, K., and Miura-Fujiwara, E., 2011. "Microstructures and mechanical properties of titanium/biodegradable-polymer FGM for bone tissue fabricated by spark plasma sintering method". *Journal of Materials Processing Technology,* **211**(12), pp. 1919–1926.

[195] Rubio, W. M., Paulino, G. H., and Silva, E. C. N., 2012. "Analysis, manufacture and characterization of Ni/Cu functionally graded structures". *Materials & Design,* **41**, pp. 255–265.

[196] Omidi, N., Jabbari, A., and Sedighi, M., 2018. "Mechanical and microstructural properties of titanium/hydroxyapatite functionally graded material fabricated by spark plasma sintering". *Powder Metallurgy,* **61**(5), pp. 417–427.

[197] Tang, X., Zhang, H., Du, D., Qu, D., Hu, C., Xie, R., and Feng, Y., 2014. "Fabrication of W–Cu functionally graded material by spark plasma sintering method". *International Journal of Refractory Metals and Hard Materials,* **42**(Complete), pp. 193–199.

[198] EL-Wazery, M. S., and EI-Desouky, A. R., 2014. "Fabrication and characteristics of 8YSZ/Ni functionally graded materials by applying spark plasma sintering procedure". *International Journal of Applied Science and Engineering,* **12**(4), pp. 313–321.

[199] Gupta, R., Kumar, R., Chaubey, A., Kanpara, S., and Khirwadkar, S., 2018. "Mechanical and microstructural characterization of W-Cu FGM fabricated by one-step sintering method through PM route". In IOP Conference Series: Materials Science and Engineering, Vol. 338 (1), IOP Publishing, p. 012042.

[200] Chaubey, A., Gupta, R., Kumar, R., Verma, B., Kanpara, S., Bathula, S., Khirwadkar, S., and Dhar, A., 2018. "Fabrication and characterization of W-Cu functionally graded material by spark plasma sintering process". *Fusion Engineering and Design,* **135**, pp. 24–30.

TH-3234_176103111

[201] Ohtsuka, A., Kawasaki, A., Watanabe, R., and Young, U., 1998. "Fabrication of $Cu/Al_2O_3/Cu$ symmetrical functionally graded material by spark plasma sintering process". *Funtai Oyobi Fummatsu Yakin/Journal of the Japan Society of Powder and Powder Metallurgy,* **45**(3), pp. 220–224.

[202] Kikuchi, K., Kang, Y.-S., and Kawasaki, A., 2000. "Fabrication of diskshaped symmetric functionally graded materials of Ni/Al_2O_3 system by SPS process". *Funtai Oyobi Fummatsu Yakin/Journal of the Japan Society of Powder and Powder Metallurgy,* **47**(3), pp. 302–307.

[203] Radwan, M., Nygren, M., Flodström, K., and Esmaelzadeh, S., 2011. "Fabrication of crack-free $SUS316L/Al_2O_3$ functionally graded materials by spark plasma sintering". *Journal of Materials Science,* **46**(17), pp. 5807–5814. cited By 15.

[204] Bahraminasab, M., Ghaffari, S., and Eslami-Shahed, H., 2017. "Al_2O_3-Ti functionally graded material prepared by spark plasma sintering for orthopaedic applications". *Journal of the Mechanical Behavior of Biomedical Materials,* **72**, pp. 82–89.

[205] Farahmand, S., Monazzah, A., and Soorgee, M., 2019. "The fabrication of Al_2O_3–Al FGM by SPS under different sintering temperatures: Microstructural evaluation and bending behavior". *Ceramics International,* **45**(17), pp. 22775–22782.

[206] Graf, B., Gumenyuk, A., and Rethmeier, M., 2012. "Laser metal deposition as repair technology for stainless steel and titanium alloys". *Physics Procedia,* **39**, pp. 376–381.

[207] Mahamood, R., and Akinlabi, E. T., 2015. "Laser metal deposition of functionally graded Ti-6Al-4V/TiC". *Materials & Design,* **84**, pp. 402–410.

[208] Reichardt, A., Dillon, R. P., Borgonia, J. P., Shapiro, A. A., McEnerney, B. W., Momose, T., and Hosemann, P., 2016. "Development and characterization of Ti-6Al-4V/TiC to 304L stainless steel gradient components fabricated with laser deposition additive manufacturing". *Materials & Design,* **104**, pp. 404–413.

[209] Li, W., Karnati, S., Kriewall, C., Liou, F., Newkirk, J., Brown Taminger, K., and Seufzer,

TH-3234_176103111

W., 2017. "Fabrication and characterization of a functionally graded material from Ti-6Al-4V/TiC to SS316 by laser metal deposition". *Additive Manufacturing,* **14**, pp. 95–104.

[210] Yan, L., Chen, X., Zhang, Y., Newkirk, J., and Liou, F., 2017. "Fabrication of functionally graded Ti and γ-TiAl by laser metal deposition". *JOM,* **69**(12), pp. 2756–2761.

[211] Sharman, A., Hughes, J., and Ridgway, K., 2018. "Characterisation of titanium aluminide components manufactured by laser metal deposition". *Intermetallics,* **93**, pp. 89–92.

[212] Zhang, J., Zhang, Y., Li, W., Karnati, S., Liou, F., and Newkirk, J. W., 2018. "Microstructure and properties of functionally graded materials Ti-6Al-4V/TiC fabricated by direct laser deposition". *Rapid Prototyping Journal,* **24**(4), pp. 677–687.

[213] Karnati, S., Zhang, Y., Liou, F. F., and Newkirk, J. W., 2019. "On the feasibility of tailoring copper-nickel functionally graded materials fabricated through laser metal deposition". *Metals,* **9**(3), p. 287.

[214] Chen, B., Su, Y., Xie, Z., Tan, C., and Feng, J., 2020. "Development and characterization of 316L/Inconel625 functionally graded material fabricated by laser direct metal deposition". *Optics and Laser Technology,* **123**.

[215] Markworth, A., Ramesh, K., and Parks, W., 1995. "Modelling studies applied to functionally graded materials". *Journal of Materials Science,* **30**, pp. 2183–2193.

[216] Lee, Y., and Erdogan, F., 1994. "Residual/thermal stresses in FGM and laminated thermal barrier coatings". *International Journal of Fracture,* **69**, pp. 145–165.

[217] Fukui, Y., Takashima, K., and Ponton, C., 1994. "Measurement of young's modulus and internal friction of an in situ Al-Al_3 Ni functionally gradient material". *Journal of materials science,* **29**, pp. 2281–2288.

[218] Gasik, M. M., and Lilius, R. R., 1994. "Evaluation of properties of W- Cu functional gradient materials by micromechanical model". *Computational materials science,* **3**(1), pp. 41–49.

TH-3234_176103111

[219] Gasik, M. M., 1998. "Micromechanical modelling of functionally graded materials". *Computational Materials Science,* **13**(1-3), pp. 42–55.

[220] Reiter, T., Dvorak, G. J., and Tvergaard, V., 1997. "Micromechanical models for graded composite materials". *Journal of the Mechanics and Physics of Solids,* **45**(8), pp. 1281–1302.

[221] Ueda, S., and Gasik, M., 2000. "Thermal-elasto-plastic analysis of W-Cu functionally graded materials subjected to a uniform heat flow by micromechanical model". *Journal of Thermal Stresses,* **23**(4), pp. 395–409.

[222] Bruck, H., and Rabin, B., 1999. "Evaluating microstructural and damage effects in rule-of-mixtures predictions of the mechanical properties of Ni-Al_2O_3 composites". *Journal of Materials Science,* **34**(9), pp. 2241–2251.

[223] Zuiker, J., and Dvorak, G., 1994. "The effective properties of functionally graded composites—i. extension of the Mori-Tanaka method to linearly varying fields". *Composites Engineering,* **4**(1), pp. 19–35.

[224] Kathavate, V. S., Pawar, D., and Adkine, A., 2019. "Micromechanics-based approach for the effective estimation of the elastic properties of fiber-reinforced polymer matrix composite". *Journal of Micromechanics and Molecular Physics,* **4**(03), p. 1950005.

[225] Bruck, H. A., and Rabin, B. H., 1999. "Evaluation of rule-of-mixtures predictions of thermal expansion in powder-processed Ni-Al_2O_3 composites". *Journal of the American Ceramic Society,* **82**(10), pp. 2927–2930.

[226] Zuiker, J. R., 1995. "Functionally graded materials: choice of micromechanics model and limitations in property variation". *Composites Engineering,* **5**(7), pp. 807–819.

[227] Chen, B., and Tong, L., 2005. "Thermomechanically coupled sensitivity analysis and design optimization of functionally graded materials". *Computer methods in applied mechanics and engineering,* **194**(18-20), pp. 1891–1911.

TH-3234_176103111

[228] Grujicic, M., and Zhang, Y., 1998. "Determination of effective elastic properties of functionally graded materials using voronoi cell finite element method". *Materials Science and Engineering: A,* **251**(1-2), pp. 64–76.

[229] Nakamura, T., Wang, T., and Sampath, S., 2000. "Determination of properties of graded materials by inverse analysis and instrumented indentation". *Acta Materialia,* **48**(17), pp. 4293–4306.

[230] Tsukamoto, H., 2015. "Microstructure and indentation properties of ZrO_2/Ti functionally graded materials fabricated by spark plasma sintering". *Materials Science and Engineering: A,* **640**, pp. 338–349.

[231] Cannillo, V., Lusvarghi, L., Siligardi, C., and Sola, A., 2007. "Prediction of the elastic properties profile in glass-alumina functionally graded materials". *Journal of the European Ceramic Society,* **27**(6), pp. 2393–2400.

[232] Zhao, C., Vleugels, J., Vandeperre, L., Basu, B., and Van der Biest, O., 1998. "Y-TZP/Ce-TZP functionally graded composite". *Journal of materials science letters,* **17**, pp. 1453–1455.

[233] Jin, G., Takeuchi, M., Honda, S., Nishikawa, T., and Awaji, H., 2004. "Thermal shock testing on Mullite/Mo fgm disks using an infrared radiation/water flow technique". In Journal of the Ceramic Society of Japan, Supplement Journal of the Ceramic Society of Japan, Supplement 112-1, PacRim5 Special Issue, The Ceramic Society of Japan, pp. S286–S290.

[234] Majzoobi, G., Mohammadi, M., and Rahmani, K., 2022. "Microstructural examination and mechanical characterization of Ti/HA and Ti/SiO_2 functionally graded materials fabricated at different loading rates". *Journal of the Mechanical Behavior of Biomedical Materials,* **136**, p. 105497.

[235] Roebben, G., Bollen, B., Brebels, A., Van Humbeeck, J., and Van der Biest, O., 1997. "Impulse excitation apparatus to measure resonant frequencies, elastic moduli, and internal friction at room and high temperature". *Review of scientific instruments,* **68**(12), pp. 4511–4515.

TH-3234_176103111

[236] Wkeglewski, W., Bochenek, K., Basista, M., Schubert, T., Jehring, U., Litniewski, J., and Mackiewicz, S., 2013. "Comparative assessment of young's modulus measurements of metal–ceramic composites using mechanical and non-destructive tests and micro-CT based computational modeling". *Computational Materials Science,* **77**, pp. 19–30.

[237] Campbell, A., and Eckhart, B. D., 2015. Validation of the IMCE RFDA system for dynamic elastic moduli measurements. Tech. rep., Oak Ridge National Lab.(ORNL), Oak Ridge, TN (United States).

[238] Voiconi, T., Marsavina, L., Linul, E., and Kováčik, J., 2014. "Determination of elastic and damping properties for closed-cell aluminium foams using Impulse Excitation Technique". In XIIIth Youth Symposium of Experimental Solid Mechanics, in Czech Republic. June 29th-July 2nd. Accessed April, Vol. 3, p. 2017.

[239] Wolff, M., Schaper, J., Dahms, M., Ebel, T., Kainer, K., and Klassen, T., 2014. "Magnesium powder injection moulding for biomedical application". *Powder metallurgy,* **57**(5), pp. 331–340.

[240] Deing, A., Luthringer, B., Laipple, D., Ebel, T., and Willumeit, R., 2014. "A porous Ti-6Al-4V implant material for medical application". *International journal of biomaterials,* **2014**.

[241] Gain, A. K., Zhang, L., and Liu, W., 2015. "Microstructure and material properties of porous hydroxyapatite-zirconia nanocomposites using polymethyl methacrylate powders". *Materials & Design,* **67**, pp. 136–144.

[242] Sukhanov, M., Velmuzhov, A., Stepanov, B., Blagin, R., Ketkova, L., Fukina, D., Kotereva, T., Modin, I., and Shiryaev, V., 2022. "The $Ga_{20}Ge_{20}Se_{60}$ glass-ceramics as a promising long-wave IR optical material". *Journal of Non-Crystalline Solids,* **590**, p. 121700.

[243] Gain, A. K., Zhang, L., and Quadir, M. Z., 2016. "Thermal aging effects on microstructures and mechanical properties of an environmentally friendly eutectic tin-copper solder alloy". *Materials & Design,* **110**, pp. 275–283.

TH-3234_176103111

[244] Schlacher, J., Chlup, Z., Hofer, A.-K., and Bermejo, R., 2023. "High-temperature fracture behaviour of layered alumina ceramics with textured microstructure". *Journal of the European Ceramic Society,* **43**(7), pp. 2917–2927.

[245] López-López, E., Erauw, J., Moreno, R., Cambier, F., and Baudín, C., 2013. "Elastic behaviour of zirconium titanate-zirconia bulk composite materials at room and high temperature". *Journal of the European Ceramic Society,* **33**(15-16), pp. 3195–3200.

[246] Chlup, Z., Drdlík, D., Hadraba, H., Ševeček, O., Šiška, F., Erhart, J., and Maca, K., 2023. "Temperature effect on elastic and fracture behaviour of lead-free piezoceramic $BaTiO_3$". *Journal of the European Ceramic Society,* **43**(4), pp. 1509–1522.

[247] Hönig, S., Koch, D., Weber, S., Etzold, S., Tonnesen, T., Telle, R., and Traon, N., 2019. "Evaluation of dynamic modulus measurement for C/C-SiC composites at different temperatures". *International Journal of Applied Ceramic Technology,* **16**(5), pp. 1723–1733.

[248] Gain, A. K., and Zhang, L., 2023. "Tribological behavior of eutectic Al–12Si alloy manufactured by selective laser melting". *Wear,* **522**, p. 204679.

[249] Xu, K., Noor, A. K., and Tang, Y. Y., 1995. "Three-dimensional solutions for coupled thermoelectroelastic response of multilayered plates". *Computer Methods in Applied Mechanics and Engineering,* **126**(3-4), pp. 355–371.

[250] , 2013. *ABAQUS/Standard User's Manual, Version 6.13.* Dassault Systèmes Simulia Corp, United States.

[251] Kumar, V., and Kumari, P., 2021. "Fabrication and characterization of axially functionally graded beam". In ACMFMS 2020+1.

[252] Kapuria, S., and Kumari, P., 2011. "Extended Kantorovich Method for Three-Dimensional Elasticity Solution of Laminated Composite Structures in Cylindrical Bending". *Journal of Applied Mechanics,* **78**(6), 08. 061004.

TH-3234_176103111

[253] Smith, M., 2009. *ABAQUS/Standard User's Manual, Version 6.9*. Dassault Systèmes Simulia Corp, United States.

[254] Kumar, V., and Kumari, P., 2022. "2-D analytical solutions for the multisegmented panel subjected to arbitrary boundary condition". *ZAMM-Journal of Applied Mathematics and Mechanics/Zeitschrift für Angewandte Mathematik und Mechanik*, p. e202200291.

[255] Efe, G. C., Altinsoy, I., Ipek, M., Zeytin, S., and Bindal, C., 2011. "Some properties of Cu-SiC composites produced by powder metallurgy method". *Kovove Mater,* **49**(2), p. 131.

[256] Chen, W., Wang, J., Wang, S., Chen, P., and Cheng, J., 2020. "On the processing properties and friction behaviours during compaction of powder mixtures". *Materials Science and Technology,* **36**(10), pp. 1057–1064.

[257] Almotairy, S. M., Alharthi, N. H., and Abdo, H. S., 2020. "Regulating mechanical properties of Al/SiC by utilizing different ball milling speeds". *Crystals,* **10**(4), p. 332.

[258] Najafpour, G., Hilal, N., and Ahmad, A. L., 2007, Ch.16. "Chapter 16 - membrane separation processes". In *Biochemical Engineering and Biotechnology*. Elsevier, pp. 351–389.

[259] Sagadevan, S., and Koteeswari, P., 2015. "Analysis of structure, surface morphology, optical and electrical properties of copper nanoparticles". *Journal of Nanomedicine Research,* **2**(5), pp. 40–48.

[260] Yadav, T. P., Yadav, R. M., and Singh, D. P., 2012. "Mechanical milling: a top down approach for the synthesis of nanomaterials and nanocomposites". *Nanoscience and Nanotechnology,* **2**(3), pp. 22–48.

[261] Delhez, R., De Keijser, T. H., and Mittemeijer, E., 1982. "Determination of crystallite size and lattice distortions through X-ray diffraction line profile analysis". *Fresenius' Zeitschrift für analytische Chemie,* **312**(1), pp. 1–16.

[262] Yogamalar, R., Srinivasan, R., Vinu, A., Ariga, K., and Bose, A. C., 2009. "X-ray peak broad-

TH-3234_176103111

ening analysis in ZnO nanoparticles". *Solid State Communications,* **149**(43-44), pp. 1919–1923.

[263] Bindu, P., and Thomas, S., 2014. "Estimation of lattice strain in ZnO nanoparticles: X-ray peak profile analysis". *Journal of Theoretical and Applied Physics,* **8**(4), pp. 123–134.

[264] Mote, V., Purushotham, Y., and Dole, B., 2012. "Williamson-Hall analysis in estimation of lattice strain in nanometer-sized ZnO particles". *Journal of theoretical and applied physics,* **6**(1), pp. 1–8.

[265] Aly, K. A., Khalil, N., Algamal, Y., and Saleem, Q. M., 2016. "Lattice strain estimation for $CoAl_2O_4$ nano particles using Williamson-Hall analysis". *Journal of Alloys and Compounds,* **676**, pp. 606–612.

[266] Venkateswarlu, K., Chandra Bose, A., and Rameshbabu, N., 2010. "X-ray peak broadening studies of nanocrystalline hydroxyapatite by Williamson–Hall analysis". *Physica B: Condensed Matter,* **405**(20), pp. 4256–4261.

[267] Huang, J., Wu, Y., and Ye, H., 1995. "Ball milling of ductile metals". *Materials Science and Engineering: A,* **199**(2), pp. 165–172.

[268] Brebels, A., and Bollen, B., 2015. "Non-destructive evaluation of material properties as function of temperature by the impulse excitation technique". *The e-Journal of Nondestructive Testing,* **20**(6).

TH-3234_176103111

Brief Biodata of the Author

Author's Name: Vivek Kumar

Date of Birth: 9th December 1991

Hometown: Khagaria, Bihar (India)

Educational Details:

Bachelor of Technology (B. Tech) [Completed] with Honors in Mechanical Engineering from Kurukshetra University, Haryana (India), in 2013.

Masters in Technology (M. Tech) [Completed] in Mechanical Engineering (Specialisation in Machine Design) from IIEST Shibpur, West Bengal (India), in 2017.

Doctor of Philosophy (Ph.D.) [Ongoing] in Mechanical Engineering from IIT Guwahati, Assam (India).

Achievements:

During my B. Tech secured 8th rank in the university's top 20 toppers list.

Qualified for GATE (Graduate Aptitude Test in Engineering) in 2014 and 2015.

Contributed as a reviewer in PRIME-2021 (an international conference) organized by the Department of Mechanical Engineering, NIT Patna, Bihar (India) from 5-7th August 2021.

During my Ph.D. won several medals for badminton in inter-departmental, inter-hostel, and campus-level competitions.

List of Publications from the Thesis

Publications in SCI Journals

1. Kumar, V., Kumari, P. (2022) Fabrication and Characterization of Cu/SiC-Based Axially Functionally Graded Beam. *Advanced Engineering Materials* 24(5), 2101239.

2. Kumar, V., Kumari, P. (2022) 2D closed form solution for bending of edge bonded dissimilar beams: an application of EKM. *Composite Structures* 289, 115420.

3. Kumar, V., Kumari, P. (2023) 2-D Analytical solutions for the multisegmented panel subjected to arbitrary boundary condition. *ZAMM - Zeitschrift für Angewandte Mathematik und Mechanik/Journal of Applied Mathematics and Mechanics* 103(2), e202200291.

4. Kumar, V., Kumari, P. (2023). Two-dimensional analytical solution for multi-segmented piezoelectric panel: an EKM approach. *Composite Structures*, 117461.

Publications in International Conferences

1. Kumar, V., Kumari, P. (2021) Fabrication and Characterization of the Axially Functionally Graded Beam. 7^{th} *Asian Conference on Mechanics of Functional Materials and Structures (ACMFMS 2020 +1)*, March 13-15, Tohoku University, Sendai, Japan.

2. Kumari, P., **Kumar, V.** (2022) 2D analytical solution for multi-segmented Auminium-steel-composite panel-An Aerospace Application. 15^{th} *World Congress on Computational Mechanics (WCCM-XV) & the* 8^{th} *Asian Pacific Congress on Computational Mechanics (APCOM-VIII)*, 31st July-5th August, Yokohama, Japan.

3. Kumar, V., Kumari, P. (2022) Processing and Characterization of the Cu-SiC based Func-

tionally Graded Materials (FGMs). 8^{th} *Asian Conference on Mechanics of Functional Materials and Structures (ACMFMS 2022)*, December 11-14, IIT Guwahati, India.

4. Kumar, V., Kumari, P. (2023). 2-D Analytical solutions of segmented piezoelectric panel using extemded Kantrovich method. 11^{th} *International Conference on Materials for Advanced Technologies (ICMAT-2023)*, Suntec, Singapore.

TH-3234_176103111